THIN FILM VAN DER WAALS HETEROSTRUCTURES CONTAINING $MoSe_2$ FROM MODULATED ELEMENTAL PRECURSORS

by

ERIK CHRISTIAN HADLAND

A DISSERTATION

Presented to the Department of Chemistry and Biochemistry
and the Graduate School of the University of Oregon
in partial fulfillment of the requirements
for the degree of
Doctor of Philosophy

December 2018

DISSERTATION APPROVAL PAGE

Student: Erik Christian Hadland

Title: Thin Film Van der Waals Heterostructures Containing $MoSe_2$ from Modulated Elemental Precursors

This dissertation has been accepted and approved in partial fulfillment of the requirements for the Doctor of Philosophy degree in the Department of Chemistry and Biochemistry by:

Shannon W. Boettcher	Chairperson
David C. Johnson	Advisor
James Hutchison	Core Member
Ben McMorran	Institutional Representative

and

Janet Woodruff-Borden	Vice Provost and Dean of the Graduate School

Original approval signatures are on file with the University of Oregon Graduate School.

Degree awarded December 2018

DISSERTATION ABSTRACT

Erik Christian Hadland

Doctor of Philosophy

Department of Chemistry and Biochemistry

December 2018

Title: Thin Film Van der Waals Heterostructures Containing $MoSe_2$ from Modulated Elemental Precursors

Transition metal dichalcogenides (TMDs) are naturally occurring layered materials that have attracted immense research interest due to their high degree of chemical tunability. In particular, $MoSe_2$ has been the focus of significant investigation stemming from reports that it converts to a direct band gap semiconductor material at ultralow dimensions. Yet, as more and more is learned about increasingly thin $MoSe_2$, efforts are now aimed at imparting the novel functionality of $MoSe_2$ into van der Waals heterostructures. This dissertation focuses on synthesis and characterization of novel $MoSe_2$-based nanolaminate structures that have been self assembled from modulated elemental precursors.

The first section describes a new treatment of x-ray fluorescence spectroscopy data and its use as a powerful probe for determining the absolute composition per unit area of a thin film with sub-monolayer accuracy. While this has widespread application in the thin film world, it is particularly useful for MER synthesis in the calibration of modulated elemental precursors. In order to crystallize a target structure, it is imperative to deposit the correct number of atoms, which is now possible with greater precision.

The second section shows the importance of rotational (i.e. “turbostratic”) disorder on lowering cross-plane thermal conductivity in two systems—$MoSe_2$ and the $(SnSe_2)_1(MoSe_2)_{1.32}$ heterostructure. The binary systems exhibits ultralow thermal conductivity that rivals that of WSe_2, yet some interlayer atomic registry was noted in TEM images. By interleaving layers of $MoSe_2$ with $SnSe_2$—which also possesses hexagonal symmetry, but has a significantly larger basal plane—the cross-plane thermal

conductivity was depressed to the lowest reported value in the literature for a fully dense solid.

The final section presents the synthesis and characterization of a new, ternary phase of Bi|Mo|Se. The structure consists of alternating layers of a “puckered” rock salt BiSe lattice and nanosheets of $MoSe_2$. Notably, the $MoSe_2$ sublattice consists of a mixture of the semiconducting 2H phase (~60%) and the metallic 1T phase (~40%). This is the result of electron injection from the BiSe into the conduction band of the $MoSe_2$, which is known to undergo a rearrangement upon reduction.

This dissertation includes previously published and unpublished coauthored materials.

CURRICULUM VITAE

NAME OF AUTHOR: Erik Christian Hadland

GRADUATE AND UNDERGRADUATE SCHOOLS ATTENDED:

University of Oregon, Eugene, OR
Wheaton College, Wheaton, IL
Hamline University, Saint Paul, MN
Pepperdine University, Malibu, CA
Normandale Community College, Bloomington, MN
Taylor University, Upland, IN

DEGREES AWARDED:

Doctor of Philosophy, Chemistry, 2018, University of Oregon
Master of Science, Chemistry, 2015, University of Oregon
Bachelor of Arts, Interdisciplinary Studies, 2009, Wheaton College

PROFESSIONAL EXPERIENCE:

Upper School Science Teacher, Minnehaha Academy, 2011-2014
Merchandise Planning Business Analyst, Target Corporation, 2010-2011
Community Health Education Intern, Asociación Vida, 2009-2010

PUBLICATIONS:

Mitchson, G.; Hadland, E.; Göhler, F.; Wanke, M.; Esters, M.; Ditto, J.; Bigwood, E.; Ta, K.; Hennig, R. G.; Seyller, T.; Johnson, D. C. *ACS Nano* **2016**, *10* (10), 9489–9499.

Hamann, D. M.; Hadland, E. C.; Johnson, D. C. *Semicond. Sci. Technol.* **2017**, *32* (9), 93004.

Gaskins, J. T.; Hopkins, P. E.; Merrill, D. R.; Bauers, S. R.; Hadland, E.; Johnson, D. C.; Koh, D.; Yum, J. H.; Banerjee, S.; Nordell, B. J.; Paquette, M. M.; Caruso, A. N.; Lanford, W. A.; Henry, P.; Ross, L.; Li, H.; Li, L.; French, M.; Rudolph, A. M.; King, S. W. *ECS J. Solid State Sci. Technol.* **2017**, *6* (10), N189–N208.

Hamann, D. M.; Bardgett, D.; Cordova, D. L. M.; Maynard, L. A.; Hadland, E. C.; Lygo, A. C.; Wood, S. R.; Esters, M.; Johnson, D. C. *Chem. Mater.* **2018**, acs.chemmater.8b02591.

ACKNOWLEDGMENTS

Throughout the course of completing this PhD program, I have learned in deeper ways that science is indeed a collaborative venture. And quite simply, we're best together. I have had the distinct privilege of working with extraordinary people here in Eugene, OR, across the country, and to the far ends of the earth. Each of them deserves my most sincere gratitude.

First, I would like to thank my advisor, Professor David C. Johnson. Thank you for taking me on as a student, seeking out the resources I have needed to do this work, and committing to my success. I have learned far more from you than I can catalog in the pages of this dissertation, and I'm sure I've not learned my last lesson from you yet. Both your scientific and gardening abilities are enviable. You should consider a dual appointment.

I have also had the great fortune to work with a tremendous group of Johnson Lab colleagues. My initial mentors, Dr. Gavin Mitchson and Dr. Sage Bauers, patiently helped me develop the skills and understanding I needed to be successful in each and every one of my projects here. In no uncertain terms, I owe them a great deal and they have my profound gratitude. I would also like to thank Drs. Jeff Ditto, Marco Esters, Matthias Falmbigl, Kyle Hite, and Suzannah Wood for all their guidance, helpful suggestions, data collection, and willingness to teach me new things. I must give special thanks to Danielle Hamann and Dmitri Cordova. Whether you knew it or not, you both provided encouragement to me and always helped keep the proverbial and not-so-proverbial gears in the lab greased. Thank you for infusing the lab with both intensity and levity when I needed them. And to two exceedingly capable undergraduate lab members—Alex Lygo and Shannon Fender—I hope you see your valuable contributions to these projects in the pages ahead. Alex, thank you for bringing your physics prowess to our ailing electrical lab. Shannon, thank you for your diligent work ethic and for always asking questions that helped us both understand our data better. And to the myriad other undergraduates, summer students, rotation students, and visiting students, I thank you as well.

I would also like to acknowledge my collaborators, Professors David G. Cahill and Thomas Seyller, along with their graduate students, Hyejin Jang and Fabian Göhler.

Your work and expertise have been essential in bringing these projects to fruition. Additionally, Dr. Doug Medlin from Sandia National Laboratory and Jenia Karapetrova from the Advanced Photon Source have helped in the collection and analysis of data presented in these projects.

Many other University of Oregon faculty and staff must also be recognized. This includes my committee—Professors Shannon Boettcher, Jim Hutchison, and Ben McMorran—and all of my class professors. In a major way, it also includes Kris Johnson and Cliff Dax from the machine shop and the electrical shop. I've lost count of the many times I came to the shop with questions or broken equipment and left with solutions. I cannot overstate my thanks to you both.

Most importantly, I need to thank my family and my partner, Princeton Miles. Simply put, each of you has been indispensable to my success here. You have been constant sources of love, support, and encouragement, and you have enriched this experience for me perhaps more than I've had the good discipline to tell you. I love you all.

Finally, I would like to acknowledge the funding sources that have supported this work, including the National Science Foundation (grants DMR-1266217 and DMR-1710214). The Advanced Photon Source at Argonne National Laboratory is a User Facility under the Office of Science and is operated for the Department of Energy Office of Science. It is supported by the DOE (contract no. DE-AC02-06CH11357). Electron microscopy facilities at Pacific Northwest National Laboratory are supported under DOE contract no. DE-AC05-76RL01830. I would also like to acknowledge the National Center for Electron Microscopy at Lawrence Berkley National Laboratory.

To my parents, Chris and Donna, who have always said “yes” to education and had my back;
To my sister, Siri, who ran a parallel race along with me;
To my partner, Princeton Miles, who encouraged me, supported me, and celebrated with me; and,
To my brand new niece, Josslyn, a poignant reminder for why I study science.

TABLE OF CONTENTS

LIST OF FIGURES

Figure Page

Figure Page

Figure Page

Figure Page

Figure Page

Figure Page

Figure Page

Figure Page

LIST OF TABLES

Chapter I:

HETEROSTRUCTURES CONTAINING DICHALCOGENIDES – NEW MATERIALS WITH PREDICTABLE NANOARCHITECTURES AND NOVEL EMERGENT PROPERTIES

1.0. *Authorship Statement*

The work in this chapter was published as an invited review article for the IOP journal Semiconductor Science and Technology in 2017 (DOI: 10.1088/1361-6641/aa7785). The review is coauthored with Danielle M. Hamann and David C. Johnson. All three authors participated in the literature survey research that makes up the contents of this review. Additionally, all three authors were active in the drafting and revision of the entire article. I am specifically responsible for much of the synthesis overview and sections pertaining to semiconductor heterostructures.

1.1. *Abstract*

Heterostructures unconstrained by epitaxy have generated considerable excitement due to the discovery of emergent properties—properties not found in either constituent. Heterostructures enable the surfaces on either side of two-dimensional (2D) layers to be used to systematically investigate phenomena such as superconductivity and magnetism in the 2D limit. The ability to choose constituents facilitates the prediction of emergent properties created by the unusual coordination environments at incommensurate interfaces. There have already been many reviews on heterostructures, focusing on a variety of topics that reflect the diverse interest in this area as well as the potential for new technologies. Hence this review focuses mainly on the synthesis and structural characterization of heterostructures containing transition metal dichalcogenides (TMD). This review only briefly discusses 2D materials and TMD/TMD heterostructure devices and the performances that have been achieved. This review provides a historical context for the rapid development of this field and discusses proposed mechanisms for emergent properties. Up to now, the materials used in heterostructures have mainly been materials with 2D structures, as these compounds can be easily cleaved into ultrathin layers. This review discusses the expansion of heterostructure constituents to include materials that do not have 2D structures. Structural changes and charge redistribution

between adjacent (or even more distant) layers are likely to be larger for 3D constituents than with 2D constituents based on known misfit layer compounds. Systematic changes in properties with layer thickness, layer sequences, and the identity of constituents will increase our understanding of emergent properties and how they can be optimized.

1.2. *Introduction*

For at least the past half century scientists have been curious about how material properties change as thicknesses are reduced to the atomic scale.[1–4] In the era before scanning tunneling microscopies, there were significant challenges in directly determining the thickness of the samples being studied. Instead indirect methods such as sheet resistance, absorbance or shadowing effects were used to infer thicknesses. Researchers reported very early that naturally anisotropic compounds, such as the transition metal dichalcogenides or graphite, with easily cleavable van der Waals planes were ideally suited to these investigations.[1,3,4] As early as 1966, the "scotch tape" method of cleaving van der Waals solids and isolating finite layers was reported.[1] As dimensions were reduced towards single layers (Figure 1.1), anomalies in exciton binding energy[2] and systematic changes in superconducting properties[3,4] were discovered. Although novel

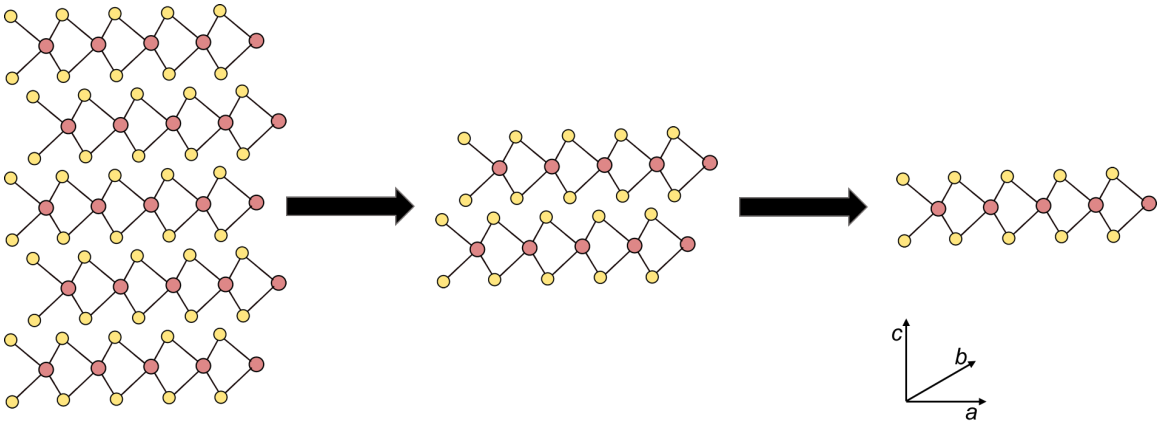

Figure 1.1. Transition metal dichalcogenides are naturally occurring layered materials with highly anisotropic bonding. Weak van der Waals forces along the *c* axis enable them to be easily cleaved to obtain monolayer structures, while strong covalent bonds in the *ab* plane preserve the crystalline structure within a layer during cleaving. The schematic illustrates the structure of five layers *(left)*, two layers *(center)* and a monolayer *(right)*. The arrows represent the thinning of the sample via cleaving.

properties were reported, the analytical challenges in determining thickness and recognizing large domains of constant thickness prevented researchers from discovering that the anomalous properties of materials such as graphene or MoS_2 were intrinsic to single layer thick two dimensional (2D) planes.

During this same era, Arthur and Choi developed molecular beam epitaxy (MBE) at Bell Labs.[5] The ability to use epitaxial interfaces to grow designed sequences of layers of materials with known thicknesses and structure dramatically increased the repertoire of potentially available functional materials.[6] The ability to imagine sequences of structures that could actually be prepared resulted in increased theoretical activity predicting properties and potential devices from proposed nanoarchitectures. Although the compositional sequences produced by MBE are typically not the thermodynamic ground state of the system, they are often sufficiently kinetically stable at normal operating conditions to be used in devices. Figure 1.2 shows a schematic energy landscape of kinetically stable heterostructures where the thermodynamic ground state is a physical mixture of the constituents. Just as in MBE, kinetic stability results from sufficiently high inter-diffusion barriers (the energy maxima in the lines connecting the heterostructures with the ground state) that prevent the layers from interdiffusing. Preparation of artificially layered materials with designed nanoarchitectures via MBE has led to fundamental discoveries in physics, including the quantum Hall effect.[7] Control of the nanoarchitecture has provided access to electronic and transport properties not available in the bulk form, and has led to many critical technology-enabling discoveries such as 2D electron gas,[8] modulation doping,[9] light emitting diodes,[10] and quantum cascade lasers.[11]

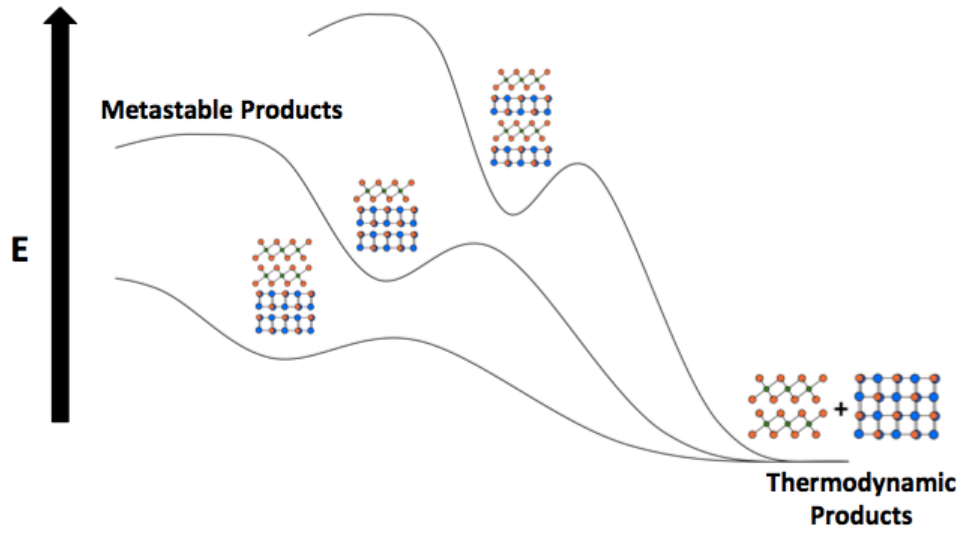

Figure 1.2. Heterostructures are local minima in the free energy landscape and different stacking arrangements will have different energies. The kinetic barrier to forming the thermodynamic mixture of bulk constituents is a consequence of the activation energy for solid-state diffusion.

The development of MBE was a tremendous advance, but is a technically challenging growth technique. Constituents need to have structures and unit cell parameters with close lattice matches between them for epitaxial growth to occur. If the two constituents do not have a close lattice match, then the interfaces will contain a large concentration of dislocations and other defects necessary to reduce the lattice strain. Besides the lattice match requirement, there are also significant challenges associated with finding deposition conditions where material A can be grown on material B and material B can be grown on material A. Finally, the growth of distinct layers at the 2-D limit is exceedingly challenging due to mixing that occurs during growth and the competition between completing the first layer and nucleating the next layer.

While MBE research focused mainly on intergrowths of semiconductors with diamond based lattices, other researchers discovered ways to prepare new materials containing intergrowths of constituents with a variety of different structures. In the early 1980's, Koma, et al. showed that it was possible to grow single layers of compounds containing van der Waals interactions between building units - molecules such as C_{60}, 1D chains such as Se or Te, and/or 2D layers such as the transition metal dichalcogenides - on substrates terminated with a van der Waals surface. [12,13] They demonstrated that the

weak van der Waals interaction between constituents drastically relaxed the lattice matching condition usually required in heteroepitaxial growth. The lack of dangling bonds at the van der Waals surfaces resulted in very abrupt interfaces with small defect levels even with lattice mismatches of up to 50%.[14] The removal of epitaxial constraints dramatically increased the number of combinations of constituents that could be utilized in the preparation of heterostructures. "van der Waals epitaxy" provided the first synthesis route to heterostructures containing ultrathin superconducting, metallic, semiconducting or insulating monolayer dichalcogenides as constituents with controlled and designed nanoarchitecture. [12,13, 14]

Van der Waals epitaxy is an innovative technique that allowed preparation of novel heterostructures, however it is still technically very demanding and the challenges of finding growth conditions compatible with growing material A on material B and B on A are similar to those experienced with epitaxial growth techniques. Around this same time period, chemists discovered thermodynamically stable materials, called misfit layer compounds (Figure 1.3), that contained interwoven monolayers of constituents that in the bulk are superconducting, metallic, semiconducting, magnetic or insulating.[15] These compounds are typically prepared directly from the elements at high temperature and single crystals are prepared via vapor transport.[16] The atomic abruptness of the interfaces in misfit layer compounds results from the distinctly different crystal structures of the constituents. Unfortunately, there is essentially no ability to prepare compounds with different constituent layer thicknesses or nanoarchitectures by changing the synthesis conditions.[15] It is also not possible to prepare isolated monolayers or heterostructured bilayers utilizing these high temperature synthesis approaches. The growth of research in the field of 2D materials and novel heterostructures did not accelerate at this time due to the technical challenges of the available growth techniques and the limited analytical tools available to characterize the resulting materials.

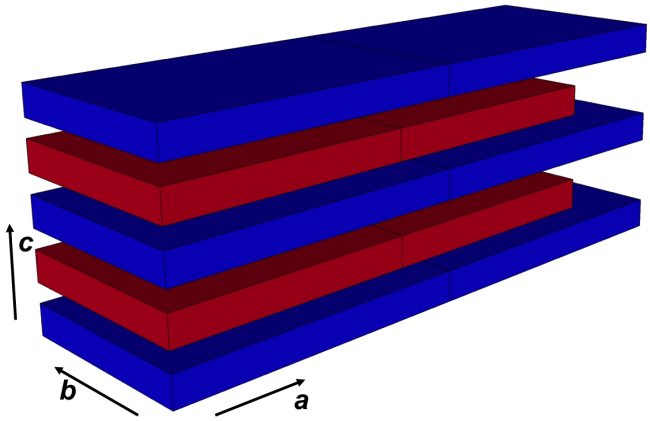

Figure 1.3. Misfit layer compounds are thermodynamically stable heterostructures of alternating layers of rock salt and transition metal dichalcogenide. A defining feature of this class of materials is that they usually possess a single commensurate in-plane lattice parameter.

The activity level in the field of 2D materials has exploded in the last decade fueled by the discovery of novel properties in graphene by Novoselov, Geim and coworkers that resulted in their sharing of the Nobel prize in Physics in 2010.[17–19] This growth in activity is a consequence of analytical advances (scanning probe microscopy, aberration corrected electron microscopes), the rediscovery of the scotch tape approach to cleave van der Waals compounds, and a breakthrough in the use of optical microscopy to rapidly identify crystals of different thickness.[20] The ‘‘Scotch-tape method’’, mentioned earlier, is simple, effective and does not require either a large investment or complicated equipment. The optical contrast mechanism of ultrathin layers on a silicon wafer coated with SiO_2 is now well understood. [21,22] This technique permits the rapid scanning of large areas to identify optimal crystals using a light microscope, which is neither expensive nor complicated. The resulting literature on graphene alone is enormous, with estimates of over 10,000 papers a year being published.[23] The second wave of research in this area has focused on related materials whose bulk structure contains strongly bonded layers separated by weak van der Waals forces, including diverse materials such as hexagonal boron nitride,[24,25] transition metal dichalcogenides,[26–32] fluorographene,[33] and new elemental analogs of graphene - germanane,[34–36] silicene,[37] and phosphorene.[38,39] There are already multiple reviews available on these materials, and the sheer number of papers published makes a comprehensive review daunting. Due to the large amount of literature on the various 2D-materials this review will focus on the emerging field of

heterostructures containing dichalcogenide layers. A schematic of various heterostructures is shown in Figure 1.4. Since there are already excellent reviews that focus on emergent properties and devices,[40,41] this review focuses on the synthesis and characterization of heterostructures.

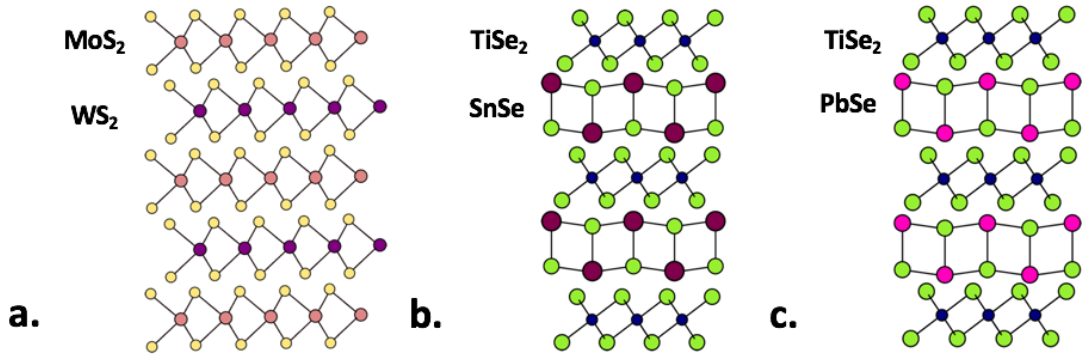

Figure 1.4. Structural schematics of heterostructures composed of various 2D materials. a. MoS_2 and WS_2 - yellow represents S, purple represents W and rose represents Mo. The constituent layers are held together by weak van der Waals interactions. b. SnSe and $TiSe_2$ - green represents Se, magenta represents Sn, and blue represents Ti. The SnSe layer does not have a layered structure, but is a fragment of a distorted rock salt structure. c. PbSe and $TiSe_2$ (green represents Se, blue represents Ti, and maroon markers represent Pb).

Researchers have discovered that the properties of monolayer materials depend on the substrate they are attached to, and that the properties can be emergent - ie. not found in either the monolayer or the substrate.[42,43] This has spawned investigations into heterostructures containing two or more 2D materials combined into a composite, and there have been considerable efforts made to understand the origin of emergent properties.[42–57] Several origins have been proposed for different emergent properties, including changes in band structure due to removing adjacent layers, finite size effects, structural changes with layer thickness, strain, and the presence of adjacent layers as discussed in the following section. We will also discuss the synthesis and characterization of dichalcogenide containing heterostructures.

1.3. *Origins of Emergent Properties*

In the context of 2D materials, an emergent property is a property that does not exist in a bulk compound, but occurs as the material becomes increasingly thinner. Frequently, the emergent property only occurs when thickness has been reduced to a monolayer.[17,26,27] In heterostructures, emergent properties arise when adjacent layers

interact with one another. These properties are not present in the individual constituent compounds.[58] Harnessing the power of heterostructure systems for a variety of uses — optoelectronic, thermoelectric, magnetic, etc. — depends on developing a set of design principles to understand how to optimize emergent properties. For synthetic groups, the ability to precisely control thicknesses and sequences of layers in a heterostructures is a critical task that is necessary for the systematic study of structure/property relationships. For theoretical groups, identifying the combination of layers and their structural characteristics that give rise to a specific set of properties is a challenge. The need is to inform what parameter spaces and nanoarchitectures must be explored to optimize desirable properties. In the following paragraphs, we discuss the underpinnings behind categories of emergent properties, highlighting the discussion with representative examples.

1.3.1. *Changes in Band Structure Due to Removing Adjacent Layers*

Perhaps the most obvious cause for emergent properties in single-layer systems is the removal of electronic interactions between adjacent layers. The loss of orbital overlap changes the band structure and, consequently, gives rise to new properties. Graphene is the prototypic example. Each carbon is sp^2 hybridized, leaving the p_z orbitals—oriented perpendicular to each hexagonal layer—half empty. In graphite, the p_z orbitals in adjacent layers interact to create a filled orbital from the bonding interaction and an empty antibonding orbital. Overlap of these bands causes graphite to be a semimetal. In a single sheet of graphene, this orbital remains half-filled leading to a zero-gap semiconductor with a linear Dirac-like spectrum around the Fermi energy,[59] resulting in the emergent properties discovered by Novoselov, Geim and coworkers.[17] The semiconducting dichalcogenides with trigonal prismatic coordination of the transition metal (MoS_2, $MoSe_2$, WS_2, WSe_2) are a second example wherein emergent properties result from a loss of interlayer interactions.[26,27] In 2010, two independent studies were published that showed MoS_2 transitions from an indirect to direct band gap material in going from a bilayer to a monolayer. [26,27] In 2013, Komsa et al. showed that wave functions at the Γ point extend from the chalcogen atoms into the Van der Waals gap, leading to strong interactions with the d_z^2 orbitals of the transition metal in the adjacent layers (for a 2H polytype).[60] The highest energy position of the valence band in the bulk

is at the Γ point. This band rises in energy due to an antibonding interaction between the layers. In the monolayer, this antibonding interaction is removed, decreasing the energy of this band as it approaches the Γ point, resulting in it being below the energy at the K point. The energy of the conduction band and its general shape do not change significantly with thickness, so the lowest energy point in the conduction band stays at the K point.[61,62] The net result is that the monolayer has a direct band gap.

Since the impact of changing coordination at interfaces is apparent even in systems with weak van der Waals interactions between layers, more significant changes are observed in heterostructures with constituent layers that are more three dimensional. Constituents that in the bulk have a rock salt structure, for example PbSe, distort significantly when they are present as a bilayer in a heterostructures adjacent to a dichalcogenide. The Pb and Se atoms that are in the same (001) plane in the bulk are puckered in the bilayer, with the Pb and Se planes displaced from one another by over 0.2 Å in $(PbSe)_1(MoSe2)_1$.[63] This distortion results from the termination of the rock salt structure and the interaction between the constituent layers. This has significant consequences for the band structure, but also impacts a range of other properties. An example is the surface segregation of alloys. There is a different chemical composition at the surface of an alloy from that in the bulk,[64] because surface energies depend strongly on the crystal structure of the alloy components.[65] Another example is changes in solubility in alloy systems. Sn and Pb are miscible in bilayers of PbSe-SnSe alloys across the entire solid solution, but the bulk phase diagram shows a large miscibility gap.[66] Changes in bonding at interfaces and between constituents at interfaces are likely to become valuable tools used to tune and control properties as they become better understood.

1.3.2. *Finite Size Effects*

As the thickness of a layer is reduced below the de Broglie wavelength of the electron wave function, there is a transition from continuous to discrete energy levels.[67] In 1993, Hicks and Dresselhaus described how changes in the density of states due to localization within a layer could greatly enhance the Seebeck coefficient in heterostructures, specifically calculating potential enhancements in thermoelectric performance for Bi_2Te_3 containing superlattices.[68] They considered the Bi_2Te_3 layer as a

two-dimensional quantum well with potential barriers formed by the physical boundaries of the layer. The calculated band structures showed sharp features in the density of states that were predicted to enhance the thermoelectric power factor.[69] The emergent properties found in graphene were also initially thought to result from changes in electronic structure due to quantum size effects. The discovery of strong photoluminescence in transition-metal dichalcogenides and the crossover from an indirect and direct band gap as thickness is reduced to a monolayer initially lead to speculation that quantum size effects might be a general phenomenon in 2-D monolayers.[26,27] Since these initial reports, MX_2 monolayers, where M (Mo, W) and X (S, Se), have been found to have other novel excitonic properties, including efficient control of valley and spin occupation by optical helicity. [28,29,70–73] Additional studies focused on the fundamental excitonic physics of low-dimensional materials and potential technological applications are being rapidly reported. [73–82]

There has also been considerable effort aimed at distinguishing between properties that emerge in ultrathin materials due to unusual features in their band structure (for example, interactions between layers in the bulk) and features that result specifically from the quantization and changes in energy that result from finite size effects.[62] One strategy for attributing particular emergent properties to either of these two effects is to study properties as a function of relative angle between monolayers or between monolayers and substrate. Figure 1.5 shows a schematic of a rotationally disordered heterostructure. If the phenomena are dominated by a finite thickness phenomena, then the effect of relative rotation angle will be relatively small.[83] If the phenomena are due to interlayer interactions or their removal, then rotation angle will have a pronounced effect.[83] First principle calculations of these systems as a function of rotation angle are challenging, because the size of the supercell varies considerably and is always considerably larger than the primitive unit cell of either a single layer or the stable bulk polymorph. Consequently, atomistic simulations are limited to special twist angles with manageable supercell sizes instead of random orientations. Simpler models that attempt to captures the essential physics are often used. There were extensive studies investigating the properties of bilayers of graphene with rotation angle soon after the novel properties of monolayer graphene were reported, showing that the interlayer

interaction changes dramatically as the angle is changed. [59,84–92] These studies suggest that interlayer interactions, rather than finite size effects, dictate the difference in properties between monolayer and bilayer graphene. Initial studies exploring the effect of rotation angle in bilayers or bilayer heterostructures of Mo and W containing dichalcogenides also show a strong dependence of properties on stacking sequence or rotation angle.[83,93–101] This supports the conclusion that the lack of interlayer bonding is an important factor in the direct band gap and novel optical properties of monolayers of these compounds. [62]

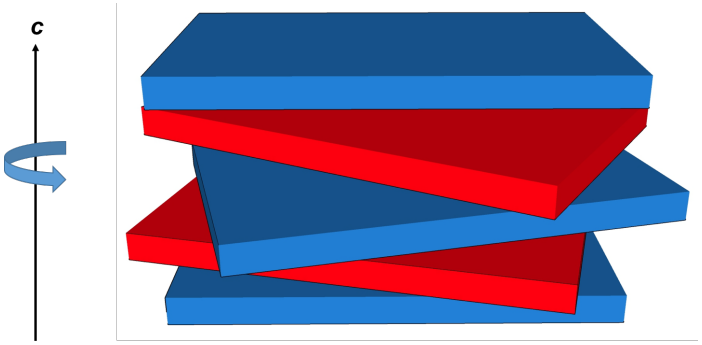

Figure 1.4. Schematic of rotationally disordered constituent layers within a heterostructures. Lattice mismatch between constituent layers will increase the distribution of rotation angles between layers.

1.3.3. *Structural Changes with Layer Thickness*

As suggested in section 3a, the most salient feature of monolayers relative to their bulk counterparts is the removal of the electronic interaction between adjacent layers. For very anisotropic compounds—those with strong bonding within layers and weak van der Waals interactions between layers—the structure of free monolayers has been calculated or assumed to be quite similar to constituent monolayers in the corresponding bulk solid,[102,103] in agreement with many transition electron microscopy images.[104–107] For less anisotropic bulk solids, however, more extensive structural changes might be expected at lower dimensions due to the increased influence of surface energy that results from the removal of adjacent layers. In an infinite crystal, the forces exerted by all the other atoms in the crystal determine the position of each individual atom. At a surface, these forces are altered, and surface atoms experience more asymmetric inter-atomic forces. Consequently, the positions of the surface atoms change from the equilibrium in the bulk,

assuming distinct spacing and/or symmetry. Indeed, surface reconstructions are a common feature of crystalline solids, with specific distortions depending on the crystal face and atoms at the surface.[108] Surface reconstructions can extend into the bulk, with the extent of distortion decreasing as distance from the surface increases. Hence, structural distortions might be expected to change as a function of layer thickness, due to the relative importance of surface and volume free energies.

There is limited data available on the atomic structure of 2D layers, as most analytical techniques give only information about the symmetry of the layer or perhaps only one or two of the three atomic coordinates of the atoms in the 2D layer. Raman and other optical spectroscopies provide information about changes in symmetry and the stacking sequences of layers (i.e. polytypism).[109] A review article was recently written that describes the evolution in Raman modes and lattice vibrations in monolayer, few-layer, and bulk systems.[110] Transmission electron microscopy and scanning probe microscopies provide low resolution information about the in-plane coordinates of the atoms in 2-D layers. In-plane x-ray diffraction provides information about symmetry and the in-plane lattice parameters. The intensities can be used to refine the in plane atomic coordinates if the data is of high enough quality.[111] Partially due to the challenges in obtaining quantitative information about the structure, the majority of studies on mono- and few-layer anisotropic compounds that can be prepared using the "scotch tape" synthesis approach have assumed that the bulk structure is preserved in the monolayer. There are a few studies of heterostructures containing 3-D solids. There is a report of the structure of PbSe layers, which has a cubic rock salt structure in the bulk, as a function of thickness. A bilayer orientated with the (100) planes is the thinnest layer reported, and it has a square in plane lattice but each of the (100) planes distort such that the Pb atoms sit in a plane extending slightly into the van der Waals gap, and the Se atoms are in a plane slightly interior.[112] This puckering distortion is significant, on the order of 0.2 Å. As the PbSe layer is increased, the magnitude of this puckering distortion decreases. The structure of a four-plane PbSe layer distorts to form two bilayers, with a larger distance between the bilayers. The structure of a six-plane PbSe layer distorts to form three bilayers, with the distortion in the center bilayer different than the outer bilayers. By the time the PbSe layer reaches ten planes, the structure looks like the bulk structure with a

surface distortion. This puckering phenomenon and its comparison to the bulk PbSe structure (a) is depicted in Figure 1.6, below. It was suggested that these distortions result from the interplay between surface and volume free energies.[112]

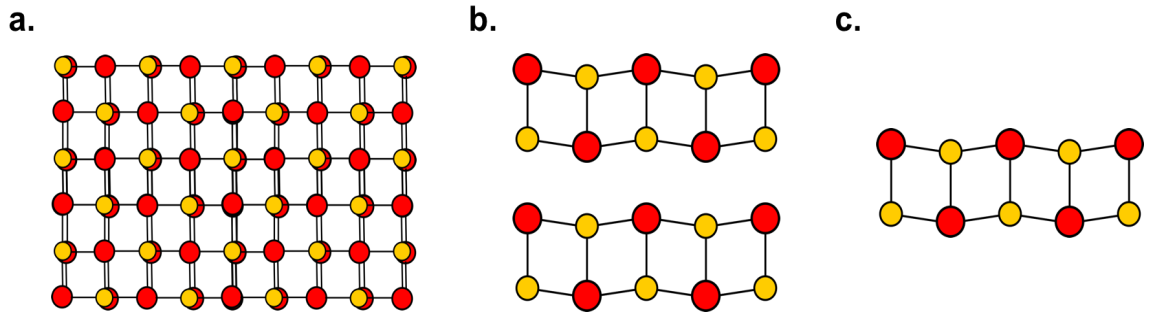

Figure 1.5. As rock salt bulk compounds are reduced to ultrathin dimensions, the lattice becomes increasingly "puckered" such that metal cations extend into the van der Waals gap while the chalcogens occupy atomic positions on the interior of the bilayer. (a) the bulk rock salt crystal structure (b) Two stacked bilayers of a puckered rock salt structured constituent (c) Structure of a single puckered 2D rock salt bilayer. The metal atoms are shown in red and the chalcogen atoms are shown in yellow.

Similar changes in structure with thickness was reported for SnSe layers sandwiched between dichalcogenide layers.[113–118] Bulk SnSe possess an orthorhombic unit cell. However, a bilayer of SnSe was found to have a square basal plane when interleaved between either $MoSe_2$ or $TaSe_2$ layers.[113,114] Interestingly, the SnSe lattice was found to have a rectangular basal plane when interleaved with $NbSe_2$,[115] showing the importance of adjacent layers. The in-plane lattice parameters in this heterostructure became increasingly different as the thickness of the SnSe layer increased.[116] Around 40 planes of SnSe are required before the lattice parameters resemble the bulk compound. Similar changes in structure are anticipated as other 3D solids are prepared as 2D layers. The changes in the structure of 2D layers of 3D solids with thickness reflects the changes in the bonding at the internal surfaces, which provides an additional mechanism to tune properties. The unique environment between 2D layers may also make it possible to prepare structures as 2D layers that are not stable as 3D solids.[117,118]

1.3.4. *Strain*

Strain has historically been a valuable tool used in semiconductor technology to optimize properties and performance in today's microelectronics devices.[119] In traditional

semiconductor devices, strain is typically created during epitaxial growth through lattice mismatch at interfaces. For fundamental studies of strain, external forces can be applied in a variety of ways to plastically deform the material in question. These studies have a long history, with the first report of strain-enhanced mobility in *n* and *p* type bulk Si and Ge occurring in 1954.[120] Many papers have explored the effect of strain on bulk materials, thin films, and epitaxially grown layers, including superlattices.[121,122] It is not surprising that soon after the discovery of the remarkable properties of graphene, strain was theoretically and experimentally explored as a tool to modify properties. [123]The effect of strain on graphene has been recently reviewed.[123]

Researchers have explored the effect of strain on properties of novel 2D materials using various approaches.[60,123–126] Theoretically changing the lattice parameters is relatively easy, and it is common, for example, to create supercells with varying degrees of strain to approximate rotational angles between layers. As Komsa and Krasheninnikov have pointed out, however, it is difficult to distinguish which features originate from the monolayer or stacking of the monolayers and which are due to the strain artificially introduced into the system to make the calculations easier.[60] Experimentally straining graphene and other 2D materials is challenging because the weak interlayer van der Waal forces that make these materials cleavable and chemically stable as monolayers also make them resilient to deformations induced by epitaxy. Indeed, dichalcogenide heterostructures epitaxially grown by Koma and coworkers[124] and epitaxial growth of TMD mono- layers on graphene[125] both resulted in layers with lattice constants very close to those of the bulk and the isolated monolayers. This is a consequence of the energy cost for straining the lattice and exceeding the incremental bonding energy between layers. van der Waal forces are significantly weaker than the covalent bonds found at the interfaces of epitaxial III-V heterostructures. The weak interlayer bonding in van der Waals heterostructures does not provide a sufficient energy barrier to trap growing layers in their strained state during growth.[60]

Researchers have been clever in using a variety of approaches to strain 2D monolayers, and the large volume of research published in this area has recently been reviewed.[126] Monolayers have been placed on substrates that have different thermal expansion coefficients, resulting in increasing strain as a function of temperature. Two-

dimensional materials have also been placed on flexible substrates, which, when bent create a tensile strain on the top of the substrate and a compressive strain on the bottom. This strain can also arise if a 2D material is placed on an elastic substrate. Compressive stress is created if the substrate is elongated before the 2D material is applied, while tensile strain occurs if the 2D layer is placed on the substrate and is subsequently elongated. In a similar manner, the piezoelectric effect can be used to stretch or compress a 2D layer on top of a suitable substrate. The van der Waals bonding between the monolayer and a substrate can maintain approximately 1% strain before releasing. A monolayer can be tacked in place by an edge coating of metal, increasing the magnitude of achievable strain. Releasing strain on a monolayer can produce layers with controlled wrinkling. This is typically accomplished by positioning a 2D layer on a stretched substrate and then releasing the tensile strain on the substrate. Micro Raman spectroscopy is a valuable tool to investigate local strain in 2D materials and heterostructures and this technique will be discussed in more detail later in this review.[127–129] Strain will continue to be a valuable tool in the pursuit to tune the properties of monolayers to both understand fundamental interactions and create devices.

1.3.5. *The Presence of Adjacent Layers*

Monolayers may be thought of as one-dimensional "particle in a box" situations, with the electrons of the layer confined to that layer. Because the potential barriers at the walls of the box are not infinite, the wave functions extend outside of the box for a couple of angstroms, decaying exponentially. These extended wave functions interact with adjacent layers or surfaces causing the layer properties to be modified.[42] This interaction with adjacent layers can significantly modify the band structures of the individual 2D layer, even though no real chemical bonds are formed between them.[43] The resulting properties of the 2D layer depends on the alignment of bands between that 2D layer and the substrate, the density of states of each material, and the extent of charge transfer due to electrons having different chemical potentials in the various constituents. In semiconducting 2D layers, for example, the exciton binding energy and the quasiparticle band gap are influenced by the choice of substrate material and also by excited electrons within the 2D layer.[44–47] When a semiconducting single layer transition metal dichalcogenide is placed on a metallic substrate, a strong band gap renormalization is

observed.[48,49] Interactions between monolayers and a substrate can be strong enough to modulate electronic properties even if the interface is not epitaxial.[50,51] The number of papers describing different behaviors of monolayers on various substrates is rapidly expanding and researchers are investigating a wide range of monolayers and substrates both theoretically and experimentally.[52–57] Theoretical predictions about non-lattice matched monolayers are complicated by the large unit cells required to avoid introducing significant strain into the constituents and by the difficulties in treating the van der Waals interactions and charge transfer at interfaces.[60,130] Experimentally, applying a gate voltage to a substrate or changing the Fermi level by chemical doping are both being used to discover new phenomena in 2D monolayers.[131,132] The dependence of properties of monolayers on changes in chemical potential provide a mechanism to create novel sensors.[133,134]

1.4. *Heterostructures Containing Transition Metal Dichalcogenides*

Adding an additional layer (or layers) on top of a monolayer on a substrate, creating a three-component sandwich, produces additional complexity. Since many potential devices will use monolayers that are buried as part of an overall architecture, research in this area will expand considerably as the ease of both manipulating monolayers and directly growing different monolayers on top of one another increases. We will refer to these composites as heterostructures, and heterostructures of transition metal dichalcogenides are the topic of the rest of this review article.

Heterostructures will grow in importance as a research field for a variety of significant reasons. First, devices will require additional layers (top and bottom) to provide electrical contacts, protect the monolayers from damage, and to generate emergent properties through the interaction between layers. By judiciously choosing adjacent top and bottom layers, existing properties can be modified and novel properties can be created. The ability to predict the structures and properties of heterostructures that have not yet been created provides an opportunity for theorists to create models to probe for unique effects in systems that have not been experimentally prepared.[135] These predictions will provide significant motivation to prepare the identified systems. The resulting differences in properties from those predicted and their dependence on nanoarchitecture will lead to a greater understanding of structure-property relationships.

There is already an impressive number of papers that describe the properties of heterostructures containing graphene,[55,136–158]and a growing number of papers that describe heterostructures containing one or more dichalcogenide and the properties that arise from the interaction between constituents.[159–162] In the future, new constituent layers will be prepared and assembled with control of both thickness and the sequence of layers. Researchers will have a set of building blocks to create new materials where the nanoarchitecture and resulting interaction between constituents provide the tools to discover novel and optimize known properties. Perhaps, much like a building is designed using optimally designed composites of concrete and steel, new materials will be designed by creating nanocomposites with specific architectures to optimize emergent properties for targeted applications. This will require the development of an understanding of how emergent properties of 2D layers arise and how 2D layers interact to form composites that outperform individual materials.

1.4.1. *Synthesis*

Due to their promising applications in a wide variety of devices, [163] researchers have devoted considerable effort to discovering efficient means of synthesizing monolayers and heterostructures, with ongoing efforts aimed at producing uniform structures over large areas. The "scotch tape" method enables the preparation of heterostructures composed of different monolayers, but the micromechanical manipulations require considerable skill and patience. There are also concerns about surface contamination that can affect the properties of the resulting heterostructures and the technique is limited to constituents that can be isolated and stabilized as monolayers.[137,141,164,165] However, micromechanical exfoliation is a surprisingly robust approach and there are many reports of new combinations of constituents and novel device structures being prepared using this technique.

While most of the initial work has been based on monolayers cleaved from single crystal materials, there has been substantial interest in developing approaches that provide monolayers over sizeable areas. A number of transition metal dichalcogenides have been prepared on a variety of substrates using chemical vapor deposition, sputtering and other vacuum deposition approaches where the chemical fluxes and substrate

temperatures are controlled to grow a defined number of layers of a desired material. [166–171] When the layers are parallel to the substrate, the challenge in these growth techniques is controlling the conditions to completely grow each layer before nucleating the following layer. This challenge arises from the limited number of variables that can be easily controlled, including the mass flow of reactants and temperature profiles. The synthesis of vertically oriented layers, needed for catalytically active samples, is more challenging, typically requiring a template layer.[172,173] The nucleation and growth issue is addressed by Koma's van der Waals epitaxy growth technique,[12–14] which has grown in use all over the world. A wide variety of new systems prepared using this approach are reported every year.[138,171,174–179] The in-situ monitoring of growth using low energy electron diffraction enables the growth conditions to be systematically optimized, but achieving layer-by-layer growth is challenging. A third approach to prepare a defined number of layers is to deposit a limited amount of the metal and then react this metal layer at low temperatures with chalcogen containing reactants. Both ALD[136,180–182] and physical deposition approaches[183] have been used to deposit a defined amounts of metal, however confirming that exactly a monolayer has been deposited is challenging. In a related approach, it has been shown that exchange reactions can be used to change oxide films into chalcogenide films while preserving the structure and thickness of the original film. [184]

In parallel with these layer-by-layer vacuum based growth techniques discussed briefly above, there has been a significant effort to develop low cost solution processing approaches to 2D materials.[140,184–191] Many compounds with layered structures can be exfoliated in solutions using a variety of approaches (ion intercalation, ion exchange, sonication) as summarized in several reviews.[192–194] The key to exfoliation is finding a combination of solvent and starting layered material such that the interaction of the layers and ions within the solvent is larger than the interaction between the layers of the starting layered material. For neutral systems such as graphene, the solvent-graphene interaction needs to be large to compensate for the loss of bonding between the graphene layers. For starting materials containing ions, the enthalpy of solvation of the cations needs to overcome the bonding between layers and the entropy loss associated with organizing solvent molecules around the ions. Exfoliated layered materials, which have been used

for centuries in a variety of applications, continue to grow in importance. Researchers have discovered applications ranging from catalysts and sensors, which take advantage of both unusual properties and large surface areas,[187] to polymer-exfoliated clay composites used as gas diffusion barriers.[195] Assembly of the 2D sheets created by exfoliation into heterostructures range from a sheet-by-sheet assembly of specific stacking sequences to self-assembly of sequences from solutions.[186] Groups are beginning to use liquid phase printing and spin coating techniques to make simple devices from solution precursors.[139] The scalability of solution processing and its low intrinsic cost relative to vacuum processing approaches gives solution processing a unique niche that will continue to expand.

The challenges involved in the synthesis of heterostructures with targeted nanoarchitecture are different than those in the traditional synthesis of new alloys or compounds. Since most targeted heterostructures will be metastable, the traditional high temperature or fluid phase mediated synthesis approaches that mostly yield thermodynamic products will not work. It has been recognized that approaches that control kinetics and reaction intermediates, such as molecular beam epitaxy, are required. A number of interesting approaches to dichalcogenide-containing heterostructures are being developed that rely on preparing a precursor containing some of the structure of the targeted heterostructure, which is then further processed using approaches that preserve the structure of the precursor (Figure 1.7).[66,183,196–201] The appeal of these approaches is that they avoid the challenges of finding suitable growth conditions as needed for van der Waals epitaxy, so several different constituents can be prepared on top of one another (ie A on B or C, B on A or C, and C on A or B) which is required to prepare complex layer sequences with multiple constituents. Encouragingly, theory groups are beginning to explore the growth process, which can provide insights into why some approaches work and also potential new approaches to try.[202,203]

The fundamental underpinning of the post processing of designed precursors is surprisingly similar to that involved in traditional organic synthesis. In both cases precursors are designed and then reacted to obtain desired products, with the reaction conditions and or design of the precursor used to favor the formation of targeted products. Diffusion constraints (temperature and/or protecting groups) are used to direct the system

towards desired products. The concept of energy landscapes[204] provides a valuable framework to potentially understand how the structure of the precursor and/or the reaction conditions enables the synthesis of metastable heterostructures.[205]

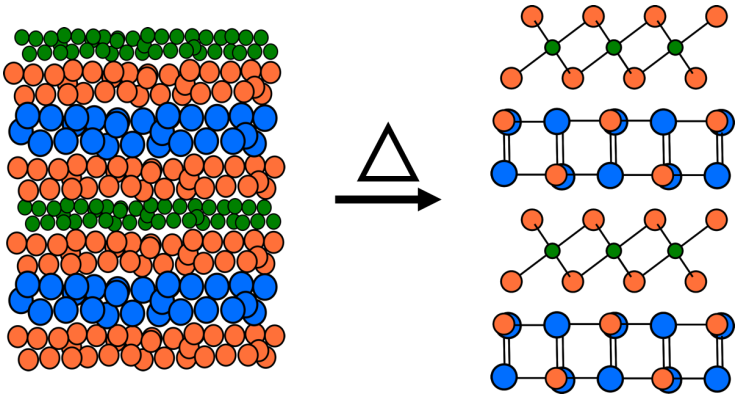

Figure 1.6. Synthesis of metastable heterostructures from a precursor with defined amounts of elements deposited. The precursor is annealed at low temperatures to self assemble the desired heterostructure.[205]

1.4.2. *Characterization*

Characterizing the structure of constituent layers within heterostructures is critical, as most emergent properties will be intimately connected with structural changes at the interfaces or throughout the thin layers. These structural changes may be due to the large surface to volume ratios in the individual constituents and/or due to interactions between the constituents. Understanding the interplay between synthesis conditions and the structure as well as the density of defects present in the heterostructures is very important, and it is limited by the ability to characterize the samples. Characterizing even the average structure of a 2D monolayers or heterostructures is, however, a major challenge due to the small amounts of material present. Determining parameters such as local and average layer thickness, bond lengths and average composition are significant analytical challenges. The development of new analytical tools, for example the easily observed optical interference pattern differences between graphene and SiO_2 as a function of the number of layers,[21,22] has been and will continue to be critical as this field advances. Numerous techniques have already been used to determine different structural features of heterostructures as discussed in the following paragraphs.

Measuring thickness of layers, both locally and over larger areas, has been a known challenge in this field. Historically, thickness was estimated through resistivity[4] or

electron microscopy measurements.[1] In the resistivity measurements, researchers assumed a constant resistivity and used the resistance per square to determine thickness.[4] The electron microscopy experiments used both cross sections and the extent of shadowing to measure thickness. [1] Both optical interference[21,22] and scanning tunneling microscopy measurements were critical new tools used by Geim[19] and Novoselov[18] to determine the thickness of different regions as they probed the properties of graphene as a function of layer thickness. Additional tools need to be developed to speed the selection of heterostructured samples and preparation conditions.

Several different x-ray techniques have been used to determine the thickness and structure of thin film samples. X-ray reflectivity (XRR), an in-FAB metrology tool in the semiconductor industry, is very sensitive approach to measuring thickness.[206] Figure 1.8 shows a calculated reflectivity pattern (middle blue trace) for a heterostructure containing 8 $MoSe_2$ trilayers and two experimental attempts to prepare an 8 layer $MoSe_2$ film. The XRR pattern represents the sum of the intensities gathered over a relatively large, cm^2 sample area. The top pattern clearly deviates from that calculated for the ideal sample, with the low angle portion of the scan, which is dominated by front surface and back surface interference, having a different period than the higher angle portion of the scan (10-13°), which is dominated by the incomplete destructive interference of the $MoSe_2$ trilayers. This suggests that while the sample contains regions with the targeted 8 trilayers of $MoSe_2$, other regions are thinner than targeted. The bottom experimental pattern closely resembles the calculated pattern, indicating that the majority of the sample contains the targeted 8 trilayers. One challenge in interpreting XRR data remains determining which interfaces in a sample dominate the intensity pattern. Ellipsometry is a complementary tool that can be used to determine film thickness. Extracting thicknesses from ellipsometry data requires assumptions about the index of refraction at the wavelengths used. Resonant X-ray reflectometry (RXRR) is a developing tool that is, in principle, capable of determining complex chemical composition profiles in a non-destructive manner, as data collected at different energies greatly constrains potential structures.[207] A challenge in extracting detailed, quantitative information from XRR, elipsometry and RXRR data is the needed to construct models. While software exists to optimize models to fit experimental data, it is possible for incorrect models to do

reasonably well in fitting limited data sets, so complementary information from other analytical techniques that can be used to develop initial models is very valuable.

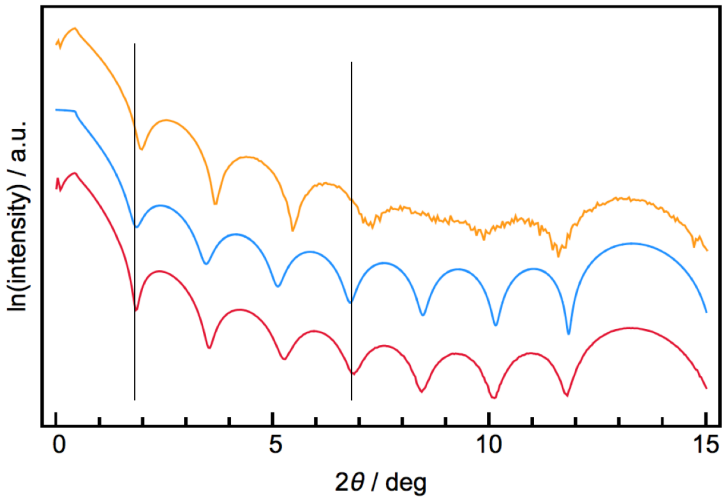

Figure 1.7. Calculated (blue) and experimental (red and yellow) XRR patterns for $MoSe_2$ films containing 8 layers.

For heterostructures containing more than one repeating layer sequence, specular x-ray diffraction provides a convenient tool to quantitatively determine the average position of atomic planes within the repeating layer sequence. There are relatively few examples in the literature where specular x-ray diffraciotn and subsequent refinement are used to determine the location of atomic planes.[208–210] Figure 1.9 contains the specular diffraction pattern of $(PbSe)_1(MoSe_2)_1$ along with a calculated pattern and the difference between them, where Rietveld refinement was used to optimze a model for the structure. The optimized structure is shown in the inset of Figure 1.9, with the inter plane distances from the model graphically displayed by the layer seperation. Due to the alignment of constiuents parallel to the substate, only the *c*-lattice parameter can be extrated from the specular diffraction pattern and the refinement provides the location of the individual planes of atoms in the *c*-direction, as well. From the arbitrary locations of the atomic planes, the interplanar distances can be determined and any deviations from the bulk structure will be observed. From this model the Mo-Se intra unit distance was found to be 0.151 nm and places the Mo plane of atoms symetrically between the two Se layers.[63] The metal layer in the dichalcogenide might not always be centered, however, as asymetric heterostructures might cause planes of atoms to shift due to the forces caused

by the presence of different neighboring layers. In the PbSe consituent, there is a disortion of the rock salt layer due to the termination of the rock salt structure and the attraction and repulsion of the cations and anions respectively to the neighboring dichalcogenide layers. The distance between the $MoSe_2$ and PbSe layers was calculated to be 0.331 nm, which is longer than the van der Waal's gaps in pure dichalcogenides, presumably due to the layers having incommensurate structures.[63] The use of Rietveld refinement with models informed by complimentary techniques allows for fairly accurate determination of constituent layer crystal structures within layered materials.

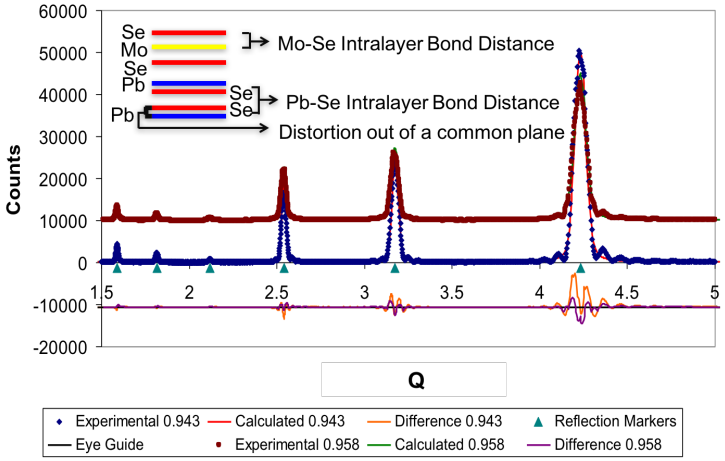

Figure 1.8. Locked-coupled theta-2theta X-ray diffraction used to understand the layer thickness of stacked unit cells of a PbSe-$MoSe_2$ heterostructure. A Rietveld refinement was conducted to optimize the structure to understand where planes of atoms are located. The inset shows a schematic of the structure of the compound with parameters that can be determined using Rietveld refinement.[63]

In-plane diffraction patterns can be used to obtain the in-plane symmetry and lattice parameters as well as additional information about the basal plane structure of the film's constituents. Figure 1.10 contains the in-plane diffraction patterns of a 4-layer, 8-layer, and 24-layer $MoSe_2$ film. The reflections in the patterns can be indexed assuming a hexagonal unit cell and the indices are shown on top of each diffraction maximum. Since all expected (*hk*0) reflections are observed with the anticipated relative intensities, the sample consists of randomly oriented domains within the large (cm^2) analytical area. The change in intensity of the reflections between patterns correlates to the difference of the thickness of material in the beam. If the sample were to contain only a single orientation, then rotating the film would result in a set of maxima corresponding to the symmetry of

the crystal system—i.e. a "pole figure" scan. If there is a second constituent in the heterostructures, the in-plane diffraction pattern would contain additional reflections, as shown in Figure 1.11 for a SnSe-$NbSe_2$-$MoSe_2$ heterostructure. The observation of all expected (*hk*0) reflections again indicates that the sample consists of domains of all orientations.

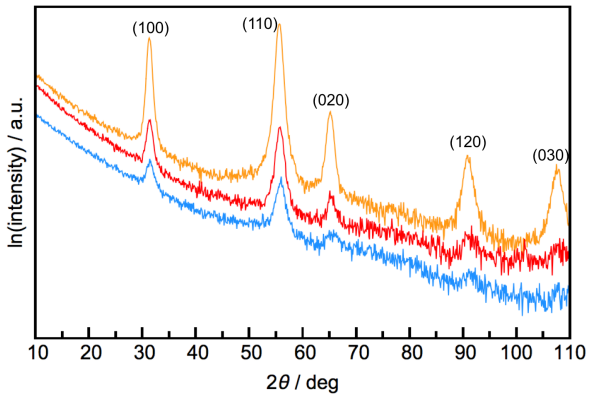

Figure 1.9. In-plane diffraction of $MoSe_2$ films with 4, 8, and 24 layers (blue, red, and yellow, respectively). All maxima can be indexed as (*hk*0) reflections of hexagonal $MoSe_2$ to determine the basal plane lattice parameter.

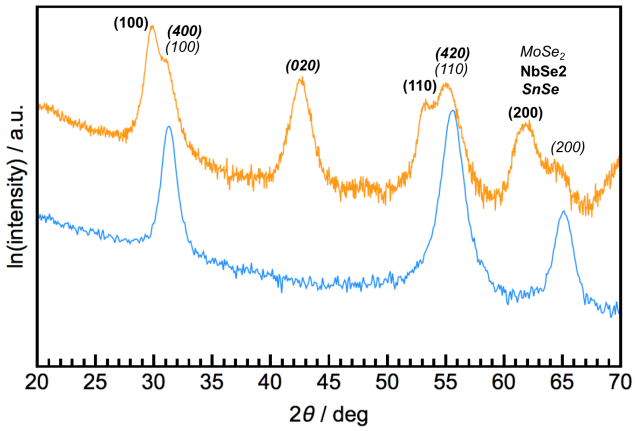

Figure 1.10. The in-plane diffraction pattern of a 24-layer $MoSe_2$ film is shown in blue. The yellow pattern is an in-plane scan of a $MoSe_2$- SnSe- $NbSe_2$ heterostructure. The additional maxima can be indexed as SnSe and $NbSe_2$ reflections, enabling the lattice parameters of all three constituent structures to be determined.[200]

Reciprocal space maps can be used to elucidate the extent of interlayer ordering. Figure 1.12 shows the reciprocal space map of $(PbSe)_1(WSe_2)_1$.[63] In this map, there are no distinct (hkl) reflections expected from the super lattice. Only broad maxima from the PbSe and WSe_2 are observed. This is consistent with extensive, random rotational

disorder between constituents. Rotational disorder is not surprising in heterostructures due to the strong in-plane bonding in constituent layers. Even when one system is chemically "soft" due to a more three-dimensional structure, such as the SnSe containing heterostructures shown in the diffraction figures, the small energy difference between different stacking configurations and the kinetically controlled synthesis approaches used to make them will both likely prevent the system from finding a distinct, low energy, long range stacking arrangement. The rotational disorder and resultant lack of (hkl) diffraction maxima limits the ability to determine average bond lengths both within and between constituent layers.

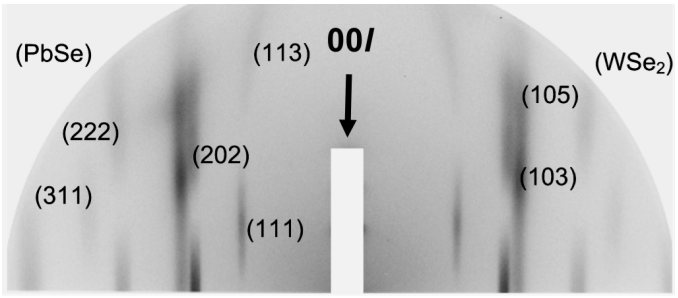

Figure 1.11. Reciprocal space map of a PbSe WSe_2 heterostructure. For both PbSe and WSe_2 there are no distinct reflections that correspond to the super-lattice period, only streaking indicating extensive rotational disorder between constituents.[63]

Transmission electron microscopy has been an indispensable tool for obtaining structural information about constituent layers and the relative orientation between them.[20,111,211–216] For example, plan view HAADF-STEM images of monolayer MoS_2 show that the molybdenum and sulfur atoms are arranged in a hexagonal configuration with Mo-S and Mo-Mo separations of ~0.19 and ~0.33 nm respectively.[211] This is consistent, within error, to the bulk structure which contains Mo trigonal prismatically coordinated by S.[211] Cross section HAADF-STEM images also corroborated trigonal prismatic coordination of Mo by S. Cross section HAADF-STEM images of all six possible heterostructure isomers containing 4 bilayers of SnSe and 4 $MoSe_2$ trilayers in the repeating unit showed that the Mo is trigonal prismatically coordinated by Se, but that there was extensive rotational disorder between adjacent $MoSe_2$ layers and between $MoSe_2$ and SnSe layers.[212] A schematic illustration of these isomers is shown in Figure 1.13. It is also possible to use HAADF-STEM images to obtain the average separation between atomic planes as demonstrated by Mitchson, et al.[111] The interplanar distances

from these experiments can be used to create initial models for Rietveld analysis of x-ray diffraction data. The location of specific atoms within monolayers and the distribution of elements between layers in heterostructures can be determined using HAADF-STEM contrast or EDX-STEM data.[213,214] These examples demonstrate how various STEM analytical techniques provide direct structural information. This insight is valuable for heterostructures both at a local level and to provide structural models for the interpretation of more global analysis techniques. Determining fine scale information, such as interlayer and interatomic distances, will become increasingly important to explain changes in properties.

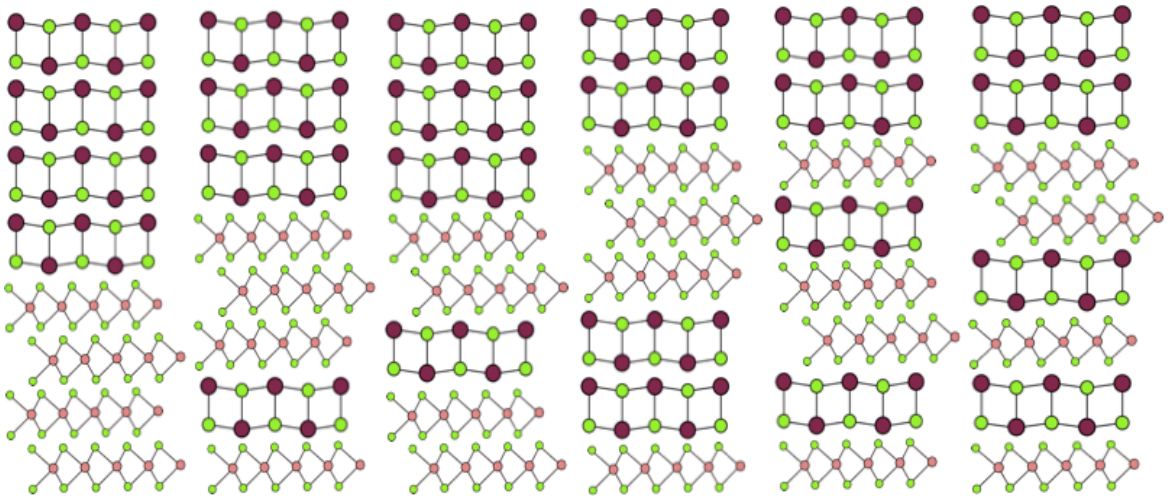

Figure 1.13. Schematic illustrations of the 6 possible sequences of layers requiring 4 dichalcogenide and 4 rock salt bilayers without repeating a portion of the sequence. Repeating one layer of each structure 4 times or two layers of each structure twice create an eight layer repeat pattern with four layers of each structure, but segments are repeated.

Scanning probe techniques offer another route to determine the structural arrangement of atoms in both monolayers and the top layers of heterostructures.[217–220] A particularly valuable use of scanning tunneling microscopy/spectroscopy has been to examine the effect of synthesis parameters on the structure and defect levels of the resulting samples.[217] Scanning probe microscopy provides the ability to map electronic states and correlate them to topographical features and specific arrangement of surface atoms.[218] Probing changes to surface structure and electronic states as a function of exposure to atmosphere or different gases is particularly important to understanding the differences in properties of samples prepared in various environments.[219] Scanning probe

microscopy is a critical tool to determine changes in thickness of layers transferred using the scotch tape approach.

Measuring composition is a significant challenge in heterostructures due to the small amount of material, small probe sizes, and resulting small analytical volumes present in many common approaches. Electron or ion beam techniques are particularly challenging due to the small analytical volumes of the probe beam in the layer of interest relative to the analytical volume buried in the substrate. While the substrate signal can be reduced by changing the accelerating energy of the beam, this also affects the excitation probabilities for different transitions in the layer being probed. Energy dispersive spectroscopic (EDS) techniques suffer from the need to subtract relatively large background signals, whereas wavelength dispersive spectroscopic techniques (WDS) have a significantly smaller background signal. This makes WDS more appropriate for trace element analysis. Instrumentation improvements are required to increase the signal level necessary to obtain both relative composition and absolute quantitative amounts. Ion beam approaches, such as time of flight secondary ion mass spectroscopy (tof-SIMS), have the sensitivity to detect monolayers, but rigorously quantifying the ion yields has also proven difficult.[221] For large area samples, techniques such as x-ray fluorescence might provide enough signals, due to the increased area probed, to quantify the extent of fractional layers, but quantifying the geometric factors affecting the signal is challenging. Atom probe tomography is another approach to determine both composition and structure, and has been shown to be particularly useful to determine local occupancies of dopant atoms in 2D heterostructures.[222]

Raman spectroscopy is the most common analytical tool used to probe 2D materials,[109,223–228] because characteristic vibrational modes can be used to identify specific monolayer materials and polytypes.[229] It is a quick, non-destructive probe of small areas and does not require complicated sample preparation. The high-frequency intralayer vibrational modes of different dichalcogenides each have characteristic frequencies. These high frequency interlayer modes do not shift much in energy or intensity from the bulk dichalcogenide with the same local coordination of the transition metal (octahedral or trigonal prismatic).[229] The low-frequency breathing and shear modes, however are different for each polytype.[109] Once vibrational modes for different materials

are tabulated, the Raman spectra of monolayer samples can be used to determine the local coordination and stacking motif of the layers. In few layer dichalcogenides and in heterostructures stacks, the changes in local symmetry due to the limited number of layers results in new Raman active modes.[230] For heterostructures or multilayer samples where the layers are not rotationally aligned, the interlayer breathing and shear modes can be highly sensitive to variation of the twist angle.[231] This complicates the Raman analysis of heterostructures and multilayers with random twist angles, and complementary techniques that more directly probe structure, such as electron or scanning probe microscopies, are frequently used in parallel.

Raman spectroscopy has become one of the first tools used for probing the properties of layered dichalcogenides and therefore has been the subject of multiple reviews. We refer interested readers to these excellent reviews. Zhang, et al. has discussed changes in Raman of transition metal dichalcogenides as a function of thickness, from monolayer to bulk. [110] A review by Saito, et al. covers the fundamentals of the polarization dependence of the Raman intensity and the Raman tensor. Zhang, et al. provide a more comprehensive review of different types of layered chalcogenides.[232] They demonstrate how low frequency modes can be used to probe the rotational angle between layers in a bilayer and to investigate the interlayer coupling of vertically stacked dichalcogenides in heterostructures.[229] Puretzky, et al. beautifully illustrate this point, using complementary electron microscopy data to demonstrate how low frequency Raman modes due to interlayer vibrations serve as fingerprints to characterize the number of layers and their stacking configurations.[233] These papers and the references they contain provide valuable insight into the importance of Raman spectroscopy as a quick initial probe of heterostructures.

1.5. *Properties*

An iterative relationship between theory and experimental probing of physical properties, particularly in the nascent stages of discovery, greatly accelerates advancing a field. Optimizing the properties of dichalcogenide-based heterostructures through rational design is in an early stage and the number of potential heterostructures is enormous even if confined to those containing dichalcogenides.[214] The more theory can be informed by

experimental data and vice versa, the faster progress there will be in predicting and engineering the properties of particular heterostructures.

An advantage of transition metal dichalcogenides as constituents of heterostructures is the wide range of properties that are known in the bulk compounds. Layered dichalcogenides can be metallic, superconducting, semiconducting, semimetallic, catalytically useful, and potential photocatalysts. A wide range of 2D magnetic properties can be found in closely related MPX_3 compounds where a phosphorus dimer substitutes for a transition metal in the hexagonal metal layer.[234–244] Transition metal dichalcogenide containing heterostructures provide an entire new set of parameters, including but not limited to - modulation doping via charge transfer between constituents, layer specific alloying, stacking sequence, rotation angle, and non-periodic graded structures - to combine, tune and/or optimize properties. Relative to more traditional tetrahedral semiconductor-based layered architectures, the chalcogenide surface layers of dichalcogenides provide the ability to abruptly change both structure and composition. The lack of covalent bonding between layers allows for a range of rotation angles between the constituent layers and for their structures to be independent of one another. This field is just beginning and the following sections review recent progress with the discussion grouped around common properties or materials.

1.5.1. *Semiconducting Heterostructures*

Emergent phenomena in dichalcogenide monolayers were first discovered in semiconducting group 6b (Mo, W) dichalcogenides. MoS_2,[26,27] $MoSe_2$,[70] WS_2,[245] and WSe_2[31] have all been reported to transition from an indirect to a direct band gap as thickness is reduced to a single monolayer. Since monolayers of these compounds are relatively easy to isolate and are stable in ambient conditions, these systems and their emergent properties have proven amenable to extensive investigation. The group 6b dichalcogenides all contain a central plane of trigonal prismatically coordinated transition metal atoms, while the tin atoms of the semiconducting SnS_2 and $SnSe_2$ compounds, which adopt TMD-like layered structures, are all octahedrally coordinated. It is interesting to note that bulk tin dichalcogenides, like the group 6b analogues, are indirect band gap semiconductors, yet at the monolayer limit, tin dichalcogenides have both have been reported to maintain the indirect band gap.[246]

In heterostructures containing these and other semiconducting dichalcogenides, the band alignment between the constituents is critically important in determining properties (see Figure 1.14). In so-called type I band alignment, the band gap of one material falls entirely within the bandgap of the other material. In type II band alignment, the two band gaps are offset from each other such that $EVB_{,1} < E_{VB,2} < E_{CB,1}$ and $E_{CB,1} < E_{CB,2.}$ In type III ("broken") band alignment, the band gap of one material falls entirely within the valence band of the other material. The first reference to heterostructures of semiconducting dichalcogenides we could find in the literature was on $SnS_2/SnSe_2/SnS_2$ heterostructures published in 1999. Van der Waals epitaxy[12] was used to prepared these heterostructures and a series of measurements were done to determine band offsets.[247] The recent interest in 2D materials has resulted in several papers reporting band offsets of heterostructures as a function of twist angle between bilayers,[93] and between different dichalcogenides that are stacked on top of one another.[248,249] There has also been considerable interest in lateral heterostructures – i.e. the in-plane junction of two different dichalcogenides.[250] Both calculations and scanning tunneling experiments examining lateral 2D heterostructures have been reported.[157,251]

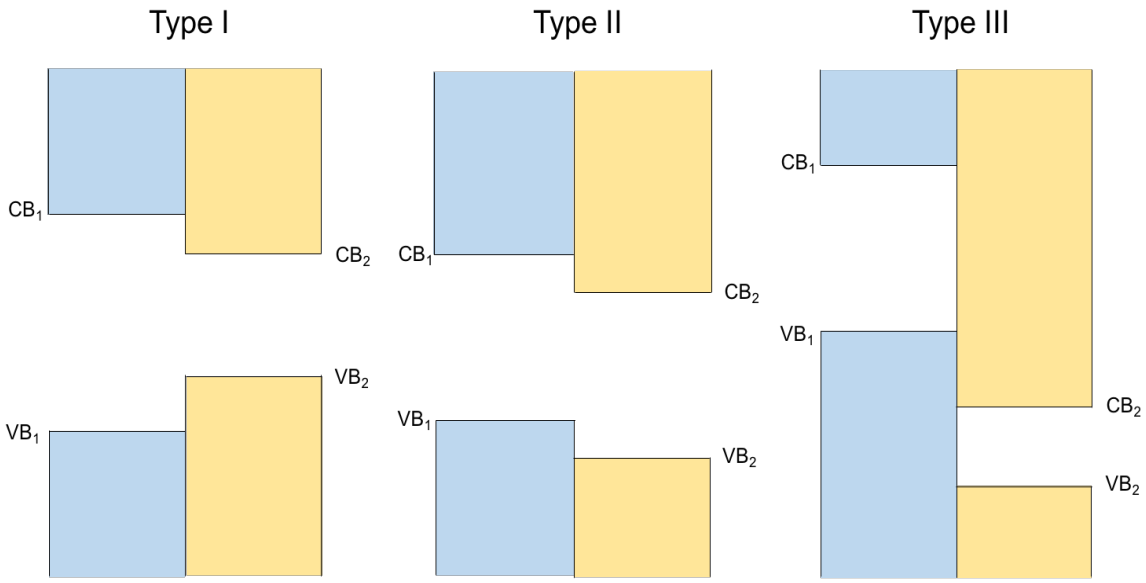

Figure 1.12. Band alignments in semiconducting heterostructures fall into one of the three categories depicted. In type I heterostructures, the band gap of one material falls entirely within the band gap of the other material. In type II heterostructures, the two band gaps are staggered such that $CB_2 < CB_1$ and $VB_2 < VB_1 < CB_2$. In type III, the band gap of one material falls entirely within the valence band of the other material.

The band alignment has an important influence on the carrier dynamics of electron-hole pairs created when light is absorbed (i.e. "excitons"). If a heterostructure has type II alignment, for example, the electron-hole pair created by the absorption of a photon in one layer can reduce its energy by transferring either the electron or hole to the adjacent constituent. In MoS_2-WS_2 heterostructures the holes can substantially reduce their energy by transferring from the MoS_2 to WS_2 and vice versa for electrons.[252,253] Significantly, the transfer of the hole between layers does not depend on the orientation of the layers, so epitaxy is not required, and this result implies that lattice mismatch should not affect the transfer rate.[253] This has been confirmed by subsequent reports showing ultrafast charge transfer in MoS_2-WSe_2,[254] $MoTe_2$-MoS_2[255] and $MoSe_2$–WSe_2[256] heterostructures. Since an electron-hole pair is tightly bound in 2D monolayers and there is a momentum mismatch between randomly rotated layers, the efficient and ultrafast charge transfer between layers has significant implications for devices prepared from heterostructures. Consequently, various aspects of the charge transfer mechanism have been explored both theoretically[257–259] and experimentally.[159] Figure 1.15 summarizes the optical transitions expected for heterostructures with type I and type II band alignments.

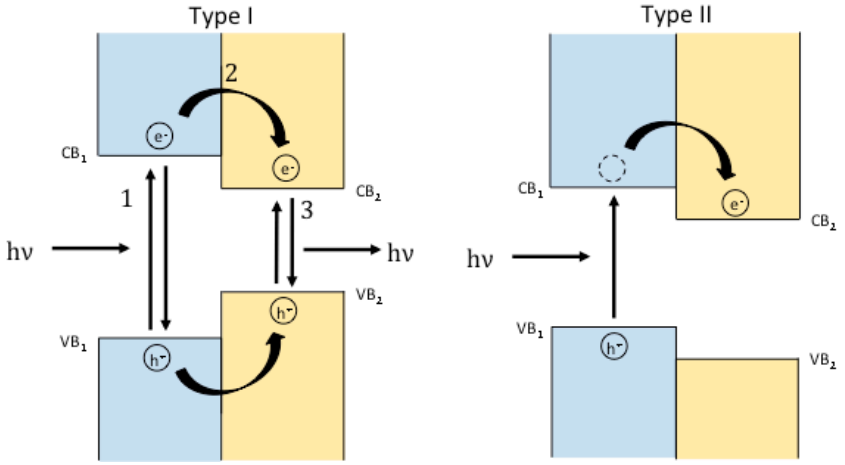

Figure 1.13. In type I alignment of the bands, photons can be absorbed if the energy of the incident light is above the respective band gaps, forming excitons. The kinetics of charge transfer between the constituents (labeled 2) and the ratio of initial absorption between the two constituents will determine the relative intensities of light emitted at the different band gap energies. In type II alignment, formation of the exciton occurs in one constituent layer and electrons will transfer into the adjacent material to achieve a lower energy state, resulting in an interlayer exciton. Since the constituents are separated only by the small van der Waals gap, the two charges remain bound.

The discovery that monolayers of the group 6b dichalcogenides have direct band gaps and the discovery of fast charge transfer in heterostructures containing them has spawned research into the electronic properties of these systems and their derivatives. These dichalcogenides interact strongly with light at the ultimate monolayer limit[260] and host highly stable excitons (i.e. high binding energies, extended lifetimes),[56,261,262] which has resulted in exciting studies that either probe or exploit these properties. The substrate influences the excitons[154] but some properties, such as the conservation of spin-valley polarization during charge transfer between two monolayers, have been found to be only weakly dependent on the twist angle between layers.[161] The unique properties of dichalcogenide monolayers and the heterostructures built from them provides a promising platform for light–matter interaction experiments[260,263] and has resulted in a continuing stream of papers building devices to take advantage of these properties. The devices include light emitting tunneling diodes,[150] floating gate memory,[156] photovoltaic devices,[160,264] and high sensitivity,[151] broadband,[153] and large area detectors.[265] Dichalcogenide nanosheets are also being explored as efficient photocatalysts and electrocatalysts for the production of hydrogen.[187,266,267] There has been considerable interest in the growth and properties of lateral heterostructures – in-plane junctions of two different dichalcogenides.[250,268] Alloying either the transition metal[269] or the chalcogen[270] can be used to tune most of the important properties of these dichalcogenides, including structural phase transitions,[271] band offsets,[272] band gaps,[273] and resulting device properties.[68,274] This field is rapidly advancing, and ultimately the emergent properties of semiconducting TMD monolayers and heterostructures may find practical applications in lasers, light-emitting diodes, detectors, and photovoltaics. The next decade will see a significant growth in our understanding of the relationship between the structural nuances of TMD's in heterostructures, such as the importance of the interactions between layers, between constituents and substrates, between the active and protecting layers, and the resulting optoelectronic properties. This understanding will be of paramount importance for the efficient optimization of the emergent properties. The ability to construct novel heterostructures with reasonable assurance that they can be made provides value to predicting their properties. These predictions will significantly speed the development of this area.

1.5.2. *Metallic Heterostructures*

The transition metal dichalcogenides, structurally related compounds, and other compounds that are potential heterostructure constituents offer a wide array of interesting properties that should, in principle, change as a function of thickness. While most of the early work has been on semiconducting monolayers, due to their novel emergent properties, the group IV and V group transition metal dichalcogenides offer additional and distinctly different opportunities. The group IV and group V transition metal dichalcogenides are semimetallic or metallic. There have been extensive studies aimed at understanding superconductivity, charge density waves, catalyst activity, and intercalation phenomena in the bulk group IV and V dichalcogenides.[275–277] The nanoscale thickness and monolayer properties of the metallic and semimetal compounds are less explored because they are typically less stable in normal atmospheric conditions than the semiconducting systems. For example, atomically thin $NbSe_2$[278] and TaS_2[279] have been reported to be unstable under ambient conditions. These stability challenges have been overcome by covering the sample with a protective layer[280] or by preparing a heterostructure containing the dichalcogenide layer of interest sandwiched between protective layers that are more stable under normal atmospheric conditions.[281,282] Properties such as superconductivity and charge density waves have been shown to be thickness dependent, but as discussed below there are often considerable differences between literature reports.

There is an earlier body of literature that provides important structural data and ideas for the current interest in heterostructures containing isolated single nanosheets of layered group IV and V dichalcogenide compounds. Thermodynamically stable heterostructures of Ti, Cr and the group V dichalcogenides were prepared starting in the late 1980's by the groups of Wiegers,[283] Meerschaut,[284] Onoda[285] and Gotoh[286]. The properties of these compounds provide valuable insights for heterostructures being pursued today. These compounds were prepared by a direct reaction of the elements at high temperature, and are thermodynamically stable compounds. Single crystals can be grown using vapor transport reactions. As an example, combining Pb, Nb and Se and heating the elements to ~1000°C results in a so called misfit layered compound containing single $NbSe_2$ layers separated by a unit cell thick layer of distorted PbSe.[287] The fact that this is stable relative

to a mixture of PbSe and $NbSe_2$ indicates that the interaction between the layers is strong, even though there is not an epitaxial relationship between the constituents. It has been suggested that charge transfer between constituents creates a significant electrostatic bond between the layers that stabilizes these compounds,[288] although there is still considerable debate.[289] The physical properties change considerably as constituent layers are altered, and there are several extensive reviews reflecting significant interest in the structure and physical properties of these unusual compounds.[15,290] None of these compounds have charge density wave transitions, but many of them are superconducting. Compounds with atoms containing magnetic moments, such as rare earth atoms, displayed magnetic order.[15] In these misfit layered compounds, the structure of each layer typically distorts to create one common in plane lattice parameter while the other axis is incommensurate.[290]

Analogs of the crystalline misfit compounds can be prepared via low temperature synthesis routes. Compounds prepared by this route contain a random twist angle between layers, which, in the clay literature, is called turbostratic disorder.[291] These turbostratically disordered polymorphs, called ferecrystals, have been shown to have charge density waves, different superconducting properties than their analogous crystalline properties, and extraordinarily small thermal conductivities.[292] The variation of heterostructure properties as a function of constituent pairings and the rotation angle between them shows the importance of layer interaction in property determination. By extension, the surface on which a heterostructures is placed will also impact property measurements. The existence of thermodynamically stable misfit compounds - monolayers of dichalcogenides with a fragment of a 3D structure between them - suggests that there are many other heterostructures, combinations of 2D layers and 3D fragments of structures, that should be, at a minimum, kinetically stable.

The ability to predict the structures of layers and their potential combinations has already resulted in a significant theoretical effort exploring potential constituents, combinations of constituents, and their potential properties. The electronic structure and band alignment of monolayers of transition metal dichalcogenides in heterostructures has been systematically investigated, exploring interfacial charge polarization and redistribution.[248] Due to both the random twist angles between layers and the different

lattice parameters for various constituents, the charge polarization and redistribution both deviate from conventional epitaxial semiconducting heterostructures based on tetrahedral semiconductors. Researchers have investigated structural and charge density wave phase transitions by probing how substrates, charge transfer between constituents, and electrostatic gating impact physical properties.[293,294] Researchers have begun to explore the properties of 2D fragments of 3D structures, for example a unit cell (or two atomic planes) of the group IV monochalcogenides, in searching for potential emergent properties.[295,296] The stability of CuS 2D layers as a function of thickness was recently reported.[297] The impact of the twist angle between ultrathin layers of Bi_2Se_3[298] and the specific arrangement of different cations within a dichalcogenide layer[299] on potential topological states has been explored, as well. Extending these studies to probe potential heterostructures would be useful for experimentalists, and the misfit layer compounds provide an opportunity to compare predictions with experimental data. One aspect yet to be explored are the energy differences between different 2D slices of a 3D structure.

Experimentalists have also been exploring both new compounds and composites to probe for emergent properties. Research has explored doping known compounds with structures that appear to consist of interleaved 2d layers to create emergent properties that might be replicated in designed heterostructures. Knowing the distribution of the doping atoms between the layers is important for understanding the origin of superconductivity[222] and is important in determining the amount of modulation doping required to induce superconductivity in a heterostructure. Alemayheu, et al. showed that it is possible to prepare heterostructures containing fragments of 3D structures by preparing several new VSe_2-$GeSe_2$ heterostructures. In this report the thickness of the VSe_2 block was varied while a monolayer of $GeSe_2$ was maintained.[197]

There has been considerable interest in finding a magnetic layer that could be used in the construction of heterostructures to probe topological properties and potential devices. One approach has been to create an interface between a magnetic insulator and a 2D layer to create a strong interfacial exchange field.[158] A second approach has been to find compounds containing magnetic ordering in layers that have strong bonding in a 2D layer separated by van der Waals bonding. The MPX_3 family of compounds, where M is Mn, Cu, Fe, In, … and X = S, Se, are semiconducting compounds due to strong electron

correlation between the layers, but result in magnetic ordering within each layer of magnetic ions.[226] Ultrathin flakes of non-magnetic members of this same family have also been explored as ferroelectrics.[300] Heterostructures containing different thicknesses of SnSe and PbSe alternating with blocks of MSe_2 trilayers (M=V, Nb, Ta) show systematic changes to the structure of the SnSe or PbSe block with thickness, and also display systematic changes in Hall coefficient and resistivity.[112,116,282,301,302] These results, while not inclusive of all that has been reported, illustrate the large number of potential heterostructures that can be prepared and several different approaches to discover emergent properties or optimize them for potential device applications.

A relatively general phenomenon that has been observed in both metallic monolayers and metallic heterostructures is an upturn in the resistivity as the temperature is lowered below approximately 30K. This has been observed in NbS_2 as the thickness is decreased[303] and also in a number of heterostructures.[201,281,304] In both the pure dichalcogenide and the heterostructures, the upturn becomes more pronounced as the thickness of the metallic layer is decreased. In the heterostructures, the upturn becomes more pronounced as increasing thickness of a semiconducting constituent separates the metallic dichalcogenide layer. The upturn in resistivity is not observed in crystalline metallic misfit layer compounds with identical composition and sequential layers as found in the ferecrystals, suggesting that the upturn is related to the disorder.[305]

Charge density wave (CDW) transitions have been extensively explored in both heterostructures and as a function of thickness of dichalcogenide layers. This interest stems from the fundamental interest in the effect of dimensionality on the CDW[165,306–310] and the potential use of CDW materials in optoelectronic devices[311] and quantum information processing.[312] Controlling the thickness of a dichalcogenide layer or the layer sequence and thickness in a heterostructures might potentially enable the CDW transition to be tuned to an optimal temperature or enable it to be controlled by an electric field.[167,313,314] A relatively large spread of reported CDW transition temperatures have been reported for nominally the same compound. For instance, an ordering temperature above 100K was reported for atomically thin $NbSe_2$,[165] while a lower ordering temperature CDW order (~ 25 K) was reported for a monolayer $NbSe_2$ grown on

graphene.[315] There are several different reports on how the CDW changes as the number of VSe_2 layers are reduced. VSe_2 exhibits a CDW transition at 100K in the bulk.[316] The onset of the CDW in thin layers of VSe_2, prepared via liquid exfoliation, is 135 K as thickness is reduced to 4-8 trilayers.[317] Micromechanically exfoliated nanoflakes have lower onset temperatures which decrease to 81K at the lowest thickness.[307] Studies of $[(SnSe)_{1.15}]_m(VSe_2)_n$ prepared by annealing designed precursors have shown that compounds with a single layer of VSe_2 separated by *m* layers of SnSe are p-type metals with a CDW that depends on the thickness of SnSe.[302] Increasing the VSe_2 layer thickness to two or more layers results in low temperature n-type metals and the suppression of the pronounced effect in transport properties at the CDW transition temperature is similar to bulk VSe_2.[318] The influence of surface contaminations, the effect of different constituents, and/or the substrate on the charge density wave transition are only beginning to be explored or discussed in the literature. Encapsulation of the dichalcogenide layer of interest has been shown to enhance the CDW order in $TiSe_2$.[319] Similarly, TaS_2 layers were encapsulated by covering them with boron nitride.[279] VSe_2 layers prepared in situ from designed precursors have shown reproducible CDW transition temperatures and systematic changes as the thickness of either the VSe_2 block or SnSe has been changed.[302,318] These results suggest that much of the observed variability of results is a consequence of the instability of monolayers of the metallic dichalcogenides under ambient conditions. It might be possible to systematically control the CDW transition temperature of heterostructures through the choice of constituents and/or controlling the position of the Fermi level through modulation doping.

Given that some of the earliest investigations of ultrathin dichalcogenides by Frindt investigated superconductivity as a function of thickness, it is surprising that until recently there has been little attention directed in this area. This seems to have changed in 2016, with several high profile reports of well-defined 2D superconducting states in atomically thin $NbSe_2$,[320] TaS_2[321] and doped MoS_2[322]. It is important to note that there were earlier reports of superconductivity in atomically thin flakes of $NbSe_2$ prepared by mechanical exfoliation which demonstrated that the carrier density in these 2D layers could be changed by an electric field. [323] While traditionally carrier concentration is altered by chemical doping via atom substitutions, changing carrier density with an

electric field minimizes potential complications such as impurity scattering. There have been several papers that show enhancement of the effective electron–phonon coupling constant, due to the change in phonon modes in monolayers.[165,278,315] All studies show a decreasing superconducting critical temperature as the thickness of the layers is decreased, although the values reported for samples of the same dichalcogenide with nominally the same thickness are different.[131,165,278,279,305,315,320] The variations may be due to different doping levels caused by neighboring layers or substrates, as Alemayheu reported a systematic increase in the Hall coefficient of $(SnSe)_1(NbSe2)_n$ heterostructures as n was decreased to 1.[324] A similar trend was observed in $(PbSe)_1(NbSe_2)_n$ layered structures,[305] although the amount of charge transfer was different due to changes in the band alignment as SnSe[281] was replaced by PbSe.[325] Researchers exploring the superconducting and structural properties of FeSe layers on a variety of substrates have reported similar modulation doping effects.[52,132,216,326–333] Adjacent layers or adsorbed surface species have begun to be used to investigate the interaction between two phenomena, for example superconductivity and ferromagnetism.[334] Monolayers are particularly sensitive to modulation doping, and phase transitions can be controlled by changing the Fermi level of adjacent layers through doping.[51] The investigation of superconductivity in 2D material is poised to see dramatic growth, as the ability to prepare stacks of constituents with different intrinsic properties will enable the interaction between phenomena to be investigated systematically.

The thermal conductivity of monolayer dichalcogenides and the heterostructures built from them has intrigued researchers since the first report, in 2007, of ultra-low thermal conductivity in heterostructures containing dichalcogenides.[335] Subsequent reports have reinforced the idea that the ultra-low thermal conductivity in the stacking direction of the turbostratically disordered heterostructures results from the random twist angles between adjacent dichalcogenide layers and between the various constituent layers.[212,336–338] Low thermal conductivity of thermodynamically stable misfit layer compounds have been correlated with the density of stacking faults between adjacent layers.[339] The in-plane thermal conductivity of the heterostructures is a factor of 3 to 5 higher in the systems that have been measured, with the absolute value probably correlated with the in-plane grain size of the constituent layers.[340] The thermal conductivity of a monolayer has been

calculated to also be anisotropic.[341] The ultra-low thermal conductivity of heterostructures provides opportunities to control the temporal features of heat pulses, which might be useful in designing phase change memory devices.

The very low thermal conductivity of heterostructures containing dichalcogenides has led to heterostructures being investigated as potential thermoelectric materials. Promising thermoelectric performance in dichalcogenide based materials have been reported for intercalates, due to the lowering of thermal conductivity and the ability to optimize carrier concentration.[342,343] Low lattice thermal conductivity and promising un-optimized power factors have been reported for dichalcogenide monolayers.[344,345] The thermodynamically stable misfit layered compounds have also been investigated as thermoelectric materials, with promising un-optimized figures of merit.[346,347] The ability to prepare heterostructures of dichalcogenides with desired thicknesses of various constituents and targeted layer sequences provides an opportunity to optimize performance while gaining a better understanding of interactions and bonding between different constituent layers.[348] The ability to prepare heterostructures with junctions between constituents that have very different properties provides an avenue to increase efficiencies[349] and discover novel phenomena.

Topological phases, including topological insulators and Weyl semimetals have been the focus of recent attention, including the 2016 Nobel Prize in Physics to David Thouless, Duncan Haldane, and Michael Kosterlitz. Many of the most common materials studied for the topological properties consist of strongly bonded layers weakly connected by van der Waals bonding. For example, $HfTe_2$, $MoTe_2$ and WTe_2 have all been reported to be topological Weyl semimetals[178,350–353] while bismuth chalcogenides, Bi_2Te_3, Bi_2Se_3 and their alloys, are the prototypic topological insulators.[354–367] Both absolute size of the particles being investigated[368] and chemical doping have been used to produce new phenomena.[369] From a materials perspective, heterostructures containing very thin constituent layers might be useful in reducing contributions from the bulk, enabling exotic topological states to be both easier to study and utilize. Heterostructures also potentially provide an avenue to prepare materials with different properties adjacent to one another,[370] for example a ferromagnetic layer adjacent to a superconducting layer,

with a defined interface between them. The use of heterostructures to probe topological properties is just beginning.

1.6. *Summary*

The ability to prepare and manipulate monolayers of dichalcogenides and other 2D materials as building blocks for heterostructures provides scientific challenges and opens new opportunities. Challenges include:

- Developing approaches to synthesize heterostructures over large areas with control of individual constituent layer thicknesses and the sequence of layers.
- Advancing measurement techniques to characterize the local composition and structure of each constituent layer.
- Developing theoretical approaches to predict band alignments, the extent of charge transfer between constituents, structural distortions and properties of heterostructures with incommensurate interfaces.

The new opportunities include:

- Predicting the structure of an essentially infinite number of new heterostructures, enabling theorists to predict the properties of compounds yet to be made.
- Creating interfaces where atoms are in unusual coordination environments, potentially leading to the discovery of more emergent properties.
- Designing heterostructures that combine multiple technologically desirable functionalities in adjacent constituent layers that tend not to co-exist.
- Using the concept of an energy landscape to develop synthetic routes to the infinite number of potential metastable heterostructures.

Tremendous progress has been made in the past decade developing approaches to make monolayers of specific compounds, understanding the origin of emergent properties at the monolayer limit, and identifying how properties change as monolayers are placed on different substrates. Understanding how incommensurate layers interact, how different combinations of constituents lead to emergent properties, and how to utilize new properties in devices are likely to dominate this field of research in the coming decade. The potential outcome of these efforts will be materials by design, with constituents and nanoarchitecture of heterostructures optimized for predicted emergent properties and the desired function of the total material in a specific device.

1.7. *Overview of Dissertation*

There is an immense body of literature that has attested to the promise of group VI TMDs in next generation semiconductor and nanoelectronic devices. This dissertation is aimed at expanding an understanding how nanoarchitecture—mainly rotational (i.e. "turbostratic") disorder and heterostructuring—affects structure, thermal transport, and electronics of $MoSe_2$- containing thin film systems. Chapters 2 and 3 outline experimental methods and characterization theory for the preparation of large area nanolaminate thin film. Chapter 2 largely focuses on x-ray scattering techniques that provide insight into structural features. Chapter 3 was published in 2018 as a collaborative effort of all current members of the David Johnson lab—Danielle M. Hamann (primary author), Dylan Bardgett, Dmitri Leo Cordova, Liese A. Maynard, Alexander C. Lygo, Suzannah R. Wood, Marco Esters, and David C. Johnson. The study recasts the use of x-ray fluorescence (XRF) spectroscopy for thin film systems with sensitivity to sub-monolayer thicknesses. Notably, this study shows how XRF may be used to determine the number of atoms of a given element per unit area, rather than simply a relative composition. My primary contribution to this work was to prepare a series of thin films with rigorously defined structures and known compositions that could be used as standards for the calibration procedure outlined in the paper.

Chapters 4-6 each consist of experiments that have been written for independent publication in the near future and of which I am the primary author. Chapter 4—written with Hyejin Jang, Niklas Wolff, Robert Fischer, Gavin Mitchson, Alexander C. Lygo, Lorenz Kienle, David G. Cahill, and David C. Johnson—demonstrates how rotational disordered in $MoSe_2$ films has tremendous implications for lowering cross-plane thermal conductivity in an otherwise well-defined crystalline system with precise layering schemes. For the first time, this rotational disorder has been probed by local-level plan view nanobeam electron diffraction in which the electron beam is aligned to the axis of crystallite rotation. Chapter 5—written with Hyejin Jang, Gavin Mitchson, David G. Cahill, and David C. Johnson—extends this study to the $MoSe_2/SnSe_2$ heterostructure in which the two interleaved structures possess a significant lattice mismatch. Effectively, this serves to further decrease structural registry between layers and depress cross-plane thermal conductivity to record breaking low values. Chapter 6—written with Fabian

Göhler, Gavin Mitchson, Thomas Seyller, and David C. Johnson—shows the synthesis and structural characterization of a novel intergrowth of BiSe and $MoSe_2$. Notably, it shows how the BiSe sublattice may be used to donate electrons into $MoSe_2$ layers to change the coordination of the Mo metal center from the semiconducting trigonal prismatic (2H) arrangement to the metallic octahedral (1T) arrangement.

Chapter II:
EXPERIMENTAL THEORY AND CHARACTERIZATION

2.0. *Authorship Statement*

I am the primary author of this chapter, and I consulted with my advisor, David C. Johnson, regarding the content related to diffraction.

2.1. *Modulated Elemental Reactants Theory*

Early solid-state synthesis techniques commonly rely on the interdiffusion of constituent materials to form a gradient of compositions across the diffusion region. Achieving mobile species in the solid phase requires high temperatures that routinely exceed 1000 °C. Where the composition matches that of a stable phase, nucleation occurs, and the new phase grows. However, a primary limitation of these early techniques is that the high temperatures limit the accessible end compounds to thermodynamically stable phases. In turn, these synthetic routes are generally limited in their ability to access metastable compounds.

Films investigated in this thesis were synthesized using the modulated elemental reactants (MER) technique.[1,2] Unlike high temperature syntheses discussed above, which depend on long-range diffusion, MER is a low temperature technique. In short, rather than starting with monoliths which must interdiffuse and nucleate new phases in one step, MER is a two-step synthesis that begins with the preparation of a layered elemental precursor. This precursor is designed to possess a local composition which closely matches that of the target compound. Effectively, this local composition matching eliminates the need for long-range diffusion, changing compound formation from a diffusion-limited process to a nucleation-limited process.[3] In turn, new families of metastable products are accessible.[4]

Preparing the precursor is accomplished by MER synthesis, which is a physical vapor deposition (PVD) technique. Elemental source materials are heated using effusion cells and electron beam evaporators to create plumes of vapor phase metal species. Adjusting the power applied to the heating elements controls the flux toward the substrate (i.e. “deposition rate”), which is located on a carousel behind a pneumatically controlled

shutter. The deposition rate for each source material is monitored by quartz crystal microbalances (QCMs), which are piezoelectric devices. By opening the shutter, the substrate is exposed to the plume of source material. After a calibration procedure for both the deposition rate and the shutter delays, elemental layers can be deposited with atomic-level thicknesses. Since the substrate is on a carousel, it can rotate from one elemental source to another in sequence, and we can sequentially build up layered elemental precursors with designed layering schemes and thicknesses to target an immensely wide array of compounds.

Following deposition, the precursor is thermally treated—according to the results of an annealing study—to induce the self assembly of the target structure.

2.2. *Synthesis of Modulated Elemental Precursors and Description of Deposition Chamber*

The designed elemental precursors are prepared in a custom-designed vacuum chamber shown in Figure 2.1.[5,6] which operates at a pressure of ~1×10^{-6} Torr. This pressure is achieved by a three-phase vacuum evacuation sequence: 1.) rough pump, 2.) turbomolecular pump, and 3.) croygenic pump. The cryogenic pump is the only pump that operates during deposition. The chamber consists of three 3-kW electron beam guns from Thermionics—used to deposit metal source materials (pertinent to this thesis: molybdenum, tin, and bismuth)—and one effusion cell which is used to deposit selenium. These source materials are purchased commercially and are all in excess of 99.99% purity. As power is applied to the heating elements, the Sn, Bi, and Se sources melt first due to their relatively low melting points, and then as power is further increased, they vaporize into a conical plume. Molybdenum, a refractory metal, does not melt at the operating pressure in the chamber. Instead, a piece cut from a molybdenum rod is arc melted both to outgas the source and create a smooth surface. Since atoms volatilize normal to the surface, this smooth surface ensures even deposition across the substrate. Additionally, the electron beam is rastered across the molybdenum surface so as to avoid boring a hole, which would narrow the shape of the molybdenum plume and change the flux of atoms incident on a particular region of the substrate throughout the course of the deposition. Piezoelectric transducers, such as QCMs, work by detecting changes to

resonant frequencies as material is deposited onto the QCM. This frequency will change as a function of added mass, and by inputting the surface area of the QCM and the density of the deposited material, the QCMs are able to monitor deposited thickness.

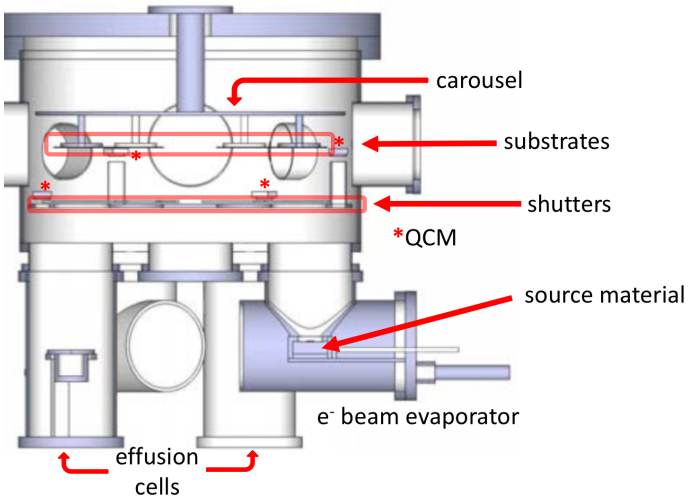

Figure 2.1. Schematic of the deposition chamber utilized to prepare modulated elemental thin film precursors. The chamber contains 3 electron beam evaporators and 1 effusion cell used to evaporate selenium. There are two additional ports for effusion cells that are currently unused.

The deposition sequence is coordinated by a LabVIEW software program, which has been written specific to the components of this deposition chamber. Users are able to program the elemental layering sequences, the deposited thicknesses within each layer, and the desired number of repeat units in the stack.

2.3 *Structure at Multiple Length Scales*

MER synthesis enables the formation of thin films (generally $t < 50$ nm) that extend over a surface area in excess of 1 in^2. Accordingly, structural analysis on vastly different length scales is necessary in order to fully characterize the film. Whereas transmission electron microscope techniques are able to provide both real and reciprocal space data pertaining to stacking orders, atomic arrangements, rotational alignment, etc, the data is at the atomic scale and cannot be treated as representative of the entire sample volume. In contrast, large area ("global") x-ray scattering techniques lose granular level details, but provide information about average structures over the entire probed area. Where the analysis at both length scales leads to a consistent interpretation, a coherent

structure extends across the sample. However, when the local level data leads to a different analysis, these data are likely showing a defect or other structural anomaly.

A variety of structural features were analyzed by a suite of both in-house and synchrotron-based x-ray scattering techniques. Information regarding microscopy techniques can be found in Jeffrey Ditto's and Gavin Mitchson's thesis work.[7,8]

2.4 *X-ray Scattering Structural Analysis*

2.4.1 Diffraction Analysis for Polycrystalline Nanolaminate Thin Films from MER

Bragg diffraction is used to characterize the repeating, crystalline features of the nanolaminate thin films. A simple diffraction setup is shown in Figure 2.2. When refracted intensity is incident on an atomic center, that atom's electron density will attenuate and scatter the x-rays. X-rays that penetrate farther into the sample prior to being diffracted have an additional path length that they must travel before they leave the film. If that incremental path length is equal to an integer number of wavelengths, the two waves will constructively interfere and register intensity at the detector. The *d*-spacing,

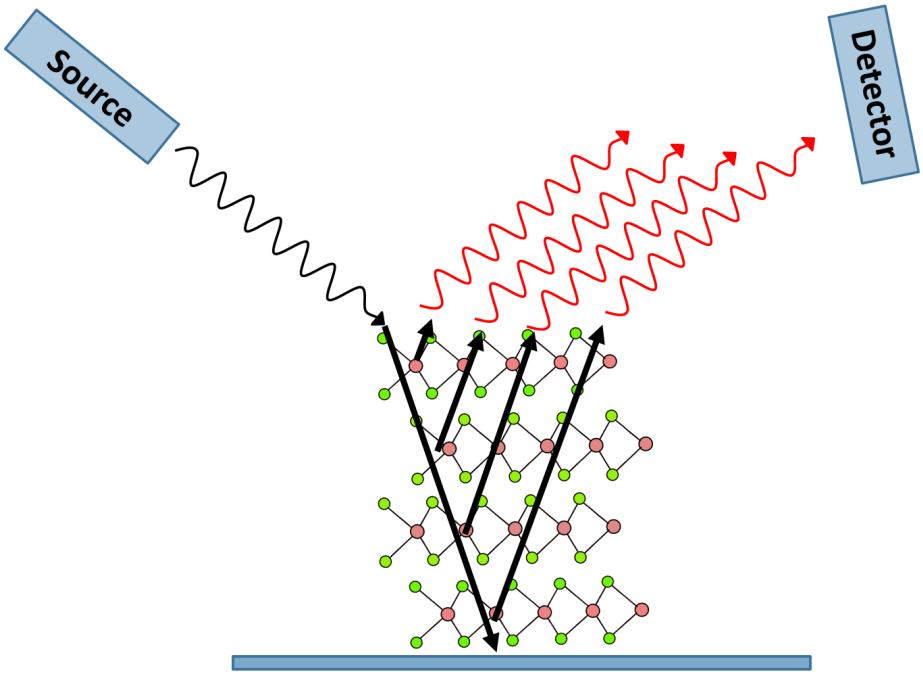

Figure 2.2. Schematic of a specular diffraction geometry, where the incident and diffracted x-rays are at the same angle relative to the substrate. The incident x-ray beam is shown on the left, and the diffracted x-rays are shown on the right.

the angle between the incident radiation and the top surface of the film (θ), and wavelength of the monochromatic beam are all related by the Bragg equation (Equation 2.1), where *n* is an integer value equal to the order of a particular reflection.

$$n\lambda = 2dsin\theta \qquad \text{(Equation 2.1)}$$

The diffraction experiments described in this thesis are somewhat different than a conventional powder diffraction experiment. Powder diffraction assumes a polycrystalline material with a semi-infinite number of crystallites with perfectly randomized orientations in three dimensions. All allowable reflections will be observed according to the symmetry of the unit cell. Conversely, the samples from this thesis are characterized by extreme preferred orientation along *z*, in that the crystallites are all oriented parallel to the substrate. This difference is depicted in Figure 2.3. As a result, specular diffraction—in which θ and 2θ are coupled and aligned to the substrate—only

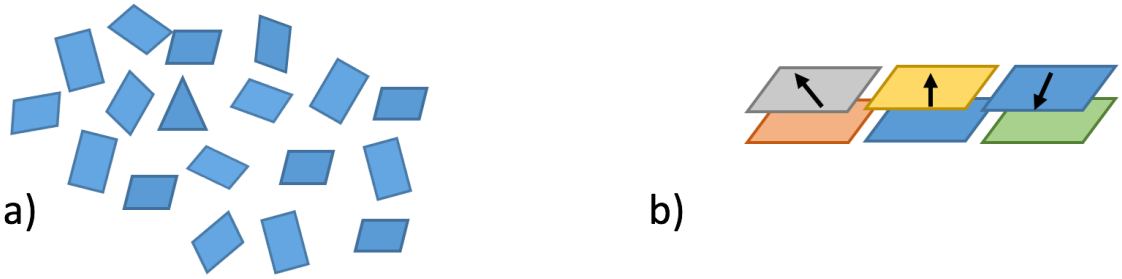

Figure 2.3. This figure shows the difference between (a) a "powder" sample, in which crystallites are perfectly disordered from one another, and (b) a sample in which the crystallites have preferred orientation. The orientation is said to be preferred in that all crystallite nanosheets are parallel to the substrate, but do not necessarily have the same rotational ordering along *z* (crystallites with different rotational angles are shown by the varying colors and arrows).

gives information pertaining to the out-of-plane structure, and only *00l* reflections will be observed. The in-plane structure must be probed separately using a different scanning geometry—grazing incidence in-plane diffraction. This scan will show *hk0* maxima with independent families of reflections observed for each constituent sublattice. Additionally, films studied in subsequent chapters of this dissertation were all found to possess a random orientation of crystallites in the *xy* plane.

Mixed *hkl* reflections are only observed by reciprocal space mapping (RSM), and show streaking along *l* due to the rotational disorder of crystallites in the *xy* plane.[9] However, a RSM is not sufficient to fully characterize this rotational disorder. Consider,

for instance, the two scenarios illustrated in Figure 2.4. In both scenarios, there are an equal number of crystallites with a given orientation. They differ in whether the misaligned crystallites are situated laterally from one another (a) or vertically from one another (b). Both scenarios would show the same information in a RSM. In order to determine which is the correct interpretation for a given sample, local level characterization (i.e. TEM data) is needed. Cross-section HAADF-STEM can show atomic columns when those columns are aligned to the electron beam, and for rotationally aligned crystallites along *z*, the same arrangements of atoms across layers will be observed. Nanobeam electron diffraction (NBED) is a plan view technique that can probe rotational alignment through thin multilayers. For more information on NBED, refer to chapter 4.

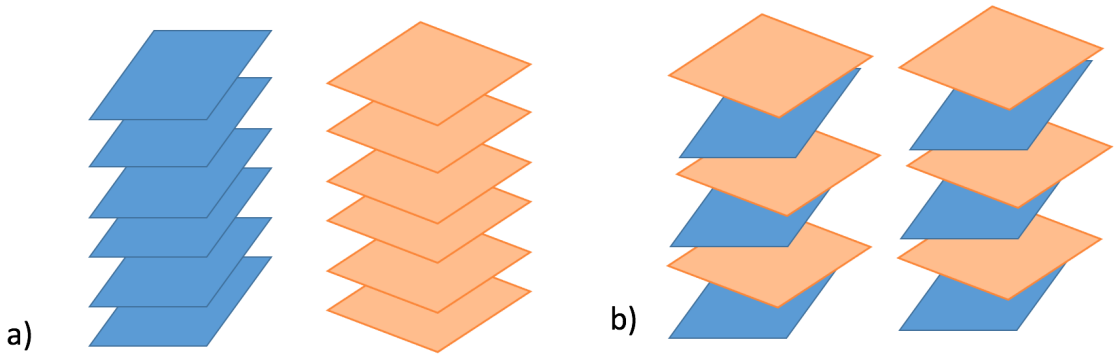

Figure 2.4. Two scenarios showing variation in the rotational alignment of crystallites. In scenario (a), vertically adjacent crystallites possess the same rotational alignment while laterally adjacent crystallites are rotationally disordered. In scenario (b), vertically adjacent crystallites are rotationally disordered while laterally adjacent crystallites possess the same rotational alignment.

X-ray diffraction occurs in reciprocal space, and so the observed diffraction pattern is the Fourier transform of the electron density modulation with respect to geometry of the scan. The periodic modulation can be described using a summation of sine and cosine functions (i.e. "Fourier Series"). And, the integrated area of a particular diffraction peak gives the relative contribution of that Fourier term necessary to describe the modulation. For example, consider the specular patterns shown below of the as-deposited film (Figure 2.5a) and the self-assembled (Figure 2.5b) $MoSe_2$ nanolaminate. Modulated precursors are not truly amorphous in that the sequential deposition scheme does create elemental layering. However, the sample is also not completely crystalline

and does not possess atomically sharp interfaces. The electron density profile of the modulated precursor can almost entirely be described using a simple sine wave functional form, which only requires the contribution of the first Fourier term. In Figure 2.5a, the maximum identified by the # (and dashed line drawn through the center of the peak) corresponds to a greater *d*-spacing than the other observed maxima in the pattern. It is related to the modulated precursor, and no other maxima in the scan can be indexed to the same *d*-spacing. Additional peaks are observed that can all be indexed as the *00l* family of reflections for published structures of $MoSe_2$, indicating that some $MoSe_2$ has

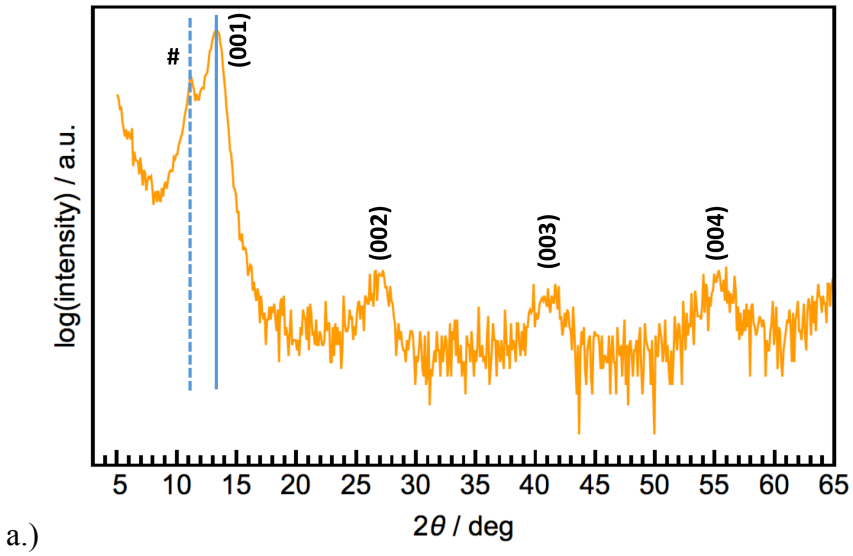

a.)

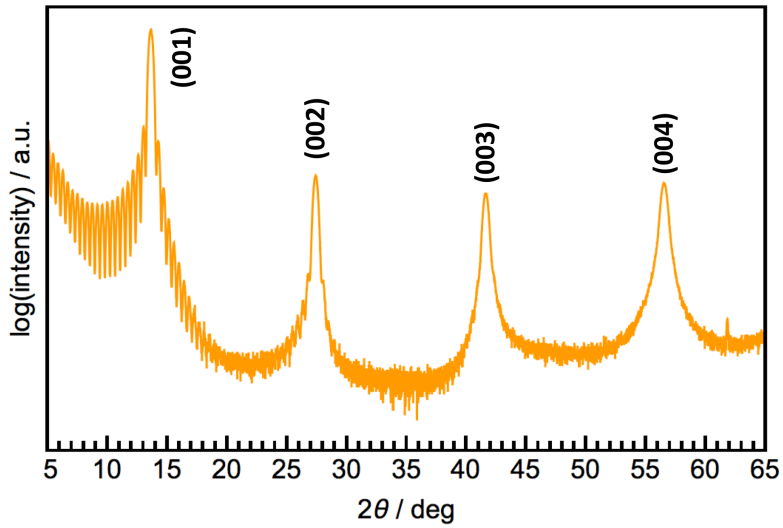

b.)

Figure 2.5. The top specular diffraction pattern of the as-deposited film shows intensity from the modulated, elemental precursor (#). The center of this peak has been identified with a dashed line. The remaining maxima—including the (001) reflection identified by the vertical solid line—can all be indexed to the $MoSe_2$ structure.

nucleated upon deposition. However, the integrated area underneath these reflections is quite small, indicating a very limited amount of $MoSe_2$ formation. For the $MoSe_2$ reflections in Figure 2.5a, the first reflection is, by multiple orders of magnitude, the most intense, and the intensities of the other terms barely rise above the level of the noise in the scan. This indicates that the self-assembled structure is not yet precisely ordered and requires further thermal treatment.

Conversely, the atomically sharp interfaces of the self-assembled product (Figure 2.5b) are more adequately described by a square well functional form, and several Fourier terms—sine/cosine functions—must be summed to approximate a square well. Hence, the intensities and integrated areas of the (002), (003), and (004) reflections are all significantly greater.

2.4.2 X-Ray Reflectivity Analysis and Finite Crystal Effects for Nanolaminate Thin Films

X-ray reflectivity (XRR) is a low-angle specular scattering technique that gives information regarding the density, thickness (t), and "smoothness" (Δt) of a thin film—among some other information that is not pertinent to this thesis. XRR analysis requires a precisely aligned sample in a $\theta/2\theta$ scanning geometry. An example of a XRR pattern of

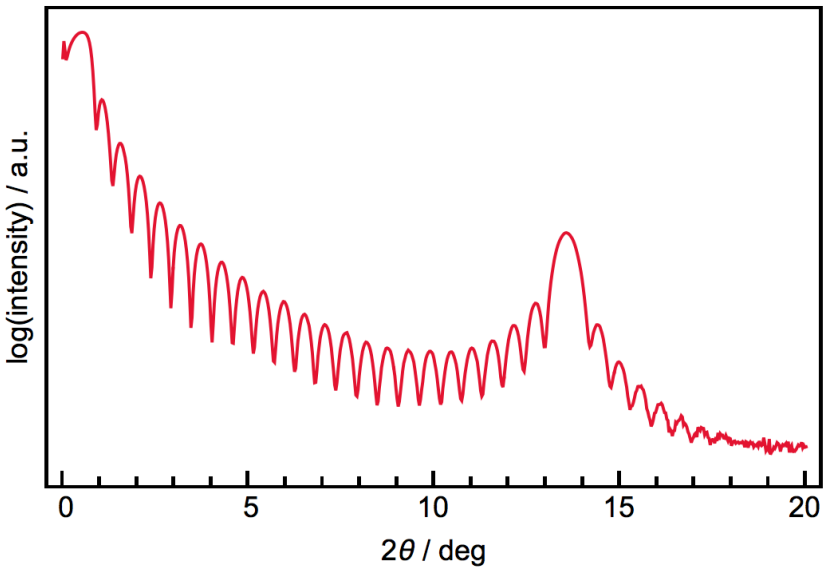

Figure 2.6. Sample low-angle specular scan of a 24-layer $MoSe_2$ film. The intensity spike at 13.5° is due to the coherent Bragg diffraction of the 24 layers. The lower amplitude oscillations are "Kiessig fringes" from reflectivity.

a 24-layer $MoSe_2$ film is shown in Figure 2.6. At very low angles, when an x-ray beam is incident on a planar thin film sample, all x-rays scatter ("reflect") off the air-film (i.e. "top") interface. However, at the "critical angle", θ_c, which varies directly with density, x-rays intensity begins to refract into the film. The fraction of reflected and refracted intensity as a function of θ is described by the Fresnel equations, which state that at lower angles, a higher fraction of incident light is reflected off the top interface. Refracted intensity will subsequently scatter off the film-substrate ("bottom") interface. The observed pattern at the detector is, therefore, the interference pattern of intensity off the top and bottom interfaces of the film. This process is illustrated in Figure 2.7.

The observed intensity will gradually oscillate between constructive and destructive interference as a function of angle (θ_i) and thickness (t), giving rise to a set of set of subsidiary maxima and minima.[10] The frequency of these "Kiessig fringes" is directly related to film thickness. The amplitude of the fringes is determined by the density differential between the substrate and the film. Using the critical angle, fringe index (n), and the angle of a subsidiary maximum, a d-spacing (i.e. film thickness") may be calculated at each particular fringe by a modified form of the Bragg equation given in Equation 2.XX, which accounts for the shift due to the critical angle. In theory, for a film containing only a precise number of well-defined, uniform layers across the entire probed

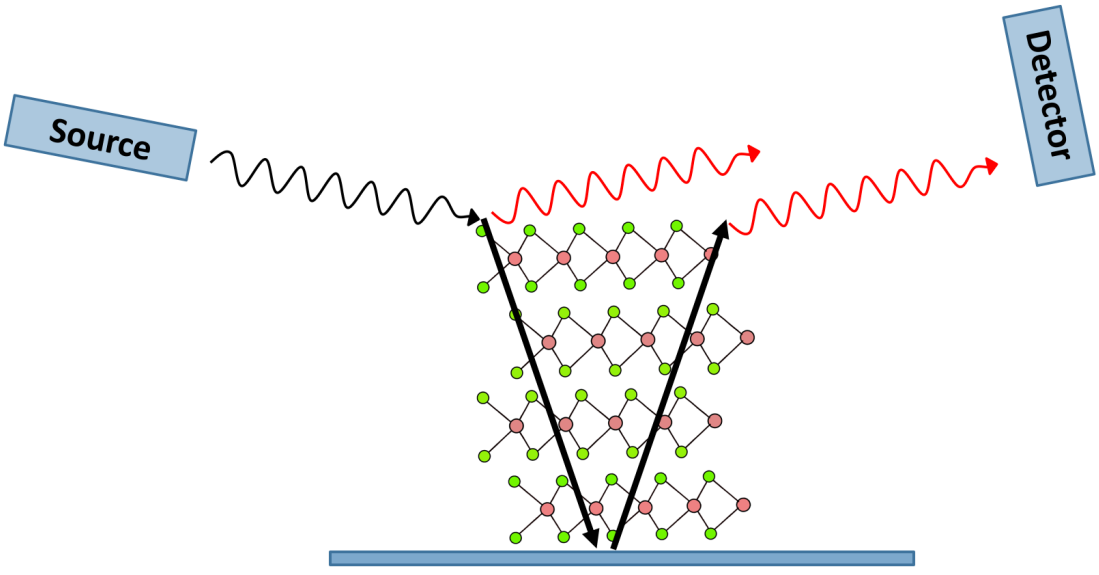

Figure 2.7. Schematic of a diffractometer setup for an x-ray reflectivity (XRR) experiment. As can be seen in the image, intensity results from interference off the top and bottom interfaces of the film.

volume, the thicknesses calculated from each fringe should be the same. However, aberrations to the structure can shift the position of these maxima by different amounts. By fitting a linear regression to a plot of $\sin^2\theta$ versus the square of the fringe index (n^2), the thickness of the film can be obtained using all the fringes simultaneously, yielding a statistical approximation for film thickness. As can be seen in Equation 2.2, the slope of the linear regression is equal to $1/d^2$, where d is the thickness of the film.[11]

$$sin^2\theta_i = \left(\frac{\lambda}{2}\right)^2 \frac{n^2}{d^2} + sin^2\theta_c \qquad \text{(Equation 2.2)}$$

Because reflected intensity diminishes with increasing angle, the lowest angle regions of the pattern are most sensitive to global thickness. The higher angle regions become increasingly sensitive to diffraction phenomena from finite size crystal effects in the internal structure. For example, consider a $MoSe_2$ film consisting of 24 perfectly parallel, stacked layers (Figure 2.7). When all 24 layers diffract in phase, the complete constructive interference results in a large spike in intensity (i.e. "Bragg peak"). However, between Bragg reflections, the diffracted x-rays from each of the 24 layers will also go through periodic incomplete constructive and destructive interference. These are referred to as "Laue Oscillations", and they can be observed to much higher angles than Kiessig fringes. For a film with *n* discrete layers, there are *n-1* ways to find subsidiary minima between Bragg peaks. This effect is only observed thin crystals with a modest number of unit cells. As the number of unit cells increases in the stack, the Laue oscillations will get closer and closer to one another, and at $t > \sim 100$ nm, it is generally no longer possible to resolve them—depending on the instrumental broadening of the diffractometer. For monoliths, only noise is observed between Bragg reflections. Accordingly, in a specular scan, it is important to bear in mind that the observed pattern is the summation of these Kiessig fringes, Laue oscillations, and diffraction maxima.

The three effects can all be observed in the traces found in Figure 2.8. The position of the (001) Bragg reflection corresponds to a *c*-lattice parameter of 6.53 Å. For a perfect 24-layer film, like the one shown in the yellow trace, the thickness calculated from each subsidiary maximum is equal to *c* times the 24 layers in the stack. The fringes at the lowest angle give a thickness greater than the true thickness of the film, as they are convoluted by the critical angle. However, in this pristine pattern, the thicknesses

calculated from each subsidiary maximum are all quite similar and decrease monotonically (to within the error). In this case, the Kiessig fringes and Laue oscillations are describing exactly the same 24-layer structure, and one coherent scattering pattern is observed.

Conversely, the blue trace below—self assembled from a 24 repeat unit precursor where each layer contained ~5% atomic deficiency—shows two distinct groupings of maxima at different angle regimes. The Bragg reflection still corresponds to the same 6.53 Å *c*-lattice parameter. In this pattern, the Laue oscillations—sensitive to the crystalline regions of the film—predominate at higher angles and give *d*-spacings that are approximately equal to *c* times 23 layers (~151 Å). However, the Kiessig fringes—sensitive to global film thickness—predominate at lower angles and show that on average the film is ~147 Å. The balance between reflectivity effects (Kiessig fringes) and diffraction effects (Laue oscillations) shifts at $2\theta \approx 9°$, which is where the breakdown in the pattern is observed as the two regions are describing subtly different structures.

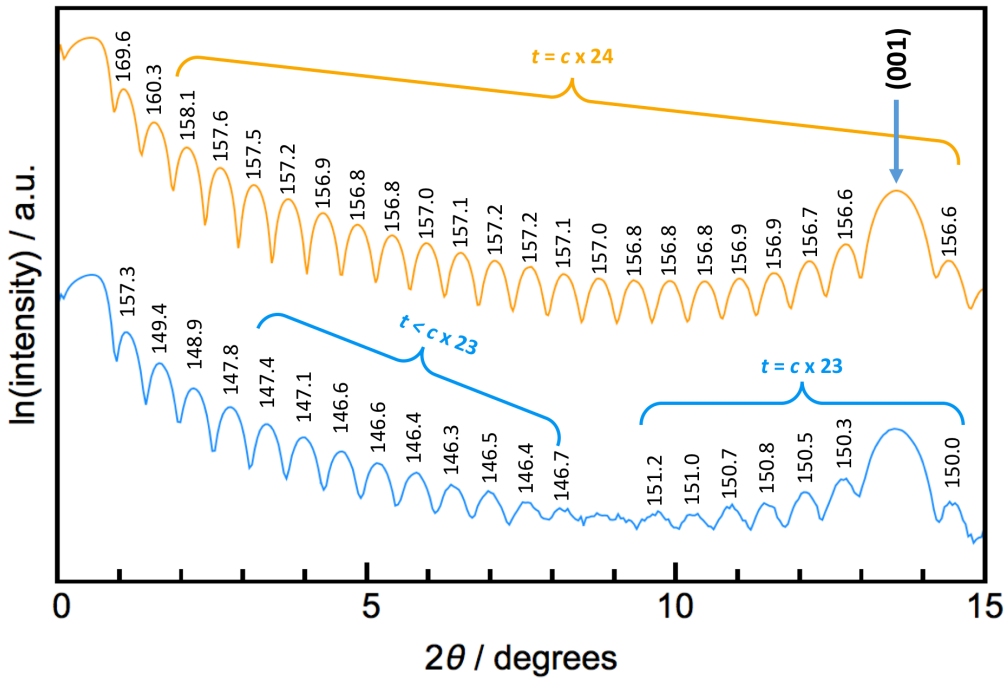

Figure 2.8. Low angle specular scans from two films. In the top scan (yellow) of a pristine 24-layer film, the reflectivity and diffraction effects result from exactly 24 coherently stacked layers. The lower scan (blue) is deficient in Mo and Se, so the competition between the reflectivity and diffraction contributions can be easily seen.

The overlapping reflectivity and diffraction effects can also be seen and easily compared in Figure 2.9. The top (yellow) trace is a diffraction pattern gathered in a perfectly specular geometry. And the observed intensity is a summation of reflected and diffracted intensity—Kiessig fringes and Laue oscillations. The two traces below (red and blue) are off specular diffraction patterns taken at different offset angles and only contain information related to diffraction. The specular trace has a background level that decays from 5°-10° due to the fact that, per the Fresnel equations, reflected intensity drops off with increasing angle. The background angle then builds again as diffracted intensity becomes more significant. In contrast, the red and blue traces have different background levels (yet similar to one another) because the reflectivity intensity has been removed. To help compare the three traces, vertical lines have been drawn at arbitrary minima. Notably, the positions of these minima all line up perfectly at both low and high angles. This indicates that the total thickness is related only to precisely crystalline layers and does not include any noncrystalline regions at the bottom, middle, or top of the film that would add thickness beyond simple product of c and the number of $MoSe_2$ trilayers in the stack.

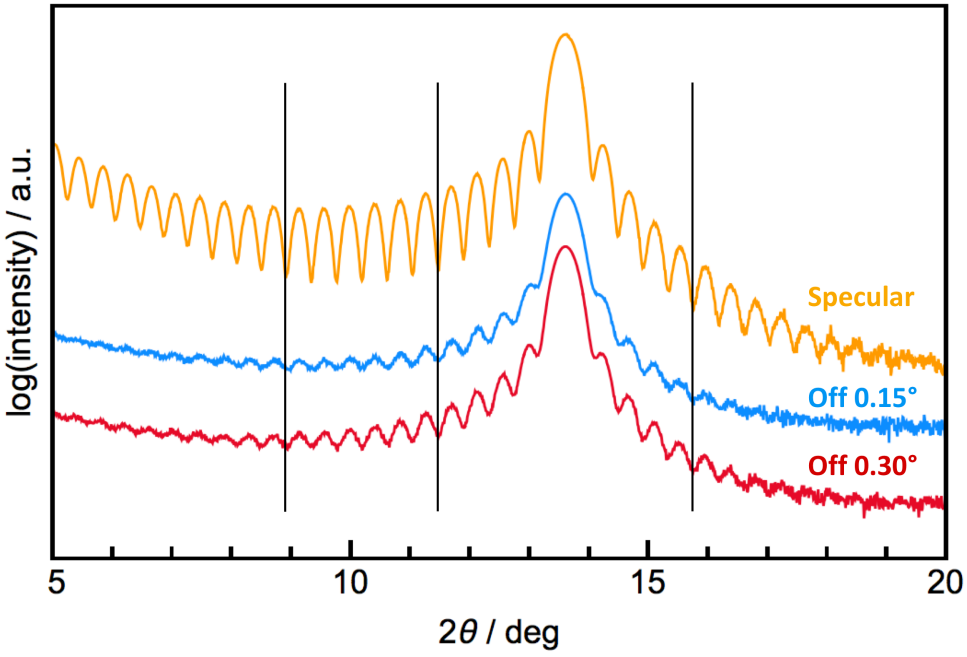

Figure 2.9. Stacked comparison of a specular (yellow) and two off-specular (red and blue) low-angle patterns. By offsetting the θ and 2θ angles, it is possible to deconvolute the reflectivity and diffraction intensity.

For perfectly parallel top and bottom interfaces, Kiessig fringes will be observed until reflected intensity drops below noise in the scan or the detection limit of the instrument. However, as the two interfaces deviate from a parallel geometry, coherent scattering and interference patterns will break down at lower and lower 2θ. This deviation is sometimes referred to as "roughness", however this is not the same as topographic RMS roughness given by surface probe such as atomic force microscopy. Instead, roughness given by XRR data is better understood as the variability in the thickness (Δt) of the planar regions of the film. It is insensitive to any granular, non-planar surface aberrations. Roughness varies inversely with the highest angle 2θ to which Kiessig fringes are resolved in the pattern ($\theta_{n,max}$), per the Parratt relationship shown in Equation 2.3.[12]

$$\Delta t = \frac{\lambda}{4\sqrt{\theta_{n,max}-\theta_c}} \qquad \text{(Equation 2.3)}$$

2.4.3 Considerations for Off-Specular Diffraction and Rietveld Analysis

The out-of-plane structure can be refined by Rietveld analysis from the *00l* family of reflections, which gives the position of atomic planes within the unit cell. The refinement is done using the FullProf software package. However, FullProf is not designed to accommodate the particularities of the samples discussed in this dissertation—namely, the total preferred orientation and added diffraction effects due to the thin dimensions. Working around the first problem can be addressed by simply putting very small "dummy" in-plane lattice parameters into the software, effectively pushing those reflections out of the range of the scan. However, the reflectivity contribution and finite size crystal effects must be removed from the scan entirely. This can be accomplished by collecting an off-specular diffraction pattern, where θ and 2θ are slightly offset from one another (say, $2\theta = 10°$ and $\theta = 4.7°$).

For most ferecrystalline samples, this offset will eliminate the subsidiary maxima and minima between Bragg reflections, and the structure can be refined. However, for some samples with exceedingly planar interfaces, the Laue oscillations may persist as they are a diffraction phenomenon and not related to reflectivity. Figure 2.10 shows an off-specular scan at an offset angle of 0.3°, enough to remove the reflectivity effects.

However, as can be seen, the diffraction contribution to these oscillations are still observed. Unfortunately, with this effect still present in the scan, the pattern cannot be refined.

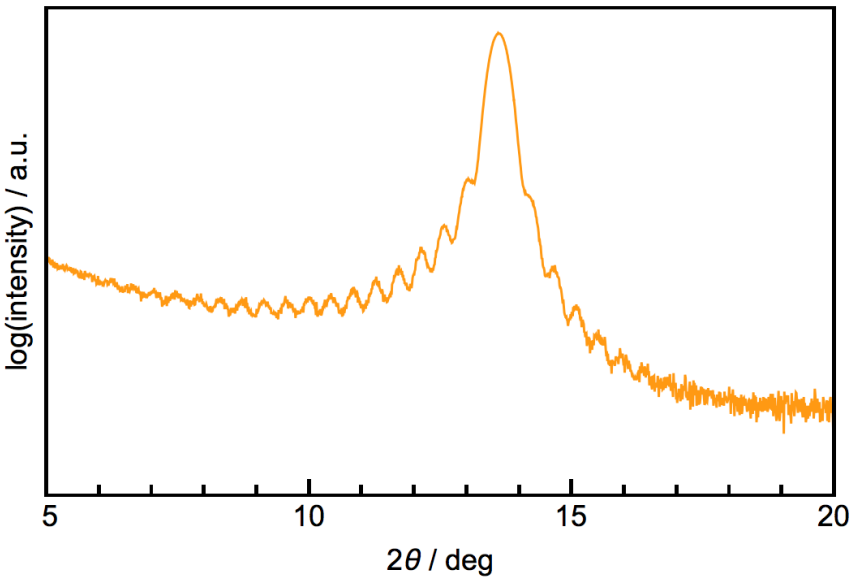

Figure 2.10. The off-specular diffraction pattern of the out-of-plane structure (offset angle 0.3°) shows Laue oscillations on either side of the (001) Bragg reflection.

2.4.4 Le Bail Fitting and Rietveld Structural Refinement

Structural refinement ought to begin by completing a Le Bail fit. The benefit of using Le Bail fitting instead of calculating lattice parameters from each peak using the Bragg equation is that it fits an entire family of reflections within a space group together, simultaneously. This is particularly useful for deconvoluting overlapping maxima—say, in a refinement of the in-plane structure of a multiphase intergrowth. While Le Bail fitting allows for better statistics in identifying peak centers and lattice parameters, it is important to bear in mind that it does not fit intensity ratios. Hence, it cannot be used for quantitative phase analysis.

FullProf works by creating a model pattern for the structure and then fitting that model to the experimental data using a least squares algorithm.[13] Completing a Le Bail fit prior to the Rietveld refinement makes it possible to fix lattice parameters, which reduces the number of adjustable parameters. This is beneficial because models can quickly become unstable due to the limited number of reflections. Minimizing the number of variables, particular at the beginning of the refinement, lends stability.

CHAPTER III:

SUB-MONOLAYER ACCURACY IN DETERMINING THE NUMBER OF ATOMS PER UNIT AREA IN ULTRATHIN FILMS USING X-RAY FLUORESENCE

3.0. *Authorship Statement*

The work in this chapter has been published in the American Chemical Society journal Chemistry of Materials in 2018. The article has been coauthored with Danielle M. Hamann (primary author), Dylan Bardgett, Dmitri Leo Cordova, Liese A. Maynard, Alexander C. Lygo, Suzannah R. Wood, Marco Esters, and David C. Johnson. My primary contribution to the project was to prepare samples with rigorously defined structures (and corresponding figures for structural characterization) and precise compositions. These samples were used as standards in the calibration procedure we demonstrate in the paper.

3.1. *Abstract*

The composition and thickness of thin films determines their physical properties, making the ability to measure the number of atoms of different elements in films, both technologically and scientifically important. For thin films, below a certain thickness, the X-ray fluorescence intensity of an element is proportional to the number of atoms. Converting this intensity to the number of atoms per unit area is challenging due to experimental geometries and other correction factors. Hence, the ratio of intensities is more commonly used to determine the composition in terms of element ratios using standards or a model. Here, the number of atoms per unit area was determined using X-ray structure information for over 20 different crystallographically aligned samples with integral unit cell thicknesses. The proportionality constant between intensity and the number of atoms per unit area was determined from linear fits of the background subtracted XRF intensity plotted versus the calculated number of atoms per unit area for each element. The results demonstrate that XRF is very sensitive, capable of measuring changes in the number of atoms of less than 1 % of a monolayer for some elements in a variety of sample matrices. Using the calibrated values, an 8-unit cell thick $MoSe_2$ was grown and characterized, demonstrating the usefulness of being able to quantify the number of atoms per unit area in a film.

3.2. *Introduction*

The discovery that isolated two-dimensional layers have extraordinary properties that are not found in their bulk counterparts has resulted in intense experimental and theoretical interest in these materials.[1–12] A distinct challenge towards the future use of these materials in new technologies is developing techniques to grow single layers of various 2D solids over large areas. While a variety of techniques have been explored to prepare monolayers, chemical vapor deposition involving a volatile metal source has become increasingly popular.[13–26] Typically, "about a monolayer" of a metal is deposited on a surface and treated at high temperatures with a second reagent to form domains of the desired monolayer on substrates.[27–29] Since the deposited metal species is typically not volatile once the precursor has reacted on the surface, time is the parameter tuned to get close to monolayer coverage. This type of monolayer synthesis creates an analytical need to be able to quickly measure fractional monolayer amounts of elements on a substrate, ideally without significant sample preparation.

More generally, measuring the number of atoms per unit area of each element in a thin film is a challenging analytical problem and critically important in many situations. Physical properties depend on both composition and thickness of constituent layers in devices, and the properties of compound films are a sensitive function of composition. A variety of approaches have been used to determine composition, including Rutherford backscattering, electron probe microanalysis, particle-induced X-ray emission, X-ray photoelectron spectroscopy, time of flight secondary ion mass spectrometry, and a variety of electron microscopy techniques.[27–30] Most of these techniques involve expensive instrumentation and several also require significant sample preparation. Sensitivity and converting the signal to the number of atoms of each element per unit area can also be very challenging, particularly if the signal is sensitive to the matrix. Typically, only a composition ratio is determined, as taking the ratio of two different elements eliminates several difficult to determine proportionality factors that depend on geometry, other instrument dependent factors, and the sample itself.

X-ray fluorescence (XRF) is a metrology method that can determine both composition and thickness of thin films and has several advantages. While it requires the

use of standards to obtain instrument parameters and absorption corrections need to be made (via standards with similar matrices or modeling), it is quick and precise. Early work on the XRF analysis of thin films focused on using a variety of different methods to correct for absorption effects in the thin film geometry.[31,32] This lead to the development of XRF as a tool to characterize relatively simple multilayer films in the advance of materials for a variety of applications, including memory devices and optical recording.[33,34] More recent reports have shown that XRF is also a useful approach to characterize patterned thin films, with intensity differences before and after patterning proportional to the amount of material removed during the patterning process.[35] While a significant challenge has been to accurately correct the XRF data for absorption effects, there is at least one report where XRF using wavelength-dispersive X-ray detection was used to examine films that are thin enough that absorption can be ignored.[36] This study showed that a resolvable composition difference of 0.025 atomic percent could be obtained with relatively short counting times in a series of chalcopyrite solar cells.

In this paper, we present data showing that XRF intensity is proportional to the number of atoms per unit area in ultrathin films and the intensity is relatively insensitive to the matrix. The number of atoms per unit area for a subset of exceptionally smooth films was calculated using data from a combination of x-ray reflectivity, specular diffraction, and in-plane diffraction scans. Calculating the proportionality constant between XRF intensity and the number of atoms per unit area simply requires division of the measured XRF intensity by the calculated number of atoms per unit area. The proportionality constant in over 20 samples with a range of thicknesses is consistent for the elements examined, indicating this is a valid approach. Once the proportionality constant is known for an element, preparing films of known compounds with defined atomic ratios between the previously studied element and other elements enables the determination of the proportionality constant for previously unstudied elements without the need for exceptionally smooth films. The consistency of results for films containing a wide range of different matrix constituents makes this a simple, relatively inexpensive, nondestructive, and fast method to measure the number of atoms in an ultrathin film. This study demonstrates that XRF is capable of detecting changes in the amounts of an element equivalent to a fraction of a monolayer for all elements examined, and less than

1% of a monolayer for some elements. For films with thicknesses around a monolayer, the XRF intensity of the substrate before the film is deposited needs to be subtracted from the total signal of the film plus substrate to achieve this accuracy.

3.3. *Experimental*

Precursors were synthesized in a high-vacuum physical vapor deposition system, with depositions occurring at pressures below 5×10^{-7} Torr. Metals were deposited using electron beam guns, and selenium was deposited using an effusion cell. A computer controlled pneumatic shutter system was used to control the sequence and thickness of the elemental layers.[37,38] The rate of deposition and the thickness of each of the elemental layers deposited were measured and controlled using quartz crystal microbalances, with rates maintained at 0.1 - 0.3 Å/s at the substrate.

X-ray fluorescence data was collected using a Rigaku ZSX Primus II wavelength dispersive X-ray fluorescence spectrometer with a rhodium X-ray source. This instrument measures intensities of characteristic X-ray emission lines as a function of crystal angle. Samples were loaded onto a small metal puck with either a 30 mm, 20 mm, or 10 mm diameter masking-frame. Incident X-rays were passed through either a 10 mm or 20 mm diaphragm before contacting the spinning sample in a vacuum. Fluoresced X-rays were reflected off selected crystals into a detector. Intensity was measured by integrating the area under the entire peak measured in intensity as a function of two-theta using MATLAB's cubic smoothing spline function (csaps) with the smoothing parameter set to zero smoothing (function value 1). The two-theta limits of integration were held constant. Data were also collected for substrates without any deposited film, referred to as blanks. The intensity data measured for the blanks was treated in the same manner as the deposited samples. The resulting integrated counts were subtracted from the integrated intensity of the coated substrates to correct for the background signal and any signal from the substrate itself.

X-ray diffraction (XRD) was used to characterize the structure of the samples that were subsequently analyzed by XRF. Low angle and specular XRD scans were collected using a Bruker d8-discover diffractometer. Grazing incidence in-plane XRD scans were collected on a Rigaku Smartlab diffractometer. All diffraction patterns were collected

with Cu Kα radiation.

3.4. *Results and Discussion*

The intensity of the XRF signal I_{ij} for a particular element i of interest in a film with a characteristic line j at wavelength λ_{ij} is given by:[36,39]

$$I_{ij} = \{ K_j(\lambda_s) C_i / \mu_T(\lambda_{ij}) \} \{ 1 - \exp [-\mu_T(\lambda_{ij})\rho d] \} \quad \text{(Equation 3.1)}$$

In Equation 3.1, C_i is the mass fraction of element i in the film, ρ is the average film density, d is the film thickness, and $\mu_T(\lambda_{ij})$ is the total mass absorption coefficient at λ_{ij}. $K_j(\lambda_s)$ is a product of many constants, including a constant representing the spectrometer geometry, the intensity of the excitation X-ray source, and the excitation probability for the characteristic line j under the spectrum of intensities of the excitation source. If the thickness of the analyzed film is thin enough, $\mu_T(\lambda_{ij})\rho d$ becomes small, and for films within this thickness regime (defined in more detail later), the exponential can be expanded as a power series. If only the leading terms are kept, Equation 1 simplifies to:

$$I_{ij} = C_i K_j(\lambda_s) \rho d \quad \text{(Equation 3.2)}$$

For such thin films the intensity of the XRF signal is thus expected to be directly proportional to the product of C_i, ρ, and d, which is the number of atoms of element i in the area of the film probed. The deviation between equation 1 and Equation 3.2 as a function of film thickness for a representative film is shown in Figure A.1 in the supporting information.

To test the applicability of this approximation, a series of films with thicknesses below 120 nm containing a variety of elements with different elemental ratios were prepared using physical vapor deposition. Quartz crystal microbalances were used to measure the amount of material deposited onto the silicon substrates. Figure 3.1a and Figure 3.1b and Figure A.2 in the supplemental information each contain a graph of the background corrected intensity of the XRF signal as a function of the thickness of each element deposited. The intensity data for each element was found to be proportional to the amount of the element in the film. The linear relationship between intensity and amount of material indicates that the absorption of both the incident and fluorescence X-rays are negligible in these films. The greater the slope of the line, the more sensitivity there is to small changes in the amount of the element in the film. Table 3.1 summarizes

the slopes and associated errors as well as the X-ray absorption line used for all of elements that were studied. Figure A.3 in the supporting information explains how each line was chosen for each element in question.

The spread of the data points about the linear relationship in Figure 3.1 results from several potential sources, including the limits of the reproducibility of the deposition process itself (for example the shape of the deposition plumes), limits to resolution of the quartz crystal monitors, and limits to the reproducibility of the XRF measurements. To assess the reproducibility of the XRF measurements, the XRF intensity of the same sample was measured repeatedly over a time period of 6 months, using a variety of sample masks of nominally the same size that define the sample size analyzed. The intensities for most elements studied were constant to less than a third of a percent. This suggests that the majority of the deviation in the plotted intensity versus amount deposited plots is due to errors in the amount of material deposited from either the crystal monitors or the deposition process itself.

The sensitivity of the XRF intensity to the amount of material deposited makes it a valuable tool to improve deposition reproducibility. For example, the amount of Se deposited on a sample was found to systematically increase with time when high melting point metals were evaporated in the same deposition even though the thicknesses deposited onto the quartz crystal microbalance was kept constant. The excess Se resulted from Se evaporating from chamber walls as they were heated by infrared radiation from the electron beam deposition. The sensitivity of the XRF data combined with tracking the data as a function of time and experimental conditions is a powerful tool to improve deposition processes.

The approximation that $\mu_T(\lambda_i)\varrho d$ is small neglects absorption corrections to the measured fluorescence intensity. When $\mu_T(\lambda_i)\varrho d = 0.1$, the difference between the intensities calculated with and without absorption corrections yields an error of ~5%. Absorption corrections become more important as the energy of the x-ray fluorescence line decreases as show in Figures A.4 - A.6 in the supporting information.[40,41] Table 3.1 contains estimates of the thickness where the error in neglecting absorption becomes 5%, assuming a film with a mass absorption coefficient ~10^3 cm^2/g and a density ~10 g/cm^3.

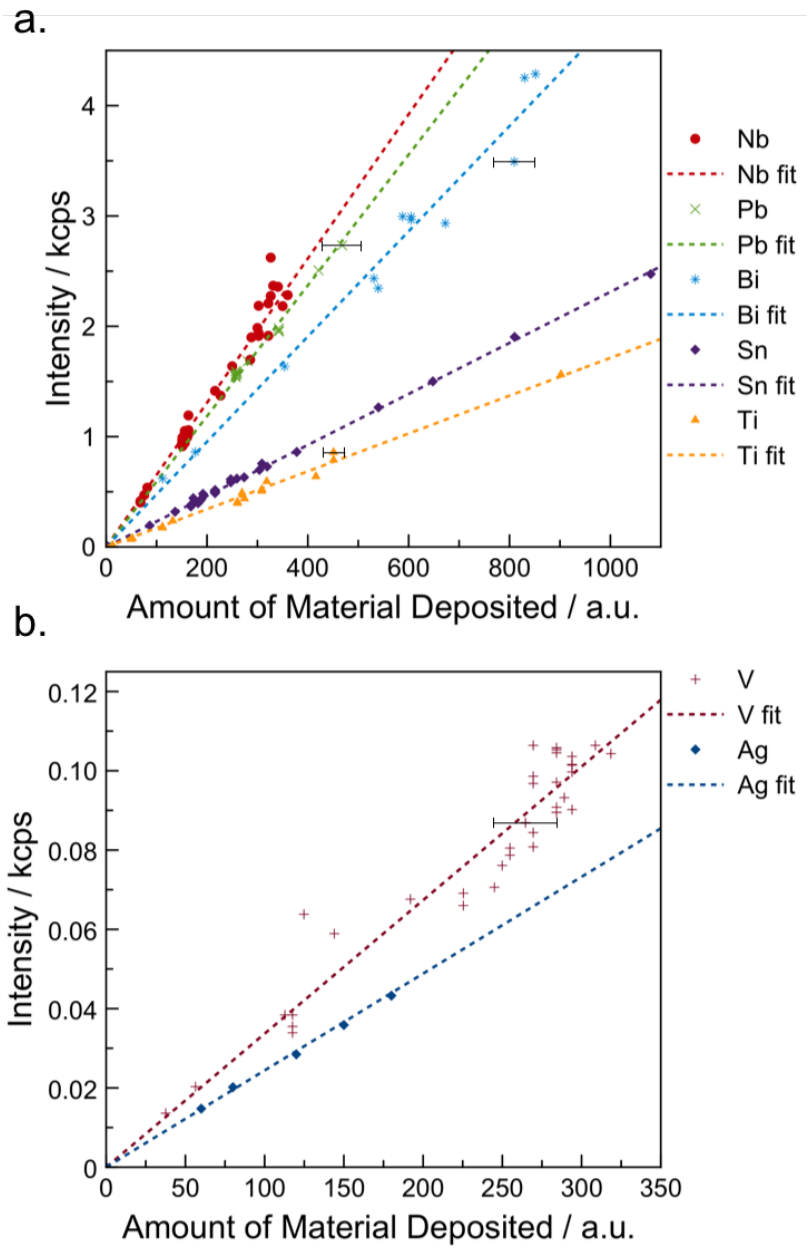

Figure 3.1. The change in the XRF intensity as a function of the thickness of material deposited as measured by quartz crystal monitors for a variety of different elements (shown with different colors and symbols). The error in the amount of material deposited for each element is shown for a single data point and when error bars are absent the error is the size of the marker. The lines are fits assuming that the XRF intensity is directly proportional to the amount of material deposited. Slopes for each line can be found in Table 3.1.

Element	Line Used	Slope	Maximum Film Thickness (nm)
Ag	Lα	0.00024(1)	150
Bi	Lα	0.00477(9)	1300
Mo	Lα	0.03019(9)	100
Nb	Lα	0.00653(6)	100
Pb	Mα	0.00592(4)	100
Se	Lα	0.00319(3)	50
Sn	Lα	0.00231(1)	200
Ti	Kα	0.00171(3)	200
V	Kα	0.000337(5)	250

Table 3.1. The slopes of the lines in Figure 3.1 for each element along with the fluorescence line used. The maximum film thickness is the thickness where absorption reduces the intensity of fluorescence of the given element by 5%.

For most elements, this corresponds to a film that is more than a hundred nanometers thick. While the exact thickness depends on the element being probed, the mass absorption coefficient of the matrix, and the density of the film, the approximation that $\mu_T(\lambda_i)\rho d$ is small is a conservative approximation for thicknesses less than 50 nm for most elements. Films below this thickness are common in many research projects and in many devices prepared by sequential deposition of layers. The supporting information contains calculations of the thickness value when the calculated intensity of the given material using Equation 2 is 5% higher than the intensity calculated for Equation 1 for samples containing Bi, Pb, or Se in their matrix using Kα, Lα, and Mα lines.

While quantifying the relative amount of an element in a film is valuable when monitoring a process, determining the number of atoms per unit area is significantly more valuable in many research applications. Unfortunately, $K(\lambda_s)$ is a product of many constants that are difficult to quantify or calculate and both the average film density and thickness are generally difficult to experimentally determine. Our approach to quantifying the amount of material in a film per unit area is to synthesize standards where the number

of atoms of each element per unit area can be calculated from diffraction data. Figure 3.2 contains representative X-ray reflectivity (XRR), specular XRD and in-plane XRD scans of one of these films, a sample of $[(PbSe)_{1.12}]_1[NbSe_2]_1$. The Kiessig fringes in the XRR scan provide a measure of the smoothness of the film and allow the total thickness and the total number of repeats of the film to be calculated. The number of repeat units in the film is equal to the number of Kiessig fringes plus 2. The specular diffraction scan shows that the film is crystallographically aligned with the substrate and enables the *c*-axis lattice parameter to be determined. The value of the *c*-lattice parameter informs on how many of each layer type are in the repeat unit. The total thickness of the film divided by the *c*-axis lattice parameter yields an integer, indicating that all of the film thickness comes from the crystalline material. Assuming there are no impurity phases present that are not evident in the diffraction scans, for example an amorphous phase, this allows us to calculate the number of atoms of each element per unit area as the product of the number of crystallographically aligned unit cells obtained from the specular diffraction information times the number of atoms per unit cell from the structure solution divided by the area per unit cell obtained from the in-plane lattice parameters.

As an example, using the data in Figure 3.2, the formula to calculate atoms per unit area is given by:

$$\text{Total } \frac{\text{atoms}}{\text{Å}^2} = \sum_{\text{Constituent Layers}} \left(\frac{\text{\# of atoms per unit cell in basal plane}}{\text{area of the basal plane per unit cell}} \right) (\text{\# of layers}) \qquad \text{(Equation 3.3)}$$

In Figure 3.2, the XRR pattern of $[(PbSe)_{1.12}]_1[NbSe_2]_1$ has 20 Kiessig fringes present between the critical angle and the first Bragg reflection, indicating that there are 22 repeat units of the $[(PbSe)_{1.12}]_1[NbSe_2]_1$ structure in the film. The total thickness of the film is obtained from the spacing between the Kiessig fringes. The specular diffraction pattern shown in Figure 3.2b yields a *c*-axis lattice parameter of 12.39(2) Å which matches the targeted *c*-axis lattice parameter for a $[(PbSe)_{1.12}]_1[NbSe_2]_1$ heterostructure.[42] Dividing the total thickness by the *c*-axis lattice parameter yields the number of repeating layers in the film, which in this case is 22, agreeing with the number of layers determined from the number of Kiessig fringes. Since the repeating unit contains one layer of PbSe and one layer of $NbSe_2$, the number of layers in Equation 3.3 is 22 for both constituents.

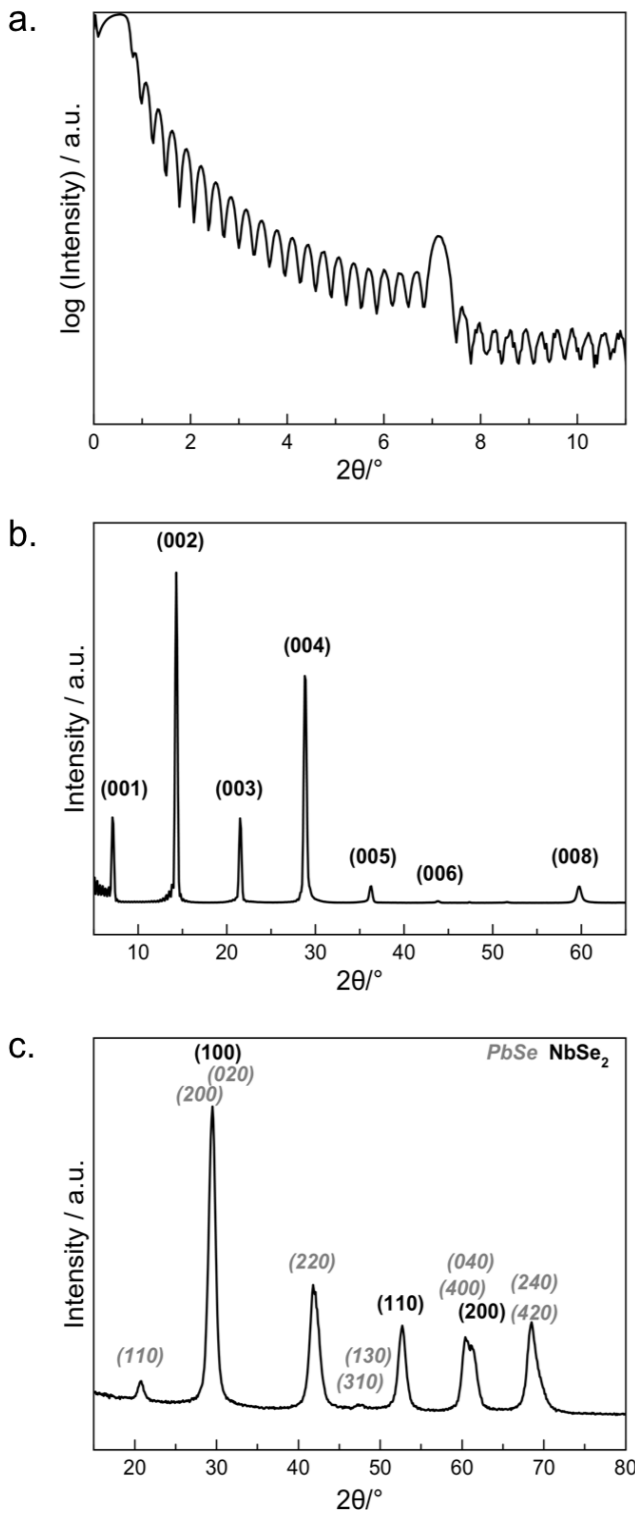

Figure 3.2. Three different diffraction scans of a $[(PbSe)_{1+\delta}]_1$ $[NbSe_2]_1$ film. (a) XRR scan. (b) Specular XRD. (c) Grazing incidence in-plane XRD scan. The crystallographic indices are given above each reflection and were used to determine the total film thickness from (a), the c-axis unit cell parameter from (b) and the in-plane unit cell parameters from (c).

In-plane XRD is used to determine the number of atoms and the area of the basal planes in each unit cell. All the reflections in the in-plane diffraction pattern (Figure 3.2c) can be indexed as hk*0* reflections for PbSe and $NbSe_2$, consistent with the formation of a $[(PbSe)_{1.12}]_1[NbSe_2]_1$ heterostructure.[42] The indices are consistent with a rectangular basal plane for PbSe (distorted rock-salt structure) and a hexagonal basal plane for $NbSe_2$. The number of atoms per unit cell in the basal plane follow from the crystal structure of each constituent (4 Pb and 4 Se for PbSe and 1 Nb and 2 Se for $NbSe_2$). The indexed patterns are then used to calculate the *a*-lattice and *b*-lattice parameters for the PbSe constituent (6.06 Å and 6.14 Å, respectively) and the *a*-lattice parameter for the $NbSe_2$ constituent (3.47 Å). The resulting basal plane areas for each constituent, assuming that they are stoichiometric, are 12.5 $Å^2$ for PbSe and 9.47 $Å^2$ for $NbSe_2$. Using this information, we calculate that the $[(PbSe)_{1.12}]_1[NbSe_2]_1$ film contains 2.37 Pb atoms/$Å^2$, 2.11 Nb atoms/$Å^2$ and 6.58 Se atoms/$Å^2$.

Figure 3.3 shows the XRF intensity for a number of different elements versus the calculated number of atoms of each element in a number of films containing a variety of different rock salt structured constituents and transition metal dichalcogenides that have diffraction data similar to that displayed in Figure 3.2. The data for each element is well described by straight lines through the origin, where the slopes provide the conversion factor between intensity and atoms per unit area. The supporting information contains data for other elements (Figure A.7), reinforcing that this is a reasonable approach to obtain the proportionality constant between the XRF intensity and number of atoms in the analytical volume. The largest error in this approach is the assumption that the films do not contain either significant defect densities or amorphous phases that are not evident in the diffraction scans. The observed linear behavior for films containing a variety of different constituents suggests that the approximation is valid and using the slope averages this error over many samples. The graph for selenium (Figure 3.4) has the largest deviations. We believe points above the line are the result of small amounts of amorphous Se in grain boundaries, inclusions, and on the surface of the films, which could be removed by additional annealing time. Points below the line are likely the result of Se loss due to annealing the samples for too long in an open system. The ability to accurately and non-destructively measure Se content will aid researchers to adjust the annealing temperatures

and times to obtain stoichiometric Se content.

Once the conversion factor is known for a particular element, the conversion factor for other elements can be determined by measuring XRF intensities of stoichiometric compounds that contain elements with known and unknown conversion factors. For example, to obtain the conversion factor for Se, XRF measurements on thin films with stoichiometric $SnSe_2$ can be used. The conversion factor of Se is then determined using the XRF intensities of Sn and Se, the known conversion factor of Sn (Figure 3.3), and the stoichiometry of the crystal. Figure 3.4 illustrates this process for three $SnSe_2$ and two $TiSe_2$ films, where the validity of this approach is confirmed by the consistency of the calculated conversion factor with that determined from crystal structure information as presented in Figure 3.3 for other elements.

While the number of atoms per unit area in a thin film via XRF can be determined with less than 1% error, the error increases as the amount of an element approaches zero as subtracting the background signal becomes more significant. Figure 3.5 shows the signal from the Sn Lα emission line for a silicon substrate and the substrate with 0.11 atoms of Sn/$Å^2$ (~140% of the amount of Sn in a single layer of $SnSe_2$)). The background intensity constitutes roughly 20% of the total intensity under the Sn Lα background intensity correctly. For Sn films deposited on silicon substrates under these data collection times and conditions (less than an hour total scan time for both film and blank substrate), the error of the net intensity measurements in our instruments indicates that changes of less than 1 % of a monolayer film of $SnSe_2$ can be detected. The sensitivity of detecting small changes of an element depends on the change in intensity of the XRF signal for that element, which is proportional to the slope of the lines in Figure 3.1, and on the specific diffracting crystals and detectors used. For example, the intensity of the Pb emission from the Mα line is about 10 times more intense per atom than the intensity of the Ti emission from the Kα line in our instrument. Therefore, we can detect smaller changes in Pb atoms/$Å^2$ than Ti atoms/$Å^2$. Sensitivities for several elements based on the data collected in this study are given in Table 3.2.

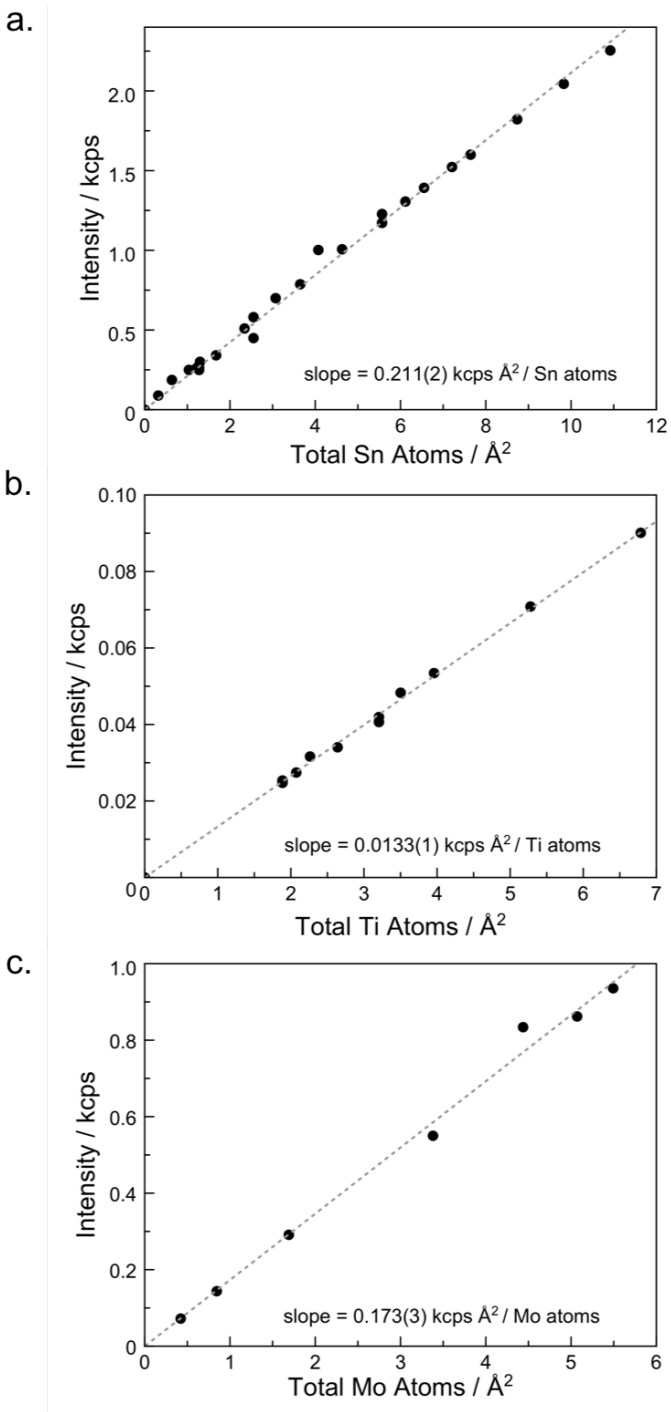

Figure 3.3. Graphs of the XRF intensity versus the number of atoms per unit area of several elements calculated from diffraction information such as that shown in Figure 3.2 for a number of different films.

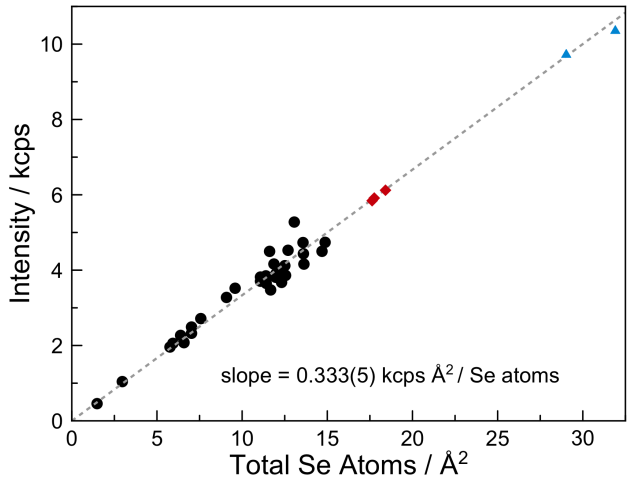

Figure 3.4. XRF intensity versus the total number of Se atoms per unit area determined from diffraction information (black), from films of $SnSe_2$ (red) and from films of $TiSe_2$ (blue). For the $SnSe_2$ and $TiSe_2$ films, the information in Figure 3.3 was used to determine the number of cation atoms in these films from the measured Sn and Ti XRF intensities. These values were then used to calculate the number of Se atoms in each of the films.

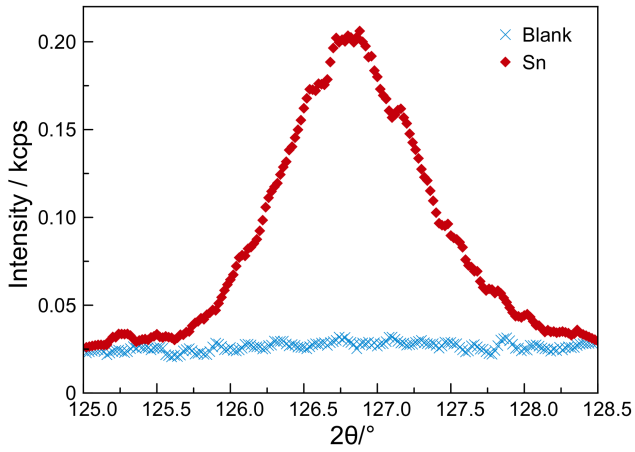

Figure 3.5. The Sn-La emission intensity from a film with 0.11 Sn/Å^2 and the blank Si substrate before deposition of Sn.

For ultra-thin films (a monolayer or less), the ability to subtract the background intensity accurately and reproducibly is obviously critical, making the choice of the emission line an important factor. Figure A.3 in the supporting information illustrates this point, showing the measured intensity of a Pb-containing sample and its blank substrate for three different emission lines, the Lα, the $L\beta_1$, and Mα. While the signal intensity is largest for the Lα emission line, the low and constant intensity measured on the blank substrate for the Mα line makes it the preferred emission line.

The ability to quickly measure the number of atoms per unit area of each element in a film enables films to be prepared with a precise number of unit cells such as that shown in Figure 3.2. To demonstrate this, a film where eight elemental Mo and Se layers were sequentially deposited onto a room temperature silicon substrate, with each pair containing the appropriate amount of these elements per unit area to form a single crystalline $MoSe_2$ layer. After annealing at 650°C, a variety of diffraction and reflectivity scans were collected. The XRR scan in Figure 3.6 is that expected for a film containing 8 identical layers, with a thickness consistent with 8 MoSe2 trilayers. The high angle annular dark field scanning transmission electron microscopy (HAADF-STEM) cross-section image of this sample, also shown in Figure 3.6, is consistent with the XRR scan. The specular diffraction pattern contains only four broad 00*l* reflections, indicating that the MoSe2 is crystallographically aligned with the substrate yielding a *c*-axis lattice parameter of 6.53(1) Å, consistent with the literature value of 6.46 Å.[43] The in-plane diffraction pattern contains only *hk*0 reflections, from which an *a*-axis lattice parameter of 3.27(3) Å was calculated. This is in good agreement with that previously reported for $MoSe_2$ (3.31 Å).[43]

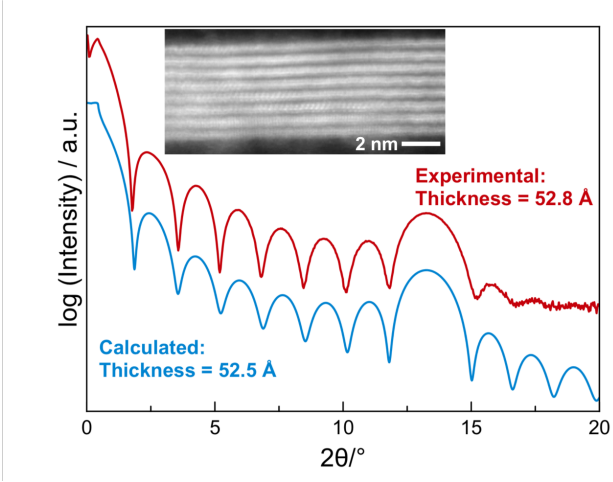

Figure 3.6. Measured and calculated XRR patterns of an 8-layer $MoSe_2$ film showing the application of this XRF method to prepare films containing a finite number of layers. The inset HAADF-STEM image shows further evidence of the formation of 8 $MoSe_2$ layers.

Element	Sensitivity
Sn ($SnSe$)	> 1%
Pb ($PbSe$)	> 1%
Nb ($NbSe_2$)	> 1%
Mo ($MoSe_2$)	2%
V (VSe_2)	7 %
Ti ($TiSe_2$)	10 %

Table 3.2. Sensitivity of the XRF measurement for a series of elements as a percent of a monolayer of the compound in parenthesis.

3.5. *Conclusion*

XRF is a sensitive and precise probe of the number of atoms per unit area of select elements in thin film samples. If films are thin enough, absorption corrections can be ignored, and the matrix has minimal impact on fluorescence intensity. The proportionality factor between intensity and the number of atoms of each element per unit area was determined using diffraction data from smooth, crystallographically aligned thin films that are an integral number of unit cells in thickness. The sensitivity of this approach enables less than 1% of a monolayer to be quantified.

3.6. *Bridge*

The XRF technique outlined in this chapter is essential for the precise control of thin film synthesis and control of nanoarchitecture. As opposed to commonly used elemental analysis techniques that only offer the relative amounts of constituents, our method is able to provide experimentalists with the absolute number of atoms per unit area. This gives a new, more exact level of information that is valuable for materials characterization even down to sub-monolayer dimensions. This technique has been utilized for all experimental chapters (4-6) that follow and has improved our ability to reliably prepare samples with few layers.

CHAPTER IV:

ULTRALOW THERMAL CONDUCTIVITY OF TURBOSTRATICALLY DISORDERED $MOSE_2$ ULTRATHIN FILMS AND IMPLICATIONS FOR HETEROSTRUCTURES

4.0. *Authorship Statement*

The work in this chapter is being submitted for publication in the IOP journal 2D Materials in 2018. The article has been coauthored with Hyejin Jang, Niklas Wolff, Robert Fischer, Alexander C. Lygo, Gavin Mitchson, Lorenz Kienle, David G. Cahill, and David C. Johnson. Hyejin Jang (advised by David G. Cahill) conducted the thermal conductivity measurements for samples and provided data for the elastic constants. Niklas Wolff (advised by Lorenz Kienle), Gavin Mitchson, and Robert Fischer all provided microscopy data. And, Alexander Lygo assisted with electrical measurements. I synthesized all samples and conducted all structural analysis. Additionally, I am the primary author of this article. David C. Johnson is my advisor, and David G. Cahill and Lorenz Kienle collaborated on the interpretation of data and drafting of the article.

4.1. *Abstract*

Films containing 8, 16, 24, 32 and 64 $MoSe_2$ layers were synthesized using the modulated elemental reactants (MER) method. X-ray reflectivity patterns showed that the annealed films were the targeted number of $MoSe_2$ layers thick with atomically smooth interfaces. In-plane x-ray diffraction scans contained only *hk*0 reflections for crystalline $MoSe_2$ monolayers. Specular x-ray diffraction patterns contained only 00*l* reflections, also indicating that the *hk*0 plane of the $MoSe_2$ layers are parallel to the substrate. Both x-ray diffraction and nanobeam electron diffraction indicated that the *hk*0 planes are rotationally disordered with respect to one another, with all orientations equally probable for large areas. The rotational disorder between $MoSe_2$ layers is present even when analyzed spots are within 10 nm of one another. Cross-plane thermal conductivities of 0.063 – 0.089 W m^{-1} K^{-1} were measured by time domain thermoreflectance, with the thinnest films exhibiting the lowest conductivity. The structural analysis suggests that the ultralow thermal conductivity is a consequence of rotational disorder, which increases the separation between $MoSe_2$ layers and creates significant anharmonicity. Since rotational

disorder between adjacent layers in heterostructures is expected if the constituents have incommensurate lattices, this study indicates that these heterostructures will have very low cross-plane thermal conductivity.

4.2. *Introduction*

In the past decade, van der Waals heterostructures have attracted significant research interest[1–4] due to emergent optoelectronic,[5–7] magnetic,[8,9] topological,[10–12] and catalytic[13] properties that arise when two or more nanosheets are assembled in a stacked configuration. Depending on the selected constituents, layers can either operate relatively independent of one another,[14] or states may be coupled to create novel or modified behavior.[5,15,16] The modular design of heterostructures enables researchers to vary the constituents, layer thicknesses or stacking sequence to tune a targeted property.[2] More recently there have been efforts to understand more precisely how the rotation angle between layers affects properties and gives rise to extended in-plane structural and electronic superlattices (i.e. Moiré lattices). Studies have shown exotic electronic properties in graphene systems as a function of rotation angle including the ability to couple[15,17,18] and decouple[19,20] electronic states. In transition metal dichalcogenide systems, similar phenomena depend on rotation angle including carrier lifetime, collection efficiency, band gap and structural modulations.[21–25] These investigations are particularly relevant to nanoelectronics, where interactions between constituents become more important as interfaces become a larger fraction of devices.[26]

While electronic, optical, and structural changes in single layers and heterostructures of van der Waals materials have been widely studied, there has been much less emphasis on thermal properties. Thermal conductivity between dissimilar materials is an important design parameter in many applications, with high thermal conductivity desired for some (heat dissipation in electronics) and low thermal conductivity desired for others (thermoelectric materials). Theoretical investigations of the in-plane thermal transport properties of monolayers of transition metal dichalcogenides have yielded a wide range of in-plane thermal conductivity values, with values from 1.35 to 103 W m^{-1} K^{-1} calculated for MoS_2 and 17 to 43 W m^{-1} K^{-1} calculated for $MoSe_2$.[27–36] Measured in-plane thermal conductivities range from 34 to 84 W m^{-1} K^{-1}

for MoS_2 and values around 60 W m^{-1} K^{-1} for mono- and few-layer $MoSe_2$.[37–40] The cross-plane thermal conductivity of $MoSe_2$ is reported to be ~1 W m^{-1} K^{-1}.[41] There are fewer reports on the interfacial thermal resistance between dichalcogenides and substrates or between dichalcogenides and other 2D materials, with calculated values[42–45] ranging between 1 and 5×10^{-8} m^2 K W^{-1} and experimental reports ranging from 1×10^{-6} to 1×10^{-8} m^2 K W^{-1} depending on how the interfaces are prepared.[40,45–47] For the calculations done on van der Waals heterostructures, the constituent structures were distorted to form a supercell, and the resulting in-plane thermal conductivity was found to depend on the extent of distortion required to form the supercell.[47,48]

The thermal conductivity of superlattices provides a lower limit to the average thermal conductance of an interface, G, though the relationship $\Lambda = Gd/2$,[49] where Λ is the thermal conductivity and d is the period of the superlattice. This equation assumes that the thermal resistance of the interfaces dominates the thermal conductivity. Unfortunately, there have been no reports of the thermal conductivity of van der Waals superlattices, due to the synthetic challenges in preparing these structures via epitaxial growth techniques.[50] One might expect different behavior than in systems with strong covalent bonds across the interfaces due to the highly anisotropic bonding environment, with strong covalent bonds in the *xy* plane and non-epitaxial and weak van der Waals associations along the superlattice direction, *z*. The weak van der Waals bonding across the interface also creates the opportunity for an arbitrary rotational angle between two constituents. In 2007, Chiritescu et al. reported a 30-fold reduction in cross-plane thermal conductivity in WSe_2 prepared by modulated elemental reactants as compared to bulk single crystal WSe_2.[51] The rationale given for the observed reduction was the rotational disorder between WSe_2 sheets evident in X-ray diffraction data. Surprisingly, significantly higher cross-plane thermal conductivity has been reported in TMDs with extensive defects and non-planar sheets.[52] Since the in-plane lattice structure of the reported WSe_2 is very similar to the bulk compound, it is reasonable to assume that the low cross-plane thermal conductivity is a result of a large interfacial resistance between WSe_2 layers caused by the rotational disorder. Using the measured value of the cross-plane thermal conductivity (0.05 W m^{-1} K^{-1}) and the measured spacing of the layers, an interfacial conductance of 1.5×10^8 W m^{-2} K^{-1} (or an interfacial resistance of 6×10^{-9} m^2

K $W^{-1)}$ is calculated. This is an order of magnitude lower than the conductance reported for Si-Ge superlattices[49,53] and similar to the conductance reported for Ti-Al_2O_3, 2×10^8 W m^{-2} K^{-1}.

In this work we present the synthesis, in-depth structural characterization, and cross-plane thermal conductivity analysis of $MoSe_2$ ultrathin films with targeted thicknesses to probe the correlation between local rotational order at van der Waal interfaces and thermal conductivity. Specular X-ray diffraction analysis indicates that the films are crystallographically aligned to the substrate and uniform in thickness over a large area (~2 cm × 2 cm). The spacing between $MoSe_2$ layers is larger than that reported for the crystalline polymorphs and the measured film thickness is consistent with the targeted integer number of $MoSe_2$ layers. In-plane diffraction reveals only *hk*0 reflections of crystalline $MoSe_2$ and indicates that the $MoSe_2$ grains are randomly orientated with grain sizes on the order of 10-100 nm. The in-plane lattice parameter is consistent with that reported for $MoSe_2$ prepared at high temperatures. Cross section high angle annular dark field high-resolution scanning transmission electron microscopy (HAADF HRSTEM) reveals flat and parallel $MoSe_2$ layers with the targeted number of $MoSe_2$ layers. Plan view transmission electron diffraction patterns indicate that the layers are rotationally disordered from one another and nanobeam electron diffraction patterns indicate that the orientations of the layers change over a 10-nm length scale. In-plane electrical conductivity measurements show an activated behavior, with activation energy of 0.2 eV. Cross-plane thermal conductivity was evaluated by time domain thermoreflectance and found to be between 0.063 – 0.089 W m^{-1} K^{-1}, which is more than an order of magnitude smaller than previous reports. Assuming the thermal conductivity is dominated by low conductance at the interfaces, we calculate an interfacial conductance of ~2×10^8 W m^{-2} K^{-1} (or an interfacial resistance = 5×10^{-9} m^2 K W^{-1}) for rotationally disordered $MoSe_2$. Our results show that ultralow cross-plane thermal conductivity can be achieved in a highly periodic $MoSe_2$ array in which interlayer rotational disorder is the salient structural feature.

4.3. *Results and Discussion*

Samples were prepared by depositing a targeted number of Mo|Se bilayers and annealing the samples at low temperatures to self assemble $MoSe_2$. Deposition parameters for the modulated elemental precursor were calibrated so that the amount of Mo and Se in a deposited bilayer yielded a 1:2 ratio of the elements. These values were adjusted during this study to yield precursors with varying amounts of excess Se as this improved the quality of the resulting XRR and XRD patterns. The thickness of the deposited layers was then scaled so the number of atoms in each Mo|Se bilayer matched the number of atoms in a single Se-Mo-Se trilayer of $MoSe_2$ (subsequently called a monolayer). Samples were prepared with a range of total thicknesses by varying the number of Mo|Se bilayers deposited. Samples were annealed at 650 °C for 60 minutes in a N_2 atmosphere followed by a 60 minute anneal at 550 °C in a sealed tube with a Se partial pressure. The specular diffraction patterns of all samples contained only the 00*l* reflections expected for $MoSe_2$ that is crystallographically aligned to the silicon substrate (native oxide).

Figure 4.1 contains both calculated (red) and experimental (yellow and blue) low angle reflectivity patterns of samples where 24 $MoSe_2$ monolayers were targeted. The patterns contain periodic oscillations called Kiessig fringes, which result from two superimposed phenomena—the interference of scattered x-rays off the top and bottom interfaces of the film and the incomplete destructive interference of the 24 $MoSe_2$ monolayers. The position of the Kiessig fringes at low angles is dominated by the reflectivity of the sample, and their location depends the average total film thickness via Bragg's law corrected for refraction. The position of the Kiessig fringes closer to the 001 Bragg reflection for $MoSe_2$ is dominated by the incomplete destructive interference of the finite size crystal, and their location is related to the number of monolayers and their spacing, which is the c-axis lattice parameter. The annealed film from the stoichiometric precursor (blue) was ~10 Å thinner than the target thickness, leading to a film with less than 24 layers of $MoSe_2$. There is a difference between the thickness calculated from the position of the low angle Kiessig fringes (between 22 and 23 monolayers) and the higher angle fringes near the Bragg reflection (23 monolayers), indicating that different regions of the film have slightly different thicknesses. The interference between these two areas

of the film results in a reduction in the amplitude of the Kiessig fringes between 7° and 10° relative to that in the calculated pattern. Precursors deposited with the correct amount of Mo but a 10-15% excess of Se form films with Kiessig fringe amplitudes closer to that expected from the calculation; and the excess Se is expelled upon annealing as monitored using XRF.[54] The agreement between the experimental (yellow) and calculated (red) reflectivity patterns indicates that this sample contains 24 parallel monolayers, which is consistent with the cross-sectional STEM images discussed later. The samples used in this study were all prepared from precursors with ~10% excess Se.

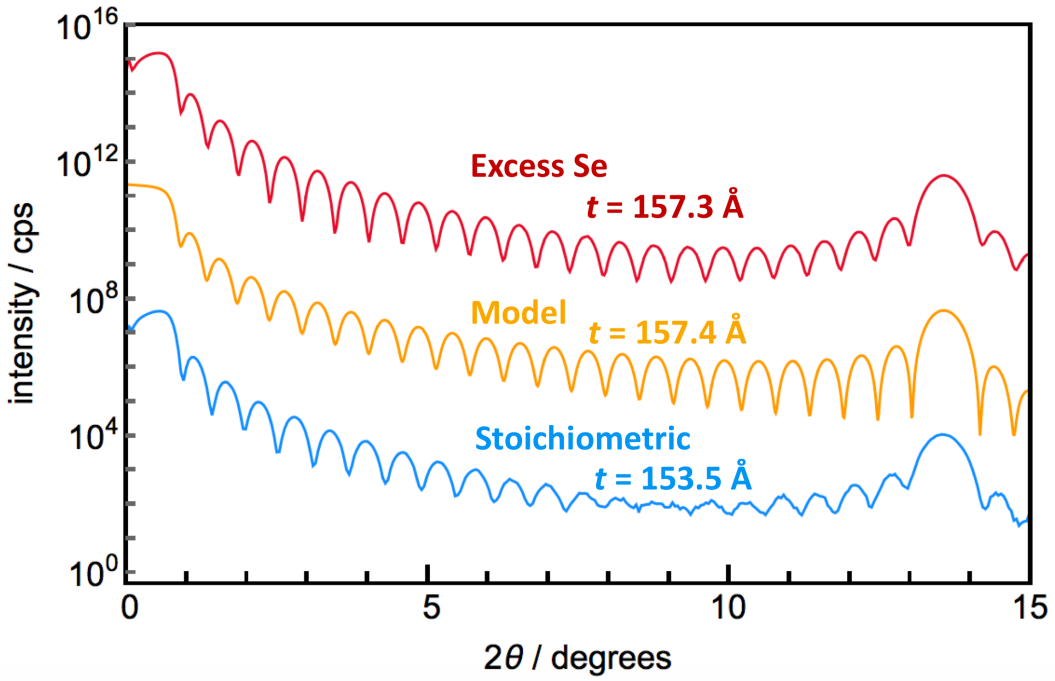

Figure 4.1. Low-angle reflectivity patterns for two samples designed to form 24 layers of $MoSe_2$. The yellow trace (middle) is a calculated pattern that was used as a comparison for the two experimental patterns (red and blue). The blue (bottom) trace was annealed from a stoichiometric precursor with ~5 % deficiency in Mo, whereas the red trace (top) contained a ~10% Se excess and the correct amount of Mo to form 24 layers.

Films containing 8 to 64 monolayers of $MoSe_2$ were prepared by changing the number of Mo|Se bilayers deposited in the precursor. Figure 4.2 contains the experimental and calculated X-ray reflectivity patterns for 8- and 16-layer structures. The agreement between the experimental (red) traces and calculated (blue) traces demonstrates the ability to prepare films with a targeted number of $MoSe_2$ monolayers over the entire

probed area (~4 cm^2). The Parratt relationship relates the angle to which resolved fringes are observed to how parallel the bottom and top surfaces of the sample are over the probed area.[55] The observation of fringes to $2\theta > 15°$ indicates sub-Angstrom smoothness.

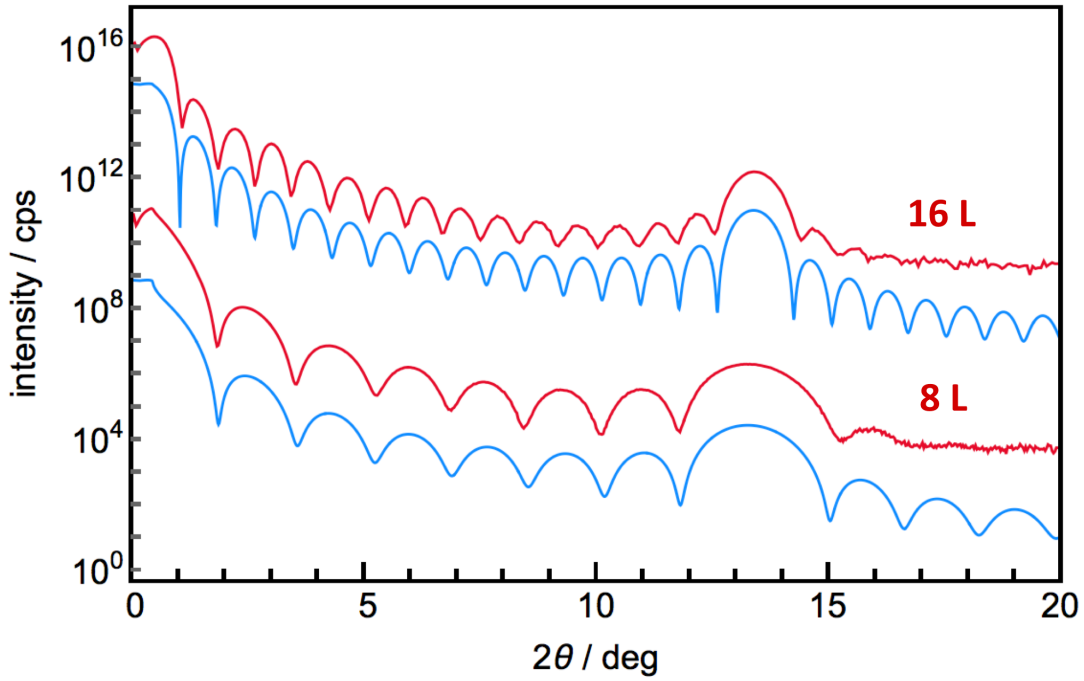

Figure 4.2. Low-angle reflectivity patterns of 8- and 16- layer $MoSe_2$ films that show strong agreement between the calculated (blue) and experimental (red) traces.

Specular diffraction patterns were collected to determine the out-of-plane structure of the samples. All the observed Bragg maxima (Figure 4.3) can be indexed as the 00*l* family of reflections, indicating that the $MoSe_2$ layers are parallel to the substrate. Rocking curve measurements were done on the 00*l* reflections to measure the extent of preferred alignment, yielding half widths of 1.1 degrees θ. These half widths are significantly narrower that the ~15 degrees θ reported by Muratore et al.[52] The line widths of the reflections broaden as the number of layers decreases and the coherence length becomes limited by the film thickness. *c*-axis lattice parameters were calculated for the different samples (see Table 1), yielding an average value of 6.531(2) Å, which is larger than previously reported *c*-axis lattice parameters (6.46(1) Å) for 2H, 3R, or 4H $MoSe_2$ prepared by high temperature syntheses.[56–60] We believe that this increased c-axis lattice parameter is a consequence of the rotational disorder between adjacent $MoSe_2$

layers. Even larger *c*-axis lattice parameters have been reported for $MoSe_2$ prepared using a variety of low T synthesis techniques.[61–63] The larger c-axis lattice parameters from these syntheses was not explicitly discussed, but for some approaches may be a consequence of included solvent molecules between the $MoSe_2$ layers.

Rietveld refinement of the specular diffraction pattern of the $MoSe_2$ sample with 64 layers was conducted to gain insight into the cause of the expanded *c*-axis lattice parameter. Figure 4.3 contains the experimental and calculated diffraction patterns, with a schematic of the refined model inset within the figure. The van der Waals gap from our refined model, taken as the distance between the Se planes in adjacent $MoSe_2$ layers, 0.321(1) nm, is 0.008 nm larger than that reported in the literature for $MoSe_2$ prepared at high temperatures (0.3128 nm). The Se-Mo interatomic distance (0.165(7) nm) is also larger than that reported in the literature for the thermodynamic product (0.1615(1) nm). We checked to see if the samples were off stoichiometry, but our XRF analysis indicates that the stoichiometry of all the samples are $MoSe_{1.99(2)}$. The increase in the c-lattice parameter is a consequence of both of these distances increasing, which we speculate is caused by the rotational disorder between adjacent $MoSe_2$ layers.

Grazing-incidence x-ray diffraction (GIXRD) was collected to obtain information about the in-plane structure of the samples. All of the patterns contain Bragg maxima that can be indexed as *hk0* reflections using a hexagonal unit cell (Figure 4.4), consistent with the preferred orientation of $MoSe_2$ layers. The *a*-axis lattice parameters of the different $MoSe_2$ films were determined using LaBail fits of the diffraction patterns. The value obtained, 0.331(1) nm, agrees with literature values for $MoSe_2$, which range from 0.329 nm for $MoSe_2$ prepared at high temperature[57–60], to as low as 3.22 for films prepared at low temperature.[7] The Debye-Scherrer equation was used with line widths obtained from the LaBail fits to obtain an estimate of 10 nm for the in-plane grain sizes. In-plane pole figures indicate that the crystallites are randomly oriented in the *xy*-plane over the ~4 cm^2 analytical area.

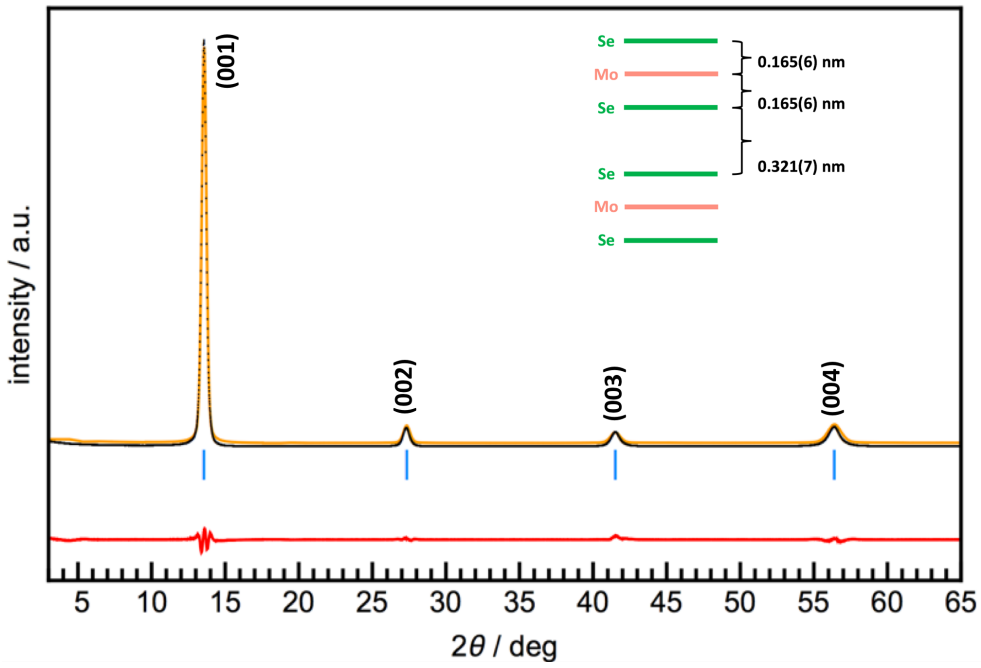

Figure 4.3. Specular diffraction patterns show only the 00*l* family of Bragg reflections, indicating that $MoSe_2$ nanosheets run parallel to the substrate. The structural refinement shows a slightly increased interplanar distance between Se and Mo planes, which is consistent with other low temperature syntheses. Experimental data points are shown in black, and the refinement is shown in yellow. The residuals are in red.

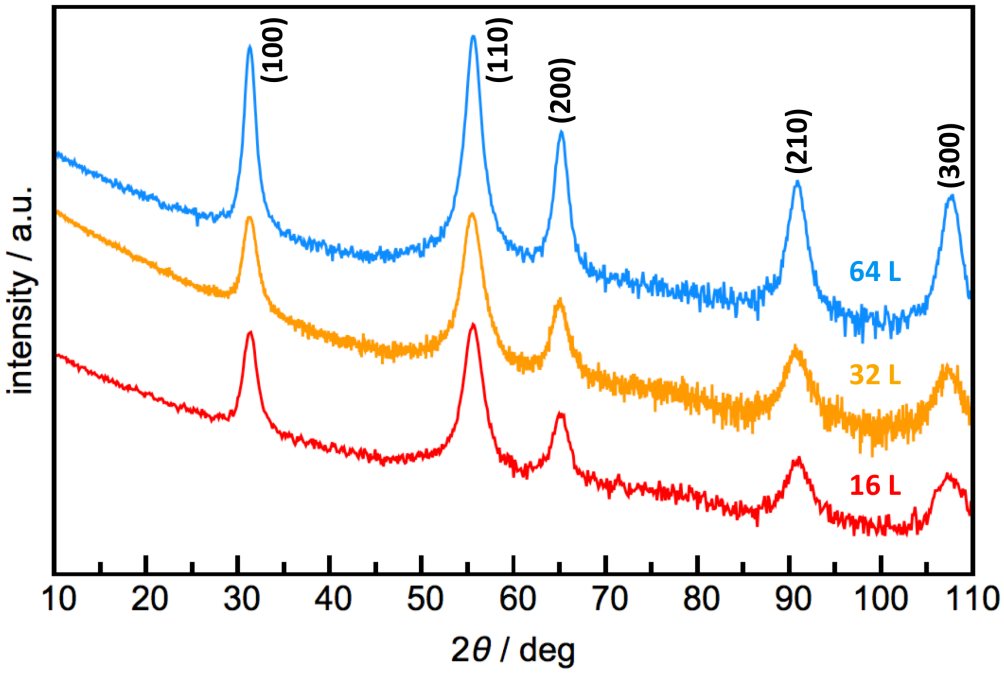

Figure 4.4. Representative GIXRD patterns of 16-, 32-, and 64-layer films showing only *hk0* reflections due to the preferred orientation of the crystallites.

Cross-sectional HAADF-STEM images were collected to gain additional information about the structure of the $MoSe_2$ layers and their stacking. Figure 4.5 contains images of the 8- and 24-layer samples, which contain layers of alternating contrast corresponding to the nanosheets (bright) and van der Waals gaps (dark) with the layers parallel to the substrate. The number of Mo|Se layers in the precursors have been retained in the crystalized films, which contain atomically sharp interfaces and highly parallel layers in agreement with the diffraction data discussed previously. Areas with

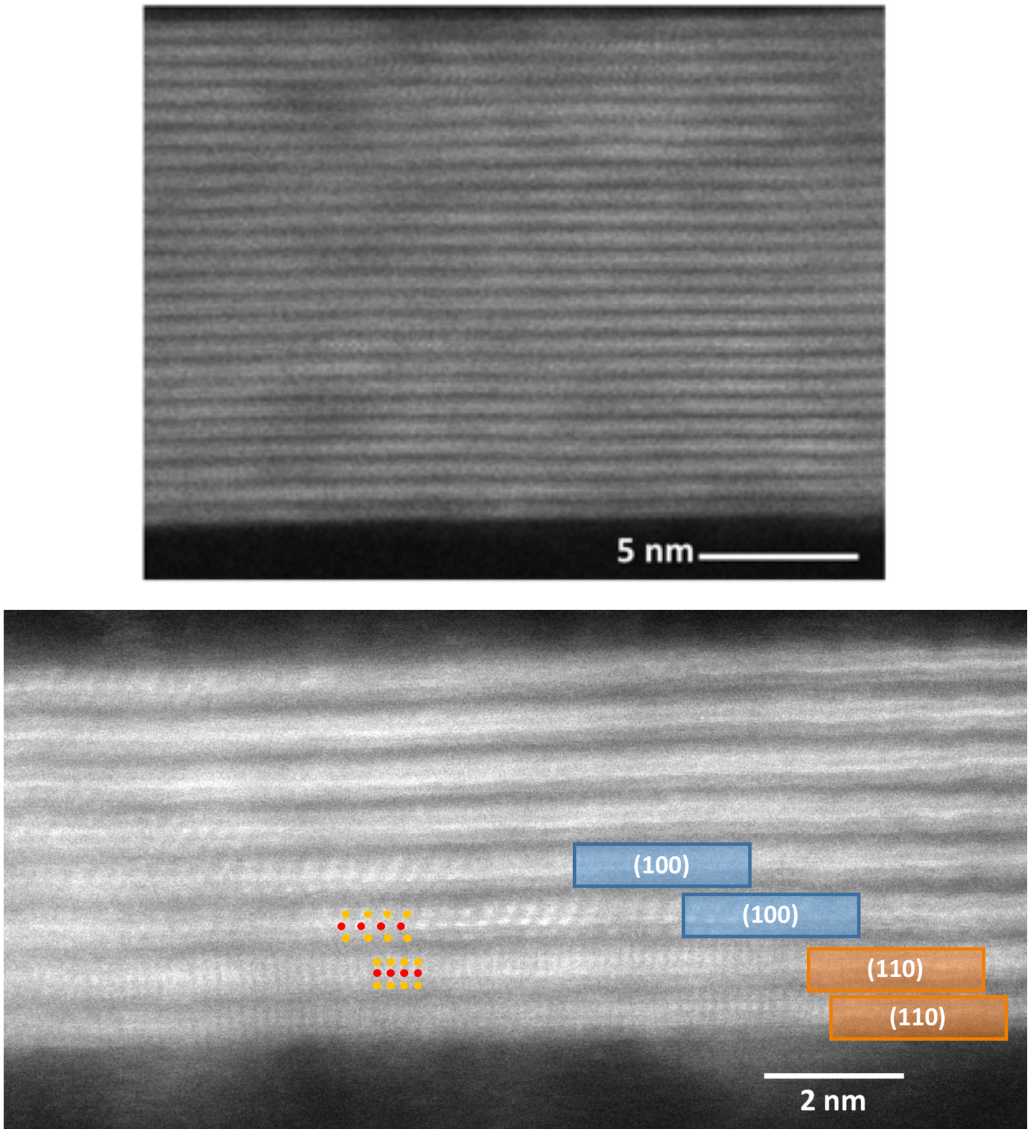

Figure 4.5. Cross-Sectional HAADF-STEM images of 24-layer and 8-layer $MoSe_2$ films. Grain orientations and zone axes are indicated in the shaded boxes, and the arrangement of atoms is shown with red spheres corresponding to Mo atomic columns and gold spheres corresponding to Se atomic columns.

resolvable zone axes are not frequent and neither are areas with alignment between layers, such as that in the image of the 8-layer sample. This is consistent with the rotational disorder previously reported from other films made via MER synthesis and the pole figure measurements discussed earlier. A periodic stacking of the layers observed in the thermodynamic phases of $MoSe_2$ is not observed. A non-representative area of the 8-layer film is shown in Figure 4.5 because it contains a rare region where the bottom 2 layers have a (110) orientation while layers 3 and 4 have the (100) axis aligned with the beam. The observed chevron arrangement of the atoms within the $MoSe_2$ nanosheets where the electron beam is aligned down the (100) axis is consistent with trigonal prismatic coordination of the Mo atoms. Layers 5-8 do not show resolvable zone axes, indicating that they possess different rotational orientations. Most of the areas viewed in the STEM investigation did not show any, or at most a single layer with a resolvable zone axis. A high density of independent nucleation sites probably causes the rotational disorder between layers during the self-assembly of the precursor. Faster growth along a $MoSe_2$ sheet than heterogeneous nucleation of an adjacent layer at the interface of an existing layer results in the random rotational orientation. Grain sizes within a layer agree with the diffraction estimates using Debye-Scherrer analysis (on the order of ~10 nm).

The HAADF HRSTEM images in Figure 4.5 demonstrate a well-defined layered structure. This is different from previous reports of WSe_2 also made by MER synthesis. Cross section high-resolution TEM images showed nonplanar layers with small in-plane grain sizes.[64] This result was inconsistent, however, with previously reported x-ray diffraction data on the same sample,[51] indicating that the sample may have been damaged during TEM sample preparation.

Plan view HRTEM data and nanobeam electron diffraction (NBED) patterns were collected over a 250 × 250-nm region of the 8-layer sample to obtain information on the local rotational disorder. Figure 4.6 shows a representative 3 × 3 grid of these NBED patterns collected with a focused 8-nm electron beam on a square grid with 10 nm between the centers of the electron beam. All of the patterns contain multiple hexagons of varying orientation and intensity, reflecting the local orientations of the hexagonal $MoSe_2$ basal planes. The local orientations change significantly from spot to spot. The grain orientations are randomly distributed and they change intensity independently of one

another, consistent with the rotational disorder inferred from the cross section HRSTEM data. If all of the patterns over the 250 × 250-nm area are stacked on top of one another, rings of uniform diffraction intensity are obtained (see SI), consistent with the x-ray pole figure experiment discussed earlier. Different grain orientations can be identified in each individual pattern, and are represented by the different color hexagons in the central pattern of Figure 4.6. These orientations were tracked from the central pattern to the adjacent regions. If a specific orientation is still observed, a hexagon of that color is shown. If the orientation is missing in an adjacent region, the hexagon is not shown. While a specific orientation may exist on diffraction patterns collected on adjacent spots, the majority of the orientations change even at this length scale.

By the evaluation of smaller scale, e.g. 5 × 5 nm^2 fast Fourier transforms (FFTs) of HRTEM micrographs as depicted in Figure 4.7, further statements about the rotationally disordered layers could be deduced as explained in the SI. The rotational disorder of NBED patterns on the larger scale is congruent with the superposition phase contrast visible in Figure 4.7a. However, confined areas of rotational alignment could be identified from the 7b HRTEM contrast and 7c FFT analyses, showing single hexagon patterns. Further, a color coded mapping 7d of hexagon orientations prolonging or disappearing in adjacent squares reveals certain rotational ordering on 10-30 nm length scales within $MoSe_2$ layers (See SI for details). This is consistent with FFT's done on 5 nm areas of the plan view HAADF STEM data, as shown in the SI. The changes in grain orientation observed in Figure 4.7 are consistent with the estimates of the in-plane grain size and illustrate the extensive local rotational disorder between $MoSe_2$ layers on the nanometer scale.

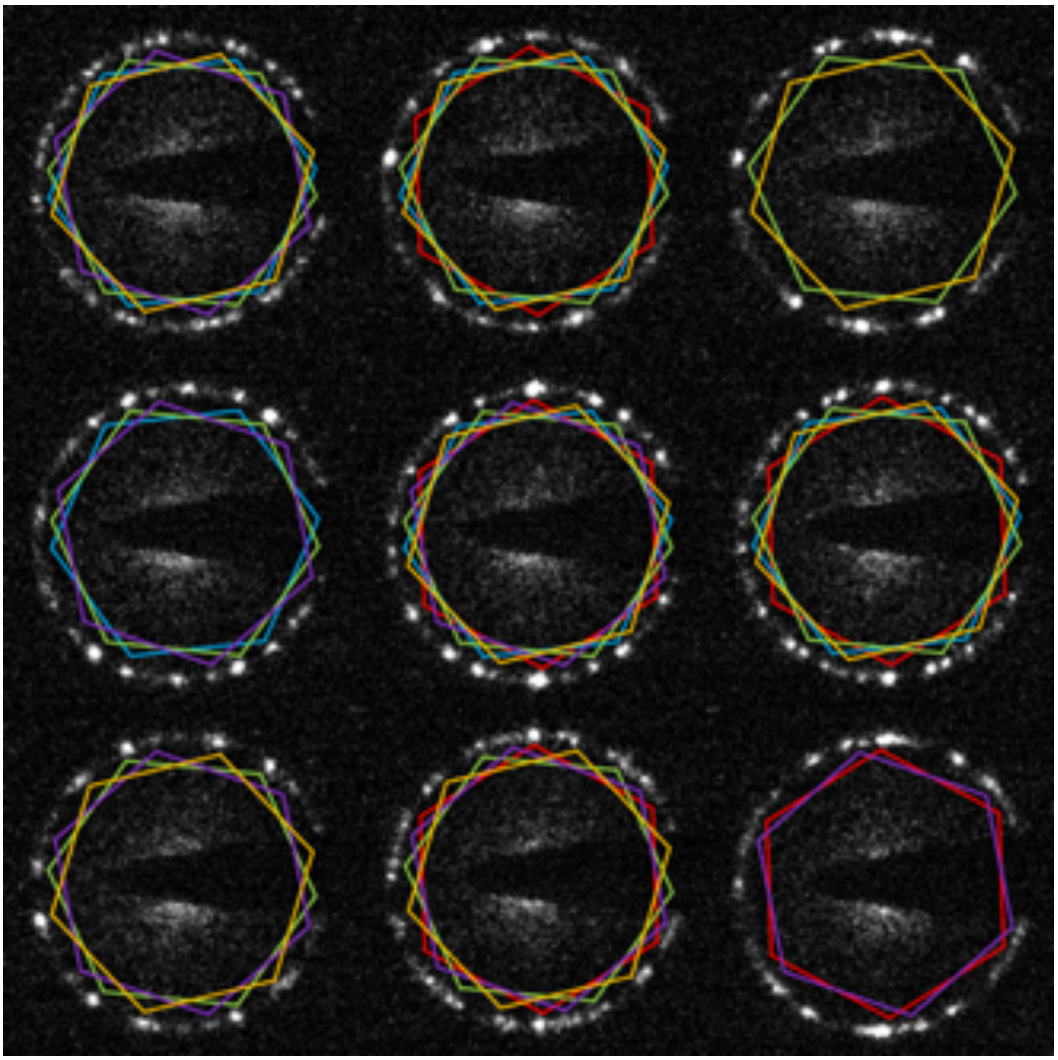

Figure 4.6. Nanobeam electron diffraction patterns of $MoSe_2$ domains separated by 10 nm. Grain orientations are highlighted by colored hexagons in the central SAED image. If one of these orientations persists in a neighboring SAED image, the color hexagon corresponding to that orientation is superimposed on the image.

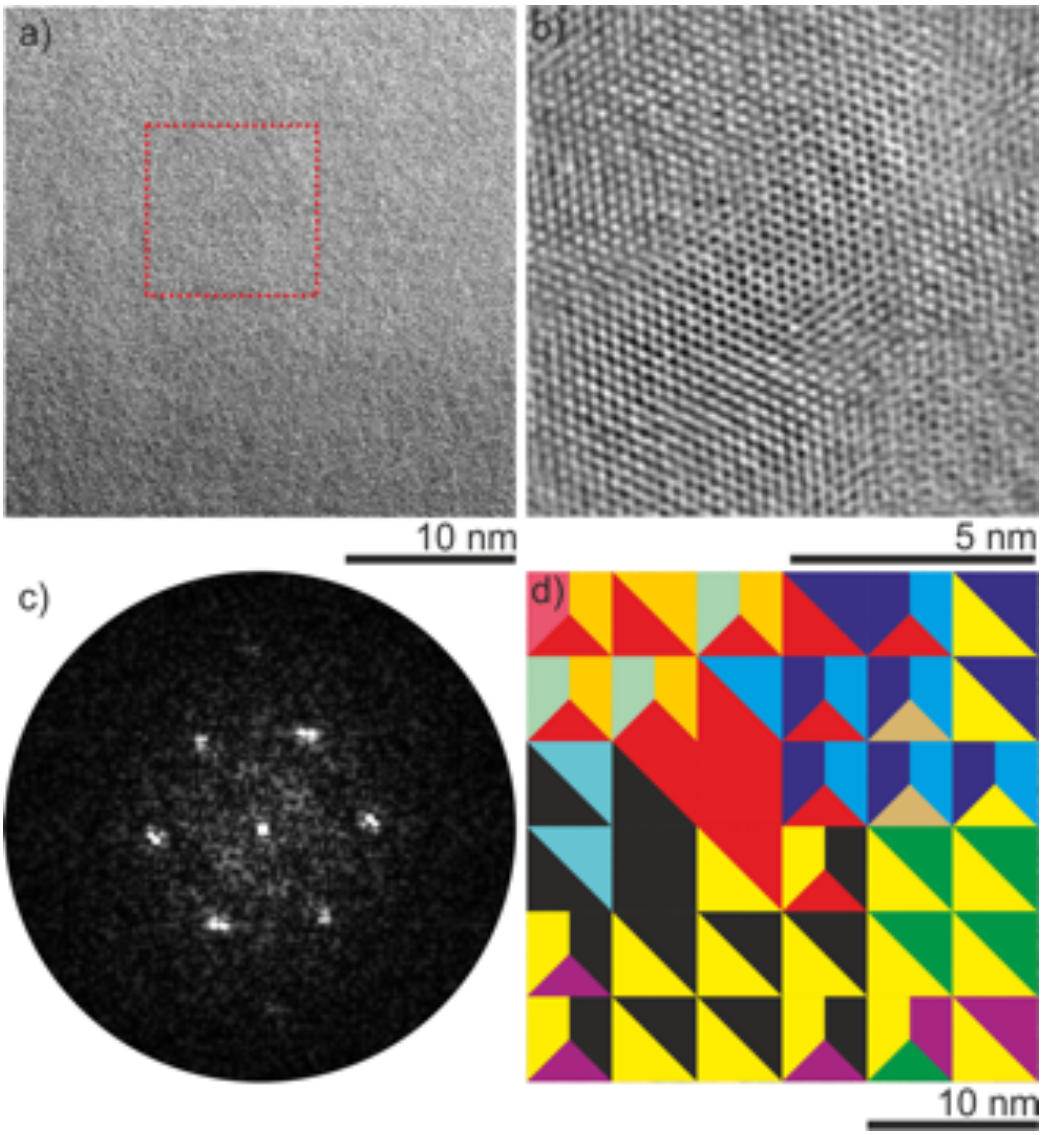

Figure 4.7. Plan view HRTEM study of a 8-layer $MoSe_2$ sample. a) HRTEM micrograph showing confuse phase contrast originating from the rotational disorder of stacked layers. b) Magnified area of the red box in a) showing a small area in which all 8-layers are rotationally aligned. c) Single orientation FFT pattern of the image depicted in b). d) Color coded map showing different hexagon orientations extracted from individual 5x5 nm² FFT's on adjacent positions up to the order of three differentiable rotations.

Electrical resistivity was measured at temperatures between 165 K – 295 K using the van der Pauw method. The resistivity increased exponentially from 0.83 Ωm at room temperature to 10.73 Ωm at 165 K, indicating that the films are semiconducting. A linear regression of $\ln \rho$ v. T^{-1} (Figure 4.8) yielded a band gap of 0.17(1) eV, which is approximately one order of magnitude smaller than the optical band gaps reported for

bulk 2H $MoSe_2$ and large-grain monolayer structures.[65] While studies report a narrowing of band gaps in rotationally disordered systems by ~15%,[21] the lower band gap in our system obtained from the resistivity suggests that we are not observing the intrinsic band gap, but instead we are measuring the activation energy of a defect band.[66]

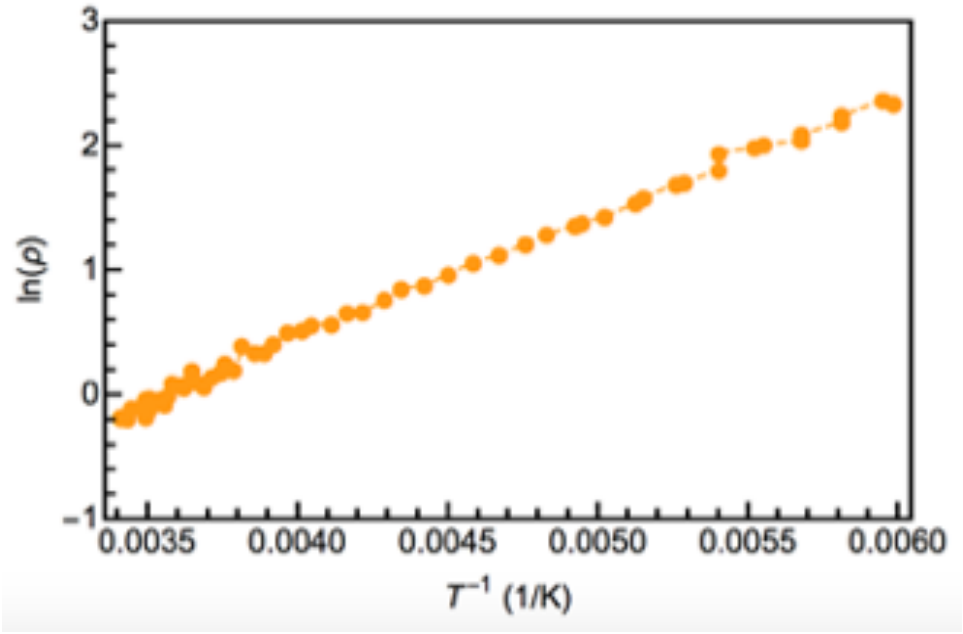

Figure 4.8. The linear relationship between ln ρ and T^{-1} indicates that films are semiconducting.

Thermal conductivity measurements were made using the time domain thermoreflectance (TDTR) method[67] on the 16, 32, and 64-layer films with a 80-nm-thick aluminum film as an optical transducer sputtered on the $MoSe_2$ films. The thermal model is compared with the measured TDTR data to determine two free parameters: thermal conductivity of $MoSe_2$ (Λ) and interfacial thermal conductance between Al and $MoSe_2$ (G). The experimental heat capacity of $MoSe_2$ is used as 1.89 J K^{-1} cm^{-3}.[68] Due to the extremely low thermal conductivity of the $MoSe_2$ films, the TDTR measurement is most sensitive to Λ and less sensitive to G. Therefore, the thermal conductivity of $MoSe_2$ is evaluated at G=100±70 MW m^{-2} K^{-1}, which is the typical range of G,[69] i.e., the upper bound is for the interface between metals and dielectrics, and the lower bound is for the interface between metals and 2D van der Waals materials. The summary of the thermal conductivity of 16, 32, and 64-layer films is given in Table 1. Note that the positive (negative) uncertainty of Λ corresponds to G=30 (170) MW m^{-2} K^{-1}.

The measured cross-plane thermal conductivities, 0.07 W m^{-1} K^{-1} to 0.09 W m^{-1} K^{-1}, are extremely low for a fully dense solid. These values are approximately a factor of 50 smaller than what has been reported for bulk dichalcogenides of Mo, W, and Ti for which values ranged from 1.75 W m^{-1} K^{-1} for a purchased single crystal of WSe_2 to 4.7 W m^{-1} K^{-1} for a natural mined single crystal of MoS_2.[51,52,70–72] Thermal conductivity values for crystals of Mo and W dichalcogenides grown via vapor transport range from a low of 1.2 W m^{-1} K^{-1} for WSe_2 to a high of 3.5 W m^{-1} K^{-1} for $MoSe_2$.[70,73,74] Samples of MoS_2 prepared by annealing Mo films in S vapor have thermal conductivities close to those of bulk crystals.[52,75] These values are generally in agreement with calculated values.[76,77] Intercalation has been shown to lower the cross-plane thermal conductivity of dichalcogenides by a factor of 2 to 3,[72,75] significantly less than the reduction observed here. Very low cross-plane thermal conductivities have been published for disordered dichalcogenide films prepared by magnetron sputtering, 0.1-0.3 W m^{-1} K^{-1}.[52] In these thin film studies, however, the wavy stacking arrangement of nanosheets was thought to scatter phonons. Models that accommodate reduced symmetry along z have corroborated that stacking disorder and lattice expansions on the order of 2-3% can reduce cross-plane thermal conductivity to ~0.4 W m^{-1} K^{-1}.[78]

The longitudinal speed of sound along the *z*-axis (v_L) of the Al-sputtered $MoSe_2$ films can be determined by using picosecond acoustics.[79] The elastic constant, C_{33}, can be calculated as $C_{33}=\rho v_L^2$, where ρ is the theoretical mass density of $MoSe_2$, 7.0 g cm^{-3}, and is shown in Table 1. The C_{33} of 38–44 GPa is comparable to that of other transition metal dichalcogenides, e.g., 52 GPa for MoS_2 bulk[75] and 43 GPa for ReS_2 exfoliated flake.[69] We speculate that the 50-fold reduction in the cross-plane thermal conductivity of the rotationally disordered $MoSe_2$ films would be attributed to the suppressed group velocity of transverse phonon modes, rather than that of longitudinal modes. However, measurement of the transverse speed of sound or shear modulus is challenging, and experimental evidence is still lacking.

Results presented in this study suggest that rotational disorder in otherwise well-defined crystalline systems is sufficient to reduce thermal conductivity to ultralow values. The structural analysis indicates that our films consist of a highly periodic $MoSe_2$ array with flat (non-wavy) monolayers. While the c-axis lattice parameter is ~1% larger than

single crystals, this expansion is coherent throughout the sample. The in-plane x-ray diffraction pole figures show that the layers have a random rotational orientation over the large area probed. The nanobeam electron diffraction data shows that this interlayer rotational disorder exists at the nanoscale. The ultralow thermal conductivity values reported here are consistent with the cross-plane thermal conductivities reported for WSe_2 and dichalcogenide containing heterostructures prepared using MER with semiconducting rock salt layers, with values ranging from 0.05 – 0.35 $Wm^{-1}K^{-1}$.[51,80–84]

The rotational misalignment between layers creates very anisotropic environment in the *xy* plane for the Se atoms, as the Se in one layer is no longer sitting in the middle of a triangle of Se atoms from the adjacent layer.[85] Assuming that the low thermal conductivity measured here for rotationally disordered layers is solely due to a low thermal conductance at the interface, we calculate a lower limit of 2×10^8 W m^{-2} K^{-1} for the interfacial conductance. This is a factor of 5 smaller than that calculated for the interface conductance of a 2H-1T MoS_2 heterostructure (1×10^9 W m^{-2} K^{-1}) for different special orientations investigated.[86] The lower thermal conductance for identical layers that are rotationally disordered with respect to one another, suggests that rotational misalignment between adjacent monolayers in van der Waals heterostructures might result in even smaller interfacial conductance. This would result in even lower thermal conductivity if the degree of rotational disorder were maximized.

# $MoSe_2$ Layers	*a* (Å)	*c*(Å)	Λ ($Wm^{-1}K^{-1}$)	C_{33} (GPa)
64	3.309(5)	6.532(2)	$0.090^{+0.004}_{-0.002}$	44±3
32	3.313(1)	6.526(2)	$0.07^{+0.012}_{-0.002}$	32±5
24	3.309(1)	6.528(5)	-	-
16	3.310(1)	6.536(9)	$0.07^{+0.03}_{-0.004}$	38±8
8	3.308(4)	6.53(1)	-	-

Table 4.1. Summary of lattice parameters from x-ray diffraction, cross-plane thermal conductivity (Λ), and *z*-axis longitudinal elastic constant (C_{33}) for the rotationally disordered $MoSe_2$ films in this study.

4.4. *Bridge*

Using the XRF technique outlined in Chapter 3, we were able to synthesize $MoSe_2$ with precise layering schemes down to ultrathin dimensions. Previous work on the thermal conductivity of ferecrystalline TMDs had called into question the structural characterization of the thin films, suggesting that low thermal conductivity may not have been a result of rotational disorder, but rather poorly defined crystalline systems. This work shows a rigorous structural characterization of an exceedingly well defined crystalline nanolaminate. Additionally, it provides local level characterization of rotational disorder. This shows more definitively the relationship between low thermal conductivity and rotational disorder specifically. A natural corollary to this project would be to synthesize an intergrowth wherein interlayer atomic registry is further inhibited and rotational disorder is maximized. One strategy to achieve this is to interleave structures with significant lattice mismatches, and that is the subject of the work presented in Chapter 5.

CHAPTER V:

SYNTHESIS, CHARACTERIZATION, AND ULTRALOW THERMAL CONDUCTIVITY OF THE LATTICE-MISMATCHED $(SnSe_2)_1(MoSe_2)_{1.32}$ HETEROSTRUCTURE

5.0. *Authorship Statement*

The work in this chapter is being submitted for publication in the Wiley-VCH journal Angewandte Chemie in 2018. The article has been coauthored with Hyegin Jang, Matthias Falmbigl, Gavin Mitchson, David G. Cahill, David C. Johnson. Hyejin Jang (advised by David G. Cahill) conducted all the time domain thermoreflectance measurements. Gavin Mitchson collected all microscopy data. I synthesized all samples, determined optimal thermal treatments, conducted all structural analysis (with some assistance from Matthias Falmbigl), and gathered all electrical data. I am the primary author of this article. David C. Johnson is my advisor, and David G. Cahill has collaborated on the interpretation of data and drafting of the article.

5.1. *Abstract*

An intergrowth of alternating $MoSe_2$ and $SnSe_2$ layers was prepared using the Modulated Elemental Reactants (MER) synthesis in order to achieve a heterostructure with high lattice mismatch in the basal planes. Structural characterization shows the formation of two independent lattices that closely resemble parent structures and an ability to select the number of unit cells in the stack. Specular diffraction shows only *00l* reflections while grazing incidence in-plane x-ray diffraction shows only *hk0* reflections, indicating that nanosheets are aligned parallel to the substrate. Additionally, crystallites are rotationally disordered from one another, which is apparent even at the local level by HAADF-STEM imaging. The cross-plane thermal conductivity for films of varying thicknesses between 8 and 32 unit cells was analyzed by time domain thermoreflectance and found to be 0.043 -0.058 $Wm^{-1}K^{-1}$, with the thinnest films exhibiting the lowest conductivity. Our work shows that a heavily lattice-mismatched heterostructure can maximize rotational disorder and depress thermal conductivity to record breaking lows even in otherwise well-defined crystalline systems.

5.2. *Introduction*

Low thermal conductivity is important in many technological applications, for example when materials are used as thermoelectric materials, as thermal barrier coatings for gas turbine blades,[1,2] as insulating components in phase change memory devices,[3] or simply as thermal insulation.[4] Low thermal conductivity is generally found in amorphous glasses[5], where the atomic scale disorder results in vibrations being attenuated on a length scale near that of the inter-atomic separation. Adding porosity further reduces thermal conductivity,[6] but negatively impacts mechanical and electrical properties. Materials with highly anisotropic bonding environments can also have very low thermal conductivities as the interfaces can effectively scatter atomic vibrational waves.[7] The lowest thermal conductivities have been found for layered materials with rotationally disordered interfaces.[8–10]

Since thermal conductivity depends on atoms transferring vibrational energy to one another, we hypothesized that creating a heterostructure with an incommensurate structural relationship between the layers would maximize rotational disorder and also increase the distances between the layers, both contributing to ultralow thermal conductivity. We targeted $SnSe_2(MoSe_2)_{1.32}$ because both constituents are layered compounds with hexagonal structures similar to that of WSe_2, but there is a large difference in their in-plane lattice parameters. The different size hexagonal lattices of Se atoms at the interfaces were expected to prevent the constituent layers from stacking coherently, resulting in extensive rotational disorder between the layers and a larger van der Waals gap because the Se layers could not nest with one another.

5.3. *Results and Discussion*

We prepared $SnSe_2(MoSe_2)_{1.32}$ by repeatedly depositing the sequence of elemental layers, Se|Mo|Se|Sn, with each M|Se bilayer containing the number of atoms required to form the respective dichalcogenides with a slight excess of Se. Annealing these films in a dry N_2 atmosphere resulted in the self assembly of the targeted structure, but when we increased temperature enhance the structural coherence of the layers, x-ray fluorescence spectroscopy indicated the samples lost an equivalent of Se, forming SnSe.[11] Annealing precursors in a sealed tube with a Se partial pressure prevented the loss of Se

and enabled us to reproducibly obtain $(MoSe_2)_{1.32}SnSe_2$ with highly ordered crystals and controlled thicknesses as shown in Figure 5.1. The low-angle diffraction patterns in Figure 5.1a contain the first two *00l* Bragg reflections of the targeted heterostructure as well as Kiessig fringes, which result from both the finite thickness of the both film and incomplete destructive interference of the finite number of unit cells. The observation of Kiessig fringes to $2\theta > 15°$ indicates a $\Delta t < 1$ Å by the Parratt relationship.[12] Beneath the experimental traces is a calculated pattern for a film containing 16 unit cells of $(MoSe_2)_{1.32}SnSe_2$. The agreement between the calculated and experimental patterns indicates that each of the deposited layers self assembles into a unit cell of the target structure. The reflections in the specular diffraction patterns (Figure 5.1b) can all be indexed as *00l* reflections of the heterostructure, yielding a *c*-axis lattice constant of 1.307(5) nm for all of the films prepared. This lattice parameter is about 0.05 nm larger than the sum of the thicknesses of $MoSe_2$ (0.6464 nm)[13–17] and $SnSe_2$ (0.6137 nm)[18,19] layers in their respective bulk structures. The in-plane diffraction pattern (Figure 5.1c) contains maxima that can be indexed as *hk0* reflections of the $MoSe_2$ and $SnSe_2$ hexagonal structures yielding *a*-axis lattice parameters of 0.331(1) nm and 0.381(3) nm, respectively. Each of the lattice parameters is < 1% larger than their corresponding bulk structures.[18,19] The larger c-axis lattice parameter of the heterostructures is probably a consequence of the difference in the in-plane lattice parameters of the layers, which prevents nesting between the layers as found in 2H $MoSe_2$.[18,19]

Cross-section HAADF STEM images of representative areas of a sample designed to have 24 unit cells are presented in Figure 5.2. Figure 5.2a contains an image from the top to the bottom of the sample. The slightly alternating contrast every other layer suggests a periodic stacking of $SnSe_2$ (high contrast) and $MoSe_2$ (low contrast) layers. The image shows that the sample contains the targeted number of layers, that the layering scheme is retained throughout the probed area, and that there are atomically smooth interfaces between discrete layers. This analysis agrees with the diffraction data in Figure 5.1. Figure 5.2b shows a region where several different zone axes are present. The contrast of the central metal planes of each of the trilayers alternates slightly between brighter and dimmer due to the high contrast Sn atoms and the relatively lower contrast Mo atoms. The observed atomic arrangements for the $SnSe_2$ and $MoSe_2$ sublattices are

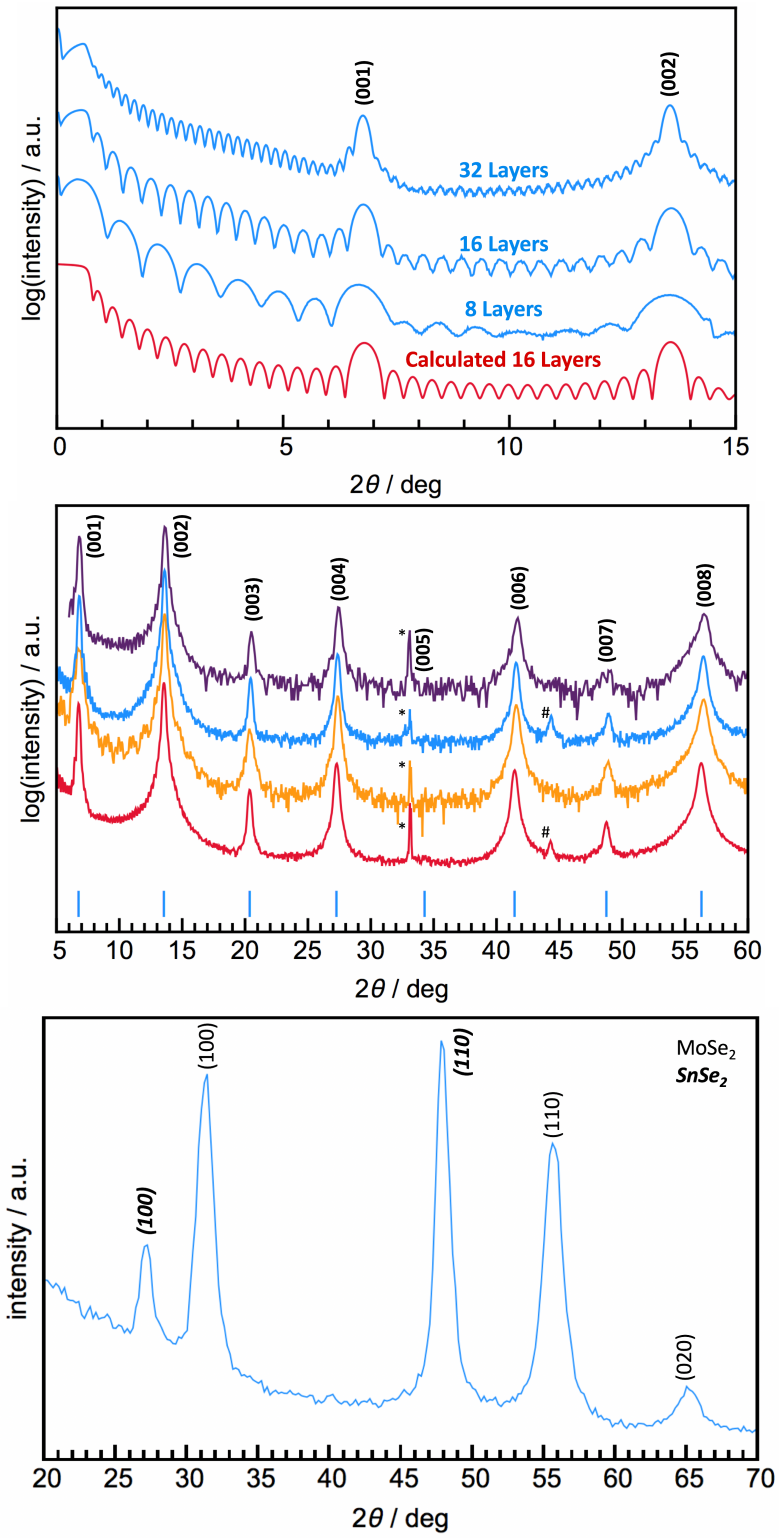

Figure 5.1. Diffraction data from $SnSe_2(MoSe_2)_{1.32}$ samples: (a) Low angle x-ray reflectivity data of experimental patterns (blue traces) and calculated pattern (red trace); (b) representative specular diffraction patterns of four samples (* = substrate reflections, # = stage reflections); and (c) in-plane diffraction containing *hk0* maxima that are indexed to the different constituent structures.

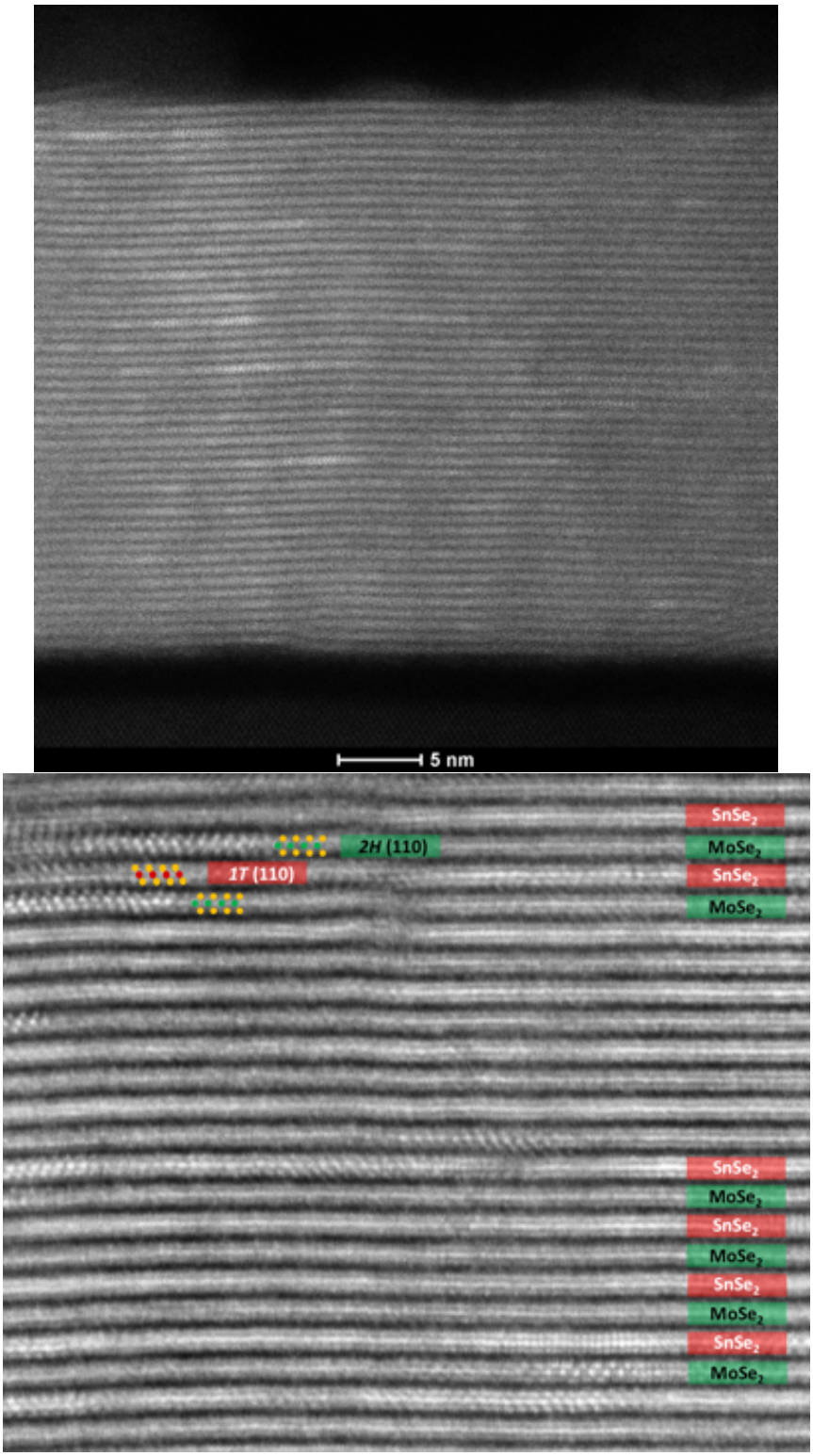

Figure 5.2. HAADF STEM images of representative 24-unit cell stack. (a) Resolvable interfaces consistent with the designed layering scheme throughout the entire thickness of the film (b) Intermittently aligned zone axes support no epitaxial coherence between adjacent layers. Scale bar = 2 nm

consistent with the octahedral coordination of Sn and trigonal prismatic coordination of Mo in the respective binary dichalcogenides. We observe few zone axes and see an even lower instance of adjacent layers that are both aligned down zone axes, suggesting that there is a high degree of rotational disorder and no favored stacking of the layers.

Energy-dispersive X-ray spectroscopy (EDS) images were obtained (Figure 5.3) to probe for potential intermixing of cations. The data shows alternating intensity of Sn and Mo with a periodicity equal to that of the superlattice from the specular diffraction. The regions of highest Mo intensity correspond to the lowest intensity of Sn, indicating that there is little-to-no mixing of Sn onto Mo sites. However, the spectra do show some Mo intensity on Sn planes. High Se intensity was observed both above and below each of the Sn and Mo planes. These observations are consistent with transition metal dichalcogenide nanosheets aligned parallel to the silicon substrate.

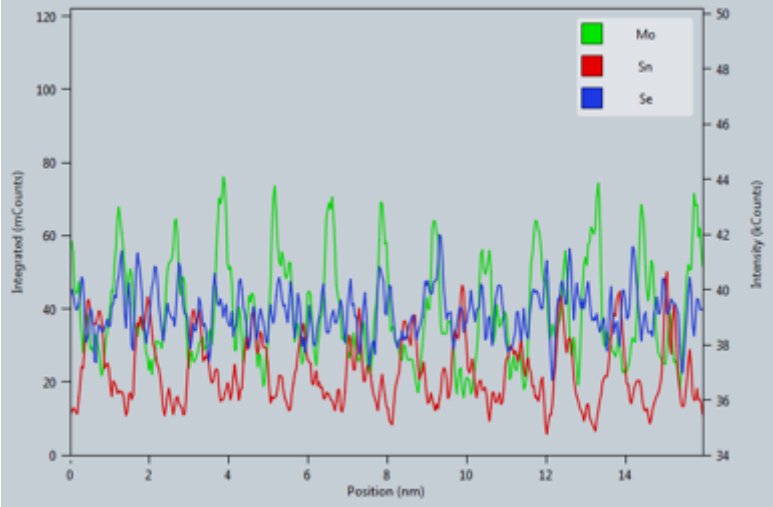

Figure 5.3. An EDS map of Sn, Mo, and Se along *z* showing a clear ordering of elemental planes.

Rietveld refinements were done on both the in-plane and specular diffraction patterns to gain information about interatomic distances and symmetry. The in-plane diffraction pattern was modeled with octahedrally coordinated Sn and trigonal prismatically coordinated Mo. All atoms were constrained to be on special position sites, and only the respective *a*-axis lattice parameters, thermal parameters, and scales for each phase were refined. The strong agreement between the measured and calculated intensity (Figure 5.4) supports the presence of layers with structures similar to the respective binary bulk compounds. The relative intensity of the two patterns suggest a 20% +/- 10%

excess of intensity contribution from the octahedrally coordinated phase relative to the calculated misfit parameter. The excess intensity of the $SnSe_2$ layer may result from larger grain sizes, as the line widths for the maxima corresponding to the $SnSe_2$ sublattice are narrower than for those corresponding to $MoSe_2$. The EDS maps were used to create a starting model for the refinement. Figure 5.4b shows the specular refinement of the

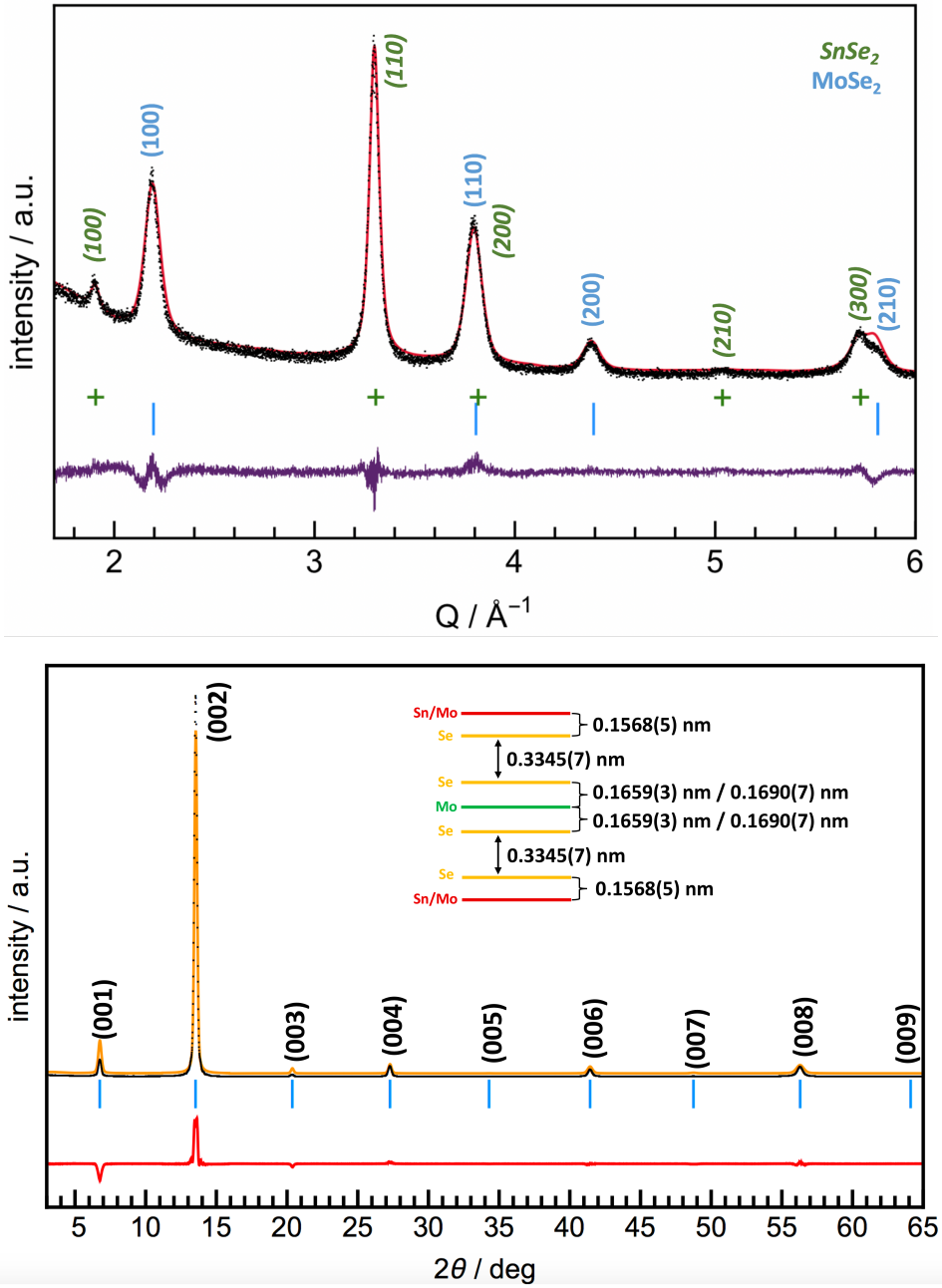

Figure 5.4. Rietveld refinements of the in-plane (a) and specular (b) diffraction patterns shows formation of a vertical superlattice with alternating $SnSe_2$ and $MoSe_2$ layers.

heterostructure, which was used to determine the interlayer spacing for the Sn, Se and Mo planes. The spacings between Mo and Se planes was found to be 0.1642(3) nm. This interplanar distance is consistent with previously reported trigonal prismatic $MoSe_2$ structures (0.1667 nm).[13–17] Due to the fact that the EDS data indicated the presence of Mo on Sn sites within the $SnSe_2$ sublattice, one plane for each type of atom was included at the same site. The occupancies were refined to evaluate the amount of each cation present at that site. The spacing between Sn (mixed with Mo) and Se planes was found to be 0.1568(5) nm, which is between the metal-chalcogen distances in each of the pure $MoSe_2$ and $SnSe_2$ lattices—0.1667 nm[13–17] and 0.1534 nm[18,19], respectively. The refined van der Waals gap is 0.3327(1) nm, which is 0.0198 nm larger than that $MoSe_2$ van der Waals gap and 0.0258 nm larger than the $SnSe_2$ van der Waals gap. This expansion is likely the result of the in-plane lattice mismatch between the constituents, resulting in the inability of, adjacent layers to settle (or nest) as found in the 2H and 3R polytypes of $MoSe_2$.

Electrical resistivity data was obtained using the van der Pauw method between 150 K – 295 K. The resistivity seems to depend exponentially on temperature, indicating semiconducting behavior, increasing from 0.067 Ωm at 295 K to 2.35 Ωm at 150 K (Figure 5.4). However, the temperature range over which we could collect resistivity data was too limited to definitively confirm activated behavior, and measurements over an expanded temperature range are needed to further investigate this. A linear regression of $\ln \rho$ v. T^{-1} yielded an activation energy of 0.20(3) eV, which is significantly smaller than the reported band gaps of monolayer $MoSe_2$ (~1.55 eV[20–22]), bulk $MoSe_2$ (~1.4 eV[23]), or $SnSe_2$ (~0.8 – 1.1 eV[24–26]). The observed activated behavior is likely due to either a dopant band, perhaps from Mo atoms in the $SnSe_2$ layer as suggested by our EDS data, or an interlayer band gap. A calculation done on a $SnSe_2/MoSe_2$ heterostructure with a type II alignment and yielded an interlayer band gap on the order of 0.1 eV.[27]

Cross-plane thermal conductivity was measured with time-domain thermal reflectance (TDTR), and results of this study are presented in Table 5.1. Thermal conductivities varied from 0.043 $Wm^{-1}K^{-1}$ for the thinnest film containing 8 $SnSe_2/MoSe_2$ unit cells to 0.057 $Wm^{-1}K^{-1}$ for a film containing 32 $SnSe_2/MoSe_2$ unit cells. These ultralow cross-plane thermal conductivities are similar to those reported for

turbostratically disordered WSe_2,[4] which is the lowest value previously reported for any fully dense solid. Reported values for single crystal dichalcogenides are all significantly higher, ranging from 1.75 $Wm^{-1}K^{-1}$ for single crystalline WSe_2 to 4.7 $Wm^{-1}K^{-1}$ for a mined single crystal of MoS_2.[8,28–31] Mo and W dichalcogenide films grown via high temperature synthesis have reported cross-plane thermal conductivities ranging from 1.2 $Wm^{-1}K^{-1}$ for WSe_2 to 3.5 $Wm^{-1}K^{-1}$ for $MoSe_2$.[32,33] These high thermal conductivities are generally in agreement with theoretical work.[34,35] There are several prior reports of lowering the cross plane thermal conductivity of dichalcogenide systems by lowering the structural order. TMD samples prepared by magnetron sputtering with extensive structural disorder both within and between the Se-M-Se trilayers have cross plane thermal conductivities between 0.1 – 0.3 $Wm^{-1}K^{-1}$.[36] Additionally, electrochemical intercalation lowers thermal conductivity in TMDs by ~50-70%, which has been correlated with lattice expansion at the van der Waals gaps.[31,33]Models that account for reduced symmetry along *z* by including stacking disorder and/or 2-3% lattice expansions reduce through-plane thermal conductivity, but only to ~0.4 $Wm^{-1}K^{-1}$.[37] The ultralow cross-plane thermal conductivity we report in this work is slightly lower than previous reports of turbostratically disordered structures synthesized by the MER synthesis scheme—0.05 $Wm^{-1}K^{-1} \leq \Lambda \leq 0.35\ W^{-1}K^{-1}$.[8–10,38–40]

# $SnSe_2/MoSe_2$ Layers	$SnSe_2$ *a* (nm)	$MoSe_2$ *a* (nm)	*c* (nm)	Λ $(Wm^{-1}K^{-1})$
32	0.3809(4)	0.3111(1)	1.3073(3)	$0.058^{+0.??}_{-0.??}$
16	0.3811(7)	0.3114(4)	1.303(1)	$0.052^{+0.??}_{-0.??}$
8	0.3812(7)	0.3099(6)	1.302(6)	$0.043^{+0.??}_{-0.??}$

Table 5.1. Summary of lattice parameters from x-ray diffraction and cross-plane thermal conductivity (Λ) from TDTR for rotationally disordered $SnSe_2/MoSe_2$ films in this study. Errors for Λ forthcoming prior to publication.

This study shows that interleaving two structures with significant lattice mismatch can lower thermal conductivity to ultralow values. The detailed structural characterization shows that the heterostructure is highly periodic containing alternating

$MoSe_2$ and $SnSe_2$ planar nanosheets that retain the in-plane structure of their bulk lattices. The large mismatch between basal plane structures maximizes rotational disorder and increases the van der Waals gap in the heterostructures. The interplanar rotational disorder gives rise to highly anisotropic bonding environments which maximizes anharmonicity. This work suggests that turbostratic disorder can be maximized by layering two materials with a large, incoherent mismatch, and that this disorder effectively reduces thermal conductivity.

5.4. *Bridge*

Chapter 4 demonstrated the significant influence of rotational disorder in depressing the cross-plane thermal conductivity of TMD nanolaminate films. In this study, we build on this finding by strategically interleaving two constituents with hexagonal symmetry, but a significant lattice mismatch in order to diminish the extent of atomic registry between layers. In this study, we report the synthesis—enabled by the XRF method in Chapter 3—and characterization of a rotationally disordered ferecrystalline heterostructure of $SnSe_2$ and $MoSe_2$ with the lowest cross-plane thermal conductivity reported in the literature. Having established a key design principle for low thermal conductivity materials, Chapter 6 is aimed at designing a material with potential for improving electrical contacts for $MoSe_2$-containing devices by gaining control of the Mo center's coordination.

CHAPTER VI:
MIXED PHASE 1T/2H $MoSe_2$ in $(BiSe)_{0.97}MoSe_2$ HETEROSTRUCTURE

6.0. *Authorship Statement*

This study is being prepared for publication in 2018. The article has been coauthored with Fabian Göhler, Gavin Mitchson, Shannon Fender, Thomas Seyller, and David C. Johnson. I am the primary author, though all authors have assisted in the interpretation of data and drafting of the article. Gavin Mitchson provided all microscopy data for this project. Shannon Fender assisted in the collection of data for the annealing study. And, Fabian Göhler conducted the x-ray photoelectron spectroscopy data. I synthesized all samples, conducted the structural characterization, and gathered the electrical data. David C. Johnson is my advisor, and Thomas Seyller advises Fabian Göhler.

6.1. *Abstract*

We report the synthesis and characterization of a new intergrowth of alternating BiSe and $MoSe_2$ layers that has been prepared by modulated elemental reactants. Specular and in-plane diffraction characterization shows that nanosheets are oriented parallel to the substrate. The heterostructure was found to have a *c*-lattice parameter of 1.245(2) nm. The in-plane hexagonal structure (a = 0.3320(5) nm) of the $MoSe_2$ appears undistorted from reports of thermodynamic phases. However, the BiSe sublattice forms a puckered rock salt structure with a rectangular basal plane (a = 0.4613(5) nm, b = 0.4261(4) nm). High angle annular dark field scanning transmission electron microscopy shows two distinct coordination environments for Mo centers in the $MoSe_2$ layer—both the metallic octahedral (1T) and the semiconducting trigonal prismatic (2H). Estimates by x-ray photoelectron spectroscopy show that ~40% of the $MoSe_2$ has been converted to the 1T phase. Conversion of 2H $MoSe_2$ has most commonly been accomplished by mobile intercalation species (i.e. Li) and reverts to the 2H phase at T > 180 °C, yet we report thermal treatment of the BiSe/$MoSe_2$ heterostructure at T ≤ 350 °C and retention of the 1T phase. Room temperature electrical measurements show that resistivity is 0.10 mΩm.

6.2. *Introduction*

Group 6 transition metal dichalcogenides (TMDs) have attracted tremendous research interest following the discovery that they transition to direct band gap materials at the monolayer limit—MoS_2,[1,2] $MoSe_2$,[3] WS_2,[4] and WSe_2[5]. This makes them attractive candidates for integration into a variety of ultrathin electronic and optoelectronic devices,[6,7] such as field effect transistors (FETs),[8] light emitting diodes (LEDs),[9,10] and photovoltaics.[11,12] Their naturally occurring layered structure—with a strong covalent network in the *xy* plane and weak van der Waals forces along the *z* axis—makes isolation of monolayers a relatively facile procedure.[13] Additionally, surface sites are free of dangling bonds that commonly give rise to deep-gap trap states in more isotropic semiconductors, such as silicon and III-V materials. As more is learned about the unique properties of 2D TMDs, there has also been a parallel body of literature in van der Waals heterostructures, in which 2D components are stacked on top of or alongside one another to impart coupled or tunable functionality to devices.[14] Heterostructures have been shown as viable routes to extend exciton lifetimes,[15] tune band gaps,[16] and improve carrier collection efficiencies.[17] Studies commonly report mobility as an all-inclusive metric to evaluate device quality/performance; however, there is considerable variation in mobility values reported for similar devices due to the difficulty of making an Ohmic contact to MoX_2 (X = S, Se), even for similar films made by common syntheses.[18] Device performance for TMDs and TMD heterostructures relies heavily on the ability overcome a significant Schottky barrier to achieve a low-resistance, Ohmic contact that will push these materials toward their theoretically predicted intrinsic transports. However, common strategies—degenerately doping source/drain regions—or bulk semiconductors (Si) cannot be realized in 2D materials systems due to their extremely thin dimensions.[19]

Group 6 TMDs undergo a phase transition upon electron injection, which has proven useful in nanoelectronic devices. Commonly achieved by lithium intercalation, the semiconductor 2H phase (trigonal prismatic coordination) will rearrange to the metallic 1T phase (octahedral coordination).[13,20] Notably, Kappera et al created a 2H-MoS_2 transistor with 1T-MoS_2 source/drain contacts and reported significantly improved contact performance (low contact resistance) with zero gate bias.[18,21] This phase engineering strategy has also been utilized in both $MoTe_2$ systems[22] as well as WSe_2

systems, where the phase transition was shown to be reversible upon annealing at 180 °C, which presents an obstacle for higher temperature applications.[23] Additionally, the use of lithium as an intercalant is not ideal due to its high mobility and volatility. These serve to hamper the ability for position selective conversion to the 1T phase and narrow the temperature range over which the 1T phase is retained. Depositing a metallic contact in sequence using a vapor deposition technique has been suggested.[24] A recent review article suggests that further investigation into stabilizing the metallic 1T phase is needed if phase engineering is to be a viable contact engineering strategy.[25]

In this study, we present the synthesis of a new BiSe/$MoSe_2$ intergrowth and characterization of its structure and properties. To the best of our knowledge, this is the first report of a Bi|Mo|Se compound, and there is currently no ternary phase diagram. We used a sequential physical vapor deposition technique in which elemental layers are deposited to form a modulated elemental precursor that is subsequently heated to induce self assembly into an interleaved BiSe/$MoSe_2$ heterostructure. Structural analysis shows self assembly of a superlattice consisting of 1 BiSe and 1 $MoSe_2$ layer. Ultimately, our goal was to investigate the ability of the BiSe to donate electrons into the conduction band of the $MoSe_2$ sublattice and induce the 2H→1T phase transition. Previous work has shown that BiSe is capable of donating electrons to other TMD lattices—namely, $NbSe_2$ and $TiSe_2$.[26–28] The coordination in the $MoSe_2$ sublattice was probed XPS and HAADF-STEM and found to consist of mixed 2H/1T phases. IV curves gathered for resistivity analysis show Ohmic behavior for the heterostructure, consistent with what has been reported for other 1T phase group 6 dichalcogenide devices. Our work demonstrates that a sequential vapor deposition technique is a viable alternative to lithium intercalation strategies for 2H→1T conversion in $MoSe_2$. Additionally, as the BiSe layer is non-volatile, we report retention of the 1T phase even after heating at 350 °C, which represents an expanded temperature stability range.

6.3. *Experimental*

The heterostructure precursors were prepared by the modulated elemental reactants (MER) method, which is a modified physical vapor deposition technique described in detail elsewhere.[29,30] In short, commercially-obtained elemental source

materials are heated at the base of a custom-build deposition chamber—bismuth and molybdenum by Thermoinics electron beam guns and selenium in an effusion cell—at $P < 1 \times 10^{-6}$ torr to generate plumes of metal atoms that are aimed at a silicon or quartz substrate above. The rate of evaporation for each source—0.03 nm/s, 0.02nm/s, and 0.05 nm/s for bismuth, molybdenum, and selenium, respectively—is monitored by a set of piezoelectric quartz crystal microbalances (QCMs), which interface with the heating elements and their deposition controllers via a LabVIEW software package. This ensures a constant rate of deposition and precise control with respect to the deposited thickness. The Si (100) substrate (or fused silica for electrical samples) sits on a motorized carousel that moves back and forth between elemental sources to enable the sequential deposition. The plumes are blocked from the substrate by a set of pneumatically controlled shutters that actuate by the LabVIEW software for precise time intervals in conjunction with information from the rate monitors. Samples were subsequently transported through atmosphere to an inert atmosphere (dry N_2, $P_{O2} < 1$ ppm) for annealing on a hot plate. Atomic composition was evaluated using a Rigaku ZSX Primus II wave dispersive X-ray fluorescence (XRF) spectrometer with a rhodium source, per the procedure described by Hamann et al.[31]

Low angle X-ray reflectivity (XRR) and high angle X-ray diffraction (XRD) measurements for both the as-deposited and thermally treated films were obtained using a Bruker D8 Discover diffractometer, equipped with Cu Kα radiation and a Göbel mirror. An out-of-plane structural refinement was performed on the self assembled heterostructure by Rietveld analysis using the FullProf software package. The refinement provided information about the ordered atomic planes along the c-axis. Grazing incidence in-plane X-ray diffraction (GIXRD) was performed on a Rigaku SmartLab (Cu Kα radiation) to monitor phase evolution during the annealing study. The in-plane structure was then probed using glancing angle X-ray diffraction at the Advanced Photon Source (33-BM-C), and the *a*- and *b*- lattice parameters were determined by LeBail fitting using FullProf. We obtained real space images of the compound to evaluate the structure by high angle annular dark field scanning transmission transmission electron microscopy (HAADF-STEM) using an aberration-corrected Thermo Fischer Titan (300 kV electron beam) at Pacific Northwest National Laboratory. Prior to imaging, samples were prepped

by creating electron transparent lamellae. The lift-outs were made by a wedge-prep method[32] with a Ga^+ focused ion beam on a Thermo Fischer Helios Nanolab, 600i. Temperature-dependent resistivity measurements were taken between 150 - 295 K using the van der Pauw method.[33]

6.4. *Discussion*

Precursors were prepared by depositing a repeat sequence of Bi|Se|Mo|Se elemental layers. The precursors were designed such that the local composition of each layer mimicked that of the target crystalline nanolaminate. The target atoms per $Å^2$ for each element in the precursor were calculated from the binary structures. Using values calculated from intergrowths containing either $MoSe_2$ or BiSe structures also prepared by MER synthesis give essentially the same answer.[27] The amount of each element in the precursor was measured by x-ray fluorescence (XRF) spectroscopy. The intensities for each element were converted to atoms per unit area using to calibration standards. The atoms per area of each element in the precursor was compared with calculated values.[31] The period of the repeating sequence of elemental layers in the precursor was measured using x-ray reflectivity and found to be 1.331(7) nm, which is slightly larger than the simple sum of the lattice parameters of the constituents. This expansion is likely due to inefficient packing arrangements of atoms in non-crystalline film or extra Se deposited, which has been found to facilitate self-assembly.

Once the modulated elemental precursors were prepared with the desired composition, an annealing study was conducted to determine if the target $BiSe/MoSe_2$ structure formed and to identify the optimal thermal treatment for the self-assembly. Samples were annealed for 10 minutes at temperatures between 50 °C and 450 °C on a hot plate in a dry nitrogen atmosphere with oxygen concentration < 1 ppm. Samples were measured at each temperature step using XRF spectroscopy to monitor the composition and x-ray diffraction to evaluate structural evolution. Specular diffraction patterns of the thermally treated precursors at each temperature step are shown in Figure 6.1. The as-deposited scan shows a broad reflection at low angle due to the elemental layering and weaker broader reflections at higher angle from the beginning of the self assembly process during deposition. The higher angle reflections steadily intensify and narrow

when annealed at higher temperatures up to 450 °C as the sample self assembles. The reflections can all be indexed using a single index, showing only the *00l* family of reflections. This indicates preferred orientation, with BiSe and $MoSe_2$ nanosheets oriented parallel to the substrate. The *c*-axis lattice parameter increases monotonically with temperature up to 350 °C, at which point there is no longer a discernible change. The 001 reflection is shifted to slightly higher angles in the as-deposited and low temperature samples, but it comes into alignment with the index assigned to the higher order peaks at 350 °C and above. The *c*-lattice parameter after annealing at 350°C is 1.245(2) nm. This is close to the *c*-axis lattice parameter reported previously for $(BiSe)_1(MSe_2)_1$ compounds, where M = Nb and Ti.[26,34] Evidence of a secondary phase is observed at 450 °C, with maxima growing in at $2\theta \approx 19°, 48°$, which is likely due to the conversion of the BiSe sublattice into the more thermodynamically stable Bi_2Se_3.[35] The intensity of the first order reflection also decreases after annealing at temperatures above 350 °C.

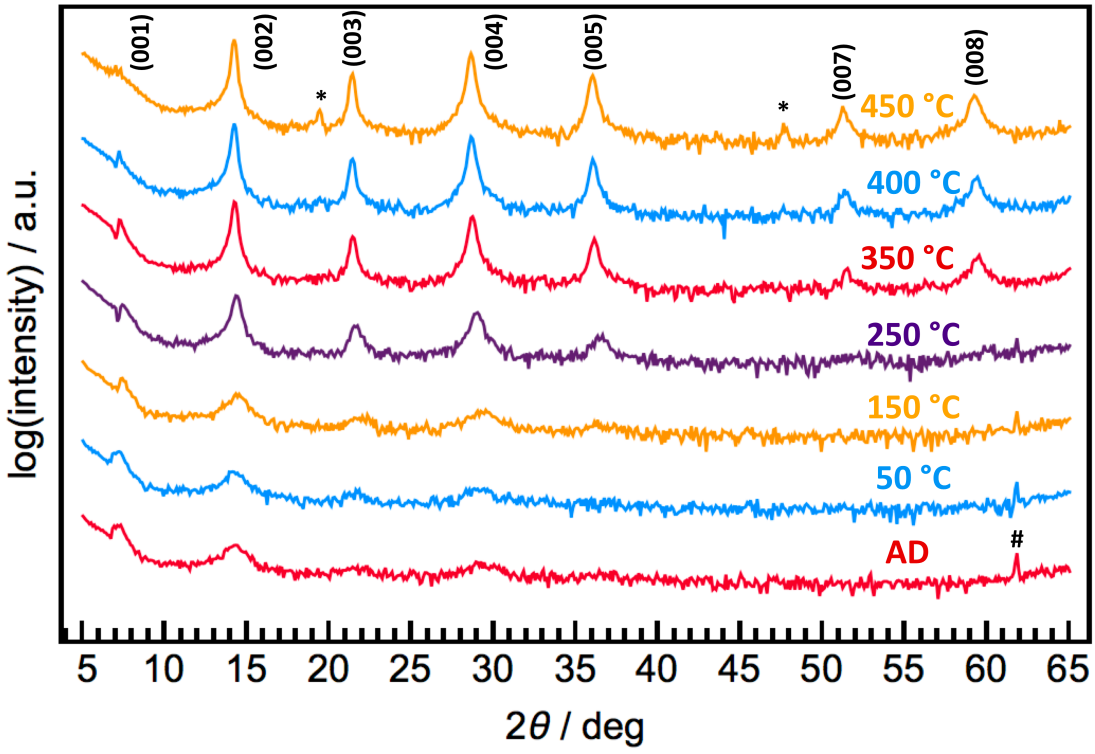

Figure 6.1. The out-of-plane diffraction shows evolution of a superlattice with heat treatment at increasing temperature. The secondary phase peaks due to the formation of Bi_2Se_3 have been identified by the asterisk (*), and the small maximum at $2\theta \approx 62°$ (#) is a contribution from the diffractometer stage.

Low angle x-ray reflectivity (XRR) scans collected as a function of annealing time at a temperature of 350 °C are shown in Figure 6.2. The scans contain the first two Bragg reflections from the targeted heterostructures and periodic oscillations (i.e "Kiessig fringes") resulting from the interference of scattered intensity off the top and bottom interfaces of the film and from the incomplete destructive interference of the finite number of repeating layers deposited (Laue reflections). As annealing time increases, the Kiessig fringes become more intense and can be observed to higher angles. As described by the Parratt relationship, this indicates that the top and bottom of the film are becoming more parallel.[36] The self assembly of the layers into the targeted compound also increases the intensity of the Laue reflections. The number of minima between the critical angle and the first Bragg reflection in the sample annealed 30 minutes indicates that the number of self-assembled layers matches the number of repeat units that were applied during deposition. The thickness of the film, 39.83(5) nm, was calculated from the position of each fringe maximum using Bragg's law corrected for refraction. For a perfect sample the thickness of the film should be equal to the *c*-lattice parameter determined from the high

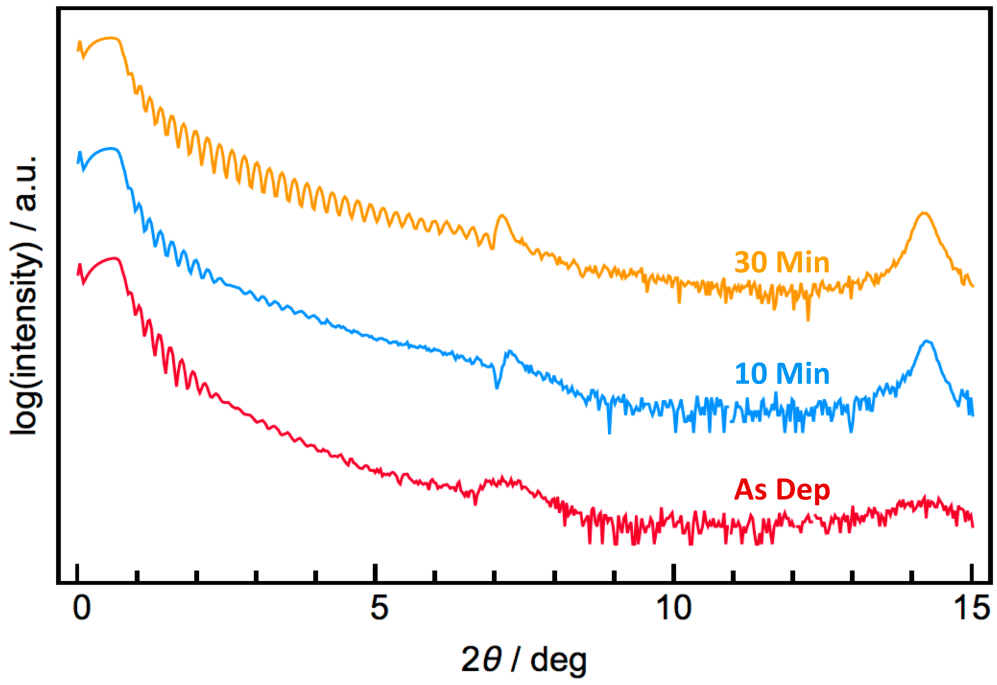

Figure 6.2. Low-angle diffraction (XRR) patterns show that as annealing time is increased, the target number of unit cells self assemble across the film.

angle specular diffraction pattern (1.245(2) nm) multiplied by the number of unit cells deposited (in this case, 32 layers). The calculated thickness (39.84(6) nm) is within error of the measured thickness 39.83(5) nm. The x-ray measurements taken together indicate that the film contains 32 repeating periods, each containing a single layer of $MoSe_2$ and BiSe.

Grazing-incidence in-plane (*hk0*) diffraction scans collected as a function of annealing temperature are shown in Figure 6.3. The as-deposited scan contains only very weak and broad maxima, suggesting that crystalline BiSe and $MoSe_2$have not formed on deposition. The intensity of the broad reflections increases slightly after annealing at 200 °C, but distinct reflections for BiSe and $MoSe_2$ only become evident when the film is heated at 300 °C. XRF intensity for all elements remained constant at the target stoichiometry until 350 °C. At 450 °C an additional reflection appears, which is consistent with the formation of Bi_2Se_3. XRF intensity indicates a loss of Se and Bi, with a larger percentage loss of Bi leading to the formation of the more selenium rich Bi_2Se_3. Accordingly, optimal thermal treatment was determined to be 350 °C for 30 minutes.

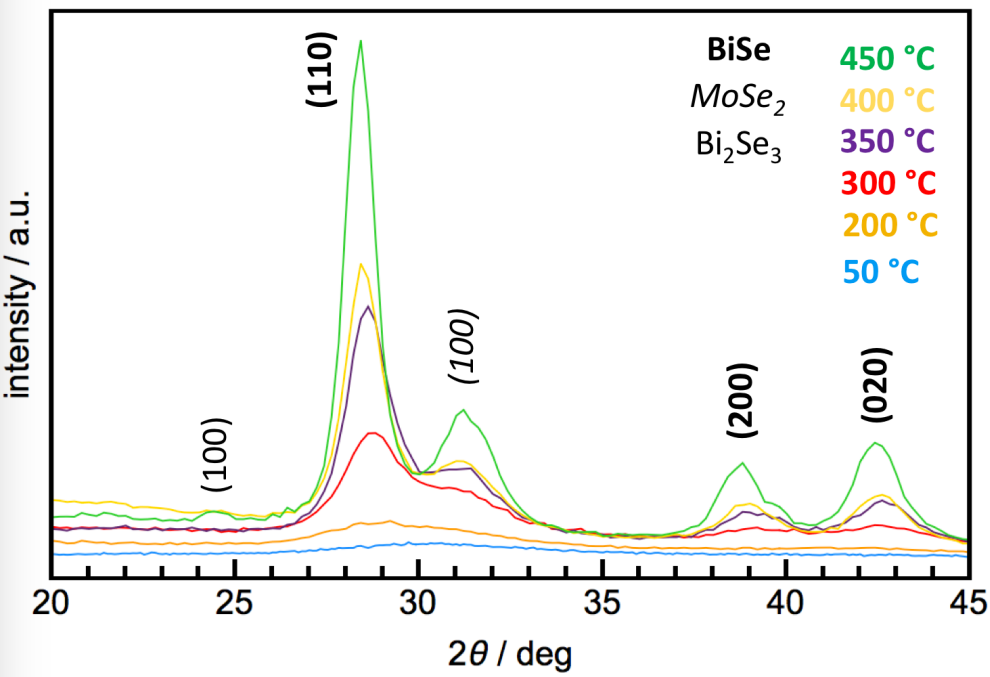

Figure 6.3. All maxima in the in-plane diffraction can be indexed to the target BiSe and $MoSe_2$ sublattices with the exception of the reflection at $2\theta \approx 24.5°$, which may be assigned to Bi_2Se_3.

All of the reflections in the in-plane diffraction patterns (Figure 6.4) of precursors annealed at 350 °C for 30 minutes could be indexed as *hk*0 reflections arising from independent hexagonal and rectangular lattices. The lattice parameters of each were refined using a Le Bail fit as summarized in Table 6.1. The lattice parameter of the hexagonal sublattice (a = 0.3320(5) nm) is consistent with that of $MoSe_2$.[37–41] The fitting of the rectangular basal plane unit cell yielded lattice parameters of a = 0.4613(5) nm and b = 0.4261(4) nm. These values are similar to those previously reported for other BiSe heterostructures containing one layer of interleaved TMD (a = 0.447 nm, b = 0.4285 nm for $(BiSe)_{1.11}NbSe_2$;[26] a = 0.4562(2) nm, b = 0.424(1) nm for $(BiSe)_{1.15}TiSe_2$[34]), however the difference between the a and b lattice parameters is slightly larger. Mitchson et al. showed that the lattice parameters of the BiSe sublattice depended on the amount of

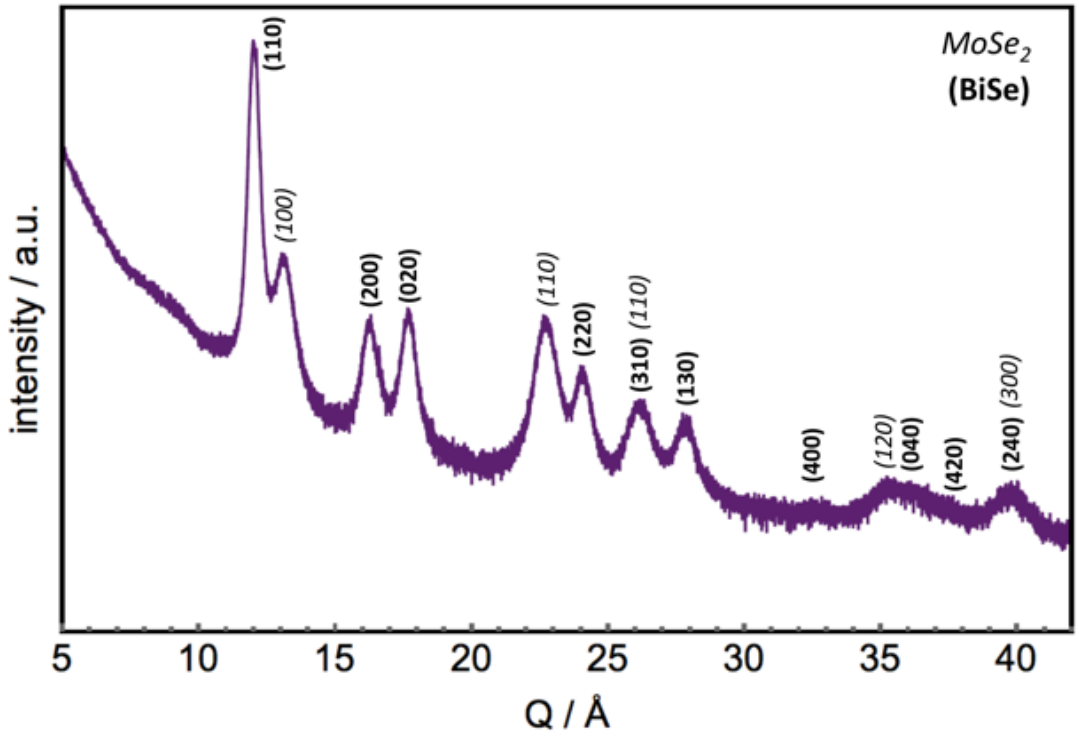

Figure 6.4. In-plane diffraction shows *hk0* Bragg maxima which can be indexed to an undistorted hexagonal $MoSe_2$ sub-lattice and an orthorhombic BiSe sublattice.

$MoSe_2$ a (nm)	BiSe a (nm)	BiSe b (nm)	XRD Misfit
0.3320(5)	0.4613(5)	0.4261(4)	0.97

Table 6.1. In-plane lattice parameters for each sublattice from Le Bail fitting.

charge that was transferred from the BiSe lattice into adjacent TX_2 layers based on changes observed in $(BiSe)_{1.16}(NbSe_2)_n$ compounds as n is increased.[27] Additionally, Wood et al. reported changes to the dimensions of the BiSe sublattice as well as carrier concentration in the $(BiSe)_{1.14}[(TiSe2)_n]$ system as n 2→4. This suggests that the distorted lattice observed here may be rationalized on the basis of charge transfer from the BiSe lattice.

Rietveld refinement of the specular diffraction pattern was conducted to determine the position of the atomic planes along the c-axis (Figure 6.5). The distance between the Mo and Se planes in $MoSe_2$, 0.1642(3) nm, is 0.003 nm smaller than that found the binary compound. The distance between Se plane of the $MoSe_2$ layer and Bi plane in the BiSe layer (i.e. "van der Waals gap") is 0.013 – 0.004 nm larger than what is reported in other ferecrystalline compounds prepared by MER.[26–28,42] While a single plane containing Bi and Se would be expected if it self-assembled into an ideal rock salt structure, a significant difference between the position of the Bi and Se planes is

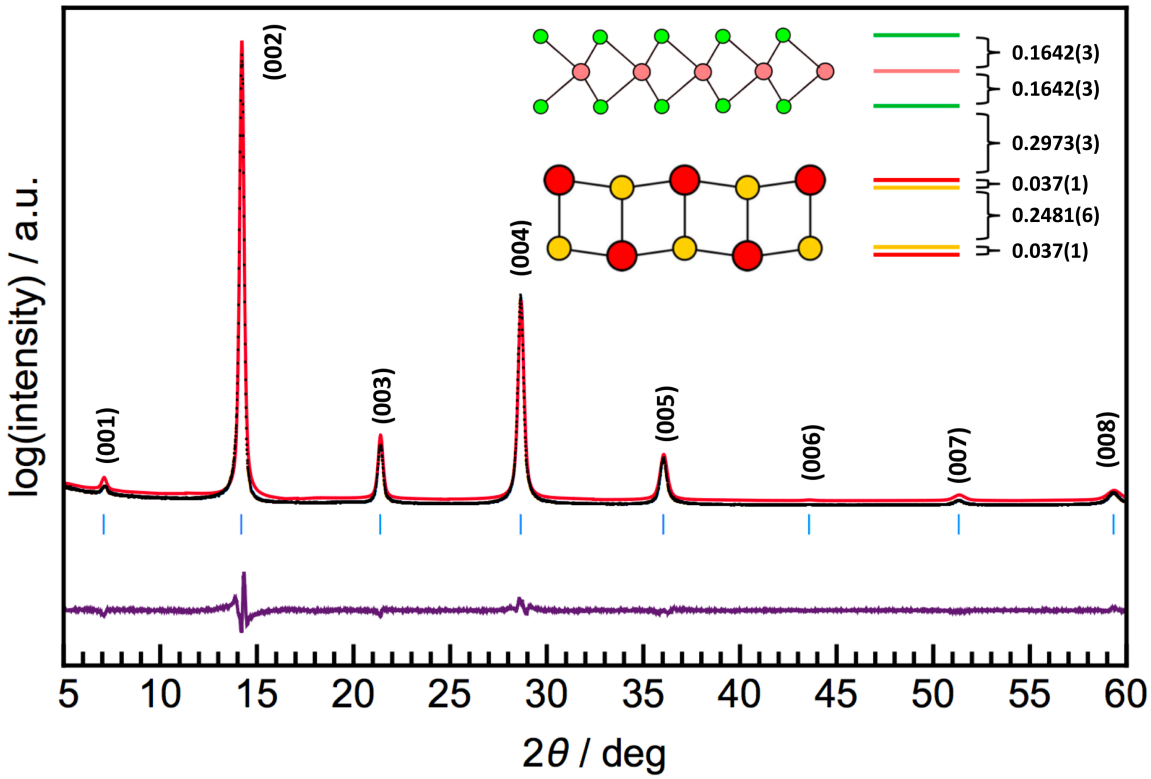

Figure 6.5. Rietveld analysis shows a puckered rock salt lattice. The purple trace at the bottom of the figure is the residuals between the calculated and experimental patterns. All distances in the inset are given in nanometers.

observed, 0.037(1) nm. The Bi plane is shifted towards the Se plane in $MoSe_2$. This amount of puckering observed is on the same order as what has been reported for other BiSe-containing systems.[26–28] Weigers suggested that interlayer charge transfer between two constituents in the superlattice causes the cations in the MX layer to protrude into the interlayer gap toward the anion (X) atomic centers in the TX_2 layer.

In order to further evaluate the structure of the two lattices and investigate their stacking, cross-sectional high angle annular dark field scanning transmission electron microscopy (HAADF STEM) images were collected and a representative image is shown in Figure 6.6. The image contains alternating 2D bilayers and trilayers consistent with the expected rock salt structured BiSe and $MoSe_2$ respectively. The constituent layers are flat with atomically sharp interfaces. These observations are consistent with the low- and high-angle specular diffraction data. The orientations of each layer vary throughout the image. When zone axis orientations are observed, those for BiSe are consistent with a distorted rock salt structure. Two distinct coordination environments were observed in the $MoSe_2$ layers, however. Chevrons are observed in some regions of the cross-section images, consistent with a (110) orientation of a TX_2 compound in which the transition metal atom has trigonal prismatic coordination. Diagonal slashes are observed in other layers, however, consistent with a (110) orientation of a TX_2 compound with the transition metal atoms having octahedral coordination.

While the thermodynamically stable coordination of Mo in $MoSe_2$ is trigonal prismatic, octahedral coordination of Mo is observed in $LiMoSe_2$.[13,20] This suggests that there may be two different oxidation states for the Mo in $(BiSe)_{0.97}MoSe_2$. The different layers do not appear to form discrete, continuous layers, but instead nanoscale regions of both appear to be randomly distributed.

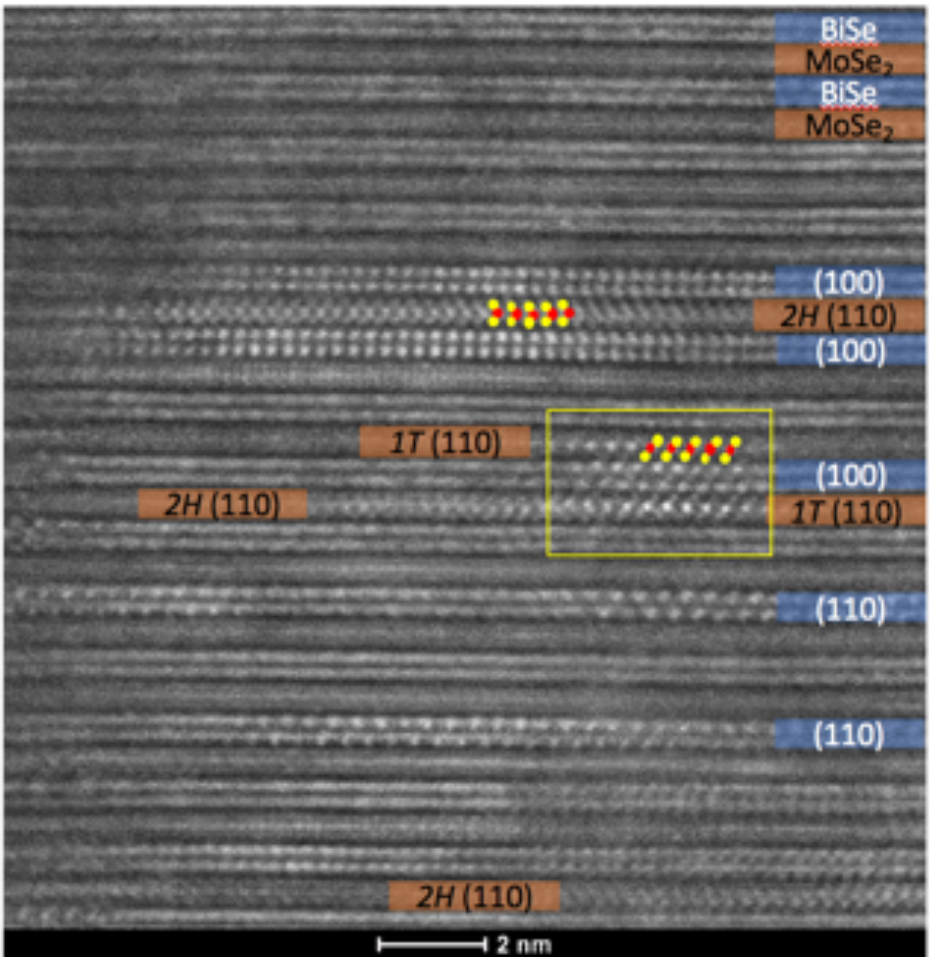

Figure 6.6. Cross section HAADF-STEM image showing alternating layers of BiSe and $MoSe_2$. The $MoSe_2$ layers display two distinct atomic arrangements consistent with octahedrally and trigonal prismatically coordinated Mo atomic centers in the TMD layer.

X-ray photoelectron spectra (XPS) were collected to obtain an estimate for the relative amounts of 1T and 2H regions in $(BiSe)_{0.97}MoSe_2$. Spectra were collected from freshly cleaved, buried interfaces by fixing a peg to the top of the film and breaking along the van der Waals gaps to expose interior interfaces. This process was repeated on 5 different sample areas, and a representative spectrum is presented in Figure 6.7. The photoelectrons from regions where Mo has octahedral coordination have different

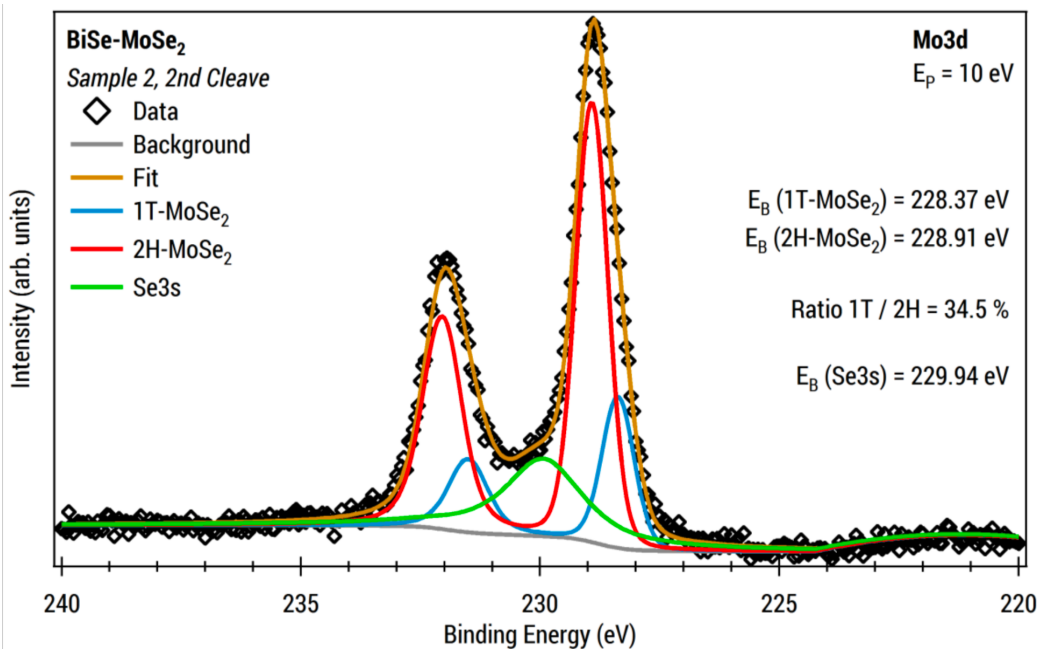

Figure 6.7. The XPS data represented by the black diamonds does not adequately match a single coordination environment. The proportioned fits shown in red and blue are indicative of how much of each phase is present in the probed sample volume.

binding energies from regions where Mo has trigonal prismatic coordination.[43] The binding energies of these two signals coincide with a signal from the Se 3s. The individual signals from the Se 3s, trigonal prismatic Mo, and octahedral Mo are shown in green, red, and blue, respectively, in Figure 6.7. In order to estimate the relative amount of each phase, linear combinations of these three signals were taken to fit the data. The integrated intensity ratios of signals from octahedral and trigonal prismatic Mo in the 5 measured samples varied between 34% and 48% octahedral. We estimate that 40% ± 10% of the $MoSe_2$ is present in the 1T phase, which is consistent with analysis of the HAADF STEM images.

Electrical resistivity data was collected as a function of temperature (Figure 6.8) using the van der Pauw method on samples deposited on quartz substrates through a cross-shaped mask. Contacts were made by pressing indium on the edges of the cross geometry films. The room temperature resistivity is four orders of magnitude smaller than that measured for a binary $MoSe_2$ also made by MER synthesis. The measured resistivity increases as temperature is decreased. The temperature dependence indicates an activated conduction mechanism with an additional contribution to the conductivity

that appears to be relatively constant through the probed temperature region. At the lowest temperatures measured, the slope of the ln(resistivity) versus 1/T yields an activation energy of 0.005 eV for the carriers. For the higher temperatures measured, the slope increases, suggesting activation from an additional band with a larger activation energy.

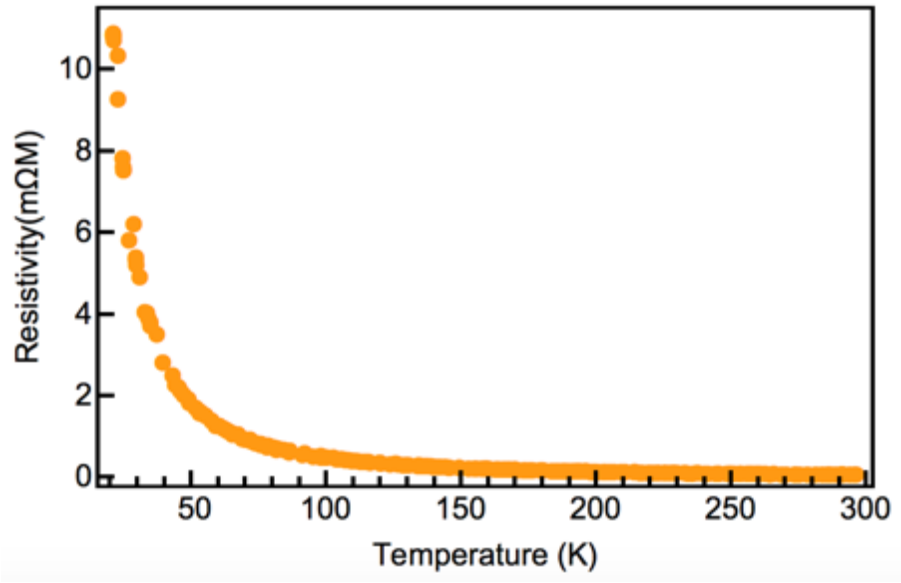

Figure 6.8. Temperature-dependent resistivity analysis which shows activated conduction behavior.

The magnitude and temperature dependence of the electrical resistivity of $(BiSe)_{0.97}MoSe_2$ reflects charge donation from the BiSe layer to the $MoSe_2$ layer. 1T $MoSe_2$ is metallic and 2H $MoSe_2$ is a semiconductor with a band gap of ~1.53 eV.[3] Turbostratically disordered $MoSe_2$ where Mo has trigonal prismatic coordination is a semiconductor with an activation energy from electrical measurements of 0.19 eV (see chapter 4). The structural characterization presented here indicates that the $MoSe_2$ layers in $(BiSe)_{0.97}MoSe_2$ consist of regions with octahedral and trigonal prismatic coordination. The observed activated conductivity suggests that there is not a continuous network of octahedrally coordinated $MoSe_2$ regions. The activation energy is approximately a factor of three lower than that reported for turbostratically disordered $MoSe_2$.

6.5. *Conclusion*

We prepared a new compound of interleaved BiSe and $MoSe_2$ layers by vapor deposition synthesis. Electron donation from the BiSe into the $MoSe_2$ resulted in a mixed

octahedral/trigonal prismatic coordination environment for the $MoSe_2$ sublattice. The electrical data shows that the heterostructure is three orders of magnitude more conductive than the binary $MoSe_2$ film, which is consistent with the inclusion of the metallic 1T phase. Further study should be done to investigate the possibility of affecting the fraction of the two $MoSe_2$ phases by varying the number of BiSe bilayers in the unit cell. Additionally, phase engineering has been suggested as a means of improving contacts to $MoSe_2$, making this material potentially interesting for device applications.

6.6. *Bridge*

Conversion of semiconducting 2H $MoSe_2$ to the metallic 1T polymorph is generally accomplished in the literature with the use of lithium, a mobile and volatile intercalating agent. The ability to control the coordination environment of Mo centers with the use of a non-mobile and non-volatile intergrowth offers the possibility for position selective conversion and further demonstrates the immense utility of nanolaminate heterostructures such as those discussed in this dissertation. This particular heterostructure is exciting for its potential use as an Ohmic contact material for other $MoSe_2$-containing van der Waals structures. This could potentially be used to gather additional electrical data on the heterostructures in the preceding chapters.

CHAPTER 7:
CONCLUSIONS, SUMMARY, AND OUTLOOK FOR FUTURE WORK

As a material class, van der Waals compounds and their corresponding heterostructures represent an immensely versatile platform on which to design next generation nanoelectronics. Modulated elemental reactants (MER) is a powerful synthesis model in its ability to access kinetically stable compounds at low temperatures with seemingly limitless layering schemes for metal chalcogenides. The structures studied in this dissertation all pertain to one material—$MoSe_2$—that has been the subject of significant research interest in the past decade.

Re-engineering the analysis of x-ray fluorescence (XRF) spectroscopy data enabled us to create an ultrasensitive probe for MER synthesis. Our new method for XRF data treatment is able to provide the number of atoms per unit area in a thin film. This gives experimentalists an unprecedented ability to measure absolute composition. This tool enabled the preparation of $MoSe_2$ samples with an integer numbers of layers in the self assembled products. In addition to making some of the thinnest samples ever prepared in the Johnson lab, we were also able to make $MoSe_2$ films with such precisely defined layers that we saw, for the first time, diffraction phenomena (Laue oscillations) previously not observed in ferecrystalline materials. The XRF method we outline has sub-monolayer elemental sensitivity, and it would be a worthwhile endeavor for future lab members to study the preparation of thinner $MoSe_2$ films than those that have been presented in this dissertation (8 unit cells).

Turbostratic disorder in TMD films has long been thought to depress cross-plane thermal conductivity. However, subsequent electron microscopy called the global level diffraction characterization published in the original work into question. In this dissertation, definitive structural characterization is shown at both the global and granular level of a highly periodic $MoSe_2$ array, wherein the salient structural feature is rotational disorder. This structural feature is enough to reduce cross-plane thermal conductivity to near-record breaking lows. It was noteworthy however, from the cross-section HAADF-STEM images, that low levels of interlayer rotational alignment were occasionally observed.

To further probe the relationship between turbostratic disorder and cross-plane thermal conductivity, a heterostructure of alternating $SnSe_2$ and $MoSe_2$ layers was prepared. The lattice-mismatched interfaces between the two constituents decrease the frequency of atomic registry across layers. Accordingly, record-breaking low cross-plane thermal conductivity was observed. It is interesting to note that for both the $MoSe_2$ and $SnSe_2/MoSe_2$ systems, cross-plane thermal conductivity is lowest for the thinnest films. A more robust investigation and explanation of this is needed in the future.

A variety of studies have shown $MoSe_2$ to be a good electron acceptor of high energy electrons, and other studies have shown BiSe to be a strong electron donor. The final project in this dissertation presented the synthesis and characterization of an entirely new Bi|Mo|Se phase of alternating BiSe and $MoSe_2$ layers. Within the context of this heterostructure, $MoSe_2$ possesses a mixture of the semiconducting 2H and metallic 1T phases, which appear to be randomly distributed throughout the volume of the film. No continuous conducting path was detected laterally across the film.

The preparation of this heterostructure is exciting for its potential future applications. There has been a rapidly growing body of literature pertaining to the many known and theoretical uses of $MoSe_2$ in next generation nanoelectronics and optoelectronics; however, making an Ohmic contact to $MoSe_2$ has presented a formidable challenge. Phase engineering by electron injection from a BiSe sublattice offers the possibility of patterning 1T contacts to functional 2H regions. Yet, before this can be realized, more investigation of the Bi|Mo|Se system must be done. Assuming electrons are injected from the BiSe sublattice, it stands to reason that increasing the number of BiSe layers between $MoSe_2$ layers may have an effect on the percent conversion to the 1T phase. Additionally, if 3 layers of $MoSe_2$ were made between BiSe sheets, cross-section HAADF-STEM images would show whether 2H → 1T conversion was limited to interfacial $MoSe_2$ layers or if it was observed evenly across interfacial and buried layers.

APPENDIX (A):
SUPPLEMENTAL INFORMATION FOR CHAPTER 3

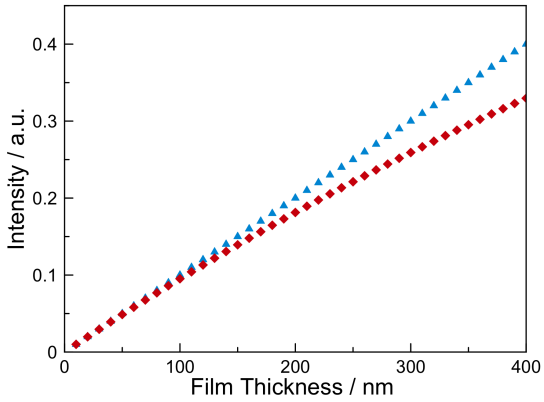

Figure A.1. Graph of intensity (arbitrary units) versus film thickness (nm) according to Equation 1 (red diamonds) and Equation 2 (blue triangles). The error in intensity of assuming film thickness is small is less than 5% for thicknesses below 100 nm. For this plot, the mass absorption coefficient $\mu_T(\lambda_i)$ of the wavelength of interest and film density ρ were chosen to be 1000 cm^2/g and 7 g/cm^3, respectively. The values of each were chosen to be representative of typical films with a Lα emission lines.

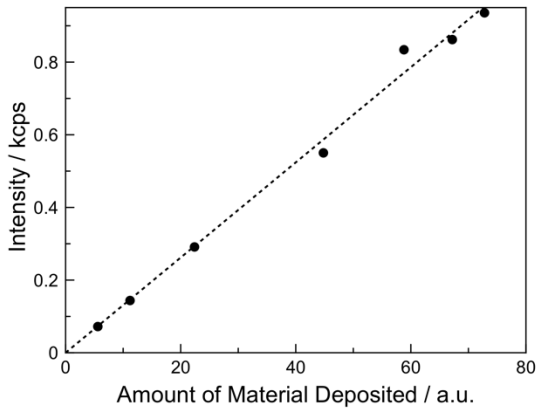

Figure A.2. XRF intensity as a function of the amount of molybdenum deposited from an electron beam gun. Mo was deposited using a different physical vapor deposition system and a different XRF diaphragm was used to define an area during the XRF experiments, so there is a different metric for the arbitrary units of the amount of material deposited and in the XRF intensity in Figure B versus the films shown in Figure 1.

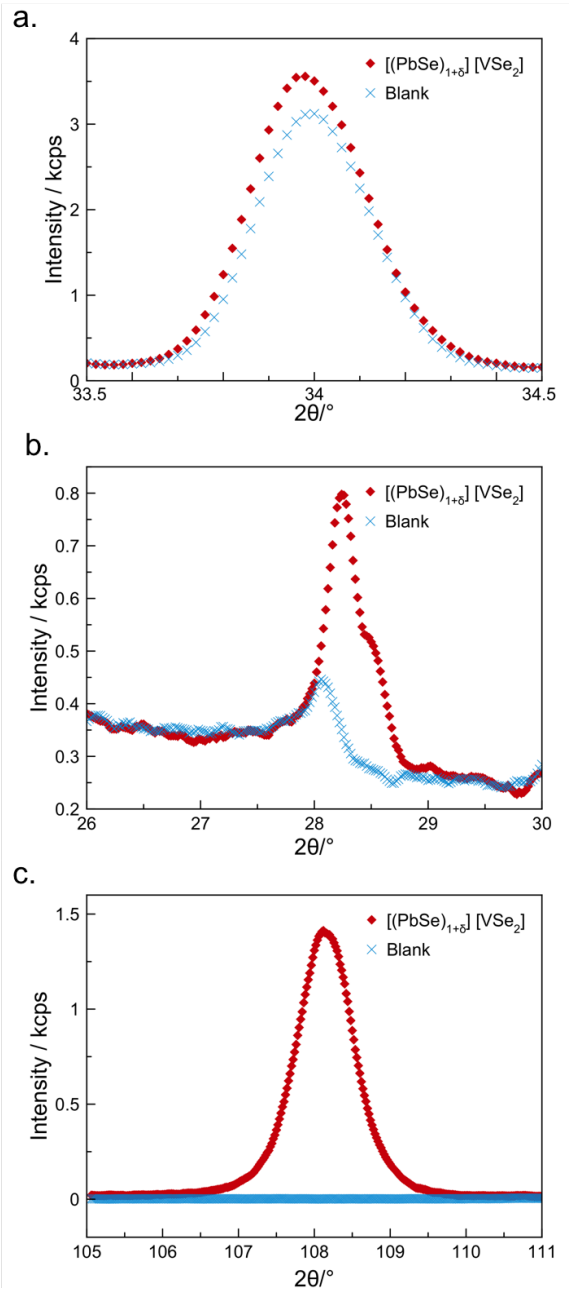

Figure A.3. X-ray emission lines for the (a) Lα, (b) $L\beta_1$, and (c) Mα of Pb were tested to determine the best parameters for measuring the amount of Pb in each sample. The Mα line was chosen as it showed the largest difference in intensity between the sample containing Pb and the blank substrate.

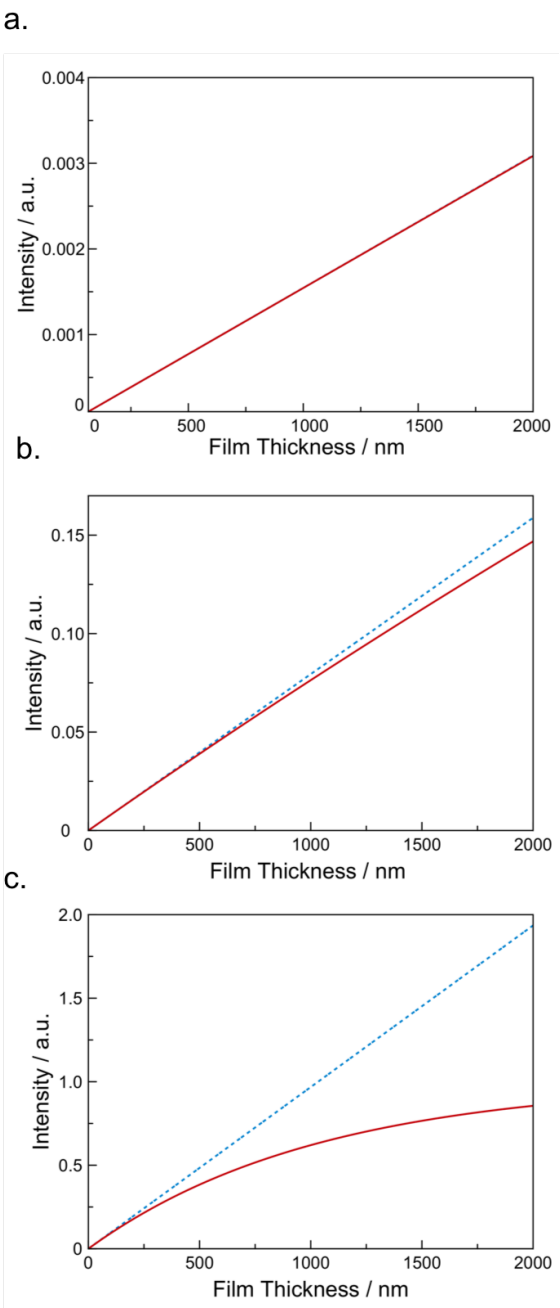

Figure A.4. Calculated X-ray emission intensities for the (a) Kα, (b) Lα, and (c) Mα lines of Bi in a film of Bi_2Se_3. The values inserted into Equations 1 and 2 are: ρ = 7.71 g/cm^3, μ(Mα) = 1300 cm^2/g, μ(Lα) = 100 cm^2/g, and μ(Kα) = 2.0 cm^2/g. The total mass attenuation coefficient μ is calculated form the weighted average of the individual attenuation coefficients of each element present in the film. Equation 2 yields the blue dashed line and the values from Equation 1 are given by the red continuous line.

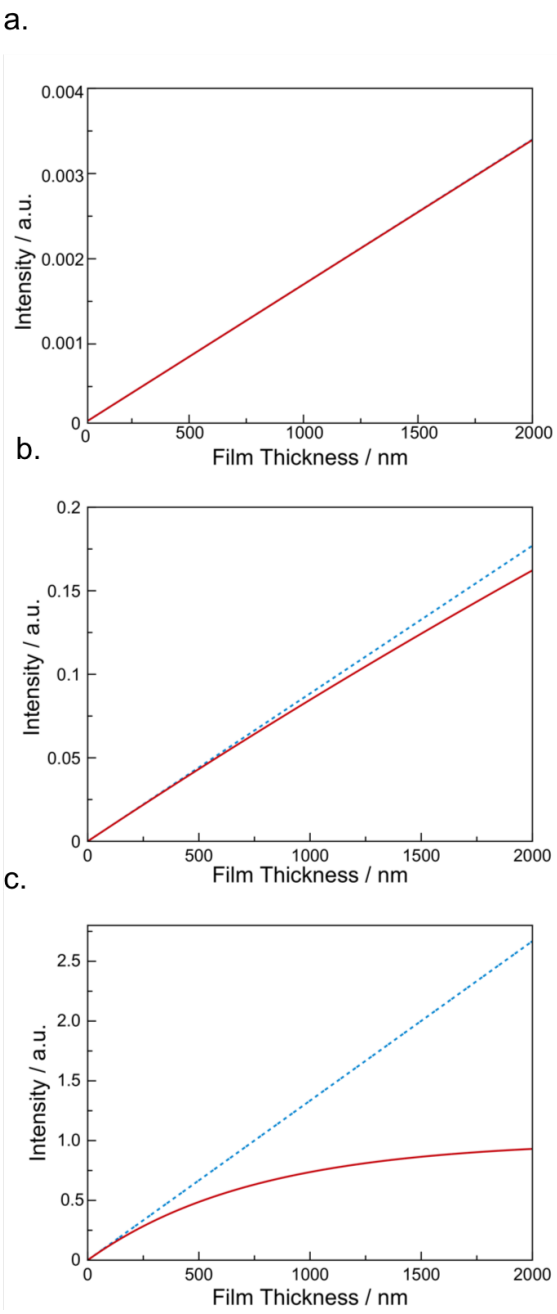

Figure A.5. Calculated X-ray emission intensities for the (a) Kα, (b) Lα, and (c) Mα lines of Pb in a film of PbSe. The values inserted into Equations 1 and 2 are: ρ = 8.29 g/cm^3, μ(Mα) = 1600 cm^2/g, μ(Lα) = 100 cm^2/g, and μ(Kα) = 2.0 cm^2/g. The total mass attenuation coefficient μ is calculated form the weighted average of the individual attenuation coefficients of each element present in the film. Equation 2 yields the blue dashed line and the values from Equation 1 are given by the red continuous line.

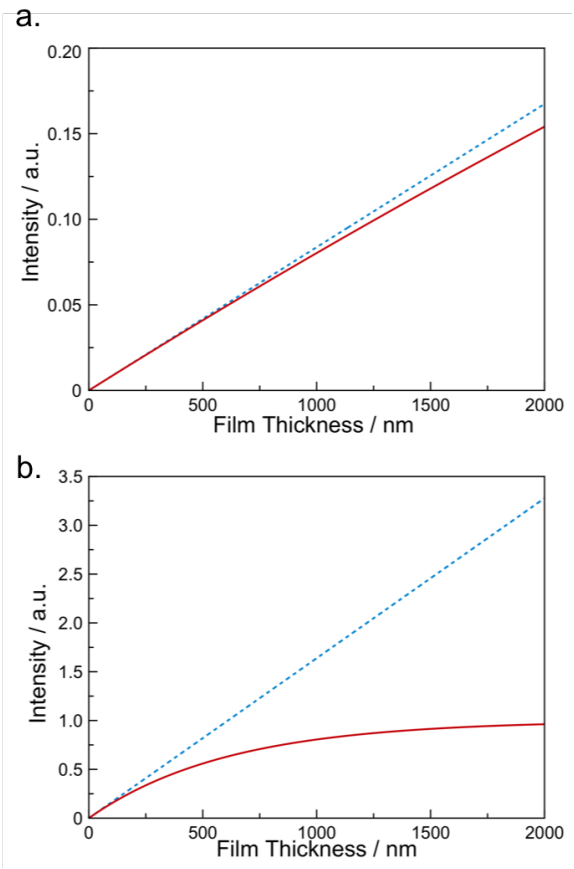

Figure A.6. Calculated X-ray emission intensities for the (a) Kα and (b) Lα lines of Se in a film of PbSe. The values inserted into Equations 1 and 2 are: ρ = 8.29 g/cm^3, μ(Lα) = 2000 cm^2/g, and μ(Kα) = 100 cm^2/g. The total mass attenuation coefficient μ is calculated form the weighted average of the individual attenuation coefficients of each element present in the film. Equation 2 yields the blue dashed line and the values from Equation 1 are given by the red continuous line.

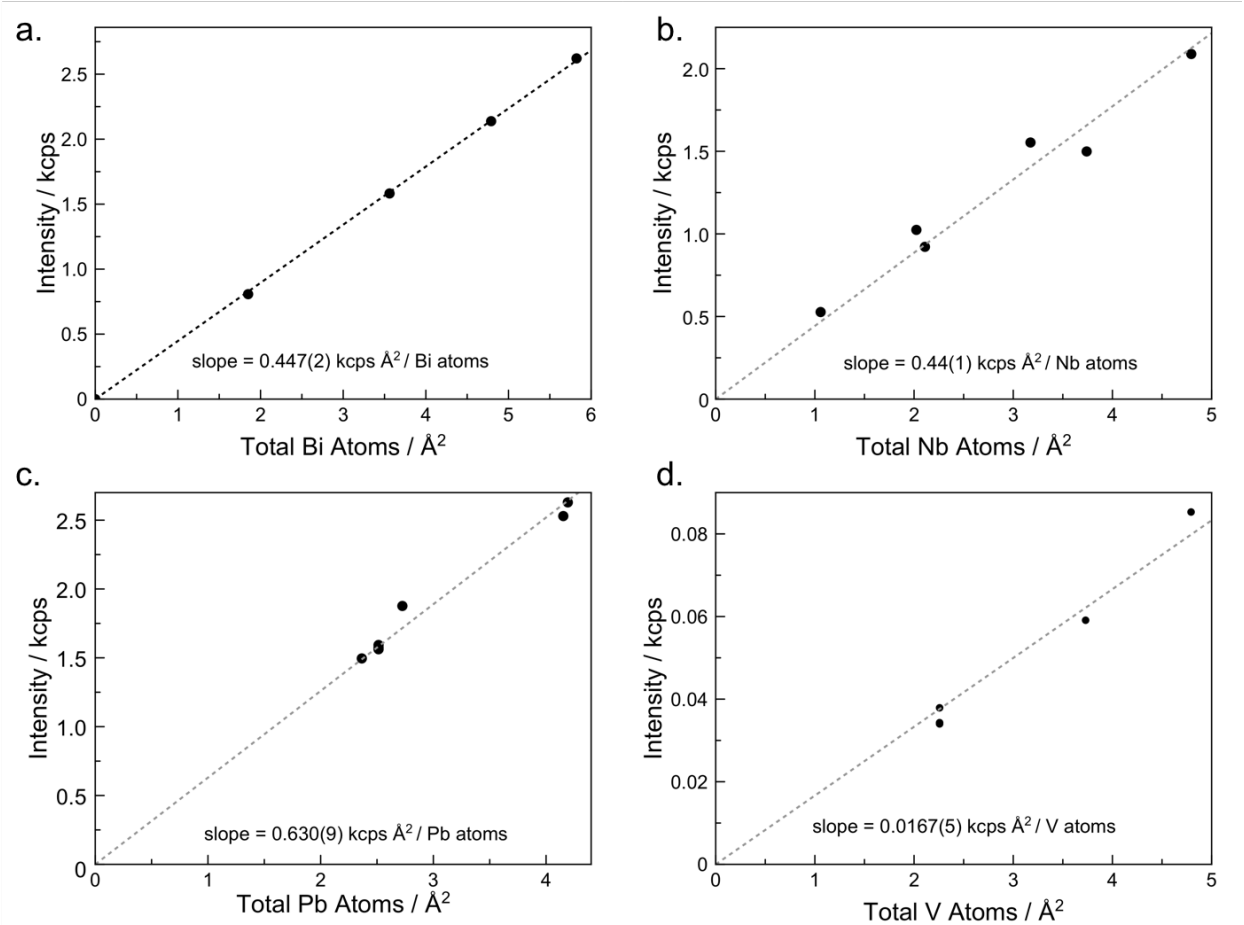

Figure A.7. A graph of intensity versus atoms per $Å^2$ for the elements (a) Bi, (b) Nb, (c) Pb, and (d) V found in a variety of samples, each consisting of a different element matrix. This shows the versatility of using XRF to probe various elements in a variety of samples.

REFERENCES CITED

CHAPTER I

(1) Frindt, R. F. Single Crystals of MoS_2 Several Molecular Layers Thick. *J. Appl. Phys.* **1966**, *37* (4), 1928–1929.

(2) Consadori, F.; Frindt, R. F. Crystal Size Effects on the Exciton Absorption Spectrum of WSe_2. *Phys. Rev. B* **1970**, *2* (12), 4893–4896.

(3) Gavaler, J. R.; Janocko, M. A.; Hulm, J. K.; Jones, C. K. Superconducting Properties as a Function of Thickness in NbN Films. *Physica* **1971**, *55*, 585–591.

(4) Frindt, R. F. Superconductivity in Ultrathin $NbSe_2$ Layers. *Phys. Rev. Lett.* **1972**, *28* (5), 299–301.

(5) Cho, A. Y.; Arthur, J. R. Molecular Beam Epitaxy. *Prog. Solid State Chem.* **1975**, *10*, 157–191.

(6) Veuhoff, E. *Handbook of Compound Semiconductors: Growth, Processing, Characterization and Devices*; Holloway, P. H., McGuire, G. E., Eds.; Noyes Publications: Park Ridge, NJ, 1995.

(7) von Klitzing, K. The Quantized Hall Effect. *Rev. Mod. Phys.* **1986**, *58* (3), 519–531.

(8) Thornton, T. J.; Pepper, M.; Ahmed, H.; Andrews, D.; Davies, G. J. One-Dimensional Conduction in the 2D Electron Gas of a GaAs-AlGaAs Heterojunction. *Phys. Rev. Lett.* **1986**, *56* (11), 1198–1201.

(9) Dingle, R.; Störmer, H. L.; Gossard, A. C.; Wiegmann, W. Electron Mobilities in Modulation-doped Semiconductor Heterojunction Superlattices. *Appl. Phys. Lett.* **1978**, *33* (7), 665–667.

(10) Wierer, J. J.; David, A.; Megens, M. M. III-Nitride Photonic-Crystal Light-Emitting Diodes with High Extraction Efficiency. *Nat. Photonics* **2009**, *3* (3), 163–169.

(11) Faist, J.; Capasso, F.; Sirtori, C. Quantum Cascade Laser. *Science.* **1994**, *264*, 1–4.

(12) Koma, A.; Sunouchi, K.; Miyajima, T. Fabrication and Characterization of Heterostructures with Subnanometer Thickness. *Microelectron. Eng.* **1984**, *2*, 129–136.

(13) Koma, A. Van Der Waals Epitaxy—a New Epitaxial Growth Method for a Highly Lattice-Mismatched System. *Thin Solid Films* **1992**, *216*, 72–76.

(14) Koma, A.; Yoshimura, K. Ultrasharp Interfaces Grown with Van Der Waals Epitaxy. *Surf. Sci.* **1986**, *174*, 556–560.

(15) Wiegers, G. A. Misfit Layer Compounds: Structures and Physical Properties. *Prog. SolidSt. Chem* **1996**, *24*, 1–139.

(16) Wulff, J.; Meetsma, A.; Van Smaalen, S.; Haange, R. J.; De Boer, J. L.; Wiegers, G. A. Structure, Electrical Transport, and Magnetic Properties of the Misfit Layer Compound $(PbS)_{1.13}TaS_2$. *J. Solid State Chem.* **1990**, *84* (1), 118–129.

(17) Novoselov, K. S.; Geim, A. K.; Morozov, S. V.; Jiang, D.; Zhang, Y.; Dubonos, S. V.; Grigorieva, I. V.; Firsov, A. A. Electric Field Effect in Atomically Thin Carbon Films. *Science.* **2004**, *306* (5696).

(18) Novoselov, K. S. Nobel Lecture: Graphene: Materials in the Flatland. *Rev. Mod. Phys.* **2011**, *83* (3), 837–849.

(19) Geim, A. K. Nobel Lecture: Random Walk to Graphene. *Rev. Mod. Phys.* **2011**, *83* (3), 851–862.

(20) Novoselov, K. S.; Jiang, D.; Schedin, F.; Booth, T. J.; Khotkevich, V. V; Morozov, S. V; Geim, A. K. Two-Dimensional Atomic Crystals. *Proc. Natl. Acad. Sci. U. S. A.* **2005**, *102*, 10451–10453.

(21) Abergel, D. S. L.; Russell, A.; Fal'ko, V. I. Visibility of Graphene Flakes on a Dielectric Substrate. *Appl. Phys. Lett.* **2007**, *91* (6), 63125.

(22) Blake, P.; Hill, E. W.; Castro Neto, A. H.; Novoselov, K. S.; Jiang, D.; Yang, R.; Booth, T. J.; Geim, A. K. Making Graphene Visible. *Appl. Phys. Lett.* **2007**, *91* (6), 63124.

(23) Geim, A. K.; Grigorieva, I. V. Van Der Waals Heterostructures. *Nature* **2013**, *499*, 419–425.

(24) Lee, G.-H.; Yu, Y.-J.; Lee, C.; Dean, C.; Shepard, K. L.; Kim, P.; Hone, J. Electron Tunneling through Atomically Flat and Ultrathin Hexagonal Boron Nitride. *Appl. Phys. Lett.* **2011**, *99* (24), 243114.

(25) Britnell, L.; Gorbachev, R. V.; Jalil, R.; Belle, B. D.; Schedin, F.; Katsnelson, M. I.; Eaves, L.; Morozov, S. V.; Mayorov, A. S.; Peres, N. M. R.; et al. Electron Tunneling through Ultrathin Boron Nitride Crystalline Barriers. *Nano Lett.* **2012**, *12* (3), 1707–1710.

(26) Splendiani, A.; Sun, L.; Zhang, Y.; Li, T.; Kim, J.; Chim, C.-Y.; Galli, G.; Wang, F. Emerging Photoluminescence in Monolayer MoS_2. *Nano Lett.* **2010**, *10* (4), 1271–1275.

(27) Mak, K. F.; Lee, C.; Hone, J.; Shan, J.; Heinz, T. F. Atomically Thin MoS_2: A New Direct-Gap Semiconductor. *Phys. Rev. Lett.* **2010**, *105* (13).

(28) Zeng, H.; Dai, J.; Yao, W.; Xiao, D.; Cui, X. Valley Polarization in MoS_2 Monolayers by Optical Pumping. *Nat. Nanotechnol.* **2012**, *7* (8), 490–493.

(29) Mak, K. F.; He, K.; Shan, J.; Heinz, T. F. Control of Valley Polarization in Monolayer MoS_2 by Optical Helicity. *Nat. Nanotechnol.* **2012**, *7* (8), 494–498.

(30) Fang, H.; Chuang, S.; Chang, T. C.; Takei, K.; Takahashi, T.; Javey, A. High-Performance Single Layered WSe_2 P-FETs with Chemically Doped Contacts. *Nano Lett.* **2012**, *12* (7), 3788–3792.

(31) Zhao, W.; Ghorannevis, Z.; Chu, L.; Toh, M.; Kloc, C.; Tan, P.-H.; Eda, G. Evolution of Electronic Structure in Atomically Thin Sheets of WS_2 and WSe_2. *ACS Nano* **2013**, *7* (1), 791–797.

(32) Tonndorf, P.; Schmidt, R.; Böttger, P.; Zhang, X.; Börner, J.; Liebig, A.; Albrecht, M.; Kloc, C.; Gordan, O.; Zahn, D. R. T.; et al. Photoluminescence Emission and Raman Response of Monolayer MoS_2, $MoSe_2$, and WSe_2. *Opt. Express* **2013**, *21* (4), 4908.

(33) Nair, R. R.; Ren, W.; Jalil, R.; Riaz, I.; Kravets, V. G.; Britnell, L.; Blake, P.; Schedin, F.; Mayorov, A. S.; Yuan, S.; et al. Fluorographene: A Two-Dimensional Counterpart of Teflon. *Small* **2010**, *6* (24), 2877–2884.

(34) Bianco, E.; Butler, S.; Jiang, S.; Restrepo, O. D.; Windl, W.; Goldberger, J. E. Stability and Exfoliation of Germanane: A Germanium Graphane Analogue. *ACS Nano* **2013**, *7* (5), 4414–4421.

(35) Dávila, M. E.; Le Lay, G. Few Layer Epitaxial Germanene: A Novel Two-Dimensional Dirac Material. *Sci. Rep.* **2016**, *6*, 20714.

(36) Acun, A.; Zhang, L.; Bampoulis, P.; Farmanbar, M.; van Houselt, A.; Rudenko, A. N.; Lingenfelder, M.; Brocks, G.; Poelsema, B.; Katsnelson, M. I.; et al. Germanene: The Germanium Analogue of Graphene. *J. Phys. Condens. Matter* **2015**, *27* (44), 443002.

(37) Zhao, J.; Liu, H.; Yu, Z.; Quhe, R.; Zhou, S.; Wang, Y.; Liu, C. C.; Zhong, H.; Han, N.; Lu, J.; et al. Rise of Silicene: A Competitive 2D Material. *Prog. Mater. Sci.* **2016**, *83*, 24–151.

(38) Liu, H.; Neal, A. T.; Zhu, Z.; Luo, Z.; Xu, X.; Tománek, D.; Ye, P. D. Phosphorene: An Unexplored 2D Semiconductor with a High Hole Mobility. *ACS Nano* **2014**, *8* (4), 4033–4041.

(39) Li, L.; Yu, Y.; Ye, G. J.; Ge, Q.; Ou, X.; Wu, H.; Feng, D.; Chen, X. H.; Zhang, Y. Black Phosphorus Field-Effect Transistors. *Nat. Nanotechnol.* **2014**, *9* (5), 372–377.

(40) Novoselov, K. S.; Mishchenko, A.; Carvalho, A.; Neto, A. H. C.; Road, O. 2D Materials and van Der Waals Heterostructures. *Science.* **2016**, *353*, aac9439.

(41) Liu, Y.; Weiss, N. O.; Duan, X.; Cheng, H.-C.; Huang, Y.; Duan, X. Van Der Waals Heterostructures and Devices. *Nat. Rev. Mater.* **2016**, *1* (9), 16042.

(42) Ulstrup, S.; Čabo, A. G.; Miwa, J. A.; Riley, J. M.; Grønborg, S. S.; Johannsen, J. C.; Cacho, C.; Alexander, O.; Chapman, R. T.; Springate, E.; et al. Ultrafast Band Structure Control of a Two-Dimensional Heterostructure. *ACS Nano* **2016**, *10* (6), 6315–6322.

(43) Ugeda, M. M.; Bradley, A. J.; Shi, S.-F.; da Jornada, F. H.; Zhang, Y.; Qiu, D. Y.; Ruan, W.; Mo, S.-K.; Hussain, Z.; Shen, Z.-X.; et al. Giant Bandgap Renormalization and Excitonic Effects in a Monolayer Transition Metal Dichalcogenide Semiconductor. *Nat. Mater.* **2014**, *13* (12), 1091–1095.

(44) Steinhoff, A.; Rösner, M.; Jahnke, F.; Wehling, T. O.; Gies, C. Influence of Excited Carriers on the Optical and Electronic Properties of MoS_2. *Nano Lett.* **2014**, *14* (7), 3743–3748.

(45) Chernikov, A.; Ruppert, C.; Hill, H. M.; Rigosi, A. F.; Heinz, T. F. Population Inversion and Giant Bandgap Renormalization in Atomically Thin WS2 Layers. *Nat. Photonics* **2015**, *9* (7), 466–470.

(46) Chernikov, A.; van der Zande, A. M.; Hill, H. M.; Rigosi, A. F.; Velauthapillai, A.; Hone, J.; Heinz, T. F. Electrical Tuning of Exciton Binding Energies in Monolayer WS_2. *Phys. Rev. Lett.* **2015**, *115* (12), 126802.

(47) Pogna, E. A. A.; Marsili, M.; De Fazio, D.; Dal Conte, S.; Manzoni, C.; Sangalli, D.; Yoon, D.; Lombardo, A.; Ferrari, A. C.; Marini, A.; et al. Photo-Induced Bandgap Renormalization Governs the Ultrafast Response of Single-Layer MoS_2. *ACS Nano* **2016**, *10* (1), 1182–1188.

(48) Grubišić Čabo, A.; Miwa, J. A.; Grønborg, S. S.; Riley, J. M.; Johannsen, J. C.; Cacho, C.; Alexander, O.; Chapman, R. T.; Springate, E.; Grioni, M.; et al. Observation of Ultrafast Free Carrier Dynamics in Single Layer MoS_2. *Nano Lett.* **2015**, *15* (9), 5883–5887.

(49) Bruix, A.; Miwa, J. A.; Hauptmann, N.; Wegner, D.; Ulstrup, S.; Grønborg, S. S.; Sanders, C. E.; Dendzik, M.; Grubišić Čabo, A.; Bianchi, M.; et al. Single-Layer MoS_2 on Au(111): Band Gap Renormalization and Substrate Interaction. *Phys. Rev. B* **2016**, *93* (16), 165422.

(50) Zhou, X.; Shi, J.; Qi, Y.; Liu, M.; Ma, D.; Zhang, Y.; Ji, Q.; Zhang, Z.; Li, C.; Liu, Z.; et al. Periodic Modulation of the Doping Level in Striped MoS_2 Superstructures. *ACS Nano* **2016**, *10* (3), 3461–3468.

(51) Zhang, C.; KC, S.; Nie, Y.; Liang, C.; Vandenberghe, W. G.; Longo, R. C.; Zheng, Y.; Kong, F.; Hong, S.; Wallace, R. M.; et al. Charge Mediated Reversible Metal–Insulator Transition in Monolayer $MoTe_2$ and $W_XMo_{1-X}Te_2$ Alloy. *ACS Nano* **2016**, *10* (8), 7370–7375.

(52) Ding, H.; Lv, Y.-F.; Zhao, K.; Wang, W.-L.; Wang, L.; Song, C.-L.; Chen, X.; Ma, X.-C.; Xue, Q.-K. High-Temperature Superconductivity in Single-Unit-Cell FeSe Films on Anatase TiO_2 (001). *Phys. Rev. Lett.* **2016**, *117* (6), 67001.

(53) Zhang, L.; Bampoulis, P.; Rudenko, A. N.; Yao, Q.; van Houselt, A.; Poelsema, B.; Katsnelson, M. I.; Zandvliet, H. J. W. Structural and Electronic Properties of Germanene on MoS_2. *Phys. Rev. Lett.* **2016**, *116* (25), 256804.

(54) Amlaki, T.; Bokdam, M.; Kelly, P. J. Z 2 Invariance of Germanene on MoS_2 from First Principles. *Phys. Rev. Lett.* **2016**, *116* (25), 256805.

(55) Zhang, J.; Xie, W.; Zhao, J.; Zhang, S. Band Alignment of Two-Dimensional Lateral Heterostructures. *2D Mater.* **2016**, *4* (1), 15038.

(56) Kaplan, D.; Gong, Y.; Mills, K.; Swaminathan, V.; Ajayan, P. M.; Shirodkar, S.; Kaxiras, E. Excitation Intensity Dependence of Photoluminescence from Monolayers of MoS_2 and WS_2/MoS_2 Heterostructures. *2D Mater.* **2016**, *3* (1), 15005.

(57) Sun, Q.; Dai, Y.; Ma, Y.; Yin, N.; Wei, W.; Yu, L.; Huang, B. Design of Lateral Heterostructure from Arsenene and Antimonene. *2D Mater.* **2016**, *3* (3), 35017.

(58) Millen, J.; Xuereb, A. The Rise of the Quantum Machines. *Phys. World* **2016**, *29* (1), 23–26.

(59) Castro Neto, A. H.; Guinea, F.; Peres, N. M. R.; Novoselov, K. S.; Geim, A. K. The Electronic Properties of Graphene. *Rev. Mod. Phys.* **2009**, *81*, 109–162.

(60) Komsa, H.-P.; Krasheninnikov, A. V. Electronic Structures and Optical Properties of Realistic Transition Metal Dichalcogenide Heterostructures from First Principles. *Phys. Rev. B* **2013**, *88*, 85318.

(61) Partoens, B.; Peeters, F. M. From Graphene to Graphite: Electronic Structure around the K Point. *Phys. Rev. B* **2006**, *74* (7), 75404.

(62) Zhang, L.; Zunger, A. Evolution of Electronic Structure as a Function of Layer Thickness in Group-VIB Transition Metal Dichalcogenides: Emergence of Localization Prototypes. *Nano Lett.* **2015**, *15* (2), 949–957.

(63) Smeller, M. M.; Heideman, C. L.; Lin, Q.; Beekman, M.; Anderson, M. D.; Zschack, P.; Anderson, I. M.; Johnson, D. C. Structure of Turbostratically Disordered Misfit Layer Compounds $[(PbSe)_{0.99}]_1[WSe_2]_1$, $[(PbSe)_{1.00}]_1[MoSe_2]_1$, and $[(SnSe)_{1.03}]_1$. *Zeitschrift für Anorg. und Allg. Chemie* **2012**, *638*, 2632–2639.

(64) Ruban, A. V.; Skriver, H. L.; Nørskov, J. K. Surface Segregation Energies in Transition-Metal Alloys. *Phys. Rev. B* **1999**, *59* (24), 15990–16000.

(65) Mrårtensson, N.; Saalfeld, H. B.; Kuhlenbeck, H.; Neumann, M. Structural Dependence of the 5*D*-Metal Surface Energies as Deduced from Surface Core-Level Shift Measurements. *Phys. Rev. B* **1989**, *39* (12), 8181–8186.

(66) Merrill, D. R.; Sutherland, D. R.; Ditto, J.; Bauers, S. R.; Falmbigl, M.; Medlin, D. L.; Johnson, D. C. Kinetically Controlled Site-Specific Substitutions in Higher-Order Heterostructures. *Chem. Mater.* **2015**, *27*, 4066–4072.

(67) Cahay, M.; Electrochemical Society (United States). Dielectric Science and Technology Division. *Quantum Confinement VI: Nanostructured Materials and Devices : Proceedings of the International Symposium*; Electrochemical Society, 2001.

(68) Hicks, L. D.; Dresselhaus, M. S. Effect of Quantum-Well Structures on the Thermoelectric Figure of Merit. *Phys. Rev. B* **1993**, *47* (19), 12727–12731.

(69) Martin Eisberg, R.; Resnick, R. *Quantum Physics of Atoms, Molecules, Solids, Nuclei, and Particles, 2nd Ed.*; John Wiley and Sons, Inc, 1974.

(70) Zhang, Y.; Chang, T.-R.; Zhou, B.; Cui, Y.-T.; Yan, H.; Liu, Z.; Schmitt, F.; Lee, J.; Moore, R.; Chen, Y.; et al. Direct Observation of the Transition from Indirect to Direct Bandgap in Atomically Thin Epitaxial MoSe2. *Nat. Nanotechnol.* **2013**, *9* (2), 111–115.

(71) Jin, W.; Yeh, P.-C.; Zaki, N.; Zhang, D.; Sadowski, J. T.; Al-Mahboob, A.; van der Zande, A. M.; Chenet, D. A.; Dadap, J. I.; Herman, I. P.; et al. Direct Measurement of the Thickness-Dependent Electronic Band Structure of MoS_2 Using Angle-Resolved Photoemission Spectroscopy. *Phys. Rev. Lett.* **2013**, *111* (10), 106801.

(72) Xiao, D.; Liu, G.-B.; Feng, W.; Xu, X.; Yao, W. Coupled Spin and Valley Physics in Monolayers of MoS_2 and Other Group-VI Dichalcogenides. *Phys. Rev. Lett.* **2012**, *108* (19), 196802.

(73) Cao, T.; Wang, G.; Han, W.; Ye, H.; Zhu, C.; Shi, J.; Niu, Q.; Tan, P.; Wang, E.; Liu, B.; et al. Valley-Selective Circular Dichroism of Monolayer Molybdenum Disulphide. *Nat. Commun.* **2012**, *3*, 887.

(74) Wang, Q. H.; Kalantar-Zadeh, K.; Kis, A.; Coleman, J. N.; Strano, M. S. Electronics and Optoelectronics of Two-Dimensional Transition Metal Dichalcogenides. *Nat. Nanotechnol.* **2012**, *7* (11), 699–712.

(75) Xu, X.; Yao, W.; Xiao, D.; Heinz, T. F. Spin and Pseudospins in Layered Transition Metal Dichalcogenides. *Nat. Phys.* **2014**, *10* (5), 343–350.

(76) Yu, H.; Liu, G.-B.; Gong, P.; Xu, X.; Yao, W. Dirac Cones and Dirac Saddle Points of Bright Excitons in Monolayer Transition Metal Dichalcogenides. *Nat. Commun.* **2014**, *5*, 3876.

(77) Li, Y.; Ludwig, J.; Low, T.; Chernikov, A.; Cui, X.; Arefe, G.; Kim, Y. D.; van der Zande, A. M.; Rigosi, A.; Hill, H. M.; et al. Valley Splitting and Polarization by the Zeeman Effect in Monolayer $MoSe_2$. *Phys. Rev. Lett.* **2014**, *113* (26), 266804.

(78) MacNeill, D.; Heikes, C.; Mak, K. F.; Anderson, Z.; Kormányos, A.; Zólyomi, V.; Park, J.; Ralph, D. C. Breaking of Valley Degeneracy by Magnetic Field in Monolayer $MoSe_2$. *Phys. Rev. Lett.* **2015**, *114* (3), 37401.

(79) Srivastava, A.; Sidler, M.; Allain, A. V.; Lembke, D. S.; Kis, A.; Imamoğlu, A. Valley Zeeman Effect in Elementary Optical Excitations of Monolayer WSe2. *Nat. Phys.* **2015**, *11* (2), 141–147.

(80) Aivazian, G.; Gong, Z.; Jones, A. M.; Chu, R.-L.; Yan, J.; Mandrus, D. G.; Zhang, C.; Cobden, D.; Yao, W.; Xu, X. Magnetic Control of Valley Pseudospin in Monolayer WSe_2. *Nat. Phys.* **2015**, *11* (2), 148–152.

(81) Xia, F.; Wang, H.; Xiao, D.; Dubey, M.; Ramasubramaniam, A. Two-Dimensional Material Nanophotonics. *Nat. Photonics* **2014**, *8* (12), 899–907.

(82) Liu, X.; Galfsky, T.; Sun, Z.; Xia, F.; Lin, E.; Lee, Y.-H.; Kéna-Cohen, S.; Menon, V. M. Strong Light–matter Coupling in Two-Dimensional Atomic Crystals. *Nat. Photonics* **2014**, *9* (1), 30–34.

(83) Wang, K.; Huang, B.; Tian, M.; Ceballos, F.; Lin, M.-W.; Mahjouri-Samani, M.; Boulesbaa, A.; Puretzky, A. A.; Rouleau, C. M.; Yoon, M.; et al. Interlayer Coupling in Twisted WSe_2/WS_2 Bilayer Heterostructures Revealed by Optical Spectroscopy. *ACS Nano* **2016**, *10* (7), 6612–6622.

(84) Lopes dos Santos, J. M. B.; Peres, N. M. R.; Castro Neto, A. H. Graphene Bilayer with a Twist: Electronic Structure. *Phys. Rev. Lett.* **2007**, *99* (25), 256802.

(85) Trambly de Laissardière, G.; Mayou, D.; Magaud, L. Localization of Dirac Electrons in Rotated Graphene Bilayers. *Nano Lett.* **2010**, *10* (3), 804–808.

(86) Park, C.-H.; Yang, L.; Son, Y.-W.; Cohen, M. L.; Louie, S. G. Anisotropic Behaviours of Massless Dirac Fermions in Graphene under Periodic Potentials. *Nat. Phys.* **2008**, *4* (3), 213–217.

(87) Barbier, M.; Vasilopoulos, P.; Peeters, F. M.; Pereira, J. M. Bilayer Graphene with Single and Multiple Electrostatic Barriers: Band Structure and Transmission. *Phys. Rev. B* **2009**, *79* (15), 155402.

(88) Hass, J.; Varchon, F.; Millán-Otoya, J. E.; Sprinkle, M.; Sharma, N.; de Heer, W. A.; Berger, C.; First, P. N.; Magaud, L.; Conrad, E. H. Why Multilayer Graphene on 4H−SiC ($000\bar{1}$) Behaves Like a Single Sheet of Graphene. *Phys. Rev. Lett.* **2008**, *100* (12), 125504.

(89) Shallcross, S.; Sharma, S.; Pankratov, O. A. Quantum Interference at the Twist Boundary in Graphene. *Phys. Rev. Lett.* **2008**, *101* (5), 56803.

(90) Latil, S.; Meunier, V.; Henrard, L. Massless Fermions in Multilayer Graphitic Systems with Misoriented Layers: *Ab Initio* Calculations and Experimental Fingerprints. *Phys. Rev. B* **2007**, *76* (20), 201402.

(91) Varchon, F.; Mallet, P.; Veuillen, J.-Y.; Magaud, L. Ripples in Epitaxial Graphene on the Si-Terminated SiC(0001) Surface. *Phys. Rev. B* **2008**, *77* (23), 235412.

(92) Tu, Q.; Lange, B.; Parlak, Z.; Lopes, J. M. J.; Blum, V.; Zauscher, S. Quantitative Subsurface Atomic Structure Fingerprint for 2D Materials and Heterostructures by First-Principles-Calibrated Contact-Resonance Atomic Force Microscopy. *ACS Nano* **2016**, *10* (7), 6491–6500.

(93) Tan, Y.; Chen, F. W.; Ghosh, A. W. First Principles Study and Empirical Parametrization of Twisted Bilayer MoS_2 Based on Band-Unfolding. *Appl. Phys. Lett.* **2016**, *109* (10), 101601.

(94) Lee, C.-H.; Lee, G.-H.; van der Zande, A. M.; Chen, W.; Li, Y.; Han, M.; Cui, X.; Arefe, G.; Nuckolls, C.; Heinz, T. F.; et al. Atomically Thin p–n Junctions with van Der Waals Heterointerfaces. *Nat. Nanotechnol.* **2014**, *9* (9), 676–681.

(95) Gong, Y.; Lin, J.; Wang, X.; Shi, G.; Lei, S.; Lin, Z.; Zou, X.; Ye, G.; Vajtai, R.; Yakobson, B. I.; et al. Vertical and in-Plane Heterostructures from WS_2/MoS_2 Monolayers. *Nat. Mater.* **2014**, *13* (12), 1135–1142.

(96) Jiang, T.; Liu, H.; Huang, D.; Zhang, S.; Li, Y.; Gong, X.; Shen, Y.-R.; Liu, W.-T.; Wu, S. Valley and Band Structure Engineering of Folded MoS_2 Bilayers. *Nat. Nanotechnol.* **2014**, *9* (10), 825–829.

(97) Terrones, H.; Lopez-Urias, F.; Terrones, M. Novel Hetero-Layered Materials with Tunable Direct Band Gaps by Sandwiching Different Metal Disulfides and Diselenides. *Sci Rep* **2013**, *3*, 1549.

(98) He, J.; Hummer, K.; Franchini, C. Stacking Effects on the Electronic and Optical Properties of Bilayer Transition Metal Dichalcogenides MoS_2, $MoSe_2$, WS_2, and WSe_2. *Phys. Rev. B* **2014**, *89* (7), 75409.

(99) Heo, H.; Sung, J. H.; Cha, S.; Jang, B.-G.; Kim, J.-Y.; Jin, G.; Lee, D.; Ahn, J.-H.; Lee, M.-J.; Shim, J. H.; et al. Interlayer Orientation-Dependent Light Absorption and Emission in Monolayer Semiconductor Stacks. *Nat. Commun.* **2015**, *6*, 7372.

(100) Huang, S.; Ling, X.; Liang, L.; Kong, J.; Terrones, H.; Meunier, V.; Dresselhaus, M. S. Probing the Interlayer Coupling of Twisted Bilayer MoS_2 Using Photoluminescence Spectroscopy. *Nano Lett.* **2014**, *14* (10), 5500–5508.

(101) Kang, J.; Li, J.; Li, S.-S.; Xia, J.-B.; Wang, L.-W. Electronic Structural Moiré Pattern Effects on MoS_2/$MoSe_2$ 2D Heterostructures. *Nano Lett.* **2013**, *13* (11), 5485–5490.

(102) Radisavljevic, B.; Radenovic, A.; Brivio, J.; Giacometti, V.; Kis, A. Single-Layer MoS_2 Transistors. *Nat. Nanotechnol.* **2011**, *6* (3), 147–150.

(103) Gong, C.; Zhang, H.; Wang, W.; Colombo, L.; Wallace, R. M.; Cho, K. Band Alignment of Two-Dimensional Transition Metal Dichalcogenides: Application in Tunnel Field Effect Transistors. *Appl. Phys. Lett.* **2013**, *103* (5), 53513.

(104) Huang, J.-K.; Pu, J.; Hsu, C.-L.; Chiu, M.-H.; Juang, Z.-Y.; Chang, Y.-H.; Chang, W.-H.; Iwasa, Y.; Takenobu, T.; Li, L.-J. Large-Area Synthesis of Highly Crystalline WSe_2 Monolayers and Device Applications. *ACS Nano* **2014**, *8* (1), 923–930.

(105) Kappera, R.; Voiry, D.; Yalcin, S. E.; Branch, B.; Gupta, G.; Mohite, A. D.; Chhowalla, M. Phase-Engineered Low-Resistance Contacts for Ultrathin MoS_2 Transistors. *Nat. Mater.* **2014**, *13* (12), 1128–1134.

(106) Lee, Y.-H.; Zhang, X.-Q.; Zhang, W.; Chang, M.-T.; Lin, C.-T.; Chang, K.-D.; Yu, Y.-C.; Wang, J. T.-W.; Chang, C.-S.; Li, L.-J.; et al. Synthesis of Large-Area MoS_2 Atomic Layers with Chemical Vapor Deposition. *Adv. Mater.* **2012**, *24* (17), 2320–2325.

(107) Lu, X.; Utama, M. I. B.; Lin, J.; Gong, X.; Zhang, J.; Zhao, Y.; Pantelides, S. T.; Wang, J.; Dong, Z.; Liu, Z.; et al. Large-Area Synthesis of Monolayer and Few-Layer $MoSe_2$ Films on SiO_2 Substrates. *Nano Lett.* **2014**, *14* (5), 2419–2425.

(108) Oura, K.; Lifshits, V. G.; Saranin, A. A.; Zotov, A. V.; Katayama, M. *Surface Science: An Introduction*; Springer-Verlag: Berlin, 2003.

(109) Lee, J.-U.; Kim, K.; Han, S.; Ryu, G. H.; Lee, Z.; Cheong, H. Raman Signatures of Polytypism in Molybdenum Disulfide. *ACS Nano* **2016**, *10* (2), 1948–1953.

(110) Zhang, X.; Qiao, X.-F.; Shi, W.; Wu, J.-B.; Jiang, D.-S.; Tan, P.-H. Phonon and Raman Scattering of Two-Dimensional Transition Metal Dichalcogenides from Monolayer, Multilayer to Bulk Material. *Chem. Soc. Rev.* **2015**, *44* (9), 2757–2785.

(111) Mitchson, G.; Ditto, J.; Woods, K. N.; Westover, R.; Page, C. J.; Johnson, D. C. Application of HAADF STEM Image Analysis to Structure Determination in Rotationally Disordered and Amorphous Multilayered Films. *Semicond. Sci. Technol.* **2016**, *31* (8), 84003.

(112) Anderson, M. D.; Heideman, C. L.; Lin, Q.; Smeller, M.; Kokenyesi, R.; Herzing, A. A.; Anderson, I. M.; Keszler, D. A.; Zschack, P.; Johnson, D. C. Size-Dependent Structural Distortions in One-Dimensional Nanostructures. *Angew. Chemie Int. Ed.* **2013**, *52* (7), 1982–1985.

(113) Atkins, R.; Wilson, J.; Zschack, P.; Grosse, C.; Neumann, W.; Johnson, D. C. Synthesis of $[(SnSe)_{1.15}]_m(TaSe_2)_n$ Ferecrystals: Structurally Tunable Metallic Compounds. *Chem. Mater.* **2012**, *24*, 4594–4599.

(114) Beekman, M.; Cogburn, G.; Heideman, C.; Rouvimov, S.; Zschack, P.; Neumann, W.; Johnson, D. C. New Layered Intergrowths in the Sn-Mo-Se System. *J. Electron. Mater.* **2012**, *41* (6), 1476–1480.

(115) Falmbigl, M.; Alemayehu, M. B.; Merrill, D. R.; Beekman, M.; Johnson, D. C. In-Plane Structure of Ferecrystalline Compounds. *Cryst. Res. Technol.* **2015**, *50*, 464–472.

(116) Beekman, M.; Disch, S.; Rouvimov, S.; Kasinathan, D.; Koepernik, K.; Rosner, H.; Zschack, P.; Neumann, W. S.; Johnson, D. C. Controlling Size-Induced Phase Transformations Using Chemically Designed Nanolaminates. *Angew. Chemie - Int. Ed.* **2013**, *52*, 13211–13214.

(117) Merrill, D. R.; Moore, D. B.; Coffey, M. N.; Jansons, A. W.; Falmbigl, M.; Johnson, D. C. Synthesis and Characterization of Turbostratically Disordered $(BiSe)_{1.15}TiSe_2$. *Semicond. Sci. Technol.* **2014**, *29*, 64004.

(118) Mitchson, G.; Falmbigl, M.; Ditto, J.; Johnson, D. C. Antiphase Boundaries in the Turbostratically Disordered Misfit Compound $(BiSe)_{1+\delta}$ $NbSe_2$. *Inorg. Chem.* **2015**, *54* (21), 10309–10315.

(119) Sun, Y.; Thompson, S. E.; Nishida, T. Physics of Strain Effects in Semiconductors and Metal-Oxide-Semiconductor Field-Effect Transistors. *J. Appl. Phys.* **2007**, *101* (10), 104503.

(120) Smith, C. S. Piezoresistance Effect in Germanium and Silicon. *Phys. Rev.* **1954**, *94* (1), 42–49.

(121) CAPASSO, F. Band-Gap Engineering: From Physics and Materials to New Semiconductor Devices. *Science.* **1987**, *235* (4785).

(122) Smith, A. M.; Nie, S. Semiconductor Nanocrystals: Structure, Properties, and Band Gap Engineering. *Acc. Chem. Res.* **2010**, *43* (2), 190–200.

(123) Si, C.; Sun, Z.; Liu, F. Strain Engineering of Graphene: A Review. *Nanoscale* **2016**, *8* (6), 3207–3217.

(124) Ohuchi, F. S.; Parkinson, B. A.; Ueno, K.; Koma, A. Van Der Waals Epitaxial Growth and Characterization of $MoSe_2$ Thin Films on SnS_2. *J. Appl. Phys.* **1990**, *68* (5), 2168–2175.

(125) Shi, Y.; Zhou, W.; Lu, A.-Y.; Fang, W.; Lee, Y.-H.; Hsu, A. L.; Kim, S. M.; Kim, K. K.; Yang, H. Y.; Li, L.-J.; et al. Van Der Waals Epitaxy of MoS_2 Layers Using Graphene As Growth Templates. *Nano Lett.* **2012**, *12* (6), 2784–2791.

(126) Roldán, R.; Castellanos-Gomez, A.; Cappelluti, E.; Guinea, F. Strain Engineering in Semiconducting Two-Dimensional Crystals. *J. Phys. Condens. Matter* **2015**, *27* (31), 313201.

(127) Huang, M.; Yan, H.; Chen, C.; Song, D.; Heinz, T. F.; Hone, J. Phonon Softening and Crystallographic Orientation of Strained Graphene Studied by Raman Spectroscopy. *Proc. Natl. Acad. Sci. U. S. A.* **2009**, *106* (18), 7304–7308.

(128) Conley, H. J.; Wang, B.; Ziegler, J. I.; Haglund, R. F.; Pantelides, S. T.; Bolotin, K. I. Bandgap Engineering of Strained Monolayer and Bilayer MoS_2. *Nano Lett.* **2013**, *13* (8), 3626–3630.

(129) Sun, Y.; Liu, K.; Hong, X.; Chen, M.; Kim, J.; Shi, S.; Wu, J.; Zettl, A.; Wang, F. Probing Local Strain at MX_2 –Metal Boundaries with Surface Plasmon-Enhanced Raman Scattering. *Nano Lett.* **2014**, *14* (9), 5329–5334.

(130) Ambrosetti, A.; Ferri, N.; DiStasio, R. A.; Tkatchenko, A. Wavelike Charge Density Fluctuations and van Der Waals Interactions at the Nanoscale. *Science.* **2016**, *351* (6278).

(131) Xi, X.; Berger, H.; Forró, L.; Shan, J.; Mak, K. F. Gate Tuning of Electronic Phase Transitions in Two-Dimensional $NbSe_2$. *Phys. Rev. Lett.* **2016**, *117* (10), 106801.

(132) Song, C.-L.; Zhang, H.-M.; Zhong, Y.; Hu, X.-P.; Ji, S.-H.; Wang, L.; He, K.; Ma, X.-C.; Xue, Q.-K. Observation of Double-Dome Superconductivity in Potassium-Doped FeSe Thin Films. *Phys. Rev. Lett.* **2016**, *116* (15), 157001.

(133) Feng, Z.; Chen, B.; Qian, S.; Xu, L.; Feng, L.; Yu, Y.; Zhang, R.; Chen, J.; Li, Q.; Li, Q.; et al. Chemical Sensing by Band Modulation of a Black Phosphorus/molybdenum Diselenide van Der Waals Hetero-Structure. *2D Mater.* **2016**, *3* (3), 35021.

(134) Oakes, L.; Carter, R.; Hanken, T.; Cohn, A. P.; Share, K.; Schmidt, B.; Pint, C. L.; Liu, J. H.; Liu, X. W.; Gong, Y. J.; et al. Interface Strain in Vertically Stacked Two-Dimensional Heterostructured Carbon-MoS_2 Nanosheets Controls Electrochemical Reactivity. *Nat. Commun.* **2016**, *7*, 11796.

(135) Amin, B.; Singh, N.; Schwingenschlögl, U. Heterostructures of Transition Metal Dichalcogenides. *Phys. Rev. B* **2015**, *92* (7), 75439.

(136) Park, Y. H.; Kim, M. H.; Kim, S. Bin; Jung, H. J.; Chae, K.; Ahn, Y. H.; Park, J. Y.; Rotermund, F.; Lee, S. W. Enhanced Nucleation of High-K Dielectrics on Graphene by Atomic Layer Deposition. *Chem. Mater.* **2016**, *28* (20), 7268–7275.

(137) Wang, F.; Yin, L.; Wang, Z.; Xu, K.; Wang, F.; Shifa, T. A.; Huang, Y.; Wen, Y.; Jiang, C.; He, J. Strong Electrically Tunable $MoTe_2$/graphene van Der Waals Heterostructures for High-Performance Electronic and Optoelectronic Devices. *Appl. Phys. Lett.* **2016**, *109* (19), 193111.

(138) Mohanty, D.; Xie, W.; Wang, Y.; Lu, Z.; Shi, J.; Zhang, S.; Wang, G.-C.; Lu, T.-M.; Bhat, I. B. Van Der Waals Epitaxy of CdTe Thin Film on Graphene. *Appl. Phys. Lett.* **2016**, *109* (14), 143109.

(139) Kelly, A. G.; Finn, D.; Harvey, A.; Hallam, T.; Coleman, J. N. All-Printed Capacitors from Graphene-BN-Graphene Nanosheet Heterostructures. *Appl. Phys. Lett.* **2016**, *109* (2), 23107.

(140) Youn, D. H.; Stauffer, S. K.; Xiao, P.; Park, H.; Nam, Y.; Dolocan, A.; Henkelman, G.; Heller, A.; Mullins, C. B. Simple Synthesis of Nanocrystalline Tin Sulfide/N-Doped Reduced Graphene Oxide Composites as Lithium Ion Battery Anodes. *ACS Nano* **2016**, *10* (12), 10778–10788.

(141) Pizzocchero, F.; Gammelgaard, L.; Jessen, B. S.; Caridad, J. M.; Wang, L.; Hone, J.; Bøggild, P.; Booth, T. J. The Hot Pick-up Technique for Batch Assembly of van Der Waals Heterostructures. *Nat. Commun.* **2016**, *7*, 11894.

(142) Henck, H.; Pierucci, D.; Chaste, J.; Naylor, C. H.; Avila, J.; Balan, A.; Silly, M. G.; Asensio, M. C.; Sirotti, F.; Johnson, A. T. C.; et al. Electrolytic Phototransistor Based on Graphene-MoS_2 van Der Waals P-N Heterojunction with Tunable Photoresponse. *Appl. Phys. Lett.* **2016**, *109* (11), 113103.

(143) Clark, G.; Schaibley, J. R.; Ross, J.; Taniguchi, T.; Watanabe, K.; Hendrickson, J. R.; Mou, S.; Yao, W.; Xu, X. Single Defect Light-Emitting Diode in a van Der Waals Heterostructure. *Nano Lett.* **2016**, *16* (6), 3944–3948.

(144) Jobst, J.; van der Torren, A. J. H.; Krasovskii, E. E.; Balgley, J.; Dean, C. R.; Tromp, R. M.; van der Molen, S. J.; Cuk, T.; Tanaka, S.; Matsunami, M.; et al.

Quantifying Electronic Band Interactions in van Der Waals Materials Using Angle-Resolved Reflected-Electron Spectroscopy. *Nat. Commun.* **2016**, *7*, 13621.

(145) Wallbank, J. R.; Ghazaryan, D.; Misra, A.; Cao, Y.; Tu, J. S.; Piot, B. A.; Potemski, M.; Pezzini, S.; Wiedmann, S.; Zeitler, U.; et al. Tuning the Valley and Chiral Quantum State of Dirac Electrons in van Der Waals Heterostructures. *Science.* **2016**, *353* (6299).

(146) Byun, S.; Kim, J. H.; Song, S. H.; Lee, M.; Park, J.-J.; Lee, G.; Hong, S. H.; Lee, D. Ordered, Scalable Heterostructure Comprising Boron Nitride and Graphene for High-Performance Flexible Supercapacitors. *Chem. Mater.* **2016**, *28* (21), 7750–7756.

(147) Zhang, J.; Xie, W.; Xu, X.; Zhang, S.; Zhao, J. Structural and Electronic Properties of Interfaces in Graphene and Hexagonal Boron Nitride Lateral Heterostructures. *Chem. Mater.* **2016**, *28* (14), 5022–5028.

(148) Politano, A.; Slotman, G. J.; Roldán, R.; Chiarello, G.; Campi, D.; Katsnelson, M. I.; Yuan, S. Effect of Moiré Superlattice Reconstruction in the Electronic Excitation Spectrum of Graphene-Metal Heterostructures. *2D Mater.* **2017**, *4* (2), 21001.

(149) Sadeghi, H.; Sangtarash, S.; Lambert, C. J. Cross-Plane Enhanced Thermoelectricity and Phonon Suppression in graphene/MoS_2 van Der Waals Heterostructures. *2D Mater.* **2016**, *4* (1), 15012.

(150) Liu, C.-H.; Clark, G.; Fryett, T.; Wu, S.; Zheng, J.; Hatami, F.; Xu, X.; Majumdar, A. Nanocavity Integrated van Der Waals Heterostructure Light-Emitting Tunneling Diode. *Nano Lett.* **2017**, *17* (1), 200–205.

(151) Vu, Q. A.; Lee, J. H.; Nguyen, V. L.; Shin, Y. S.; Lim, S. C.; Lee, K.; Heo, J.; Park, S.; Kim, K.; Lee, Y. H.; et al. Tuning Carrier Tunneling in van Der Waals Heterostructures for Ultrahigh Detectivity. *Nano Lett.* **2017**, *17* (1), 453–459.

(152) Heo, J.; Jeong, H.; Cho, Y.; Lee, J.; Lee, K.; Nam, S.; Lee, E.-K.; Lee, S.; Lee, H.; Hwang, S.; et al. Reconfigurable van Der Waals Heterostructured Devices with Metal–Insulator Transition. *Nano Lett.* **2016**, *16* (11), 6746–6754.

(153) Long, M.; Liu, E.; Wang, P.; Gao, A.; Xia, H.; Luo, W.; Wang, B.; Zeng, J.; Fu, Y.; Xu, K.; et al. Broadband Photovoltaic Detectors Based on an Atomically Thin Heterostructure. *Nano Lett.* **2016**, *16* (4), 2254–2259.

(154) Giusca, C. E.; Rungger, I.; Panchal, V.; Melios, C.; Lin, Z.; Lin, Y.-C.; Kahn, E.; Elías, A. L.; Robinson, J. A.; Terrones, M.; et al. Excitonic Effects in Tungsten Disulfide Monolayers on Two-Layer Graphene. *ACS Nano* **2016**, *10* (8), 7840–7846.

(155) Gao, Y.; Liu, Q.; Xu, B. Lattice Mismatch Dominant Yet Mechanically Tunable Thermal Conductivity in Bilayer Heterostructures. *ACS Nano* **2016**, *10* (5), 5431–5439.

(156) Vu, Q. A.; Shin, Y. S.; Kim, Y. R.; Nguyen, V. L.; Kang, W. T.; Kim, H.; Luong, D. H.; Lee, I. M.; Lee, K.; Ko, D.-S.; et al. Two-Terminal Floating-Gate Memory with van Der Waals Heterostructures for Ultrahigh On/off Ratio. *Nat. Commun.* **2016**, *7*, 12725.

(157) Leenaerts, O.; Vercauteren, S.; Schoeters, B.; Partoens, B. System-Size Dependent Band Alignment in Lateral Two-Dimensional Heterostructures. *2D Mater.* **2016**, *3* (2), 25012.

(158) Wei, P.; Lee, S.; Lemaitre, F.; Pinel, L.; Cutaia, D.; Cha, W.; Katmis, F.; Zhu, Y.; Heiman, D.; Hone, J.; et al. Strong Interfacial Exchange Field in the graphene/EuS Heterostructure. *Nat. Mater.* **2016**, *15* (7), 711–716.

(159) Chen, H.; Wen, X.; Zhang, J.; Wu, T.; Gong, Y.; Zhang, X.; Yuan, J.; Yi, C.; Lou, J.; Ajayan, P. M.; et al. Ultrafast Formation of Interlayer Hot Excitons in Atomically Thin MoS_2/WS_2 Heterostructures. *Nat. Commun.* **2016**, *7*, 12512.

(160) Yu, W. J.; Vu, Q. A.; Oh, H.; Nam, H. G.; Zhou, H.; Cha, S.; Kim, J.-Y.; Carvalho, A.; Jeong, M.; Choi, H.; et al. Unusually Efficient Photocurrent Extraction in Monolayer van Der Waals Heterostructure by Tunnelling through Discretized Barriers. *Nat. Commun.* **2016**, *7*, 13278.

(161) Schaibley, J. R.; Rivera, P.; Yu, H.; Seyler, K. L.; Yan, J.; Mandrus, D. G.; Taniguchi, T.; Watanabe, K.; Yao, W.; Xu, X.; et al. Directional Interlayer Spin-Valley Transfer in Two-Dimensional Heterostructures. *Nat. Commun.* **2016**, *7*, 13747.

(162) Zhang, Q.; Chen, Y.; Zhang, C.; Pan, C.-R.; Chou, M.-Y.; Zeng, C.; Shih, C.-K.; Wang, Q. H.; Kalantar-Zadeh, K.; Kis, A.; et al. Bandgap Renormalization and Work Function Tuning in $MoSe_2$/hBN/Ru(0001) Heterostructures. *Nat. Commun.* **2016**, *7*, 13843.

(163) Li, M. Y.; Chen, C. H.; Shi, Y.; Li, L. J. Heterostructures Based on Two-Dimensional Layered Materials and Their Potential Applications. *Mater. Today* **2016**, *19*, 322–335.

(164) He, X.; Li, H.; Zhu, Z.; Dai, Z.; Yang, Y.; Yang, P.; Zhang, Q.; Li, P.; Schwingenschlogl, U.; Zhang, X. Strain Engineering in Monolayer WS_2, MoS_2, and the WS_2/MoS_2 Heterostructure. *Appl. Phys. Lett.* **2016**, *109* (17), 173105.

(165) Xi, X.; Zhao, L.; Wang, Z.; Berger, H.; Forró, L.; Shan, J.; Mak, K. F. Strongly Enhanced Charge-Density-Wave Order in Monolayer $NbSe_2$. *Nat. Nanotechnol.* **2015**, *10* (9), 765–769.

(166) Eichfeld, S. M.; Colon, V. O.; Nie, Y.; Cho, K.; Robinson, J. A. Controlling Nucleation of Monolayer WSe_2 during Metal-Organic Chemical Vapor Deposition Growth. *2D Mater.* **2016**, *3* (2), 25015.

(167) Fu, W.; Chen, Y.; Lin, J.; Wang, X.; Zeng, Q.; Zhou, J.; Zheng, L.; Wang, H.; He, Y.; He, H.; et al. Controlled Synthesis of Atomically Thin 1T-TaS_2 for Tunable Charge Density Wave Phase Transitions. *Chem. Mater.* **2016**, *28* (21), 7613–7618.

(168) Samassekou, H.; Alkabsh, A.; Wasala, M.; Eaton, M.; Walber, A.; Walker, A.; Pitkänen, O.; Kordas, K.; Talapatra, S.; Jayasekera, T.; et al. Viable Route towards Large-Area 2D MoS_2 Using Magnetron Sputtering. *2D Mater.* **2017**, *4* (2), 21002.

(169) Tu, Z.; Li, G.; Ni, X.; Meng, L.; Bai, S.; Chen, X.; Lou, J.; Qin, Y. Synthesis of Large Monolayer Single Crystal MoS_2 Nanosheets with Uniform Size through a Double-Tube Technology. *Appl. Phys. Lett.* **2016**, *109* (22), 223101.

(170) Bogaert, K.; Liu, S.; Chesin, J.; Titow, D.; Gradečak, S.; Garaj, S. Diffusion-Mediated Synthesis of MoS_2/WS_2 Lateral Heterostructures. *Nano Lett.* **2016**, *16* (8), 5129–5134.

(171) Samad, L.; Bladow, S. M.; Ding, Q.; Zhuo, J.; Jacobberger, R. M.; Arnold, M. S.; Jin, S. Layer-Controlled Chemical Vapor Deposition Growth of MoS_2 Vertical Heterostructures via van Der Waals Epitaxy. *ACS Nano* **2016**, *10* (7), 7039–7046.

(172) Vilá, R. A.; Momeni, K.; Wang, Q.; Bersch, B. M.; Lu, N.; Kim, M. J.; Chen, L. Q.; Robinson, J. A. Bottom-up Synthesis of Vertically Oriented Two-Dimensional Materials. *2D Mater.* **2016**, *3* (4), 41003.

(173) Zheng, B.; Chen, Y.; Wang, Z.; Qi, F.; Huang, Z.; Hao, X.; Li, P.; Zhang, W.; Li, Y. Vertically Oriented Few-Layered HfS_2 Nanosheets: Growth Mechanism and Optical Properties. *2D Mater.* **2016**, *3* (3), 35024.

(174) Li, C.-I.; Lin, J.-C.; Liu, H.-J.; Chu, M.-W.; Chen, H.-W.; Ma, C.-H.; Tsai, C.-Y.; Huang, H.-W.; Lin, H.-J.; Liu, H.-L.; et al. Van Der Waal Epitaxy of Flexible and Transparent VO_2 Film on Muscovite. *Chem. Mater.* **2016**, *28* (11), 3914–3919.

(175) Dau, M. T.; Vergnaud, C.; Marty, A.; Rortais, F.; Beigné, C.; Boukari, H.; Bellet-Amalric, E.; Guigoz, V.; Renault, O.; Alvarez, C.; et al. Millimeter-Scale Layered $MoSe_2$ Grown on Sapphire and Evidence for Negative Magnetoresistance. *Appl. Phys. Lett.* **2017**, *110* (1), 11909.

(176) Park, Y. W.; Jerng, S.-K.; Jeon, J. H.; Roy, S. B.; Akbar, K.; Kim, J.; Sim, Y.; Seong, M.-J.; Kim, J. H.; Lee, Z.; et al. Molecular Beam Epitaxy of Large-Area $SnSe_2$ with Monolayer Thickness Fluctuation. *2D Mater.* **2016**, *4* (1), 14006.

(177) Ji, J.; Song, X.; Liu, J.; Yan, Z.; Huo, C.; Zhang, S.; Su, M.; Liao, L.; Wang, W.; Ni, Z.; et al. Two-Dimensional Antimonene Single Crystals Grown by van Der Waals Epitaxy. *Nat. Commun.* **2016**, *7*, 13352.

(178) Aminalragia-Giamini, S.; Marquez-Velasco, J.; Tsipas, P.; Tsoutsou, D.; Renaud, G.; Dimoulas, A. Molecular Beam Epitaxy of Thin $HfTe_2$ Semimetal Films. *2D Mater.* **2016**, *4* (1), 15001.

(179) Middey, S.; Meyers, D.; Doennig, D.; Kareev, M.; Liu, X.; Cao, Y.; Yang, Z.; Shi, J.; Gu, L.; Ryan, P. J.; et al. Mott Electrons in an Artificial Graphenelike Crystal of Rare-Earth Nickelate. *Phys. Rev. Lett.* **2016**, *116* (5), 56801.

(180) Atosuo, E.; Mä Ntymä Ki, M.; Mizohata, K.; Heikkilä, M. J.; Rä Isä Nen, J.; Ritala, M.; Leskelä, M. Preparation of Lithium Containing Oxides by the Solid State Reaction of Atomic Layer Deposited Thin Films. *Chem. Mater.* **2017**, *29*, 998–1005.

(181) Park, K.; Kim, Y.; Song, J.-G.; Jin Kim, S.; Wan Lee, C.; Hee Ryu, G.; Lee, Z.; Park, J.; Kim, H. Uniform, Large-Area Self-Limiting Layer Synthesis of Tungsten Diselenide. *2D Mater.* **2016**, *3* (1), 14004.

(182) Nanayakkara, C. E.; Vega, A.; Liu, G.; Dezelah, C. L.; Kanjolia, R. K.; Chabal, Y. J. Role of Initial Precursor Chemisorption on Incubation Delay for Molybdenum Oxide Atomic Layer Deposition. *Chem. Mater.* **2016**, *28* (23), 8591–8597.

(183) Wu, C.-R.; Chang, X.-R.; Chu, T.-W.; Chen, H.-A.; Wu, C.-H.; Lin, S.-Y. Establishment of 2D Crystal Heterostructures by Sulfurization of Sequential Transition Metal Depositions: Preparation, Characterization, and Selective Growth. *Nano Lett.* **2016**, *16* (11), 7093–7097.

(184) Xia, C.; Li, P.; Li, J.; Jiang, Q.; Zhang, X.; Alshareef, H. N. General Top-Down Ion Exchange Process for the Growth of Epitaxial Chalcogenide Thin Films and Devices. *Chem. Mater.* **2017**, *29* (2), 690–698.

(185) Jawaid, A.; Che, J.; Drummy, L. F.; Bultman, J.; Waite, A.; Hsiao, M.-S.; Vaia, R. A. Redox Exfoliation of Layered Transition Metal Dichalcogenides. *ACS Nano* **2017**, *11* (1), 635–646.

(186) Sun, D.; Schaak, R. E. Solution-Mediated Growth of Two-Dimensional SnSe@GeSe Nanosheet Heterostructures. *Chem. Mater.* **2017**, *29* (2), 817–822.

(187) Cheng, Z.; Wang, F.; Shifa, T. A.; Liu, K.; Huang, Y.; Liu, Q.; Jiang, C.; He, J. Carbon Dots Decorated Vertical SnS_2 Nanosheets for Efficient Photocatalytic Oxygen Evolution. *Appl. Phys. Lett.* **2016**, *109* (5), 53905.

(188) Manna, K.; Huang, H.-N.; Li, W.-T.; Ho, Y.-H.; Chiang, W.-H. Toward Understanding the Efficient Exfoliation of Layered Materials by Water-Assisted Cosolvent Liquid-Phase Exfoliation. *Chem. Mater.* **2016**, *28* (21), 7586–7593.

(189) Chao, D.; Liang, P.; Chen, Z.; Bai, L.; Shen, H.; Liu, X.; Xia, X.; Zhao, Y.; Savilov, S. V.; Lin, J.; et al. Pseudocapacitive Na-Ion Storage Boosts High Rate and Areal Capacity of Self-Branched 2D Layered Metal Chalcogenide Nanoarrays. *ACS Nano* **2016**, *10* (11), 10211–10219.

(190) Leng, K.; Chen, Z.; Zhao, X.; Tang, W.; Tian, B.; Nai, C. T.; Zhou, W.; Loh, K. P. Phase Restructuring in Transition Metal Dichalcogenides for Highly Stable Energy Storage. *ACS Nano* **2016**, *10* (10), 9208–9215.

(191) Jawaid, A.; Nepal, D.; Park, K.; Jespersen, M.; Qualley, A.; Mirau, P.; Drummy, L. F.; Vaia, R. A. Mechanism for Liquid Phase Exfoliation of MoS_2. *Chem. Mater.* **2016**, *28* (1), 337–348.

(192) Coleman, J. N.; Lotya, M.; O'Neill, A.; Bergin, S. D.; King, P. J.; Khan, U.; Young, K.; Gaucher, A.; De, S.; Smith, R. J.; et al. Two-Dimensional Nanosheets Produced by Liquid Exfoliation of Layered Materials. *Science.* **2011**, *331* (6017).

(193) Nicolosi, V.; Chhowalla, M.; Kanatzidis, M. G.; Strano, M. S.; Coleman, J. N. Liquid Exfoliation of Layered Materials. *Science.* **2013**, *340* (6139).

(194) Stöter, M.; Rosenfeldt, S.; Breu, J. Tunable Exfoliation of Synthetic Clays. *Annu. Rev. Mater. Res.* **2015**, *45* (1), 129–151.

(195) Choudalakis, G. a.; Kalo, H.; Breu, J.; Gotsis, A. D. CO_2 Gas Barrier Properties in Polymer Nanocomposite Coatings Containing Li-Hectorite Clays. *J. Appl. Polym. Sci.* **2014**, *131* (18).

(196) Madauß, L.; Ochedowski, O.; Lebius, H.; Ban-d'Etat, B.; Naylor, C. H.; Johnson, A. T. C.; Kotakoski, J.; Schleberger, M. Defect Engineering of Single- and Few-Layer MoS_2 by Swift Heavy Ion Irradiation. *2D Mater.* **2016**, *4* (1), 15034.

(197) Alemayehu, M. B.; Falmbigl, M.; Ta, K.; Ditto, J.; Medlin, D. L.; Johnson, D. C. Designed Synthesis of van Der Waals Heterostructures: The Power of Kinetic Control. *Angew. Chemie Int. Ed.* **2015**, *54*, 15468–15472.

(198) Wood, S. R.; Merrill, D. R.; Mitchson, G.; Lygo, A. C.; Bauers, S. R.; Hamann, D. M.; Sutherland, D. R.; Ditto, J.; Johnson, D. C. Modulation Doping in Metastable Heterostructures via Kinetically Controlled Substitution. *Chem. Mater.* **2017**, *29* (2), 773–779.

(199) Mitchson, G.; Hadland, E.; Göhler, F.; Wanke, M.; Esters, M.; Ditto, J.; Bigwood, E.; Ta, K.; Hennig, R. G.; Seyller, T.; et al. Structural Changes in 2D BiSe Bilayers as *N* Increases in $(BiSe)_{1+\delta}(NbSe_2)_N$(*N*=1–4) Heterostructures. *ACS Nano* **2016**, *10* (10), 9489–9499.

(200) Westover, R. D.; Ditto, J.; Falmbigl, M.; Hay, Z. L.; Johnson, D. C. Synthesis and Characterization of Quaternary Monolayer Thick $MoSe_2$/SnSe/$NbSe_2$/SnSe Heterojunction Superlattices. *Chem. Mater.* **2015**, *27*, 6411–6417.

(201) Bauers, S.; Ditto, J.; Moore, D. B.; Johnson, D. C. Structure-Property Relationships in Non-Epitaxial Chalcogenide Heterostructures: The Role of Interface Density on Charge Exchange. *Nanoscale* **2016**, *8*, 14665–14672.

(202) Shang, S.-L.; Lindwall, G.; Wang, Y.; Redwing, J. M.; Anderson, T.; Liu, Z.-K. Lateral Versus Vertical Growth of Two-Dimensional Layered Transition-Metal Dichalcogenides: Thermodynamic Insight into MoS_2. *Nano Lett.* **2016**, *16* (9), 5742–5750.

(203) Nie, Y.; Liang, C.; Zhang, K.; Zhao, R.; Eichfeld, S. M.; Cha, P.-R.; Colombo, L.; Robinson, J. A.; Wallace, R. M.; Cho, K. First Principles Kinetic Monte Carlo Study on the Growth Patterns of WSe_2 Monolayer. *2D Mater.* **2016**, *3* (2), 25029.

(204) Schön, J. C.; Jansen, M. First Step Towards Planning of Syntheses in Solid-State Chemistry: Determination of Promising Structure Candidates by Global Optimization. *Angew. Chemie Int. Ed. English* **1996**, *35* (12), 1286–1304.

(205) Esters, M.; Johnson, D. C. Targeted Synthesis of Metastable Compounds and Intergrowths: The Moduclated Elemental Reactants Method. In *Crystal Growth: Concepts, Mechanisms, and Applications*; Li, J., Ed.; Nova Publishers: Hauppauge, 2017.

(206) Chason, E.; Mayer, T. M. Thin Film and Surface Characterization by Specular X-Ray Reflectivity. *Crit. Rev. Solid State Mater. Sci.* **1997**, *22* (1), 1–67.

(207) Macke, S.; Radi, A.; Hamann-Borrero, J. E.; Verna, A.; Bluschke, M.; Brück, S.; Goering, E.; Sutarto, R.; He, F.; Cristiani, G.; et al. Element Specific Monolayer Depth Profiling. *Adv. Mater.* **2014**, *26* (38), 6554–6559.

(208) Zhou, Z.; Palatinus, L.; Sun, J.; Kopeček, J.; Palatinus, L.; Djelal, N.; Roussel, P.; Tendeloo, G. Van; Antipov, E. V.; Kato, K.; et al. Structure Determination of Modulated Structures by Powder X-Ray Diffraction and Electron Diffraction. *Inorg. Chem. Front.* **2016**, *3* (11), 1351–1362.

(209) Moore, D. B.; Beekman, M.; Disch, S.; Zschack, P.; Häusler, I.; Neumann, W.; Johnson, D. C. Synthesis, Structure, and Properties of Turbostratically Disordered $(PbSe)_{1.18}(TiSe_2)_2$. *Chem. Mater.* **2013**, *25*, 2404–2409.

(210) Atkins, R.; Disch, S.; Jones, Z.; Haeusler, I.; Grosse, C.; Fischer, S. F.; Neumann, W.; Zschack, P.; Johnson, D. C. Synthesis, Structure and Electrical Properties of a New Tin Vanadium Selenide. *J. Solid State Chem.* **2013**, *202*, 128–133.

(211) Oviedo, J. P.; KC, S.; Lu, N.; Wang, J.; Cho, K.; Wallace, R. M.; Kim, M. J. *In Situ* TEM Characterization of Shear-Stress-Induced Interlayer Sliding in the Cross Section View of Molybdenum Disulfide. *ACS Nano* **2015**, *9* (2), 1543–1551.

(212) Gunning, N. S.; Feser, J.; Beekman, M.; Cahill, D. G.; Johnson, D. C. Synthesis and Thermal Properties of Solid-State Structural Isomers: Ordered Intergrowths of SnSe and $MoSe_2$. *J. Am. Chem. Soc.* **2015**, *137*, 8803–8809.

(213) Zhang, K.; Feng, S.; Wang, J.; Azcatl, A.; Lu, N.; Addou, R.; Wang, N.; Zhou, C.; Lerach, J.; Bojan, V.; et al. Manganese Doping of Monolayer MoS_2 : The Substrate Is Critical. *Nano Lett.* **2015**, *15* (10), 6586–6591.

(214) Merrill, D. R.; Sutherland, D. R.; Ditto, J. J.; Moore, D. B.; Falmbigl, M.; Medlin, D. L.; Johnson, D. C. The Synthesis of $[(PbSe)_{1+\delta}]_m(TiSe_2)_n[(SnSe_2)_{1+\gamma}]_m(TiSe_2)_n$ Heterostructures with Designed Nanoarchitectures by Self Assembly of Amorphous Precursors. *Nanoscale* **2016**, *8*.

(215) Fei, L.; Lei, S.; Zhang, W.-B.; Lu, W.; Lin, Z.; Lam, C. H.; Chai, Y.; Wang, Y.; Guo, Y.; Qiu, H.; et al. Direct TEM Observations of Growth Mechanisms of Two-Dimensional MoS_2 Flakes. *Nat. Commun.* **2016**, *7*, 12206.

(216) Li, F.; Zhang, Q.; Tang, C.; Liu, C.; Shi, J.; Nie, C.; Zhou, G.; Li, Z.; Zhang, W.; Song, C.-L.; et al. Atomically Resolved FeSe/$SrTiO_3$ (001) Interface Structure by Scanning Transmission Electron Microscopy. *2D Mater.* **2016**, *3* (2), 24002.

(217) Liu, H. J.; Jiao, L.; Xie, L.; Yang, F.; Chen, J. L.; Ho, W. K.; Gao, C. L.; Jia, J. F.; Cui, X. D.; Xie, M. H. Molecular-Beam Epitaxy of Monolayer and Bilayer WSe_2 : A Scanning Tunneling Microscopy/spectroscopy Study and Deduction of Exciton Binding Energy. *2D Mater.* **2015**, *2* (3), 34004.

(218) Liu, H.; Jiao, L.; Yang, F.; Cai, Y.; Wu, X.; Ho, W.; Gao, C.; Jia, J.; Wang, N.; Fan, H.; et al. Dense Network of One-Dimensional Midgap Metallic Modes in Monolayer $MoSe_2$ and Their Spatial Undulations. *Phys. Rev. Lett.* **2014**, *113* (6), 66105.

(219) Park, J. H.; Vishwanath, S.; Liu, X.; Zhou, H.; Eichfeld, S. M.; Fullerton-Shirey, S. K.; Robinson, J. A.; Feenstra, R. M.; Furdyna, J.; Jena, D.; et al. Scanning Tunneling Microscopy and Spectroscopy of Air Exposure Effects on Molecular Beam Epitaxy Grown WSe_2 Monolayers and Bilayers. *ACS Nano* **2016**, *10* (4), 4258–4267.

(220) Hill, H. M.; Rigosi, A. F.; Rim, K. T.; Flynn, G. W.; Heinz, T. F. Band Alignment in MoS_2/WS_2 Transition Metal Dichalcogenide Heterostructures Probed by Scanning Tunneling Microscopy and Spectroscopy. *Nano Lett.* **2016**, *16* (8), 4831–4837.

(221) Jespersen, M. L.; Inman, C. E.; Kearns, G. J.; Foster, E. W.; Hutchison, J. E. Alkanephosphonates on Hafnium-Modified Gold: A New Class of Self-Assembled Organic Monolayers. *J. Am. Chem. Soc.* **2007**, *129* (10), 2803–2807.

(222) Ren, X.; Singh, A. K.; Fang, L.; Kanatzidis, M. G.; Tavazza, F.; Davydov, A. V.; Lauhon, L. J. Atom Probe Tomography Analysis of Ag Doping in 2D Layered Material $(PbSe)_5(Bi_2Se_3)_3$. *Nano Lett.* **2016**, *16* (10), 6064–6069.

(223) O'Brien, M.; McEvoy, N.; Motta, C.; Zheng, J.-Y.; Berner, N. C.; Kotakoski, J.; Elibol, K.; Pennycook, T. J.; Meyer, J. C.; Yim, C.; et al. Raman Characterization of Platinum Diselenide Thin Films. *2D Mater.* **2016**, *3* (2), 21004.

(224) Grzeszczyk, M.; Gołasa, K.; Zinkiewicz, M.; Nogajewski, K.; Molas, M. R.; Potemski, M.; Wysmołek, A.; Babiński, A. Raman Scattering of Few-Layers $MoTe_2$. *2D Mater.* **2016**, *3* (2), 25010.

(225) Shi, W.; Lin, M.-L.; Tan, Q.-H.; Qiao, X.-F.; Zhang, J.; Tan, P.-H. Raman and Photoluminescence Spectra of Two-Dimensional Nanocrystallites of Monolayer WS_2 and WSe_2. *2D Mater.* **2016**, *3* (2), 25016.

(226) Wang, X.; Du, K.; Fredrik Liu, Y. Y.; Hu, P.; Zhang, J.; Zhang, Q.; Owen, M. H. S.; Lu, X.; Gan, C. K.; Sengupta, P.; et al. Raman Spectroscopy of Atomically Thin Two-Dimensional Magnetic Iron Phosphorus Trisulfide ($FePS_3$) Crystals. *2D Mater.* **2016**, *3* (3), 31009.

(227) Kim, J.-S.; Moran, S. T.; Nayak, A. P.; Pedahzur, S.; Ruiz, I.; Ponce, G.; Rodriguez, D.; Henny, J.; Liu, J.; Lin, J.-F.; et al. High Pressure Raman Study of Layered $Mo_{0.5}W_{0.5}S_2$ Ternary Compound. *2D Mater.* **2016**, *3* (2), 25003.

(228) Kim, K.; Lee, J.-U.; Nam, D.; Cheong, H. Davydov Splitting and Excitonic Resonance Effects in Raman Spectra of Few-Layer $MoSe_2$. *ACS Nano* **2016**, *10* (8), 8113–8120.

(229) Saito, R.; Tatsumi, Y.; Huang, S.; Ling, X.; Dresselhaus, M. S. Raman Spectroscopy of Transition Metal Dichalcogenides. *J. Phys. Condens. Matter* **2016**, *28* (35), 353002.

(230) Terrones, H.; Corro, E. Del; Feng, S.; Poumirol, J. M.; Rhodes, D.; Smirnov, D.; Pradhan, N. R.; Lin, Z.; Nguyen, M. A. T.; Elías, A. L.; et al. New First Order Raman-Active Modes in Few Layered Transition Metal Dichalcogenides. *Sci. Rep.* **2015**, *4* (1), 4215.

(231) Huang, S.; Liang, L.; Ling, X.; Puretzky, A. A.; Geohegan, D. B.; Sumpter, B. G.; Kong, J.; Meunier, V.; Dresselhaus, M. S. Low-Frequency Interlayer Raman Modes to Probe Interface of Twisted Bilayer MoS_2. *Nano Lett.* **2016**, *16* (2), 1435–1444.

(232) Zhang, X.; Tan, Q.-H.; Wu, J.-B.; Shi, W.; Tan, P.-H.; Xiong, Q.; Quek, S. Y.; Neto, A. H. C.; Krasheninnikov, A. V.; Suenaga, K.; et al. Review on the Raman Spectroscopy of Different Types of Layered Materials. *Nanoscale* **2016**, *8* (12), 6435–6450.

(233) Puretzky, A. A.; Liang, L.; Li, X.; Xiao, K.; Wang, K.; Mahjouri-Samani, M.; Basile, L.; Idrobo, J. C.; Sumpter, B. G.; Meunier, V.; et al. Low-Frequency Raman Fingerprints of Two-Dimensional Metal Dichalcogenide Layer Stacking Configurations. *ACS Nano* **2015**, *9* (6), 6333–6342.

(234) Kurosawa, K.; Saito, S.; Yamaguchi, Y. Neutron Diffraction Study on $MnPS_3$ and $FePS_3$. *J. Phys. Soc. Japan* **1983**, *52* (11), 3919–3926.

(235) Ouvrard, G.; Brec, R.; Rouxel, J. Structural Determination of Some MPS_3 Layered Phases (M=Mn, Fe, Co, Ni and Cd). *Mater. Res. Bull.* **1985**, *20* (10), 1181–1189.

(236) Brec, R. Review on Structural and Chemical Properties of Transition Metal Phosphorous Trisulfides MPS_3. *Solid State Ionics* **1986**, *22* (1), 3–30.

(237) Wildes, A. R.; Roessli, B.; Lebech, B.; Godfrey, K. W. Spin Waves and the Critical Behaviour of the Magnetization in. *J. Phys. Condens. Matter* **1998**, *10* (28), 6417–6428.

(238) Prouzet, E.; Ouvrard, G.; Brec, R. Structure Determination of $ZnPS_3$. *Mater. Res. Bull.* **1986**, *21* (2), 195–200.

(239) Ouvrard, G.; Fréour, R.; Brec, R.; Rouxel, J. A Mixed Valence Compound in the Two Dimensional MPS_3 Family: $V_{0.78}PS_3$ Structure and Physical Properties. *Mater. Res. Bull.* **1985**, *20* (9), 1053–1062.

(240) Ressouche, E.; Loire, M.; Simonet, V.; Ballou, R.; Stunault, A.; Wildes, A. Magnetoelectric $MnPS_3$ as a Candidate for Ferrotoroidicity. *Phys. Rev. B* **2010**, *82* (10), 100408.

(241) Kurita, N.; Nakao, K. Band Structure of Magnetic Layered Semiconductor $NiPS_3$. *J. Phys. Soc. Japan* **1989**, *58* (1), 232–243.

(242) Rule, K. C.; McIntyre, G. J.; Kennedy, S. J.; Hicks, T. J. Single-Crystal and Powder Neutron Diffraction Experiments on $FePS_3$: Search for the Magnetic Structure. *Phys. Rev. B* **2007**, *76* (13), 134402.

(243) Kurita, N.; Nakao, K. Band Structures and Physical Properties of Magnetic Layered Semiconductors MPS_3. *J. Phys. Soc. Japan* **1989**, *58* (2), 610–621.

(244) Le Flem, G.; Brec, R.; Ouvard, G.; Louisy, A.; Segransan, P. Magnetic Interactions in the Layer Compounds MPX_3 (M = Mn, Fe, Ni; X = S, Se). *J. Phys. Chem. Solids* **1982**, *43* (5), 455–461.

(245) Gutiérrez, H. R.; Perea-López, N.; Elías, A. L.; Berkdemir, A.; Wang, B.; Lv, R.; López-Urías, F.; Crespi, V. H.; Terrones, H.; Terrones, M. Extraordinary Room-Temperature Photoluminescence in Triangular WS_2 Monolayers. *Nano Lett.* **2013**, *13* (8), 3447–3454.

(246) Huang, Y.; Sutter, E.; Sadowski, J. T.; Cotlet, M.; Monti, O. L. A.; Racke, D. A.; Neupane, M. R.; Wickramaratne, D.; Lake, R. K.; Parkinson, B. A.; et al. Tin Disulfide—An Emerging Layered Metal Dichalcogenide Semiconductor: Materials Properties and Device Characteristics. *ACS Nano* **2014**, *8* (10), 10743–10755.

(247) Schlaf, R.; Pettenkofer, C.; Jaegermann, W. Band Lineup of a $SnS_2/SnSe_2/SnS_2$ Semiconductor Quantum Well Structure Prepared by van Der Waals Epitaxy. *J. Appl. Phys.* **1999**, *85* (9), 6550.

(248) Zhang, C.; Gong, C.; Nie, Y.; Min, K.-A.; Liang, C.; Oh, Y. J.; Zhang, H.; Wang, W.; Hong, S.; Colombo, L.; et al. Systematic Study of Electronic Structure and Band Alignment of Monolayer Transition Metal Dichalcogenides in Van Der Waals Heterostructures. *2D Mater.* **2016**, *4* (1), 15026.

(249) Kang, J.; Tongay, S.; Zhou, J.; Li, J.; Wu, J. Band Offsets and Heterostructures of Two-Dimensional Semiconductors. *Appl. Phys. Lett.* **2013**, *102* (1), 12111.

(250) Li, M.-Y.; Shi, Y.; Cheng, C.-C.; Lu, L.-S.; Lin, Y.-C.; Tang, H.-L.; Tsai, M.-L.; Chu, C.-W.; Wei, K.-H.; He, J.-H.; et al. Epitaxial Growth of a Monolayer WSe_2-MoS_2 Lateral P-N Junction with an Atomically Sharp Interface. *Science.* **2015**, *349* (6247), 524–528.

(251) Zhang, C.; Chen, Y.; Huang, J.-K.; Wu, X.; Li, L.-J.; Yao, W.; Tersoff, J.; Shih, C.-K.; Geim, A. K.; Grigorieva, I. V.; et al. Visualizing Band Offsets and Edge States in Bilayer–monolayer Transition Metal Dichalcogenides Lateral Heterojunction. *Nat. Commun.* **2016**, *7*, 10349.

(252) Hong, X.; Kim, J.; Shi, S.-F.; Zhang, Y.; Jin, C.; Sun, Y.; Tongay, S.; Wu, J.; Zhang, Y.; Wang, F. Ultrafast Charge Transfer in Atomically Thin MoS_2/WS_2 Heterostructures. *Nat. Nanotechnol.* **2014**, *9* (9), 682–686.

(253) Yu, Y.; Hu, S.; Su, L.; Huang, L.; Liu, Y.; Jin, Z.; Purezky, A. A.; Geohegan, D. B.; Kim, K. W.; Zhang, Y.; et al. Equally Efficient Interlayer Exciton Relaxation and Improved Absorption in Epitaxial and Nonepitaxial MoS_2/WS_2 Heterostructures. *Nano Lett.* **2015**, *15* (1), 486–491.

(254) Peng, B.; Yu, G.; Liu, X.; Liu, B.; Liang, X.; Bi, L.; Deng, L.; Sum, T. C.; Loh, K. P. Ultrafast Charge Transfer in MoS_2/WSe_2 P–n Heterojunction. *2D Mater.* **2016**, *3* (2), 25020.

(255) Pan, S.; Ceballos, F.; Bellus, M. Z.; Zereshki, P.; Zhao, H. Ultrafast Charge Transfer between $MoTe_2$ and MoS_2 Monolayers. *2D Mater.* **2016**, *4* (1), 15033.

(256) Rivera, P.; Schaibley, J. R.; Jones, A. M.; Ross, J. S.; Wu, S.; Aivazian, G.; Klement, P.; Seyler, K.; Clark, G.; Ghimire, N. J.; et al. Observation of Long-Lived Interlayer Excitons in Monolayer $MoSe_2$–WSe_2 Heterostructures. *Nat. Commun.* **2015**, *6*, 6242.

(257) Wang, H.; Bang, J.; Sun, Y.; Liang, L.; West, D.; Meunier, V.; Zhang, S.; Kudo, A.; Miseki, Y.; Alferov, Z. I.; et al. The Role of Collective Motion in the Ultrafast Charge Transfer in van Der Waals Heterostructures. *Nat. Commun.* **2016**, *7*, 11504.

(258) Li, L.; Long, R.; Prezhdo, O. V. Charge Separation and Recombination in Two Dimensional MoS_2/WS_2: Time-Domain Ab Initio Modelling. *Chem. Mater.* **2016**, acs.chemmater.6b03727.

(259) Amin, B.; Kaloni, T. P.; Schreckenbach, G.; Freund, M. S. Materials Properties of out-of-Plane Heterostructures of MoS_2 -WSe_2 and WS_2 -$MoSe_2$. *Appl. Phys. Lett.* **2016**, *108* (6), 63105.

(260) Cao, L. Two-Dimensional Transition-Metal Dichalcogenide Materials: Toward an Age of Atomic-Scale Photonics. *MRS Bull.* **2015**, *40* (7), 592–599.

(261) Chernikov, A.; Berkelbach, T. C.; Hill, H. M.; Rigosi, A.; Li, Y.; Aslan, O. B.; Reichman, D. R.; Hybertsen, M. S.; Heinz, T. F. Exciton Binding Energy and Nonhydrogenic Rydberg Series in Monolayer WS_2. *Phys. Rev. Lett.* **2014**, *113* (7), 76802.

(262) Rivera, P.; Seyler, K. L.; Yu, H.; Schaibley, J. R.; Yan, J.; Mandrus, D. G.; Yao, W.; Xu, X. Valley-Polarized Exciton Dynamics in a 2D Semiconductor Heterostructure. *Science.* **2016**, *351* (6274).

(263) Lundt, N.; Klembt, S.; Cherotchenko, E.; Betzold, S.; Iff, O.; Nalitov, A. V.; Klaas, M.; Dietrich, C. P.; Kavokin, A. V.; Höfling, S.; et al. Room-Temperature Tamm-Plasmon Exciton-Polaritons with a WSe_2 Monolayer. *Nat. Commun.* **2016**, *7*, 13328.

(264) Ahn, J.; Jeon, P. J.; Raza, S. R. A.; Pezeshki, A.; Min, S.-W.; Hwang, D. K.; Im, S. Transition Metal Dichalcogenide Heterojunction pn Diode toward Ultimate Photovoltaic Benefits. *2D Mater.* **2016**, *3* (4), 45011.

(265) Xu, Z.-Q.; Zhang, Y.; Wang, Z.; Shen, Y.; Huang, W.; Xia, X.; Yu, W.; Xue, Y.; Sun, L.; Zheng, C.; et al. Atomically Thin Lateral p–n Junction Photodetector with Large Effective Detection Area. *2D Mater.* **2016**, *3* (4), 41001.

(266) Zhou, H.; Yu, F.; Sun, J.; Zhu, H.; Mishra, I. K.; Chen, S.; Ren, Z. Highly Efficient Hydrogen Evolution from Edge-Oriented $WS_{2(1-X)}$ Se_{2X} Particles on Three-Dimensional Porous $NiSe_2$ Foam. *Nano Lett.* **2016**, *16* (12), 7604–7609.

(267) Voiry, D.; Fullon, R.; Yang, J.; de Carvalho Castro e Silva, C.; Kappera, R.; Bozkurt, I.; Kaplan, D.; Lagos, M. J.; Batson, P. E.; Gupta, G.; et al. The Role of Electronic Coupling between Substrate and 2D MoS_2 Nanosheets in Electrocatalytic Production of Hydrogen. *Nat. Mater.* **2016**, *15* (9), 1003–1009.

(268) Chen, J.; Zhou, W.; Tang, W.; Tian, B.; Zhao, X.; Xu, H.; Liu, Y.; Geng, D.; Tan, S. J. R.; Fu, W.; et al. Lateral Epitaxy of Atomically Sharp WSe_2/WS_2 Heterojunctions on Silicon Dioxide Substrates. *Chem. Mater.* **2016**, *28* (20), 7194–7197.

(269) Chen, Y.; Dumcenco, D. O.; Zhu, Y.; Zhang, X.; Mao, N.; Feng, Q.; Zhang, M.; Zhang, J.; Tan, P.-H.; Huang, Y.-S.; et al. Composition-Dependent Raman Modes of $Mo_{1-x}W_xS_2$ Monolayer Alloys. *Nanoscale* **2014**, *6* (5), 2833–2839.

(270) Feng, Q.; Mao, N.; Wu, J.; Xu, H.; Wang, C.; Zhang, J.; Xie, L. Growth of $MoS_{2(1-X)}Se_{2X}$ ($X = 0.41–1.00$) Monolayer Alloys with Controlled Morphology by Physical Vapor Deposition. *ACS Nano* **2015**, *9* (7), 7450–7455.

(271) Duerloo, K.-A. N.; Reed, E. J. Structural Phase Transitions by Design in Monolayer Alloys. *ACS Nano* **2016**, *10* (1), 289–297.

(272) Kang, J.; Tongay, S.; Li, J.; Wu, J. Monolayer Semiconducting Transition Metal Dichalcogenide Alloys: Stability and Band Bowing. *J. Appl. Phys.* **2013**, *113* (14), 143703.

(273) Tongay, S.; Narang, D. S.; Kang, J.; Fan, W.; Ko, C.; Luce, A. V.; Wang, K. X.; Suh, J.; Patel, K. D.; Pathak, V. M.; et al. Two-Dimensional Semiconductor Alloys: Monolayer $Mo_{1-x}W_xSe_2$. *Appl. Phys. Lett.* **2014**, *104* (1), 12101.

(274) Karande, S. D.; Kaushik, N.; Narang, D. S.; Late, D.; Lodha, S. Thickness Tunable Transport in Alloyed WSSe Field Effect Transistors. *Appl. Phys. Lett.* **2016**, *109* (14), 142101.

(275) Wilson, J. A.; Di Salvo, F. J.; Mahajan, S. Charge-Density Waves and Superlattices in the Metallic Layered Transition Metal Dichalcogenides. *Adv. Phys.* **1975**, *24* (2), 117–201.

(276) Friend, R. H.; Yoffe, A. D. Electronic Properties of Intercalation Complexes of the Transition Metal Dichalcogenides. *Adv. Phys.* **1987**, *36* (1), 1–94.

(277) Wilson, J. A.; Yoffe, A. D. The Transition Metal Dichalcogenides Discussion and Interpretation of the Observed Optical, Electrical and Structural Properties. *Adv. Phys.* **1969**, *18* (73), 193–335.

(278) Cao, Y.; Mishchenko, A.; Yu, G. L.; Khestanova, E.; Rooney, A. P.; Prestat, E.; Kretinin, A. V.; Blake, P.; Shalom, M. B.; Woods, C.; et al. Quality Heterostructures from Two-Dimensional Crystals Unstable in Air by Their Assembly in Inert Atmosphere. *Nano Lett.* **2015**, *15* (8), 4914–4921.

(279) Tsen, A. W.; Hovden, R.; Wang, D.; Kim, Y. D.; Okamoto, J.; Spoth, K. A.; Liu, Y.; Lu, W.; Sun, Y.; Hone, J. C.; et al. Structure and Control of Charge Density Waves in Two-Dimensional 1T-TaS_2. *Proc. Natl. Acad. Sci. U. S. A.* **2015**, *112* (49), 15054–15059.

(280) Tsen, A. W.; Hunt, B.; Kim, Y. D.; Yuan, Z. J.; Jia, S.; Cava, R. J.; Hone, J.; Kim, P.; Dean, C. R.; Pasupathy, A. N. Nature of the Quantum Metal in a Two-Dimensional Crystalline Superconductor. *Nat. Phys.* **2015**, *12* (3), 208–212.

(281) Alemayehu, M. B.; Falmbigl, M.; Ta, K.; Grosse, C.; Westover, R. D.; Bauers, S. R.; Fischer, S. F.; Johnson, D. C. Structural and Electrical Properties of $([SnSe]_{1+\delta})_m(NbSe_2)_1$ Compounds: Single $NbSe_2$ Layers Separated by Increasing Thickness of SnSe. *Chem. Mater.* **2015**, No. 3, 867–875.

(282) Alemayehu, M. B.; Ta, K.; Falmbigl, M.; Johnson, D. C. Structure, Stability, and Properties of the Intergrowth Compounds $([SnSe]_{1+\delta})_m(NbSe_2)_n$, Where $m = n = 1$–20. *J. Am. Chem. Soc.* **2015**, *137*, 4831–4839.

(283) Wiegers, G. A.; Meetsma, A.; Haange, R. J.; de Boer, J. L. Structure and Physical Properties of $(SnS)_{1.18}NbS_2$, "$SnNbS_3$", a Compound with Misfit Layer Structure. *Mater. Res. Bull.* **1988**, *23* (11), 1551–1559.

(284) Meerschaut, A.; Rabu, P.; Rouxel, J. Preparation and Characterization of New Mixed Sandwiched Layered compounds$Ln_{32}Nb_{28}S_{88}$(Ln =La, Ce). *J. Solid State Chem.* **1989**, *78* (1), 35–45.

(285) Onoda, M.; Saeki, M.; Yamamoto, A.; Kato, K.; IUCr. Structure Refinement of the Incommensurate Composite Crystal $Sr_{1.145}TiS_3$ through the Rietveld Analysis Process. *Acta Crystallogr. Sect. B Struct. Sci.* **1993**, *49* (6), 929–936.

(286) Gotoh, Y.; Goto, M.; Kawaguchi, K.; Oosawa, Y.; Onoda, M. Preparation and Characterization of a New Composite-Layered Sulfide, $(PbS)_{1.12}VS_2$, "$PbVS_3$." *Mater. Res. Bull.* **1990**, *25* (3), 307–314.

(287) Auriel, C.; Roesky, R.; Meerschaut, A.; Rouxel, J. Structure Determination and Electrical Properties of a New Misfit Layered Selenide [$(PbSe)_{1.10}NbSe_2$]. *Mater. Res. Bull.* **1993**, *28* (3), 247–254.

(288) Ohno, Y. Electronic Structure of the Misfit-Layer Compounds $PbTiS_3$ and $SnNbS_3$. *Phys. Rev. B* **1991**, *44* (3), 1281–1291.

(289) Kalläne, M.; Rossnagel, K.; Marczynski-Bühlow, M.; Kipp, L.; Starnberg, H. I.; Stoltz, S. E. Stabilization of the Misfit Layer Compound $(PbS)_{1.13}TaS_2$ by Metal Cross Substitution. *Phys. Rev. Lett.* **2008**, *100* (6), 65502.

(290) Wiegers, G. A.; Meerschaut, A. Structures of Misfit Layer Compounds $(MS)_nTS_2$ (M= Sn, Pb, Bi, Rare Earth Metals; T = Nb, Ta, Ti, V, Cr; $1.08<n<1.23$). *J. Alloys Compd.* **1992**, *178* (1–2), 351–368.

(291) Lin, Q.; Heideman, C. L.; Nguyen, N.; Zschack, P.; Chiritescu, C.; Cahill, D. G.; Johnson, D. C. Designed Synthesis of Families of Misfit-Layered Compounds. *Eur. J. Inorg. Chem.* **2008**, *2008* (15), 2382–2385.

(292) Beekman, M.; Heideman, C. L.; Johnson, D. C. Ferecrystals: Non-Epitaxial Layered Intergrowths. *Semicond. Sci. Technol.* **2014**, *29*, 64012.

(293) Silva-Guillén, J. Á.; Ordejón, P.; Guinea, F.; Canadell, E. Electronic Structure of 2H-$NbSe_2$ Single-Layers in the CDW State. *2D Mater.* **2016**, *3* (3), 35028.

(294) Li, Y.; Duerloo, K.-A. N.; Wauson, K.; Reed, E. J.; Lencer, D.; Wong, H.-S. P.; Wong, H.-S. P.; Zhou, Y.; Ramanathan, S.; Shu, M. J.; et al. Structural Semiconductor-to-Semimetal Phase Transition in Two-Dimensional Materials Induced by Electrostatic Gating. *Nat. Commun.* **2016**, *7*, 10671.

(295) Wang, H.; Qian, X. Two-Dimensional Multiferroics in Monolayer Group IV Monochalcogenides. *2D Mater.* **2017**, *4* (1), 15042.

(296) Fei, R.; Kang, W.; Yang, L. Ferroelectricity and Phase Transitions in Monolayer Group-IV Monochalcogenides. *Phys. Rev. Lett.* **2016**, *117* (9), 97601.

(297) Soares Jr, A. L.; Dos Santos, E. C.; Morales-García, A.; Heine, T.; De Abreu, H. A.; Duarte, H. A. Two-Dimensional Crystal CuS—electronic and Structural Properties. *2D Mater.* **2016**, *4* (1), 15041.

(298) Song, K.; Soriano, D.; Robles, R.; Ordejon, P.; Roche, S. How Disorder Affects Topological Surface States in the Limit of Ultrathin Bi_2Se_3 Films. *2D Mater.* **2016**, *3* (4), 45007.

(299) Liu, J.; Wang, H.; Fang, C.; Fu, L.; Qian, X. Van Der Waals Stacking-Induced Topological Phase Transition in Layered Ternary Transition Metal Chalcogenides. *Nano Lett.* **2017**, *17* (1), 467–475.

(300) Liu, F.; You, L.; Seyler, K. L.; Li, X.; Yu, P.; Lin, J.; Wang, X.; Zhou, J.; Wang, H.; He, H.; et al. Room-Temperature Ferroelectricity in $CuInP_2S_6$ Ultrathin Flakes. *Nat. Commun.* **2016**, *7*, 12357.

(301) Atkins, R.; Wilson, J.; Zschack, P.; Grosse, C.; Neumann, W.; Johnson, D. C. Synthesis of $[(SnSe)_{1.15}]_m((TaSe_2)_n$ Ferecrystals: Structurally Tunable Metallic Compounds. *Chem. Mater.* **2012**, *24*, 4594–4599.

(302) Atkins, R.; Dolgos, M.; Fiedler, A.; Grosse, C.; Fischer, S. F.; Rudin, S. P.; Johnson, D. C. Synthesis and Systematic Trends in Structure and Electrical Properties of $[(SnSe)_{1.15}]_M(VSe_2)_1$, M = 1, 2, 3, and 4. *Chem. Mater.* **2014**, *26*, 2862–2872.

(303) Zhao, S.; Hotta, T.; Koretsune, T.; Watanabe, K.; Taniguchi, T.; Sugawara, K.; Takahashi, T.; Shinohara, H.; Kitaura, R. Two-Dimensional Metallic NbS_2 : Growth, Optical Identification and Transport Properties. *2D Mater.* **2016**, *3* (2), 25027.

(304) Alemayehu, M. B.; Ta, K.; Falmbigl, M.; Johnson, D. C.; Grosse, C.; Fischer, S. F.; Neumann, W.; Zschack, P.; Johnson, D. C. Charge Transfer vs. Dimensionality: What Affects the Transport Properties of Ferecrystals? *Nanoscale* **2015**, *7* (16), 7378–7385.

(305) Grosse, C.; Alemayehu, M. B.; Falmbigl, M.; Mogilatenko, A.; Chiatti, O.; Johnson, D. C.; Fischer, S. F. Superconducting Ferecrystals: Turbostratically Disordered Atomic-Scale Layered $(PbSe)_{1.14}(NbSe_2)_n$ Thin Films. *Sci. Rep.* **2016**, *6* (1), 33457.

(306) Goli, P.; Khan, J.; Wickramaratne, D.; Lake, R. K.; Balandin, A. A. Charge Density Waves in Exfoliated Films of van Der Waals Materials: Evolution of Raman Spectrum in $TiSe_2$. *Nano Lett.* **2012**, *12* (11), 5941–5945.

(307) Yang, J.; Wang, W.; Liu, Y.; Du, H.; Ning, W.; Zheng, G.; Jin, C.; Han, Y.; Wang, N.; Yang, Z.; et al. Thickness Dependence of the Charge-Density-Wave Transition Temperature in VSe_2. *Appl. Phys. Lett.* **2014**, *105* (6), 63109.

(308) Sugawara, K.; Nakata, Y.; Shimizu, R.; Han, P.; Hitosugi, T.; Sato, T.; Takahashi, T. Unconventional Charge-Density-Wave Transition in Monolayer 1*T*-$TiSe_2$. *ACS Nano* **2016**, *10* (1), 1341–1345.

(309) He, R.; van Baren, J.; Yan, J.-A.; Xi, X.; Ye, Z.; Ye, G.; Lu, I.-H.; Leong, S. M.; Lui, C. H. Interlayer Breathing and Shear Modes in $NbSe_2$ Atomic Layers. *2D Mater.* **2016**, *3* (3), 31008.

(310) Hajiyev, P.; Cong, C.; Qiu, C.; Yu, T.; Lau, C. N. Contrast and Raman Spectroscopy Study of Single- and Few-Layered Charge Density Wave Material: 2*H*-$TaSe_2$. *Sci. Rep.* **2013**, *3*, 104101.

(311) Ogawa, N.; Miyano, K. Charge-Density Wave as an Electro-Optical Switch and Memory. *Appl. Phys. Lett.* **2002**, *80* (17), 3225–3227.

(312) Khan, J.; Nolen, C. M.; Teweldebrhan, D.; Wickramaratne, D.; Lake, R. K.; Balandin, A. A. Anomalous Electron Transport in Back-Gated Field-Effect Transistors with $TiTe_2$ Semimetal Thin-Film Channels. *Appl. Phys. Lett.* **2012**, *100* (4), 43109.

(313) Neal, A. T.; Du, Y.; Liu, H.; Ye, P. D. Two-Dimensional $TaSe_2$ Metallic Crystals: Spin–Orbit Scattering Length and Breakdown Current Density. *ACS Nano* **2014**, *8* (9), 9137–9142.

(314) Hollander, M. J.; Liu, Y.; Lu, W.-J.; Li, L.-J.; Sun, Y.-P.; Robinson, J. A.; Datta, S. Electrically Driven Reversible Insulator–Metal Phase Transition in 1*T*-TaS_2. *Nano Lett.* **2015**, *15* (3), 1861–1866.

(315) Ugeda, M. M.; Bradley, A. J.; Zhang, Y.; Onishi, S.; Chen, Y.; Ruan, W.; Ojeda-Aristizabal, C.; Ryu, H.; Edmonds, M. T.; Tsai, H.-Z.; et al. Characterization of Collective Ground States in Single-Layer $NbSe_2$. *Nat. Phys.* **2015**, *12* (1), 92–97.

(316) Bayard, M.; Sienko, M. J. Anomalous Electrical and Magnetic Properties of Vanadium Diselenide. *J. Solid State Chem.* **1976**, *19* (4), 325–329.

(317) Xu, K.; Chen, P.; Li, X.; Wu, C.; Guo, Y.; Zhao, J.; Wu, X.; Xie, Y. Ultrathin Nanosheets of Vanadium Diselenide: A Metallic Two-Dimensional Material with Ferromagnetic Charge-Density-Wave Behavior. *Angew. Chemie Int. Ed.* **2013**, *52* (40), 10477–10481.

(318) Falmbigl, M.; Fiedler, A.; Atkins, R. E.; Fischer, S. F.; Johnson, D. C. Suppressing a Charge Density Wave by Changing Dimensionality in the Ferecrystalline Compounds $([SnSe]_{1.15})_1(VSe_2)_N$ with N = 1, 2, 3, 4. *Nano Lett.* **2015**, *15*, 943–948.

(319) Li, L. J.; Zhao, W. J.; Liu, B.; Ren, T. H.; Eda, G.; Loh, K. P. Enhancing Charge-Density-Wave Order in 1*T*-$TiSe_2$ Nanosheet by Encapsulation with Hexagonal Boron Nitride. *Appl. Phys. Lett.* **2016**, *109* (14), 141902.

(320) Xi, X.; Wang, Z.; Zhao, W.; Park, J.-H.; Law, K. T.; Berger, H.; Forró, L.; Shan, J.; Mak, K. F. Ising Pairing in Superconducting $NbSe_2$ Atomic Layers. *Nat. Phys.* **2015**, *12* (2), 139–143.

(321) Navarro-Moratalla, E.; Island, J. O.; Mañas-Valero, S.; Pinilla-Cienfuegos, E.; Castellanos-Gomez, A.; Quereda, J.; Rubio-Bollinger, G.; Chirolli, L.; Silva-Guillén, J. A.; Agraït, N.; et al. Enhanced Superconductivity in Atomically Thin TaS_2. *Nat. Commun.* **2016**, *7*, 11043.

(322) Saito, Y.; Nakamura, Y.; Bahramy, M. S.; Kohama, Y.; Ye, J.; Kasahara, Y.; Nakagawa, Y.; Onga, M.; Tokunaga, M.; Nojima, T.; et al. Superconductivity Protected by Spin–valley Locking in Ion-Gated MoS_2. *Nat. Phys.* **2015**, *12* (2), 144–149.

(323) Staley, N. E.; Wu, J.; Eklund, P.; Liu, Y.; Li, L.; Xu, Z. Electric Field Effect on Superconductivity in Atomically Thin Flakes of $NbSe_2$. *Phys. Rev. B* **2009**, *80* (18), 184505.

(324) Alemayehu, M. B.; Falmbigl, M.; Ta, K.; Johnson, D. C. Effect of Local Structure of NbSe2 on the Transport Properties of $[(SnSe)_{1.16}]_1[(NbSe_2)]_n$ Ferecrystals. *Chem. Mater.* **2015**, *27*, 2158–2164.

(325) Alemayehu, M. B.; Mitchson, G.; Ditto, J.; Hanken, B. E.; Asta, M.; Johnson, D. C. Charge Transfer between PbSe and $NbSe_2$ in $[(PbSe)_{1.14}]_M(NbSe_2)_1$ Ferecrystalline Compounds. *Chem. Mater.* **2014**, *26* (5), 1859–1866.

(326) Hänke, T.; Singh, U. R.; Cornils, L.; Manna, S.; Kamlapure, A.; Bremholm, M.; Hedegaard, E. M. J.; Iversen, B. B.; Hofmann, P.; Hu, J.; et al. Reorientation of the Diagonal Double-Stripe Spin Structure at $Fe_{1+y}Te$ Bulk and Thin-Film Surfaces. *Nat. Commun.* **2017**, *8*, 13939.

(327) Tian, Y. C.; Zhang, W. H.; Li, F. S.; Wu, Y. L.; Wu, Q.; Sun, F.; Zhou, G. Y.; Wang, L.; Ma, X.; Xue, Q.-K.; et al. Ultrafast Dynamics Evidence of High Temperature Superconductivity in Single Unit Cell FeSe on $SrTiO_3$. *Phys. Rev. Lett.* **2016**, *116* (10), 107001.

(328) Zhang, Y.; Lee, J. J.; Moore, R. G.; Li, W.; Yi, M.; Hashimoto, M.; Lu, D. H.; Devereaux, T. P.; Lee, D.-H.; Shen, Z.-X. Superconducting Gap Anisotropy in Monolayer FeSe Thin Film. *Phys. Rev. Lett.* **2016**, *117* (11), 117001.

(329) Lei, B.; Cui, J. H.; Xiang, Z. J.; Shang, C.; Wang, N. Z.; Ye, G. J.; Luo, X. G.; Wu, T.; Sun, Z.; Chen, X. H. Evolution of High-Temperature Superconductivity from a Low-Tc Phase Tuned by Carrier Concentration in FeSe Thin Flakes. *Phys. Rev. Lett.* **2016**, *116* (7), 77002.

(330) Huang, Z. C.; Pu, Y. J.; Xu, H. C.; Xu, D. F.; Song, Q.; Lou, X.; Wen, C. H. P.; Peng, R.; Feng, D. L. Electronic Structure and Superconductivity of Single-Layer FeSe on Nb:$SrTiO_3$/$LaAlO_3$ with Varied Tensile Strain. *2D Mater.* **2016**, *3* (1), 14005.

(331) Zhao, L.; Liang, A.; Yuan, D.; Hu, Y.; Liu, D.; Huang, J.; He, S.; Shen, B.; Xu, Y.; Liu, X.; et al. Common Electronic Origin of Superconductivity in (Li,Fe)OHFeSe Bulk Superconductor and Single-Layer FeSe/$SrTiO_3$ Films. *Nat. Commun.* **2016**, *7*, 10608.

(332) Wang, Z. F.; Zhang, H.; Liu, D.; Liu, C.; Tang, C.; Song, C.; Zhong, Y.; Peng, J.; Li, F.; Nie, C.; et al. Topological Edge States in a High-Temperature Superconductor FeSe/$SrTiO_3$(001) Film. *Nat. Mater.* **2016**, *15* (9), 968–973.

(333) Manna, S.; Kamlapure, A.; Cornils, L.; Hänke, T.; Hedegaard, E. M. J.; Bremholm, M.; Iversen, B. B.; Hofmann, P.; Wiebe, J.; Wiesendanger, R.; et al. Interfacial Superconductivity in a Bi-Collinear Antiferromagnetically Ordered FeTe Monolayer on a Topological Insulator. *Nat. Commun.* **2017**, *8*, 14074.

(334) Zhu, X.; Guo, Y.; Cheng, H.; Dai, J.; An, X.; Zhao, J.; Tian, K.; Wei, S.; Cheng Zeng, X.; Wu, C.; et al. Signature of Coexistence of Superconductivity and Ferromagnetism in Two-Dimensional $NbSe_2$ Triggered by Surface Molecular Adsorption. *Nat. Commun.* **2016**, *7*, 11210.

(335) Chiritescu, C.; Cahill, D. G.; Nguyen, N.; Johnson, D.; Bodapati, A.; Keblinski, P.; Zschack, P. Ultralow Thermal Conductivity in Disordered, Layered WSe2 Crystals. *Science.* **2007**, *315* (5810), 351–353.

(336) Chiritescu, C.; Cahill, D. G.; Heideman, C.; Lin, Q.; Mortensen, C.; Nguyen, N. T.; Johnson, D.; Rostek, R.; Böttner, H. Low Thermal Conductivity in Nanoscale Layered Materials Synthesized by the Method of Modulated Elemental Reactants. *J. Appl. Phys.* **2008**, *104* (3), 33533.

(337) Chiritescu, C.; Mortensen, C.; Cahill, D. G.; Johnson, D.; Zschack, P. Lower Limit to the Lattice Thermal Conductivity of Nanostructured Bi_2Te_3-Based Materials. *J. Appl. Phys.* **2009**, *106* (7), 73503.

(338) Nguyen, N. T.; Berseth, P. A.; Lin, Q.; Chiritescu, C.; Cahill, D. G.; Mavrokefalos, A.; Shi, L.; Zschack, P.; Anderson, M. D.; Anderson, I. M.; et al. Synthesis and Properties of Turbostratically Disordered, Ultrathin WSe_2 Films. *Chem. Mater.* **2010**, *22* (9), 2750–2756.

(339) Wan, C.; Wang, Y.; Norimatsu, W.; Kusunoki, M.; Koumoto, K. Nanoscale Stacking Faults Induced Low Thermal Conductivity in Thermoelectric Layered Metal Sulfides. *Appl. Phys. Lett.* **2012**, *100* (10), 101913.

(340) Mavrokefalos, A.; Lin, Q.; Beekman, M.; Seol, J. H.; Lee, Y. J.; Kong, H.; Pettes, M. T.; Johnson, D. C.; Shi, L. In-Plane Thermal and Thermoelectric Properties of Misfit-Layered $[(PbSe)_{0.99}]_x(WSe_2)_x$ Superlattice Thin Films. *Appl. Phys. Lett.* **2010**, *96* (18), 181908.

(341) Ma, J.; Chen, Y.; Han, Z.; Li, W. Strong Anisotropic Thermal Conductivity of Monolayer WTe_2. *2D Mater.* **2016**, *3* (4), 45010.

(342) Bhatt, R.; Basu, R.; Bhattacharya, S.; Singh, A.; Aswal, D. K.; Gupta, S. K.; Okram, G. S.; Ganesan, V.; Venkateshwarlu, D.; Surgers, C.; et al. Low Temperature Thermoelectric Properties of Cu Intercalated $TiSe_2$: A Charge Density Wave Material. *Appl. Phys. A* **2013**, *111* (2), 465–470.

(343) Cho, J.; Losego, M. D.; Zhang, H. G.; Kim, H.; Zuo, J.; Petrov, I.; Cahill, D. G.; Braun, P. V. Electrochemically Tunable Thermal Conductivity of Lithium Cobalt Oxide. *Nat. Commun.* **2014**, *5*, 862–868.

(344) Li, G.; Ding, G.; Gao, G. Thermoelectric Properties of $SnSe_2$ Monolayer. *J. Phys. Condens. Matter* **2017**, *29* (1), 15001.

(345) Ding, G.; Gao, G. Y.; Huang, Z.; Zhang, W.; Yao, K. Thermoelectric Properties of Monolayer MSe_2 (M = Zr, Hf): Low Lattice Thermal Conductivity and a Promising Figure of Merit. *Nanotechnology* **2016**, *27* (37), 375703.

(346) Yin, C.; Hu, Q.; Wang, G.; Huang, T.; Zhou, X.; Zhang, X.; Dou, Y.; Kang, B.; Tang, J.; Liu, N.; et al. Intriguing Substitution of Conducting Layer Triggered Enhancement of Thermoelectric Performance in Misfit-Layered $(SnS)_{1.2}(TiS_2)_2$. *Appl. Phys. Lett.* **2017**, *110* (4), 43507.

(347) Wan, C.; Wang, Y.; Wang, N.; Norimatsu, W.; Kusunoki, M.; Koumoto, K. Intercalation: Building a Natural Superlattice for Better Thermoelectric Performance in Layered Chalcogenides. *J. Electron. Mater.* **2011**, *40* (5), 1271–1280.

(348) Merrill, D.; Moore, D.; Bauers, S.; Falmbigl, M.; Johnson, D. Misfit Layer Compounds and Ferecrystals: Model Systems for Thermoelectric Nanocomposites. *Materials (Basel).* **2015**, *8* (4), 2000–2029.

(349) Mashhadi, S.; Duong, D. L.; Burghard, M.; Kern, K. Efficient Photothermoelectric Conversion in Lateral Topological Insulator Heterojunctions. *Nano Lett.* **2017**, *17* (1), 214–219.

(350) Das, P. K.; Di Sante, D.; Vobornik, I.; Fujii, J.; Okuda, T.; Bruyer, E.; Gyenis, A.; Feldman, B. E.; Tao, J.; Ciancio, R.; et al. Layer-Dependent Quantum Cooperation of Electron and Hole States in the Anomalous Semimetal WTe2. *Nat. Commun.* **2016**, *7*, 10847.

(351) Chang, T.-R.; Xu, S.-Y.; Chang, G.; Lee, C.-C.; Huang, S.-M.; Wang, B.; Bian, G.; Zheng, H.; Sanchez, D. S.; Belopolski, I.; et al. Prediction of an Arc-Tunable Weyl Fermion Metallic State in $Mo_xW_{1-x}Te_2$. *Nat. Commun.* **2016**, *7*, 10639.

(352) Wang, Z.; Gresch, D.; Soluyanov, A. A.; Xie, W.; Kushwaha, S.; Dai, X.; Troyer, M.; Cava, R. J.; Bernevig, B. A. $MoTe_2$: A Type-II Weyl Topological Metal. *Phys. Rev. Lett.* **2016**, *117* (5), 56805.

(353) Sankar, R.; Narsinga Rao, G.; Muthuselvam, I. P.; Butler, C.; Kumar, N.; Senthil Murugan, G.; Shekhar, C.; Chang, T.-R.; Wen, C.-Y.; Chen, C.-W.; et al. Polymorphic Layered $MoTe_2$ from Semiconductor, Topological Insulator, to Weyl Semimetal. *Chem. Mater.* **2017**, *29* (2), 699–707.

(354) Zeugner, A.; Kaiser, M.; Schmidt, P.; Menshchikova, T. V.; Rusinov, I. P.; Markelov, A. V.; Van den Broek, W.; Chulkov, E. V.; Doert, T.; Ruck, M.; et al. Modular Design with 2D Topological-Insulator Building Blocks: Optimized Synthesis and Crystal Growth, Crystal and Electronic Structures of Bi_xTeI (X = 2, 3). *Chem. Mater.* **2017**, acs.chemmater.6b05038.

(355) Dai, J.; West, D.; Wang, X.; Wang, Y.; Kwok, D.; Cheong, S.-W.; Zhang, S. B.; Wu, W. Toward the Intrinsic Limit of the Topological Insulator Bi 2 Se 3. *Phys. Rev. Lett.* **2016**, *117* (10), 106401.

(356) Takane, D.; Souma, S.; Sato, T.; Takahashi, T.; Segawa, K.; Ando, Y. Work Function of Bulk-Insulating Topological Insulator $Bi_{2-X}Sb_XTe_{3-Y}Se_Y$. *Appl. Phys. Lett.* **2016**, *109* (9), 91601.

(357) Yan, H.; Vajner, C.; Kuhlman, M.; Guo, L.; Li, L.; Araujo, P. T.; Wang, H.-T. Elastic Behavior of Bi_2Se_3 2D Nanosheets Grown by van Der Waals Epitaxy. *Appl. Phys. Lett.* **2016**, *109* (3), 32103.

(358) Whitney, W. S.; Brar, V. W.; Ou, Y.; Shao, Y.; Davoyan, A. R.; Basov, D. N.; He, K.; Xue, Q.-K.; Atwater, H. A. Gate-Variable Mid-Infrared Optical Transitions in a $(Bi_{1-X}Sb_X)_2$ Te 3 Topological Insulator. *Nano Lett.* **2017**, *17* (1), 255–260.

(359) Kim, J.; Jhi, S.-H.; Wu, R. Engineering Topological Surface States of Cr-Doped Bi_2Se_3 Films by Spin Reorientation and Electric Field. *Nano Lett.* **2016**, *16* (10), 6656–6660.

(360) Salehi, M.; Shapourian, H.; Koirala, N.; Brahlek, M. J.; Moon, J.; Oh, S. Finite-Size and Composition-Driven Topological Phase Transition in $(Bi_{1-X}In_X)_2Se_3$ Thin Films. *Nano Lett.* **2016**, *16* (9), 5528–5532.

(361) Krieg, J.; Chen, C.; Avila, J.; Zhang, Z.; Sigle, W.; Zhang, H.; Trautmann, C.; Asensio, M. C.; Toimil-Molares, M. E. Exploring the Electronic Structure and Chemical Homogeneity of Individual Bi_2Te_3 Nanowires by Nano-Angle-Resolved Photoemission Spectroscopy. *Nano Lett.* **2016**, *16* (7), 4001–4007.

(362) Huang, W.-K.; Zhang, K.-W.; Yang, C.-L.; Ding, H.; Wan, X.; Li, S.-C.; Evans, J. W.; Han, Y. Tailoring Kinetics on a Topological Insulator Surface by Defect-Induced Strain: Pb Mobility on Bi_2Te_3. *Nano Lett.* **2016**, *16* (7), 4454–4461.

(363) Caputo, M.; Panighel, M.; Lisi, S.; Khalil, L.; Santo, G. Di; Papalazarou, E.; Hruban, A.; Konczykowski, M.; Krusin-Elbaum, L.; Aliev, Z. S.; et al. Manipulating the Topological Interface by Molecular Adsorbates: Adsorption of Co-Phthalocyanine on Bi_2Se_3. *Nano Lett.* **2016**, *16* (6), 3409–3414.

(364) Buchenau, S.; Sergelius, P.; Wiegand, C.; Bäß ler, S.; Zierold, R.; Shin, H. S.; Rübhausen, M.; Gooth, J.; Nielsch, K. Symmetry Breaking of the Surface Mediated Quantum Hall Effect in Bi_2Se_3 Nanoplates Using Fe_3O_4 Substrates. *2D Mater.* **2017**, *4* (1), 15044.

(365) Vajner, C.; Yan, H.; Guo, L.; Mathews, M.; Kuhlman, M.; Benefield, S.; Ulrich, S.; Zolghadr, E.; Kung, P.; Li, L.; et al. Thickness Identification of Epitaxial Bi_2Te_3 via Optical Contrast. *2D Mater.* **2016**, *3* (2), 21010.

(366) Park, J. Y.; Lee, G.-H.; Jo, J.; Cheng, A. K.; Yoon, H.; Watanabe, K.; Taniguchi, T.; Kim, M.; Kim, P.; Yi, G.-C. Molecular Beam Epitaxial Growth and Electronic Transport Properties of High Quality Topological Insulator Bi_2Se_3 Thin Films on Hexagonal Boron Nitride. *2D Mater.* **2016**, *3* (3), 35029.

(367) Tu, N. H.; Tanabe, Y.; Satake, Y.; Huynh, K. K.; Tanigaki, K.; Fu, L.; Kane, C. L.; Mele, E. J.; Chen, Y. L.; Hsieh, D.; et al. In-Plane Topological P-N Junction in the Three-Dimensional Topological Insulator $Bi_{2-x}Sb_xTe_{3-y}Se_y$. *Nat. Commun.* **2016**, *7*, 13763.

(368) Parra, C.; Rodrigues da Cunha, T. H.; Contryman, A. W.; Kong, D.; Montero-Silva, F.; Rezende Gonçalves, P. H.; Dos Reis, D. D.; Giraldo-Gallo, P.; Segura, R.; Olivares, F.; et al. Phase Separation of Dirac Electrons in Topological Insulators at the Spatial Limit. *Nano Lett.* **2017**, *17* (1), 97–103.

(369) Sánchez-Barriga, J.; Varykhalov, A.; Springholz, G.; Steiner, H.; Kirchschlager, R.; Bauer, G.; Caha, O.; Schierle, E.; Weschke, E.; Ünal, A. A.; et al. Nonmagnetic Band Gap at the Dirac Point of the Magnetic Topological Insulator $(Bi_{1-x}Mn_x)_2Se_3$. *Nat. Commun.* **2016**, *7*, 10559.

(370) He, Q. L.; Kou, X.; Grutter, A. J.; Yin, G.; Pan, L.; Che, X.; Liu, Y.; Nie, T.; Zhang, B.; Disseler, S. M.; et al. Tailoring Exchange Couplings in Magnetic Topological-Insulator/antiferromagnet Heterostructures. *Nat. Mater.* **2016**, *16* (1), 94–100.

CHAPTER II

(1) Noh, M.; Thiel, J.; Johnson, D. C. *Adv. Mater.* **1996**, *8* (7), 596–599.

(2) Myungkeun Noh; Christopher D. Johnson; Marc D. Hornbostel; James Thiel, and; Johnson*, D. C. **1996**.

(3) Fister, L.; Johnson, D. C. *J. Am. Chem. Soc.* **1992**, *114* (12), 4639–4644.

(4) Beekman, M.; Heideman, C. L.; Johnson, D. C. *Semicond. Sci. Technol.* **2014**, *29* (6), 64012.

(5) Fister, L.; Li, X.; McConnell, J.; Novet, T.; Johnson, D. C. *J. Vac. Sci. Technol. A Vacuum, Surfaces, Film.* **1993**, *11* (6), 3014–3019.

(6) Anderson, M. Novel Misfit Layer Systems: Synthesis and Characterization, University of Oregon, 2012.

(7) Mitchson, G. Insights from Scanning Transmission Electron Microscopy and X-ray Diffraction into the Structure and Composition of Non-Crystalline Thin Solid Films, University of Oregon, 2017.

(8) Ditto, J. Characterization of the Local Structure and Composition of Low Dimensional Heterostructures and Thin Films, University of Oregon, 2016.

(9) Smeller, M. M.; Heideman, C. L.; Lin, Q.; Beekman, M.; Anderson, M. D.; Zschack, P.; Anderson, I. M.; Johnson, D. C. *Zeitschrift für Anorg. und Allg. Chemie* **2012**, *638* (15), 2632–2639.

(10) Kiessig, H. *Naturissenschaften* **1930**, *18*, 847.

(11) Phung, T. M.; Johnson, D. C.; Antonelli, G. A. *J. Appl. Phys.* **2006**, *100* (6), 64317.

(12) Wainfan, N.; Parratt, L. G. *J. Appl. Phys.* **1960**, *31* (8), 1331–1337.

(13) Tobergte, D. R.; Curtis, S. *J. Chem. Inf. Model.* **2013**, *53* (9), 1689–1699.

CHAPTER III

(1) Novoselov, K. S.; Geim, A. K.; Morozov, S. V; Jiang, D.; Zhang, Y.; Dubonos, S. V; Grigorieva, I. V; Firsov, A. A.; Novoselov, K. S. Electric Field Effect in Atomically Thin Carbon Films. *Science.* **2007**, *306*, 183–191.

(2) Novoselov, K. S. Nobel Lecture: Graphene: Materials in the Flatland. *Rev. Mod. Phys.* **2011**, *83*, 837–849.

(3) Grubišić Čabo, A.; Miwa, J. A.; Grønborg, S. S.; Riley, J. M.; Johannsen, J. C.; Cacho, C.; Alexander, O.; Chapman, R. T.; Springate, E.; Grioni, M.; Lauritsen, J.V.; King, P.D.C.; Hofman, P.; Ulstrup. S. Observation of Ultrafast Free Carrier Dynamics in Single Layer MoS_2. *Nano Lett.* **2015**, *15*, 5883–5887.

(4) Bruix, A.; Miwa, J. A.; Hauptmann, N.; Wegner, D.; Ulstrup, S.; Grønborg, S. S.; Sanders, C. E.; Dendzik, M.; Grubišić Čabo, A.; Bianchi, M.; Lauritsen, J.V.; Khajetoorians, A.A.; Hammer, B.; Hofmann. Single-Layer MoS_2 on Au(111): Band Gap Renormalization and Substrate Interaction. *Phys. Rev. B* **2016**, *93*, 165422-1 - 165422-10.

(5) Geim, A. K. Nobel Lecture: Random Walk to Graphene. *Rev. Mod. Phys.* **2011**, *83*, 851–862.

(6) Hamann, D. M.; Hadland, E. C.; Johnson, D. C. Heterostructures Containing Dichalcogenides-New Materials with Predictable Nanoarchitectures and Novel Emergent Properties. *Semicond. Sci. Technol.* **2017**, *32*, 093004-1 - 093004-27.

(7) Jariwala, D.; Marks, T. J.; Hersam, M. C. Mixed-Dimensional van Der Waals Heterostructures. *Nat. Mater.* **2016**, *16*, 170–181.

(8) Mak, K. F.; Lee, C.; Hone, J.; Shan, J.; Heinz, T. F. Atomically Thin MoS_2: A New Direct-Gap Semiconductor. *Phys. Rev. Lett.* **2010**, *105*, 136805-1 - 136805-4.

(9) Zhao, W.; Ghorannevis, Z.; Chu, L.; Toh, M.; Kloc, C.; Tan, P. H.; Eda, G. Evolution of Electronic Structure in Atomically Thin Sheets of WS_2 and WSe_2. *ACS Nano* **2013**, *7*, 791–797.

(10) Komsa, H. P.; Krasheninnikov, A. V. Electronic Structures and Optical Properties of Realistic Transition Metal Dichalcogenide Heterostructures from First Principles. *Phys. Rev. B* **2013**, *88*, 085318-1 - 085318-7.

(11) Ulstrup, S.; Čabo, A. G.; Miwa, J. A.; Riley, J. M.; Grønborg, S. S.; Johannsen, J. C.; Cacho, C.; Alexander, O.; Chapman, R. T.; Springate, E.; Bianchi, M.; Dendzik, M.; Lauritsen, J.V.; King, P.D.C.; Hofmann, P. Ultrafast Band Structure Control of a Two-Dimensional Heterostructure. *ACS Nano* **2016**, *10*, 6315–6322.

(12) Ugeda, M. M.; Bradley, A. J.; Shi, S. F.; da Jornada, F. H.; Zhang, Y.; Qiu, D. Y.; Ruan, W.; Mo, S. K.; Hussain, Z.; Shen, Z. X.; Wang, F.; Louie, S.G.; Crommie, M.F. Giant Bandgap Renormalization and Excitonic Effects in a Monolayer Transition Metal Dichalcogenide Semiconductor. *Nat. Mater.* **2014**, *13*, 1091–1095.

(13) Xie, Y.; Wang, Z.; Zhan, Y.; Zhang, P.; Wu, R.; Jiang, T.; Wu, S.; Wang, H.; Zhao, Y.; Nan, T.; Ma, X. Controllable Growth of Monolayer MoS_2 by Chemical Vapor Deposition via Close MoO_2 Precursor for Electrical and Optical Applications. *Nanotechnology* **2017**, *28*, 084001-1 - 084001-11.

(14) Shaw, J. C.; Zhou, H.; Chen, Y.; Weiss, N. O.; Liu, Y.; Huang, Y.; Duan, X. Chemical Vapor Deposition Growth of Monolayer $MoSe_2$ Nanosheets. *Nano Res.* **2014**, *7*, 511–517.

(15) Schmidt, H.; Wang, S.; Chu, L.; Toh, M.; Kumar, R.; Zhao, W.; Castro Neto, A. H.; Martin, J.; Adam, S.; Özyilmaz, B.; Eda, G. Transport Properties of Monolayer MoS_2 Grown by Chemical Vapor Deposition. *Nano Lett.* **2014**, *14*, 1909–1913.

(16) Shang, S.L.; Lindwall, G.; Wang, Y.; Redwing, J. M.; Anderson, T.; Liu, Z.K. Lateral Versus Vertical Growth of Two-Dimensional Layered Transition-Metal Dichalcogenides: Thermodynamic Insight into MoS_2. *Nano Lett.* **2016**, *16*, 5742–5750.

(17) Ling, X.; Lee, Y. H.; Lin, Y.; Fang, W.; Yu, L.; Dresselhaus, M. S.; Kong, J. Role of the Seeding Promoter in MoS_2 Growth by Chemical Vapor Deposition. *Nano Lett.* **2014**, *14*, 464–472.

(18) Tsai, M. L.; Su, S. H.; Chang, J. K.; Tsai, D. S.; Chen, C. H.; Wu, C. I.; Li, L. J.; Chen, L. J.; He, J. H. Monolayer MoS_2 Heterojunction Solar Cells. *ACS Nano* **2014**, *8*, 8317–8322.

(19) Cain, J. D.; Shi, F.; Wu, J.; Dravid, V. P. Growth Mechanism of Transition Metal Dichalcogenide Monolayers: The Role of Self-Seeding Fullerene Nuclei. *ACS Nano* **2016**, *10*, 5440–5445.

(20) Kang, K.; Xie, S.; Huang, L.; Han, Y.; Huang, P. Y.; Mak, K. F.; Kim, C. J.; Muller, D.; Park, J. High-Mobility Three-Atom-Thick Semiconducting Films with Wafer-Scale Homogeneity. *Nature* **2015**, *520*, 656–660.

(21) Ji, Q.; Zhang, Y.; Gao, T.; Zhang, Y.; Ma, D.; Liu, M.; Chen, Y.; Qiao, X.; Tan, P. H.; Kan, M.; Fengl, J.; Sun, Q.; Liu, Z. Epitaxial Monolayer MoS_2 on Mica with Novel Photoluminescence. *Nano Lett.* **2013**, *13*, 3870–3877.

(22) Lee, Y. H.; Zhang, X. Q.; Zhang, W.; Chang, M. T.; Lin, C. Te; Chang, K. Di; Yu, Y. C.; Wang, J. T. W.; Chang, C. S.; Li, L. J.; Lin, T.W. Synthesis of Large-Area MoS_2 Atomic Layers with Chemical Vapor Deposition. *Adv. Mater.* **2012**, *24*, 2320–2325.

(23) Najmaei, S.; Liu, Z.; Zhou, W.; Zou, X.; Shi, G.; Lei, S.; Yakobson, B. I.; Idrobo, J. C.; Ajayan, P. M.; Lou, J. Vapour Phase Growth and Grain Boundary Structure of Molybdenum Disulphide Atomic Layers. *Nat. Mater.* **2013**, *12*, 754–759.

(24) Govind Rajan, A.; Warner, J. H.; Blankschtein, D.; Strano, M. S. Generalized Mechanistic Model for the Chemical Vapor Deposition of 2D Transition Metal Dichalcogenide Monolayers. *ACS Nano* **2016**, *10*, 4330–4344.

(25) Wang, S.; Rong, Y.; Fan, Y.; Pacios, M.; Bhaskaran, H.; He, K.; Warner, J. H. Shape Evolution of Monolayer MoS_2 Crystals Grown by Chemical Vapor Deposition. *Chem. Mater.* **2014**, *26*, 6371–6379.

(26) Liu, B.; Fathi, M.; Chen, L.; Abbas, A.; Ma, Y.; Zhou, C. Chemical Vapor Deposition Growth of Monolayer WSe_2 with Tunable Device Characteristics and Growth Mechanism Study. *ACS Nano* **2015**, *9*, 6119–6127.

(27) Dumcenco, D. O.; Kobayashi, H.; Liu, Z.; Huang, Y. S.; Suenaga, K. Visualization and Quantification of Transition Metal Atomic Mixing in $Mo_{1-x}W_xS_2$ Single Layers. *Nat. Commun.* **2013**, *4*, 1351.

(28) Matetskiy, A. V.; Kibirev, I. A.; Hirahara, T.; Hasegawa, S.; Zotov, A. V.; Saranin, A. A. Direct Observation of a Gap Opening in Topological Interface States of MnSe/Bi_2Se_3 Heterostructure. *Appl. Phys. Lett.* **2015**, *107*, 091604-1 - 091604-4.

(29) Hirahara, T.; Eremeev, S. V.; Shirasawa, T.; Okuyama, Y.; Kubo, T.; Nakanishi, R.; Akiyama, R.; Takayama, A.; Hajiri, T.; Ideta, S.; Matsunami, M.; Sumida, K.; Miyamoto, K.; Takagi, Y.; Tanaka, K.; Okunda, T.; Yokoyama, T.; Kimura, S.; Hasegawa, S.; Chulkov, E.V. Large-Gap Magnetic Topological Heterostructure Formed by Subsurface Incorporation of a Ferromagnetic Layer. *Nano Lett.* **2017**, *17*, 3493–3500.

(30) Ohlhausen, J. A.; Zavadil, K. R. Time-of-Flight Secondary Ion Mass Spectrometry Measurements of a Fluorocarbon-Based Self-Assembled Monolayer on Si. *J. Vac. Sci. Technol. A Vacuum, Surfaces, Film.* **2006**, *24*, 1172–1178.

(31) Laguitton, D.; Parrish, W. Simultaneous Determination of Composition and Mass Thickness of Thin Films by Quantitative X-Ray Fluorescence Analysis. *Anal. Chem.* **1977**, *49*, 1152–1156.

(32) Remmel, T.; Werho, D. Development of an Xrf Metrology Method for Composition and Thickness of Barium Strontium Titanate Thin Films. In *Advances*; 2000; Vol. 42, pp 99–108.

(33) De Weijer, P. Van; De Boer, D. K. G. Elemental Analysis of Thin Layers by X-Rays. *Philips J. Res.* **1993**, *4747*, 247–2623.

(34) Sitko, R.; Zawisz, B. Quantification in X-Ray Fluorescence Spectrometry. In *X-Ray Spectroscopy*; 2012.

(35) Vrielink, J. A. M.; Tiggelaar, R. M.; Gardeniers, J. G. E.; Lefferts, L. Applicability of X-Ray Fluorescence Spectroscopy as Method to Determine Thickness and Composition of Stacks of Metal Thin Films: A Comparison with Imaging and Profilometry. *Thin Solid Films* **2012**, *520*, 1740–1744.

(36) Klenk, M.; Schenker, O.; Probst, U.; Bucher, E. X-Ray Fluorescence Measurements of Thin Film Chalcopyrite Solar Cells. *Sol. Energy Mater. Sol. Cells* **1999**, *58*, 299–319.

(37) Esters, M. Deposition Software for the Inficon IC6 Deposition Controller https://github.com/marcoesters/deposition_ic6.

(38) Fister, L.; Li, X.; McConnell, J.; Novet, T.; Johnson, D. C. Deposition System for the Synthesis of Modulated, Ultrathin-film Composites. *J. Vac. Sci. Technol. A Vacuum, Surfaces, Film.* **1993**, *11*, 3014–3019.

(39) Sherman, J. The Theoretical Derivation of Fluorescent X-Ray Intensities from Mixtures. *Spectrochim. Acta* **1955**, *7*, 283–306.

(40) Sauter, F. Über Den Atomaren Photoeffekt Bei Großer Härte Der Anregenden Strahlung. *Ann. d. Phys* **1931**, *9*, 217.

(41) Sauter, F. Über Den Atomaren Photoeffekt in Der K-Schale Nach Der Relativistischen Wellenmechanik Diracs. *Ann. d. Phys* **1931**, *11*, 454.

(42) Alemayehu, M. B.; Mitchson, G.; Ditto, J.; Hanken, B. E.; Asta, M.; Johnson, D. C. Charge Transfer between PbSe and $NbSe_2$ in $[(PbSe)_{1.14}]_m(NbSe_2)_1$ Ferecrystalline Compounds. *Chem. Mater.* **2014**, *26* (5), 1859–1866.

(43) Bronsema, K. D.; De Boer, J. L.; Jellinek, F. On the Structure of Molybdenum Diselenide and Disulfide. *Zeitschrift für Anorg. und Allg. Chemie* **1986**, *540*, 15–17.

CHAPTER IV

(1) Novoselov, K. S.; Mishchenko, A.; Carvalho, A.; Castro Neto, A. H. *Science (80).* **2016**, *353* (6298).

(2) Geim, A. K.; Grigorieva, I. V. *Nature* **2013**, *499* (7459), 419–425.

(3) Hamann, D. M.; Hadland, E. C.; Johnson, D. C. *Semicond. Sci. Technol.* **2017**, *32* (9), 93004.

(4) Lin, Z.; McCreary, A.; Briggs, N.; Subramanian, S.; Zhang, K.; Sun, Y.; Li, X.; Borys, N. J.; Yuan, H.; Fullerton-Shirey, S. K.; Chernikov, A.; Zhao, H.; McDonnell, S.; Lindenberg, A. M.; Xiao, K.; LeRoy, B. J.; Drndić, M.; Hwang, J. C. M.; Park, J.; Chhowalla, M.; Schaak, R. E.; Javey, A.; Hersam, M. C.; Robinson, J.; Terrones, M. *2D Mater.* **2016**, *3* (4), 42001.

(5) Rivera, P.; Schaibley, J. R.; Jones, A. M.; Ross, J. S.; Wu, S.; Aivazian, G.; Klement, P.; Seyler, K.; Clark, G.; Ghimire, N. J.; Yan, J.; Mandrus, D. G.; Yao, W.; Xu, X. *Nat. Commun.* **2015**, *6*, 6242.

(6) Hong, X.; Kim, J.; Shi, S.-F.; Zhang, Y.; Jin, C.; Sun, Y.; Tongay, S.; Wu, J.; Zhang, Y.; Wang, F. *Nat. Nanotechnol.* **2014**, *9* (9), 682–686.

(7) Zhou, X.; Zhou, N.; Li, C.; Song, H.; Zhang, Q.; Hu, X.; Gan, L.; Li, H.; Lü, J.; Luo, J.; Xiong, J.; Zhai, T. *2D Mater.* **2017**, *4* (2), 25048.

(8) Jiang, S.; Shan, J.; Mak, K. F. *Nat. Mater.* **2018**, *17* (5), 406–410.

(9) Kim, H. H.; Yang, B.; Patel, T.; Sfigakis, F.; Li, C.; Tian, S.; Lei, H.; Tsen, A. W. **2018**.

(10) Kou, L.; Wu, S.-C.; Felser, C.; Frauenheim, T.; Chen, C.; Yan, B. *ACS Nano* **2014**, *8* (10), 10448–10454.

(11) Rajput, S.; Li, Y.-Y.; Weinert, M.; Li, L. *ACS Nano* **2016**, *10* (9), 8450–8456.

(12) Märkl, T.; Kowalczyk, P. J.; Le Ster, M.; Mahajan, I. V; Pirie, H.; Ahmed, Z.; Bian, G.; Wang, X.; Chiang, T.-C.; Brown, S. A. *2D Mater.* **2017**, *5* (1), 11002.

(13) Deng, D.; Novoselov, K. S.; Fu, Q.; Zheng, N.; Tian, Z.; Bao, X. *Nat. Nanotechnol.* **2016**, *11* (3), 218–230.

(14) Tongay, S.; Fan, W.; Kang, J.; Park, J.; Koldemir, U.; Suh, J.; Narang, D. S.; Liu, K.; Ji, J.; Li, J.; Sinclair, R.; Wu, J. *Nano Lett.* **2014**, *14* (6), 3185–3190.

(15) Ohta, T.; Robinson, J. T.; Feibelman, P. J.; Bostwick, A.; Rotenberg, E.; Beechem, T. E. *Phys. Rev. Lett.* **2012**, *109* (18), 186807.

(16) Fang, H.; Battaglia, C.; Carraro, C.; Nemsak, S.; Ozdol, B.; Kang, J. S.; Bechtel, H. a; Desai, S. B.; Kronast, F.; Unal, A. a; Conti, G.; Conlon, C.; Palsson, G. K.; Martin, M. C.; Minor, A. M.; Fadley, C. S.; Yablonovitch, E.; Maboudian, R.; Javey, A. *Proc. Natl. Acad. Sci. U. S. A.* **2014**, *111* (17), 6198–6202.

(17) Shallcross, S.; Sharma, S.; Kandelaki, E.; Pankratov, O. A. *Phys. Rev. B* **2010**, *81* (16), 165105.

(18) Kim, K.; DaSilva, A.; Huang, S.; Fallahazad, B.; Larentis, S.; Taniguchi, T.; Watanabe, K.; LeRoy, B. J.; MacDonald, A. H.; Tutuc, E. *Proc. Natl. Acad. Sci. U. S. A.* **2017**, *114* (13), 3364–3369.

(19) Meng, L.; Zhang, Y.; Yan, W.; Feng, L.; He, L.; Dou, R.-F.; Nie, J.-C. *Appl. Phys. Lett.* **2012**, *100* (9), 91601.

(20) Trambly de Laissardière, G.; Namarvar, O. F.; Mayou, D.; Magaud, L. *Phys. Rev. B* **2016**, *93* (23), 235135.

(21) Zhang, C.; Chuu, C.-P.; Ren, X.; Li, M.-Y.; Li, L.-J.; Jin, C.; Chou, M.-Y.; Shih, C.-K. *Sci. Adv.* **2017**, *3* (1), e1601459.

(22) Liu, K.; Zhang, L.; Cao, T.; Jin, C.; Qiu, D.; Zhou, Q.; Zettl, A.; Yang, P.; Louie, S. G.; Wang, F.; Li, G. H.; Yankowitz, M.; Kim, K.; Havener, R. W.; Laissardiere, G. T. de; Mayou, D.; Magaud, L.; Luican, A.; Novoselov, K. S.; Hofstadter, D. R.; Bistritzer, R.; MacDonald, A. H.; Dean, C. R.; Hunt, B.; Ponomarenko, L. A.; Wang, Q. H.; Geim, A. K.; Grigorieva, I. V.; Mak, K. F.; Splendiani, A.; Qiu, D. Y.; Felipe, H.; Louie, S. G.; Cao, T.; Mak, K. F.; He, K. L.; Shan, J.; Heinz, T. F.; Zeng, H. L.; Radisavljevic, B.; Lopez-Sanchez, O.; Feng, J.; Qian, X. F.; Huang, C. W.; Li, J.; Wu, S.; Yuan, H.; Lee, Y. H.; Najmaei, S.; Zande, A. M. van der; Lauritsen, J. V.; Bollinger, M. V.; Li, Y.; Lee, C.; Molina-Sanchez, A.; Wirtz, L.; Giannozzi, P. *Nat. Commun.* **2014**, *5*, 4966.

(23) Wang, K.; Huang, B.; Tian, M.; Ceballos, F.; Lin, M.-W.; Mahjouri-Samani, M.; Boulesbaa, A.; Puretzky, A. A.; Rouleau, C. M.; Yoon, M.; Zhao, H.; Xiao, K.; Duscher, G.; Geohegan, D. B. *ACS Nano* **2016**, *10* (7), 6612–6622.

(24) Kang, J.; Li, J.; Li, S. S.; Xia, J. B.; Wang, L. W. *Nano Lett.* **2013**, *13* (11), 5485–5490.

(25) Heo, H.; Sung, J. H.; Cha, S.; Jang, B.-G.; Kim, J.-Y.; Jin, G.; Lee, D.; Ahn, J.-H.; Lee, M.-J.; Shim, J. H.; Choi, H.; Jo, M.-H. *Nat. Commun.* **2015**, *6*, 7372.

(26) Goyal, V.; Balandin, A. A. *Appl. Phys. Lett.* **2012**, *100* (7), 73113.

(27) Hong, Y.; Zhang, J.; Zeng, X. C. *J. Phys. Chem. C* **2016**, *120* (45), 26067–26075.

(28) Peng, B.; Zhang, H.; Shao, H.; Xu, Y.; Zhang, X.; Zhu, H. *RSC Adv.* **2016**, *6* (7), 5767–5773.

(29) Kandemir, A.; Yapicioglu, H.; Kinaci, A.; Çağın, T.; Sevik, C. *Nanotechnology* **2016**, *27* (5), 55703.

(30) Norouzzadeh, P.; Singh, D. J. *Nanotechnology* **2017**, *28* (7), 75708.

(31) Wang, H.; Qin, G.; Li, G.; Wang, Q.; Hu, M. *2D Mater.* **2017**, *5* (1), 15022.

(32) Jiang, J.-W.; Park, H. S.; Rabczuk, T. *J. Appl. Phys.* **2013**, *114* (6), 64307.

(33) Liu, X.; Zhang, G.; Pei, Q.-X.; Zhang, Y.-W. *Appl. Phys. Lett.* **2013**, *103* (13), 133113.

(34) Li, W.; Carrete, J.; Mingo, N. *Appl. Phys. Lett.* **2013**, *103* (25), 253103.

(35) Gu, X.; Yang, R. *Appl. Phys. Lett.* **2014**, *105* (13), 131903.

(36) Cai, Y.; Lan, J.; Zhang, G.; Zhang, Y.-W. *Phys. Rev. B* **2014**, *89* (3), 35438.

(37) Yan, R.; Simpson, J. R.; Bertolazzi, S.; Brivio, J.; Watson, M.; Wu, X.; Kis, A.; Luo, T.; Hight Walker, A. R.; Xing, H. G. *ACS Nano* **2014**, *8* (1), 986–993.

(38) Sahoo, S.; Gaur, A. P. S.; Ahmadi, M.; Guinel, M. J.-F.; Katiyar, R. S. *J. Phys. Chem. C* **2013**, *117* (17), 9042–9047.

(39) Liu, J.; Choi, G.-M.; Cahill, D. G. *J. Appl. Phys.* **2014**, *116* (23), 233107.

(40) Zhang, X.; Sun, D.; Li, Y.; Lee, G.-H.; Cui, X.; Chenet, D.; You, Y.; Heinz, T. F.; Hone, J. C. *ACS Appl. Mater. Interfaces* **2015**, *7* (46), 25923–25929.

(41) Kim, J.-Y.; Choi, S. M.; Seo, W.-S.; Cho, W.-S. *Therm. Electron. Prop. Exfoliated Met. Chalcogenides Bull. Korean Chem. Soc* **2010**, *31* (11).

(42) Zhang, J.; Hong, Y.; Wang, X.; Yue, Y.; Xie, D.; Jiang, J.; Xiong, Y.; Li, P. *J. Phys. Chem. C* **2017**, *121* (19), 10336–10344.

(43) Farahani, H.; Rajabpour, A.; Khanaki, M.; Reyhani, A. *Comput. Mater. Sci.* **2018**, *142*, 1–6.

(44) Ong, Z.-Y.; Cai, Y.; Zhang, G. *Phys. Rev. B* **2016**, *94* (16), 165427.

(45) Yuan, P.; Li, C.; Xu, S.; Liu, J.; Wang, X. *Acta Mater.* **2017**, *122*, 152–165.

(46) Taube, A.; Judek, J.; Łapińska, A.; Zdrojek, M. *ACS Appl. Mater. Interfaces* **2015**, *7* (9), 5061–5065.

(47) Hong, Y.; Ju, M. G.; Zhang, J.; Zeng, X. C. *Phys. Chem. Chem. Phys.* **2018**, *20* (4), 2637–2645.

(48) Gao, Y.; Liu, Q.; Xu, B. *ACS Nano* **2016**, *10* (5), 5431–5439.

(49) G., C. D.; Bullen, A.; Lee, S.-M. *15 ECTP Proc.* **2000**, *32*, 135–142.

(50) Chen, P.; Zhang, Z.; Duan, X.; Duan, X. *Chem. Soc. Rev.* **2018**, *47* (9), 3129–3151.

(51) Chiritescu, C.; Cahill, D. G.; Nguyen, N.; Johnson, D.; Bodapati, A.; Keblinski, P.; Zschack, P. *Science* **2007**, *315* (5810), 351–353.

(52) Muratore, C.; Varshney, V.; Gengler, J. J.; Hu, J. J.; Bultman, J. E.; Smith, T. M.; Shamberger, P. J.; Qiu, B.; Ruan, X.; Roy, A. K.; Voevodin, A. A. *Appl. Phys. Lett.* **2013**, *102* (8), 81604.

(53) Costescu, R. M.; Wall, M. A.; Cahill, D. G. *Phys. Rev. B* **2003**, *67* (5), 54302.

(54) Hamann, D. M.; Bardgett, D.; Cordova, D. L. M.; Maynard, L. A.; Hadland, E. C.; Lygo, A. C.; Wood, S. R.; Esters, M.; Johnson, D. C. *Chem. Mater.* **2018**, acs.chemmater.8b02591.

(55) Wainfan, N.; Parratt, L. G. *J. Appl. Phys.* **1960**, *31* (8), 1331–1337.

(56) Bronsema, K. D.; De Boer, J. L.; Jellinek, F. *Zeitschrift f**r Anorg. und Allg. Chemie* **1986**, *540* (9–10), 15–17.

(57) Evans, B. L.; Hazelwood, R. A. *Phys. Status Solidi* **1971**, *4* (1), 181–192.

(58) Kalikhman, V. L. *Inorg. Mater.* **1983**, *19* (7), 957–962.

(59) Brixner, L. H. *J. Inorg. Nucl. Chem.* **1962**, *24* (3), 257–263.

(60) Towle, L. C.; Oberbeck, V.; Brown, B. E.; Stajdohar, R. . *Science (80-.).* **1966**, *154* (3751), 895–896.

(61) Fan, R. *Chem. Mater.* **2001**, *13* (3), 802–805.

(62) Fan, C.; Yue, Q.; Yang, J.; Wei, Z.; Yang, S.; Li, J. *Appl. Phys. Lett.* **2014**, *104* (20), 202105.

(63) Xenogiannopoulou, E.; Tsipas, P.; Aretouli, K. E.; Tsoutsou, D.; Giamini, S. A.; Bazioti, C.; Dimitrakopulos, G. P.; Komninou, P.; Brems, S.; Huyghebaert, C.; Radu, I. P.; Dimoulas, A. *Nanoscale* **2015**, *7* (17), 7896–7905.

(64) Kim, S.; Zuo, J. M.; Nguyen, N. T.; Johnson, D. C.; Cahill, D. G. *J. Mater. Res.* **2008**, *23* (4), 1064–1067.

(65) Mann, J.; Ma, Q.; Odenthal, P. M.; Isarraraz, M.; Le, D.; Preciado, E.; Barroso, D.; Yamaguchi, K.; von Son Palacio, G.; Nguyen, A.; Tran, T.; Wurch, M.; Nguyen, A.; Klee, V.; Bobek, S.; Sun, D.; Heinz, T. F.; Rahman, T. S.; Kawakami, R.; Bartels, L. *Adv. Mater.* **2014**, *26* (9), 1399–1404.

(66) Kumar, S.; Schwingenschlö, U. .

(67) Cahill, D. G. *Rev. Sci. Instrum.* **2004**, *75* (12), 5119–5122.

(68) Blinder, A. V.; Bolgar, A. S.; Trofimova, Z. A. *Powder Metall. Met. Ceram.* **1993**, *32* (3), 234–239.

(69) Jang, H.; Ryder, C. R.; Wood, J. D.; Hersam, M. C.; Cahill, D. G. *Adv. Mater.* **2017**, *29* (35), 1700650.

(70) Jiang, P.; Qian, X.; Gu, X.; Yang, R. *Adv. Mater.* **2017**, *29* (36), 1701068.

(71) Liu, J.; Choi, G.-M.; Cahill, D. G. *J. Appl. Phys.* **2014**, *116* (23), 233107.

(72) Bhatt, R.; Basu, R.; Bhattacharya, S.; Singh, A.; Aswal, D. K.; Gupta, S. K.; Okram, G. S.; Ganesan, V.; Venkateshwarlu, D.; Surgers, C.; Navaneethan, M.; Hayakawa, Y. *Appl. Phys. A* **2013**, *111* (2), 465–470.

(73) Pisoni, A.; Jaćim, J.; Gaál, R.; Náfrádi, B.; Berger, H.; Révay c, Z.; Forró a, L. *Anisotropic transport properties of tungsten disulfide*; 2016; Vol. 114.

(74) Brixner, L. H.; Teufer, G. *Inorg. Chem.* **1963**, *2* (5), 992–996.

(75) Zhu, G.; Liu, J.; Zheng, Q.; Zhang, R.; Li, D.; Banerjee, D.; Cahill, D. G. *Nat. Commun.* **2016**, *7*, 13211.

(76) Wei, X.; Wang, Y.; Shen, Y.; Xie, G.; Xiao, H.; Zhong, J.; Zhang, G. *Appl. Phys. Lett.* **2014**, *105* (10), 103902.

(77) Ding, Y.; Chen, M.; Xiao, B. *RSC Adv.* **2016**, *6* (10), 7817–7828.

(78) Erhart, P.; Hyldgaard, P.; Lindroth, D. O. *Chem. Mater.* **2015**, *27* (16), 5511–5518.

(79) O'Hara, K. E.; Hu, X.; Cahill, D. G. *J. Appl. Phys.* **2001**, *90* (9), 4852–4858.

(80) Gunning, N. S.; Feser, J.; Beekman, M.; Cahill, D. G.; Johnson, D. C. *J. Am. Chem. Soc.* **2015**, *137* (27), 8803–8809.

(81) Gunning, N. S.; Feser, J.; Falmbigl, M.; Beekman, M.; Cahill, D. G.; Johnson, D. C. *Semicond. Sci. Technol.* **2014**, *29* (12), 124007.

(82) Heideman, C. L.; Tepfer, S.; Lin, Q.; Rostek, R.; Zschack, P.; Anderson, M. D.; Anderson, I. M.; Johnson, D. C. *J. Am. Chem. Soc.* **2013**, *135* (30), 11055–11062.

(83) Chiritescu, C.; Cahill, D. G.; Heideman, C.; Lin, Q.; Mortensen, C.; Nguyen, N. T.; Johnson, D.; Rostek, R.; Böttner, H. *J. Appl. Phys.* **2008**, *104* (3), 33533.

(84) Li, Z.; Bauers, S. R.; Poudel, N.; Hamann, D.; Wang, X.; Choi, D. S.; Esfarjani, K.; Shi, L.; Johnson, D. C.; Cronin, S. B. *Nano Lett.* **2017**, *17* (3), 1978–1986.

(85) Wu, X.; Luo, T. *J. Appl. Phys.* **2014**, *115* (1), 14901.

(86) Mortazavi, B.; Rabczuk, T. *RSC Adv.* **2017**, *7* (18), 11135–11141.

CHAPTER V

(1) Padture, N. P.; Gell, M.; Jordan, E. H.; Sechrist, Z. A.; George, S. M. *Science* **2002**, *296* (5566), 280–284.

(2) Clarke, D. R.; Oechsner, M.; Padture, N. P. *MRS Bull.* **2012**, *37* (10), 891–898.

(3) Raoux, S.; Xiong, F.; Wuttig, M.; Pop, E. *MRS Bull.* **2014**, *39* (8), 703–710.

(4) Wicklein, B.; Kocjan, A.; Salazar-Alvarez, G.; Carosio, F.; Camino, G.; Antonietti, M.; Bergström, L. *Nat. Nanotechnol.* **2015**, *10* (3), 277–283.

(5) Cahill, D. G.; Watson, S. K.; Pohl, R. O. *Phys. Rev. B* **1992**, *46* (10), 6131–6140.

(6) Jain, A.; Rogojevic, S.; Ponoth, S.; Gill, W. N.; Plawsky, J. L.; Simonyi, E.; Chen, S.-T.; Ho, P. S. *J. Appl. Phys.* **2002**, *91* (5), 3275–3281.

(7) Costescu, R. M.; Cahill, D. G.; Fabreguette, F. H.; Sechrist, Z. A.; George, S. M. *Science (80-.).* **2004**, *303* (5660), 989–990.

(8) Chiritescu, C.; Cahill, D. G.; Nguyen, N.; Johnson, D.; Bodapati, A.; Keblinski, P.; Zschack, P. *Science* **2007**, *315* (5810), 351–353.

(9) Gunning, N. S.; Feser, J.; Falmbigl, M.; Beekman, M.; Cahill, D. G.; Johnson, D. C. *Semicond. Sci. Technol.* **2014**, *29* (12), 124007.

(10) Gunning, N. S.; Feser, J.; Beekman, M.; Cahill, D. G.; Johnson, D. C. *J. Am. Chem. Soc.* **2015**, *137* (27), 8803–8809.

(11) Hamann, D. M.; Bardgett, D.; Cordova, D. L. M.; Maynard, L. A.; Hadland, E. C.; Lygo, A. C.; Wood, S. R.; Esters, M.; Johnson, D. C. *Chem. Mater.* **2018**, acs.chemmater.8b02591.

(12) Wainfan, N.; Parratt, L. G. *J. Appl. Phys.* **1960**, *31* (8), 1331–1337.

(13) Bronsema, K. D.; De Boer, J. L.; Jellinek, F. *Zeitschrift f*[illegible]*r Anorg. und Allg. Chemie* **1986**, *540* (9–10), 15–17.

(14) Evans, B. L.; Hazelwood, R. A. *Phys. Status Solidi* **1971**, *4* (1), 181–192.

(15) Kalikhman, V. L. *Inorg. Mater.* **1983**, *19* (7), 957–962.

(16) Brixner, L. H. *J. Inorg. Nucl. Chem.* **1962**, *24* (3), 257–263.

(17) Towle, L. C.; Oberbeck, V.; Brown, B. E.; Stajdohar, R. . *Science (80-.).* **1966**, *154* (3751), 895–896.

(18) Busch, A.; Fröhlich, C. /; Hulliger, C. /; Busch, G.; Fröhlich, C.; Hulliger, F. **1961**.

(19) Pałosz, B.; Salje, E.; IUCr. *J. Appl. Crystallogr.* **1989**, *22* (6), 622–623.

(20) Mann, J.; Ma, Q.; Odenthal, P. M.; Isarraraz, M.; Le, D.; Preciado, E.; Barroso, D.; Yamaguchi, K.; von Son Palacio, G.; Nguyen, A.; Tran, T.; Wurch, M.; Nguyen, A.; Klee, V.; Bobek, S.; Sun, D.; Heinz, T. F.; Rahman, T. S.; Kawakami, R.; Bartels, L. *Adv. Mater.* **2014**, *26* (9), 1399–1404.

(21) Tongay, S.; Narang, D. S.; Kang, J.; Fan, W.; Ko, C.; Luce, A. V.; Wang, K. X.; Suh, J.; Patel, K. D.; Pathak, V. M.; Li, J.; Wu, J. *Appl. Phys. Lett.* **2014**, *104* (1), 12101.

(22) Tongay, S.; Zhou, J.; Ataca, C.; Lo, K.; Matthews, T. S.; Li, J.; Grossman, J. C.; Wu, J. *Nano Lett.* **2012**, *12* (11), 5576–5580.

(23) Kim, B. S.; Rhim, J.-W.; Kim, B.; Kim, C.; Park, S. R. *Sci. Rep.* **2016**, *6* (1), 36389.

(24) Martínez-Escobar, D.; Ramachandran, M.; Sánchez-Juárez, a.; Narro Rios, J. S. *Thin Solid Films* **2013**, *535* (1), 390–393.

(25) Fernandes, P. A.; Sousa, M. G.; Salomé, P. M. P.; Leitão, J. P.; Da Cunha, A. F. **2013**, *15*.

(26) Gonzalez, J. M.; Oleynik, I. I. *Phys. Rev. B* **2016**, *94* (12), 125443.

(27) Chen, P.; Shang, J.; Yang, Y.; Wang, R.; Cheng, X. *Annealing tunes interlayer coupling and optoelectronic property of bilayer SnSe2/MoSe2 heterostructures*; 2017; Vol. 419.

(28) Muratore, C.; Varshney, V.; Gengler, J. J.; Hu, J. J.; Bultman, J. E.; Smith, T. M.; Shamberger, P. J.; Qiu, B.; Ruan, X.; Roy, A. K.; Voevodin, A. A. *Appl. Phys. Lett.* **2013**, *102* (8), 81604.

(29) Jiang, P.; Qian, X.; Gu, X.; Yang, R. *Adv. Mater.* **2017**, *29* (36), 1701068.

(30) Liu, J.; Choi, G.-M.; Cahill, D. G. *J. Appl. Phys.* **2014**, *116* (23), 233107.

(31) Bhatt, R.; Basu, R.; Bhattacharya, S.; Singh, A.; Aswal, D. K.; Gupta, S. K.; Okram, G. S.; Ganesan, V.; Venkateshwarlu, D.; Surgers, C.; Navaneethan, M.; Hayakawa, Y. *Appl. Phys. A* **2013**, *111* (2), 465–470.

(32) Pisoni, A.; Jaćim, J.; Gaál, R.; Náfrádi, B.; Berger, H.; Révay c, Z.; Forró a, L. *Anisotropic transport properties of tungsten disulfide*; 2016; Vol. 114.

(33) Zhu, G.; Liu, J.; Zheng, Q.; Zhang, R.; Li, D.; Banerjee, D.; Cahill, D. G. *Nat. Commun.* **2016**, *7*, 13211.

(34) Wei, X.; Wang, Y.; Shen, Y.; Xie, G.; Xiao, H.; Zhong, J.; Zhang, G. *Appl. Phys. Lett.* **2014**, *105* (10), 103902.

(35) Ding, Y.; Chen, M.; Xiao, B. *RSC Adv.* **2016**, *6* (10), 7817–7828.

(36) Gu, X.; Yang, R. *Appl. Phys. Lett.* **2014**, *105* (13), 131903.

(37) Erhart, P.; Hyldgaard, P.; Lindroth, D. O. *Chem. Mater.* **2015**, *27* (16), 5511–5518.

(38) Heideman, C. L.; Tepfer, S.; Lin, Q.; Rostek, R.; Zschack, P.; Anderson, M. D.; Anderson, I. M.; Johnson, D. C. *J. Am. Chem. Soc.* **2013**, *135* (30), 11055–11062.

(39) Chiritescu, C.; Cahill, D. G.; Heideman, C.; Lin, Q.; Mortensen, C.; Nguyen, N. T.; Johnson, D.; Rostek, R.; Böttner, H. *J. Appl. Phys.* **2008**, *104* (3), 33533.

(40) Li, Z.; Bauers, S. R.; Poudel, N.; Hamann, D.; Wang, X.; Choi, D. S.; Esfarjani, K.; Shi, L.; Johnson, D. C.; Cronin, S. B. *Nano Lett.* **2017**, *17* (3), 1978–1986.

CHAPTER VI

(1) Mak, K. F.; Lee, C.; Hone, J.; Shan, J.; Heinz, T. F. *Phys. Rev. Lett.* **2010**, *105* (13), 136805.

(2) Splendiani, A.; Sun, L.; Zhang, Y.; Li, T.; Kim, J.; Chim, C. Y.; Galli, G.; Wang, F. *Nano Lett.* **2010**, *10* (4), 1271–1275.

(3) Zhang, Y.; Chang, T.-R.; Zhou, B.; Cui, Y.-T.; Yan, H.; Liu, Z.; Schmitt, F.; Lee, J.; Moore, R.; Chen, Y.; Lin, H.; Jeng, H.-T.; Mo, S.-K.; Hussain, Z.; Bansil, A.; Shen, Z.-X. *Nat. Nanotechnol.* **2013**, *9* (2), 111–115.

(4) Zhao, W.; Ghorannevis, Z.; Chu, L.; Toh, M.; Kloc, C.; Tan, P.-H.; Eda, G. *ACS Nano* **2013**, *7* (1), 791–797.

(5) Gutiérrez, H. R.; Perea-López, N.; Elías, A. L.; Berkdemir, A.; Wang, B.; Lv, R.; López-Urías, F.; Crespi, V. H.; Terrones, H.; Terrones, M. *Nano Lett.* **2013**, *13* (8), 3447–3454.

(6) Wang, Q. H.; Kalantar-Zadeh, K.; Kis, A.; Coleman, J. N.; Strano, M. S. *Nat. Nanotechnol.* **2012**, *7* (11), 699–712.

(7) Peng, B.; Ang, P. K.; Loh, K. P. *Nano Today* **2015**, *10* (2), 128–137.

(8) Radisavljevic, B.; Radenovic, A.; Brivio, J.; Giacometti, V.; Kis, A. *Nat. Nanotechnol.* **2011**, *6* (3), 147–150.

(9) Ross, J. S.; Klement, P.; Jones, A. M.; Ghimire, N. J.; Yan, J.; Mandrus, D. G.; Taniguchi, T.; Watanabe, K.; Kitamura, K.; Yao, W.; Cobden, D. H.; Xu, X. *Nat. Nanotechnol.* **2014**, *9* (4), 268–272.

(10) Withers, F.; Del Pozo-Zamudio, O.; Mishchenko, A.; Rooney, A. P.; Gholinia, A.; Watanabe, K.; Taniguchi, T.; Haigh, S. J.; Geim, A. K.; Tartakovskii, A. I.; Novoselov, K. S. *Nat. Mater.* **2015**, *14* (3), 301–306.

(11) Furchi, M. M.; Pospischil, A.; Libisch, F.; Burgdörfer, J.; Mueller, T. *Nano Lett.* **2014**, *14* (8), 4785–4791.

(12) Pospischil, A.; Furchi, M. M.; Mueller, T. *Nat. Nanotechnol.* **2014**, *9* (4), 257–261.

(13) Fan, X.; Xu, P.; Zhou, D.; Sun, Y.; Li, Y. C.; Nguyen, M. A. T.; Terrones, M.; Mallouk, T. E. *Nano Lett.* **2015**, *15* (9), 5956–5960.

(14) Hamann, D. M.; Hadland, E. C.; Johnson, D. C. *Semicond. Sci. Technol.* **2017**, *32* (9), 93004.

(15) Rivera, P.; Schaibley, J. R.; Jones, A. M.; Ross, J. S.; Wu, S.; Aivazian, G.; Klement, P.; Seyler, K.; Clark, G.; Ghimire, N. J.; Yan, J.; Mandrus, D. G.; Yao, W.; Xu, X. *Nat. Commun.* **2015**, *6*, 6242.

(16) Zhang, C.; Chuu, C.-P.; Ren, X.; Li, M.-Y.; Li, L.-J.; Jin, C.; Chou, M.-Y.; Shih, C.-K. .

(17) Hong, X.; Kim, J.; Shi, S.-F.; Zhang, Y.; Jin, C.; Sun, Y.; Tongay, S.; Wu, J.; Zhang, Y.; Wang, F. *Nat. Nanotechnol.* **2014**, *9* (9), 682–686.

(18) Kappera, R.; Voiry, D.; Yalcin, S. E.; Branch, B.; Gupta, G.; Mohite, A. D.; Chhowalla, M. *Nat Mater* **2014**, *13* (12), 1128–1134.

(19) Chuang, H.-J.; Chamlagain, B.; Koehler, M.; Perera, M. M.; Yan, J.; Mandrus, D.; Tománek, D.; Zhou, Z. *Nano Lett.* **2016**, *16* (3), 1896–1902.

(20) Wang, H.; Lu, Z.; Xu, S.; Kong, D.; Cha, J. J.; Zheng, G.; Hsu, P.-C.; Yan, K.; Bradshaw, D.; Prinz, F. B.; Cui, Y. *Proc. Natl. Acad. Sci. U. S. A.* **2013**, *110* (49), 19701–19706.

(21) Kappera, R.; Voiry, D.; Yalcin, S. E.; Jen, W.; Acerce, M.; Torrel, S.; Branch, B.; Lei, S.; Chen, W.; Najmaei, S.; Lou, J.; Ajayan, P. M.; Gupta, G.; Mohite, A. D.; Chhowalla, M. *APL Mater.* **2014**, *2* (9), 92516.

(22) Cho, S.; Kim, S.; Kim, J. H.; Zhao, J.; Seok, J.; Keum, D. H.; Baik, J.; Choe, D.-H.; Chang, K. J.; Suenaga, K.; Kim, S. W.; Lee, Y. H.; Yang, H. *Science* **2015**, *349* (6248), 625–628.

(23) Ma, Y.; Liu, B.; Zhang, A.; Chen, L.; Fathi, M.; Shen, C.; Abbas, A. N.; Ge, M.; Mecklenburg, M.; Zhou, C. *ACS Nano* **2015**, *9* (7), 7383–7391.

(24) Allain, A.; Kang, J.; Banerjee, K.; Kis, A. *Nat. Mater.* **2015**, *14* (12), 1195–1205.

(25) Zhao, Y.; Xu, K.; Pan, F.; Zhou, C.; Zhou, F.; Chai, Y. *Adv. Funct. Mater.* **2017**, *27* (19), 1603484.

(26) Mitchson, G.; Falmbigl, M.; Ditto, J.; Johnson, D. C. *Inorg. Chem.* **2015**, *54* (21), 10309–10315.

(27) Mitchson, G.; Hadland, E.; Göhler, F.; Wanke, M.; Esters, M.; Ditto, J.; Bigwood, E.; Ta, K.; Hennig, R. G.; Seyller, T.; Johnson, D. C. *ACS Nano* **2016**, *10* (10), 9489–9499.

(28) Wood, S. R.; Merrill, D. R.; Falmbigl, M.; Moore, D. B.; Ditto, J.; Esters, M.; Johnson, D. C. *Chem. Mater.* **2015**, *27* (17), 6067–6076.

(29) Lin, Q.; Smeller, M.; Heideman, C. L.; Zschack, P.; Koyano, M.; Anderson, M. D.; Kykyneshi, R.; Keszler, D. A.; Anderson, I. M.; Johnson, D. C. *Chem. Mater.* **2010**, *22* (3), 1002–1009.

(30) Atkins, R.; Wilson, J.; Zschack, P.; Grosse, C.; Neumann, W.; Johnson, D. C. *Chem. Mater.* **2012**, *24* (23), 4594–4599.

(31) Hamann, D. M.; Bardgett, D.; Cordova, D. L. M.; Maynard, L. A.; Hadland, E. C.; Lygo, A. C.; Wood, S. R.; Esters, M.; Johnson, D. C. *Chem. Mater.* **2018**, acs.chemmater.8b02591.

(32) Schaffer, M.; Schaffer, B.; Ramasse, Q. *Ultramicroscopy* **2012**, *114*, 62–71.

(33) van der Pauw, L. J. *Phillips Tech. Rev.* **1958**, *20*, 220–224.

(34) Merrill, D. R.; Moore, D. B.; Coffey, M. N.; Jansons, A. W.; Falmbigl, M.; Johnson, D. C. *Semicond. Sci. Technol.* **2014**, *29* (6), 64004.

(35) and, C. P. V.; Tirado, J. L.; and, K. A.; Jumas, J. C.; and, A. A. T.; Kra, G. **1999**.

(36) Wainfan, N.; Parratt, L. G. *J. Appl. Phys.* **1960**, *31* (8), 1331–1337.

(37) Bronsema, K. D.; De Boer, J. L.; Jellinek, F. *Zeitschrift f*[illegible]*r Anorg. und Allg. Chemie* **1986**, *540* (9–10), 15–17.

(38) Towle, L. C.; Oberbeck, V.; Brown, B. E.; Stajdohar, R. . *Science (80-.).* **1966**, *154* (3751), 895–896.

(39) Brixner, L. H. *J. Inorg. Nucl. Chem.* **1962**, *24* (3), 257–263.

(40) Evans, B. L.; Hazelwood, R. A. *Phys. Status Solidi* **1971**, *4* (1), 181–192.

(41) Kalikhman, V. L. *Inorg. Mater.* **1983**, *19* (7), 957–962.

(42) Alemayehu, M. B.; Falmbigl, M.; Ta, K.; Johnson, D. C. *Chem. Mater.* **2015**, *27* (6), 2158–2164.

(43) Eda, G.; Yamaguchi, H.; Voiry, D.; Fujita, T.; Chen, M.; Chhowalla, M. *Nano Lett.* **2011**, *11* (12), 5111–5116.